Development of nanostructured metal oxides for solar fuels (Alternative Format Thesis)

Regue Grino, Miriam

Award date:
2020

Awarding institution:
University of Bath

Development of nanostructured metal oxides for solar fuels

Miriam Regue Grino

A thesis submitted for the degree of Doctor of Philosophy

University of Bath

Department of Chemical Engineering

September 2019

Copyright notice

Restrictions on use and licensing

This thesis/portfolio may be made available for consultation within the University Library and may be photocopied or lent to other libraries for the purposes of consultation.

Access to this thesis/portfolio in print or electronically is restricted until _____

Signed on behalf of the Doctoral College_____

Declaration of authorship

I am the author of this thesis and the work described therein was carried out by myself personally. Contribution of other researchers in each individual work is detailed in 'Declaration of authorship' sections.

Candidate's signature

Table of contents

Acknowledgements

I would like to express my sincere gratitude to my main supervisor Dr. Salvador Eslava for giving me the opportunity to develop my PhD in his research group, as well as for his excellence guidance, support and advice during all these years. His motivation, enthusiasm and expertise in research have truly inspired me. A further thank you goes to all Eslava group members, in particular Emma, Ria, Shawn, Jifang and Santosh. It has been a great pleasure to work with all of you.

I would also like to thank my co-supervisor, Dr. Andrew Johnson for all his support and advice in this PhD. His expertise in chemical vapor deposition has truly helped me. Furthermore, my thanks also go to all Johnson group members for all their help.

My thanks also go to the various people that have helped me in this journey- Philip Fletcher, Ursula Potter and Gabriele Kociok-Köhn from the Material and Characterization facility of the University of Bath, the technical team of the Chemical Engineering department and Camilo Mesa from Imperial College London for his help with transient absorption spectroscopy measurements.

A thank you must also go to the people from the Institute of Solar Fuels in Helmholtz Zentrum Berlin (HZB) where I carried out my three months internship. In particular, I would like to thank Dr. Ibbi Ahmet and Dr. Prince Saurabh Bassi for all their enormous help and support during these months. I had an amazing time there, thank you!

Thanks must also go to the fantastic people I met while my time in Bath – Maria, Leyorla, Cei, Isabella, Felix, Carlos, Jane and Alba. Thanks for all the great time we have spent together.

A very special thank you goes to my family: my parents, Josep and Lourdes, my brother Robert and his partner, Alba. Thanks for your enormous support.

Last but not least, my most special thanks go to Oriol. Thanks for being always by my side. This journey would not have been possible without you. Gràcies!

Abstract

Global warming is a major concern in the current world owing to its contribution to natural disasters. CO_2 is one of the main greenhouse gases causing global warming and its anthropogenic release in the environment mainly comes from the use of fossil fuels as a source of energy. Due to the increase in both the world's population and living standards, the amount of energy consumed throughout the last 50 years has almost doubled, resulting in an associated increase of CO_2 emissions in the environment. This increase in CO_2 emissions is against the recommendation recently reported in the 2018 intergovernmental panel on climate change report, in which it was suggested that CO_2 emissions should fall by about 45 % of 2010 levels by 2030 and achieve 'net zero' emissions by 2050. A feasible approach to fulfil this requirement is to change the current energy portfolio to a more sustainable one. Although several renewable sources of energy such as wind and solar are currently becoming a part of the energy mix, they suffer from intermittent cycles in which the energy production and demand are not decoupled. In this regard, photoelectrochemical (PEC) water splitting, where solar energy is used on photoelectrodes to split water to form H_2 and O_2, could be a viable complement to current renewable sources of energy and most importantly, an alternative to fossil fuels based sources of energy. H_2 is considered to be the energy vector that could contribute to a fully sustainable society.

In this PhD thesis, Chapter 1 describes the evolution of the energy consumed and sources of energy used over the last 50 years and sets the scene of the necessity to use solar fuels, in particular H_2, as an alternative to fossil fuels. A list of current methods of solar H_2 production is reviewed highlighting the benefits of the PEC technology. In Chapter 2, the fundamentals of PEC technology including requirements, processes and mechanisms involved in the PEC technology are reviewed along with the state-of-the-art of the main materials currently employed with their advantages and limitations. Chapter 3 illustrates an overview of the aerosol-assisted chemical vapor deposition (AACVD) method, a highly versatile method for the synthesis of nanostructured thin films, that is widely used in the experimental part of this thesis. Finally, Chapters 4, 5 and 6 cover the experimental work performed in this thesis. In particular, in Chapter 4 a facile approach for the synthesis of Mo-doped TiO_2 photoanodes prepared by spray pyrolysis from a polyoxotitanium oxo/alkoxy cluster is presented. This chapter investigates the role of molybdenum in the TiO_2 lattice structure and its contribution to the enhanced PEC performance. Chapter 5 illustrates the advantages of using AACVD and a different titanium oxo/alkoxy cluster for the synthesis of highly nanostructured TiO_2 photoanodes with preferential facets exposed. Characterization techniques such as TEM, XRD, linear sweep voltammetry and time-resolved microwave conductivity measurements reveal the preferential exposure of the anatase {0 1 0} facet, the excellent photocurrent

performance and the main recombination pathways of the photogenerated charges. Furthermore, it is also shown and discussed how the metastable anatase TiO_2 phase is maintained up to 1000 °C after annealing in air offering an alternative application in the smart tile ceramic industry. In Chapter 6, Zn-doped Fe_2TiO_5 photoanodes prepared by AACVD are studied for the first time. Through the use of characterization techniques such as linear sweep voltammetry, impedance spectroscopy and ultraviolet photoelectron spectroscopy measurements it is revealed that the improved PEC performance over pristine Fe_2TiO_5 photoanodes originates primarily from improved charge separation and injection efficiencies along with an increase in carrier concentration and better charge transfer kinetics.

Finally, the last chapter of this thesis summarizes the main conclusions of this work and gives a general overview of future research pathways in the field of PEC water splitting.

Publication list

M. Regue, S. Sibby, I. Y. Ahmet, D. Friedrich, F. F. Abdi, A. L. Johnson and S. Eslava, TiO_2 photoanodes with exposed {0 1 0} facets grown by aerosol-assisted chemical vapor deposition of a titanium oxo/alkoxy cluster, *J. Mater. Chem. A*, 2019, **7**, 19161-19172

I. Poli, U. Hintermair, **M. Regue**, S. Kumar, E. V. Sackville, J. Baker, T. M. Watson, S. Eslava, P. J. Cameron, Graphite-protected $CsPbBr_3$ perovskite photoanodes functionalized with water oxidation catalyst for oxygen evolution in water, *Nat. Commun*, 2019, **10**, 1-10

D. Walsh, J. Zhang, **M. Regue**, R. Dassanayake and S. Eslava, Simultaneous formation of FeO_x electrocatalyst coating within hematite photoanodes for solar water splitting, *ACS Appl. Energy Mater.*, 2019, **2**, 2043-2052

M. Regue, K. Armstrong, D. Walsh, E. Richards, A. L. Johnson and S. Eslava, Mo-doped TiO_2 photoanodes using $[Ti_4Mo_2O_8(Oet)_{10}]_2$ bimetallic oxo cages as a single source precursor, *Sustain. Energy Fuels*, 2018, **2**, 2674–2686.

M. Regue, I.Y. Ahmet, P.S. Bassi, A.L. Johnson, S. Eslava and F.F Abdi, Zn doped Fe_2TiO_5 photoanodes grown by aerosol-assisted chemical vapor deposition, *draft manuscript*

M. Regue, S. Kumar, S. Eslava, Recent advances on photocatalytic materials for solar fuel production from water and carbon dioxide, Royal Society of Chemistry, *submitted*

S. Kumar, **M. Regue**, M. A. Isaacs, E. Freeman, S. Eslava, All-inorganic $CsPbBr_3$ Nanocrystals: A Gram-Scale Mechanochemical Synthesis and Selective Photocatalytic CO_2 Reduction to Methane, *manuscript in preparation*

Chapter 1. Introduction

1.1 World energy consumption

One of the main challenges of the 21st century is to be able to supply enough energy to the world's population to at least accomplish the minimum living standards requirements. The amount of energy consumed by the world has increased significantly throughout the last 50 years, not only because of the population increase but also due to the current living standards in which energy sources have become essential. For instance, in Europe, the amount of energy consumed has almost doubled in the last 53 years (Fig. 1-1), being of *ca.* 1060 Mtoe (Millions tones oil equivalent) in 1965 and reaching up to *ca*. 2051 Mtoe in 2018.

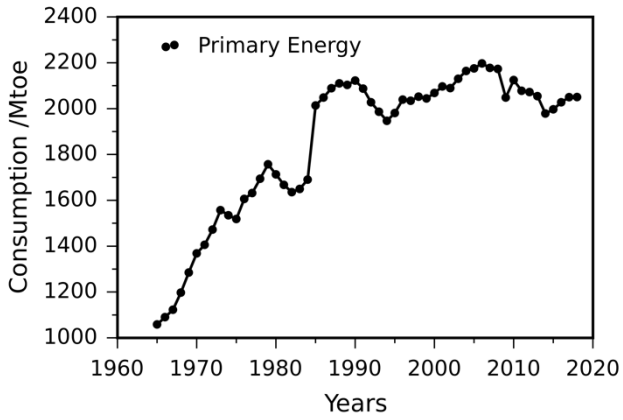

Fig. 1-1 Total primary energy consumed in Europe from 1965 to 2018. Primary energy comprises fossil fuels (such as oil, gas and natural gas) and renewable sources of energy. Data extracted from the BP 2019 Statistical Review of World Energy.[1]

This pronounced increase in the energy consumption has become detrimental for both world's population and environment, mainly because the vast majority of this energy consumed comes from fossil fuels sources of energy, such as oil, natural gas and coal. Fig. 1-2 shows the evolution of energy consumption by fuel type in Europe from 1965 until 2018. In the 1960's the majority of energy consumed came from oil followed by coal and gas, until the late 1990's, where gas consumption overtook coal. Most importantly, it was not until the 2000's, when Europe started to consume energy from renewable sources (solar, wind, geothermal and biomass). In 2017, the energy mix of Europe was made up of 14 % of renewable energies.[2]

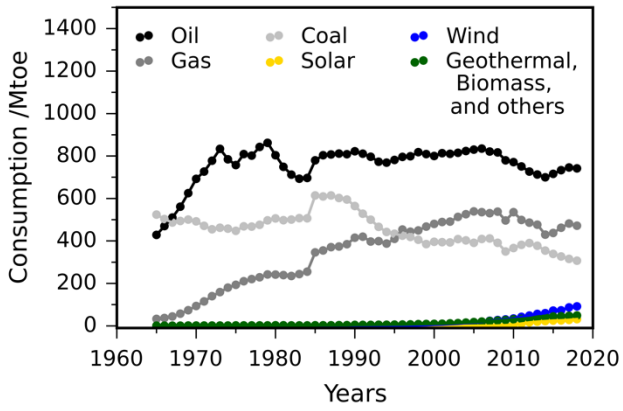

Fig. 1-2 Energy consumed by fuel in Europe from 1965 to 2018. Data extracted from the BP 2019 Statistical Review of World Energy.[1]

When comparing the energy consumed by fuel type in 1965 and 2018 (Fig. 1-3), the relative amount of fossil fuels consumed has been reduced from *ca*. 93% to 74%, even though the overall consumption throughout the years has increased, as shown in Fig. 1-2. The relative decrease in fossil fuels is mainly due to the increase in nuclear (8%) and renewable energies (15.5%).

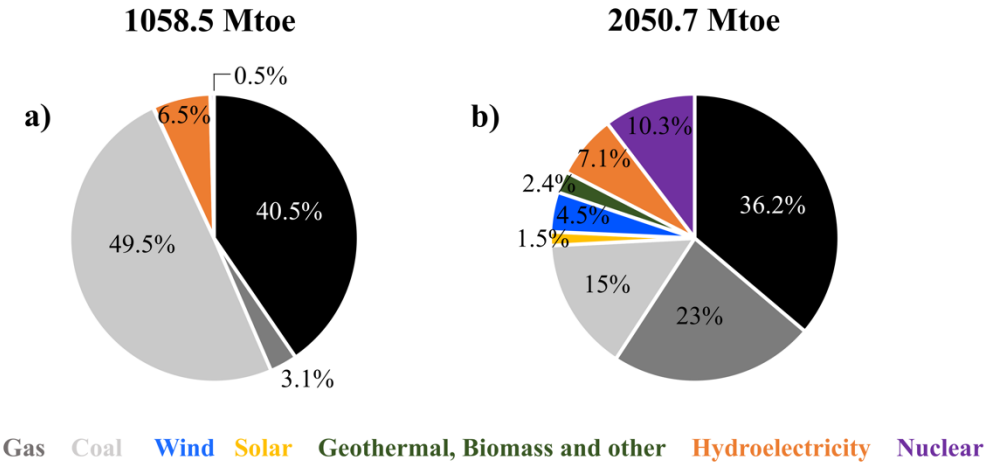

Fig. 1-3 Distribution of energy consumed by fuel in (a) 1965 and (b) 2018. The total primary energy consumption in 1965 and 2018 was of 1058.5 and 2050.7 Mtoe, respectively. Data extracted from the BP 2019 Statistical Review of World Energy.[1]

The main concern associated with the use of fossil fuels and coal is the unavoidable release of greenhouse gas emissions, in particular CO_2, which has a harmful impact on global warming and thus climate change. The burning of fossil fuels is the main source of CO_2 emissions released in the environment. Although a slight decrease in CO_2 emissions has been achieved since the early 2000's, this decrease is not enough to mitigate the effects of climate change (Fig. 1-4). In fact, in 2018 global energy-related CO_2 emissions grew by 1.7 %, being the highest rate of growth since 2013, and 70 % higher than the average increase since 2010.[3] This

sudden rise in CO_2 emissions was mainly driven by the higher energy consumption resulting from both a robust economy and extreme weather conditions in some parts of the world that required a higher energy demand for heating and cooling systems.[3] The 2018 intergovernmental panel on climate change report highlighted the urgent need of reducing these emissions in order to reduce the global temperature rise to 1.5 °C in the upcoming future. Ideally, these emissions should fall by about 45 % of the 2010 levels by 2030 and achieve 'net zero' emissions by 2050.[4] The European Union has already established and set a climate action plan to facilitate meeting these targets. For instance, by 2020 it is expected a 20 % cut in greenhouse gas emissions of the 1990 levels, a 20 % of the energy mix must be of renewable energies and a 20 % improvement in energy efficiency must be achieved. All the above should be reached through the implementation of several policy measures and actions, such as an emission trading system and a major investment in low carbon technologies, including renewable energy and both carbon capture and storage technologies. Along the same lines, the European Union also aims to reach a climate-neutral Europe by 2050. This long term strategic vision aims to meet this target by investing more into new technologies and aligning actions in key areas such as industrial policy, finance and research.[5]

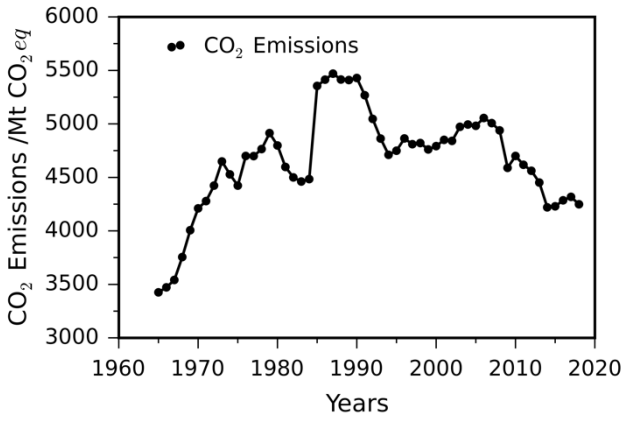

Fig. 1-4 CO_2 emissions measured in Million tons of CO_2 from 1965 to 2018. Data extracted from the BP 2019 Statistical Review of World Energy.[1]

Briefly, failing on fulfilling this could result in a global sea level rise, extreme temperatures in many regions, detrimental impacts on ecosystems and biodiversity including species loss and extinction, rise in ocean temperature, increase of ocean acidity due to high CO_2 levels and decrease of oxygen levels, risks on population health, food security, water supply and human security. Therefore, actions to move towards 'a zero emission' society must be taken and implemented, especially in sectors such as land (agriculture), energy, construction of more energy efficient buildings, transport and cities.[4]

1.2 Solar fuels

Solar fuels are a great alternative to conventional fuels derived from fossil sources. These fuels are produced by capturing the solar energy reaching the Earth's surface and storing the energy in the chemical bonds of a material, or 'fuel' so that it can be used when needed.[6] Currently, the two most important solar fuels are hydrogen (H_2) and carbon-based fuels such as methane or carbon monoxide. Both fuels are of important interest for industry; for instance H_2 can be used either as a transport fuel or feedstock, whereas carbon-based fuels, are key feedstocks for the industrial production of fertilizers, pharmaceuticals, plastics and synthetic liquid fuels.[6] The use of solar fuels, in particular H_2, can help to change the energy portfolio of the society towards a more sustainable one and overcome some of the limitations and challenges that exist even with renewable energy sources. For instance, as the contribution of solar and wind energy increases in the total energy mix, there is an increasing need of solving the issue of decoupling the energy demand and production due to intermittent cycles and the challenging transport associated with these sources of energy. In this regard, solar fuels, such as H_2, offer feasible solutions to those limitations. Firstly, solar energy can be easily stored in the chemical bonds in the form of fuel and used when needed. Secondly, solar fuels could be transported from the place where they were produced to where they are actually needed by means of air, sea or road. Fig. 1-5 shows a schematic model showing the concept of solar H_2 in a daily basis in which both storage and transportation of solar energy are used in an industry environment for either electricity generation or transport of vehicles.

Among the different solar fuels, H_2 seems to be one of the most attractive and promising fuels and for many it has been considered the only energy vector that can be used in a fully sustainable energy system, since it can be easily produced from water, giving H_2 and O_2 as the only by-products, as shown below:[7,8]

$$2H_2O \rightleftarrows 2H_2 + O_2 \; \Delta G = 237 \; KJ \; mol^{-1} \qquad 1\text{-}1$$

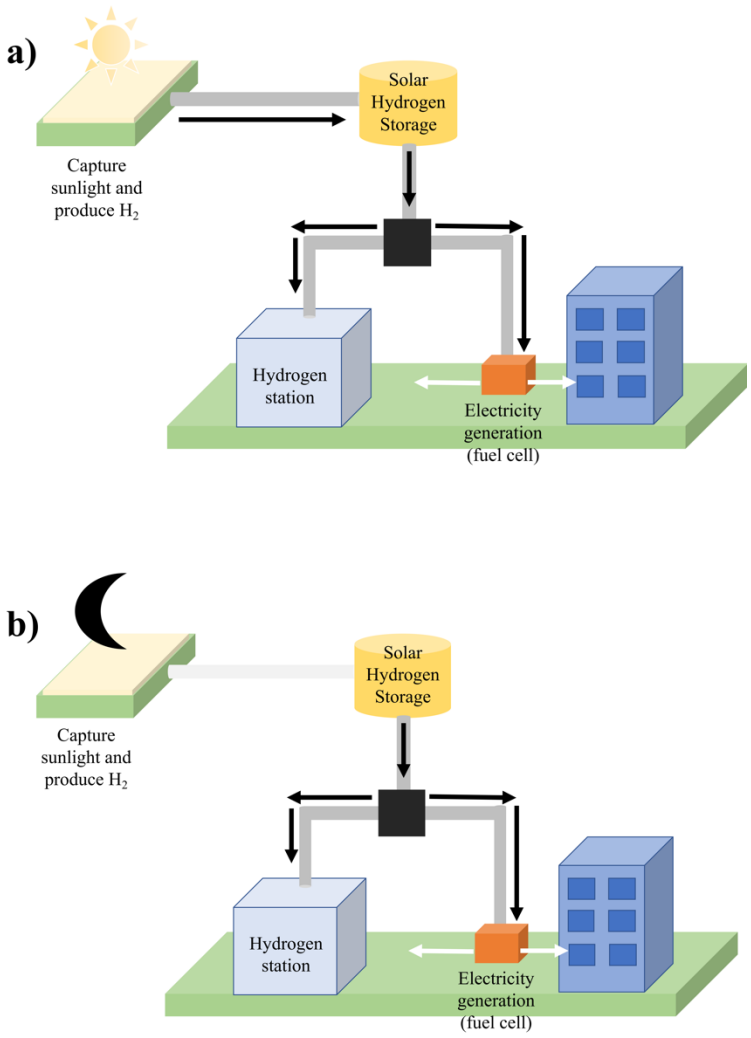

Fig. 1-5 Schematic model showing the implementation of solar H_2 as an energy carrier. (a) At day light conditions, solar H_2 is produced and can be either stored, used as a transport fuel or to produce electricity. (b) At night or cloudy periods, only stored solar H_2 is used for transport and electricity generation. Adapted from ref.[6]

1.3 Current methods of hydrogen production from renewable energies

Nowadays, steam methane reforming (SMR) accounts for 80-85 % of the world's total hydrogen production, followed by coal gasification and water electrolysis (at much less extent (4 %)).[9] As is well known, during a SMR process not only H_2 is produced but also CO_2, one of the main greenhouse gases with greatest impact to global warming. Therefore, more sustainable and environmentally friendly approaches are needed for the mass production of sustainable H_2.

In the section that follows, it will be discussed different alternatives in which sustainable H_2 can be produced from renewable energies. The main relevant features of each method will be reviewed in detail, including advantages and drawbacks of each method. The different

methods have been classified in four main categories and each category corresponds to the different ways of which the renewable energy is collected, as summarized in Fig. 1-6.[10]

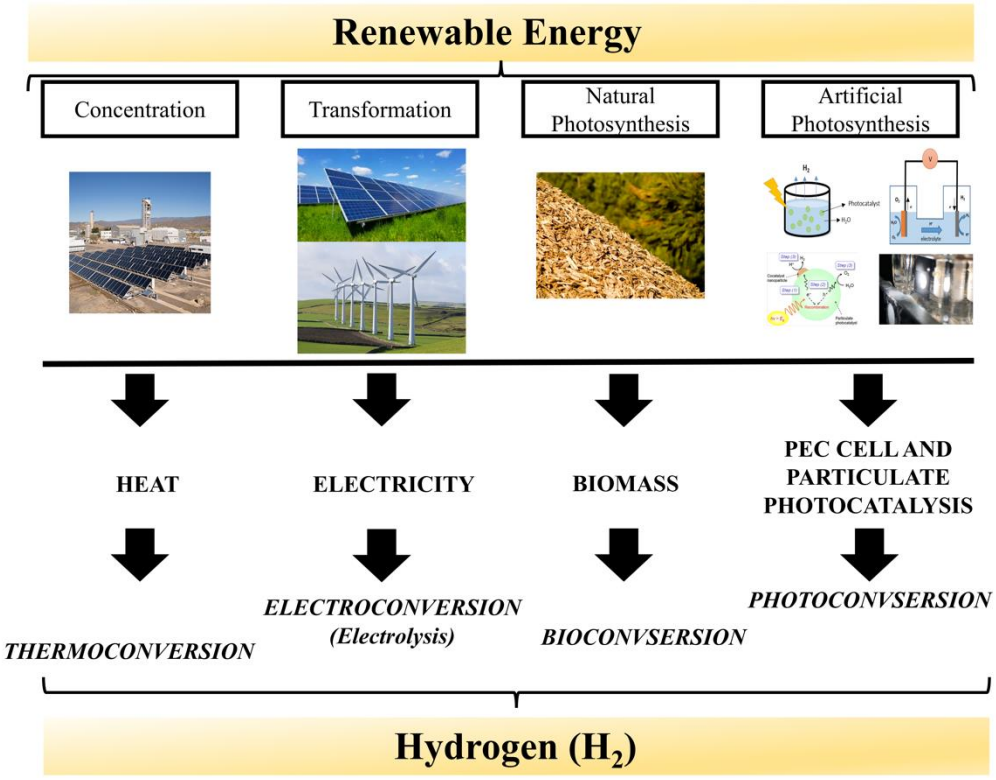

Fig. 1-6 Schematic diagram showing the main pathways of H_2 production from sustainable sources of energy. The production of H_2 has been divided in four main categories based on the different approaches from which the renewable energy has been collected.

Concentration is the first category described in Fig. 1-6. In this method, solar energy is concentrated to generate heat, which is then used to produce H_2 from water through a thermoconversion process known as solar-thermal water splitting (STWS). Briefly, STWS can occur in either a single-step or two-step process. In a single-step process, concentrated solar energy is collected using a distribution of mirrors. This solar energy is then directed to a reactor containing water which is heated to high temperatures (> 2200 °C) to drive the endothermic water splitting reaction and produce H_2 and O_2. Alternatively, in a two step-process a metal oxide is heated at high temperatures under low O_2 partial pressure (P_{O2}) to undergo reduction and produce O_2. The reduced metal oxide is then exposed to steam, which reduces to H_2 while re-oxidising back the metal oxide.[11] Although this technology seems feasible for H_2 production, with an estimated cost of $ 3-17 per kg H_2 depending on the method used, there are some issues such as severe stability and radiative energy losses associated with the use of such high temperatures.[10]

Transformation is another category from which hydrogen can be produced. In this approach, renewable energy such as solar, wind power, geothermal and tidal are used to produce

electricity that is eventually transformed for H_2 production. The most well-known method in this category is the 'electrolysis of water'. Currently, electrolysis accounts for 4 % of total global H_2 production. The estimated cost of produced H_2 using this approach ranges between $ 2.91 to 10.21 per kg H_2, depending on production scale and electrolyzer used.[10]

Alternatively, H_2 can also be produced *via natural photosynthesis* routes, where organisms such as algae, plants and trees capture solar light to store it in chemical compounds and produce fuels such as H_2, also known as bio-H_2.[10] The production of this bio-H_2 by methods such as dark and photo-fermentation, microbial electrolysis cells or algal photoheterotrophic biodegradation require mostly the use of industrial and agricultural waste instead of water. These methods of bio-H_2 production are highly appealing nowadays due to their contribution to accomplish a circular economy model, in which waste streams are used to produce H_2 as an energy carrier.[12] Nevertheless, in spite of being very attractive for the mass production of H_2, they are still far away from practical applications, mainly due to low yields, scalability issues and lack of knowledge in genetic systems. A techno-economic analysis estimated a cost of $ 10 per kg H_2 at a 2 % overall efficiency. However, if efficiencies reach 9 %, it is estimated a cost of $ 3.60 per kg H_2.[12]

Finally, the last category is *artificial photosynthesis*, which mainly encompasses photoelectrochemical (PEC) water splitting and photocatalytic water splitting using particle suspensions. These two technologies, still under development are only existing in lab scale configurations, although technical and economic analysis have demonstrated their feasibility in large scale applications.[13] These technologies rely on a semiconductor, in which after light irradiation an electron-hole pair is generated, which reacts with water to form H_2 and O_2. Both technologies, in particular PEC water splitting will be discussed in detail in the following chapter, being the primary scope of this thesis.

Overall, PEC water splitting is an appealing and promising technology over other methods of sustainable hydrogen production due to the ability to produce H_2 and O_2 at two different electrodes, facilitating the separation of both gases once produced. Furthermore, reaction takes place at room temperature, the stream of H_2 produced is of high purity, a key requirement to be used in a fuel cell, and a PEC cell can be constructed from purely inorganic materials which tend to be more stable and robust than organic or biologically based systems.[10,14] Furthermore, PEC water splitting is based on solar energy, the largest source of renewable energy. Combining both solar energy and PEC water splitting the CO_2 reduction targets could be meet. However, PEC water splitting is still limited by the material performance. If materials meeting the PEC targets are found, PEC technology could become a key approach for the production of large scale solar H_2 with a cost of $ 2-4 per kg H_2.[13]

Chapter 2. Photoelectrochemical water splitting

In this chapter, an overview of the key fundamental parameters regarding the PEC water splitting process are described. The chapter begins by describing the basics of semiconductors, the main existing configurations for water splitting applications, followed by requirements, processes and mechanisms involved in PEC water splitting. A brief summary of the foremost figures of merit and the main PEC setups is also discussed. Finally, an outline of the main materials including nanostructured materials and titanium oxo/alkoxy clusters is presented.

2.1 Semiconductor properties

Semiconductors are the main materials involved in water splitting applications. They are a type of materials in which their valence band (*VB*) and conduction band (*CB*) are separated by an energy band gap. The difference in energy between the *CB* and *VB* defines the band gap energy of the material ($E_g=E_{CB}-E_{VB}$), as shown in Fig. 2-1a.[15,16] Depending on the nature of the electronic properties of the semiconductor, two different types of optical band gap transition exist: *direct* and *indirect* transitions. A *direct* transition refers to an optical transition in which the highest point in the *VB* is located at the same *k*-vector as the lowest point of the *CB* (Fig. 2-1b). In this situation, a change in energy occurs but the crystal momentum is preserved. Alternatively, an *indirect* band gap transition refers to those systems in which there is both a change in energy and crystal momentum (Fig. 2-1c). These transitions require absorption or emission of a phonon (i.e lattice vibration) and are less likely to occur.[14]

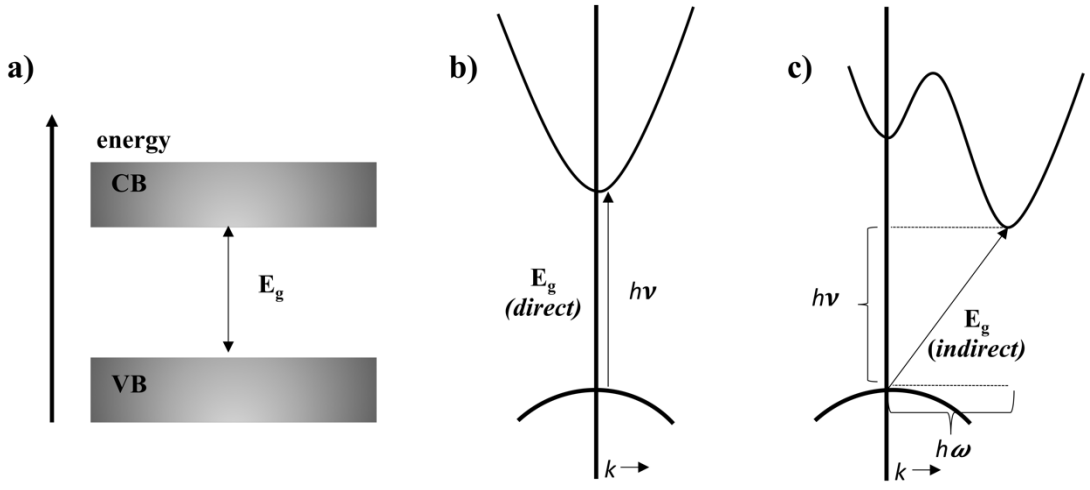

Fig. 2-1 (a) Simplified band diagram of a semiconductor. (b) Direct band gap transition. (c) Indirect band gap transition. This transition requires assistance of a phonon ($h\omega$). Adapted from ref.[14]

Each of the different energy levels is occupied by a certain number of electrons. At absolute 0 temperature (T=0 K), the lowest energy levels are all filled up with electrons up to a

maximum energy, the Fermi level (E_F). Above the Fermi level, all energy states are empty. At higher temperatures, the distribution and occupancy probability of the electrons within the different energy levels is defined by the Fermi-Dirac function *f(E)*, shown in equation 2-1:[15,16]

$$f(E) = \frac{1}{1 + \exp\left(\frac{E - E_F}{K_B T}\right)} \qquad 2\text{-}1$$

where *f(E)* defines the probability that a particle will have energy *E*, *T* is the temperature and K_B the Boltzmann constant.

Semiconductor materials are classified in two main categories: un-doped and doped semiconductors, from which the E_F will vary. For instance, for an un-doped semiconductor, also known as intrinsic semiconductor, upon light irradiation with an energy equal to or greater than the band gap energy (E_g), electrons (e^-) are excited to the conduction band (*CB*) leaving holes (h^+) in the valence band (*VB*). Under these conditions, the concentration of e^- and h^+ are equal in the semiconductor placing the E_F at the mid-gap position between the *VB* and *CB* (Fig. 2-2, first diagram). Conversely, for doped semiconductors additional energy levels are added in their electronic configuration giving rise to two main types of semiconductors: *n-type* and *p-type*. An *n-type* semiconductor contains a donor atom that gives additional electrons ($D \rightarrow D^+ + e^-_{CB}$) in the lattice causing an upward shift of E_F (Fig. 2-2, second diagram). A *p-type* semiconductor contains an acceptor atom that can produce holes, shifting down the E_F ($A \rightarrow A^- + h^+_{VB}$, Fig. 2-2, third diagram). In some semiconductors, such as metal oxides the intrinsic defects present in the structure define the electronic character of the material. For instance, the oxygen vacancies present in TiO_2 and ZnO define their *n-type* conductivity.[17,18] For such semiconductors, at room temperature, the number of free electrons and holes depend largely on the doping level rather than the thermal excitation of electrons and holes across the band gap. This implies that the position of the E_F level also relies on the concentration of donors and acceptors. Fig. 2-2 shows a schematic band diagram for an intrinsic, *n-type* and *p-type* semiconductor.[15,16]

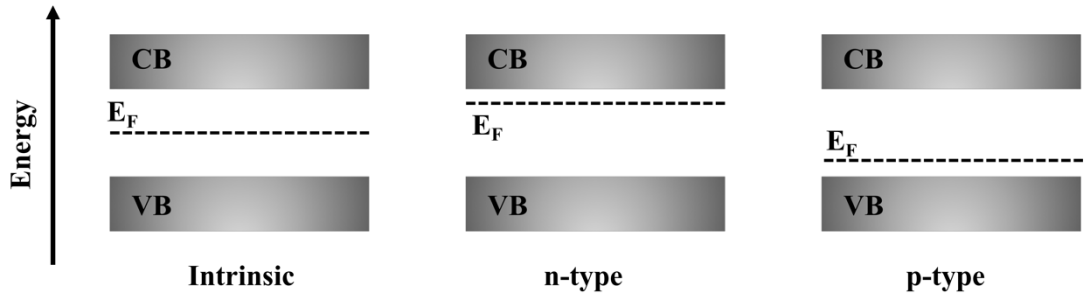

Fig. 2-2 Band diagram of an intrinsic, *p-type* and *n-type* semiconductor having the same band gap. Adapted from ref.[15]

2.2 Overview of photocatalytic water splitting

Photocatalytic water splitting can be carried out using two different approaches: (i) photocatalytic methods where typically a powder photocatalyst is dispersed in aqueous solution and (ii) photoelectrochemical methods (PEC) where photocatalysts are mounted in electrodes and an external bias is often applied to trigger the redox reactions. Depending on the number of electrodes used, the PEC cell set-up can exist in two different configurations: A two-electrode system (Fig. 2-3, right), consisting of a working electrode which contains the photocatalyst of interest and a counter electrode, usually platinum, or a three-electrode system (Fig. 2-3, left), in which a reference electrode is coupled to the system along with the other two electrodes.

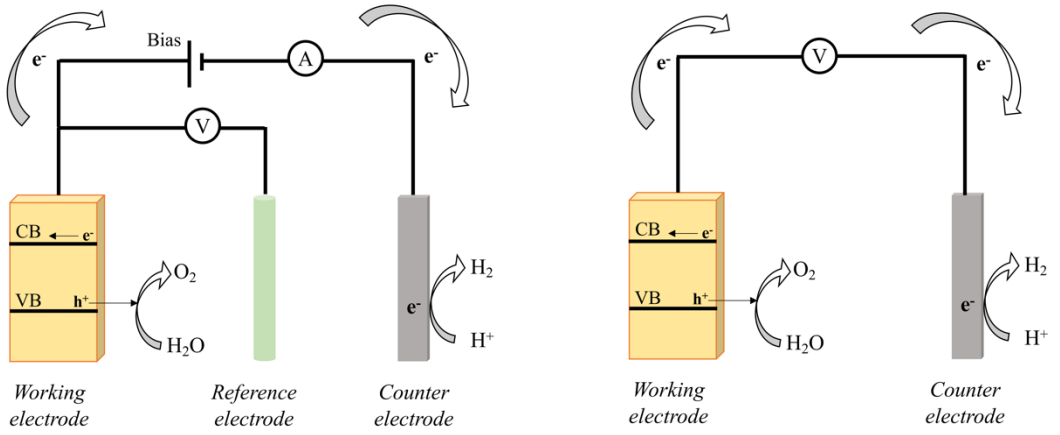

Fig. 2-3 Schematic diagram of a 3-electrode system PEC cell (left) and 2-electrode PEC system (right).

Powdered or particulate photocatalyst systems are based on heterogeneous photocatalysis, a process in which two active phases, solid (photocatalyst) and liquid (aqueous solution) are present. The main feature of these systems is their simplicity, since water splitting and thus hydrogen production occurs by irradiating a photo-reactor where powder photocatalysts have been previously dispersed in an aqueous solution. Nevertheless, several inherent problems are associated with this approach such as possible pH change during the process, especially when a scavenger is used, and difficulty in controlling light absorbance by suspended particles along with separating the photocatalyst from the water and the co-generation of H_2 and O_2.[19,20] Other relevant issues are the parasitic reactions, such as the reduction of O_2 by the photocatalyst to form superoxide (O_2^-). Alternatively, PEC methods have the potential to avoid these limitations, although other challenges such as poor material stability or efficiency are still encountered. Technical and economic large-scale studies performed in both configurations indicated that although particulate systems may offer a lower cost per kg H_2, safety concerns involved in the process, such as co-generation of H_2 and O_2 might limit its large-scale application.[13] Instead, PEC systems would be easier to scale up with fewer safety concerns. In

fact, it is estimated that if the PEC efficiency and material stability of devices improve, the cost per kg H_2 would decrease significantly, to $ 2-4 per kg H_2. In line with this, the US department of energy (DoE) targets a cost of $ 5.70 per kg H_2 by 2020 with an ultimate target of $ 2.10 per kg H_2 using PEC technology.[21] A recent life cycle assessment study on a hypothetical large-scale PEC H_2 production facility with an energy output equivalent to 1 GW continuous annual average, estimated an energy payback time of 8.1 years, an energy return on energy invested (EROEI) of 1.7 and a life-cycle primary energy balance over the projected service life of the facility of +500 PJ.[22] As in previous studies, it was concluded that the main limitations encountered are the low efficiencies and lifetime of the current PEC devices.

Both methods rely on the photocatalytic principle that takes place when a semiconductor is irradiated with an energy equivalent to or greater than its band gap. Under these conditions, electrons (e^-) in the valence band (*VB*) are excited into the conduction band (*CB*), leaving holes (h^+) in the *VB*. These photogenerated e^- and h^+ undergo redox reactions giving rise to a wide range of applications where the photocatalytic principle can be employed such as photodegradation of organic pollutants in waste water and overall water splitting.[23,24]

In order to achieve overall water splitting the *VB* and *CB* of the semiconductor must have appropriate potentials. The *CB* must have a more negative potential than the reduction potential of H^+ to H_2 (0 V_{NHE} at pH=0) whereas the *VB* must have a more positive potential than the oxidation potential of H_2O to O_2 (1.23 V_{NHE} at pH=0). Typical band positions of different metal oxides are shown in Fig. 2-4.[25,26]

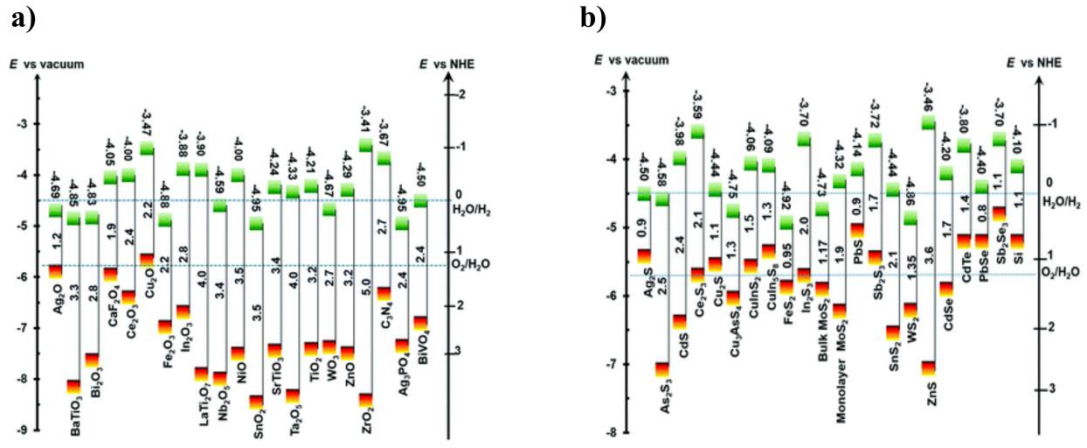

Fig. 2-4 Band edge positions with respect to the vacuum level and the NHE for a range of semiconductors at pH=0. (a) Oxides, phosphates and nitrides and (b) chalcogenides and silicon. Reproduced from ref.[26] with permission from The Royal Society of Chemistry.

The overall water splitting mechanism, regardless of the configuration used, occurs in three main steps: (1) Under light irradiation with an energy equal to or greater than the band gap of the semiconductor, photocarriers (e^- and h^+) are generated, as previously stated. (2) These

photocarriers separate and migrate to the surface of the photocatalyst avoiding recombination. For particulate approaches, both e^- and h^+ migrate to the surface (Fig. 2-5), whereas in a PEC approach, either the e^- or h^+ migrate to the surface-electrolyte interface of the photoelectrode while the other carrier migrates to the external circuit of the cell to reach the counter electrode (Fig. 2-3). (3) Finally, adsorbed species on the surface of the photocatalyst/photoelectrode are reduced/oxidized to form H_2 and O_2, respectively.[27]

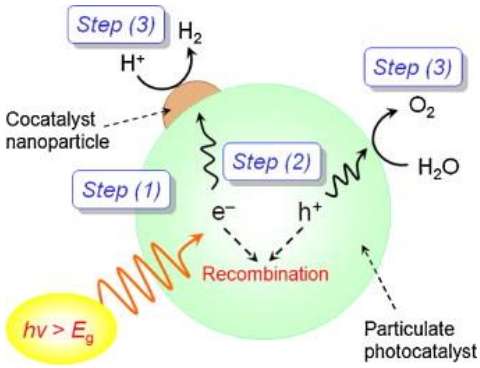

Fig. 2-5 Process involved in a photocatalytic overall water splitting on a semiconductor particle. Reprinted with permission from ref.[23] Copyright (2007) American Chemical Society.

In the following sections, a more detailed explanation and characteristics of PEC water splitting will be discussed, being the primary scope of this thesis.

2.3 Fundamentals of photoelectrochemical water splitting

PEC water splitting was first discovered in 1972 by A. Fujishima and K. Honda using TiO_2 as a photoanode connected to a platinum electrode.[28] Since then, great scientific efforts have been devoted to understand the mechanism of this technology as well as to find suitable materials to enable the design of an efficient and stable water splitting device. For instance, over 5,000 scientific research articles have been published throughout these years including a wide range of materials studied (metal oxides, chalcogenides, phosphates…) In the following sections, fundamentals of PEC water splitting including space charges and band bending in semiconductors, key parameters of a PEC device under dark and light conditions, along with figures of merit, different PEC configurations and materials will be discussed to give a general overview of the current state of the art of the PEC technology.

2.3.1 Space charges and band bending in the semiconductor-electrolyte interface

When a semiconductor is immersed in an electrolyte solution, a flow of electric current across the semiconductor-electrolyte interface occurs until the Fermi energy of the electrons in the semiconductor (E_F) is equal to the redox potential of the electrolyte (E_{redox}), meaning that electronic equilibrium has been reached. At this point, there is an uneven distribution of charges at the semiconductor-electrolyte region which differs from the bulk material. This region is known as the *space-charge layer*, at the semiconductor side, and *electrolytic double*

layer at the electrolyte side, the latter consisting of the *Helmholtz layer* and the *diffuse Gouy-Chapman layer* (Fig. 2-6).[25] The *Helmholtz layer* is the closest region to the semiconductor interface, comprising physically adsorbed ions and some of the ions in solution. On the other hand, the *diffuse Gouy-Chapman layer* comprises mainly the ions present in the electrolyte, which are surrounded by a solvation cloud of water molecules.

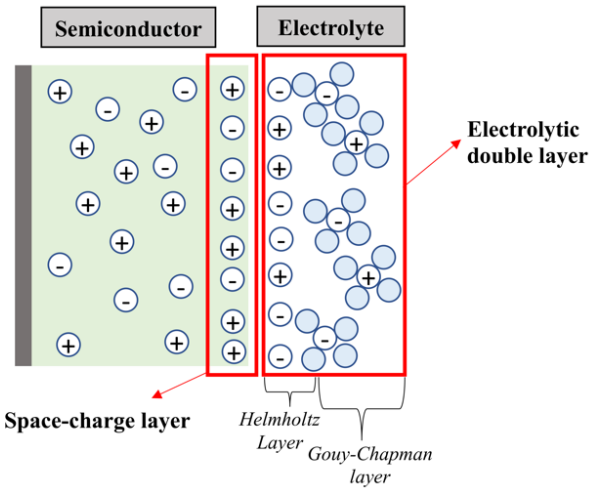

Fig. 2-6 Schematic diagram of the space-charge layer and electrolytic double layer at the semiconductor-electrolyte interface. Adapted from ref.[14]

Achieving the electronic equilibrium in the semiconductor-electrolyte interface requires, in most cases, a change in the *CB* and *VB* of the semiconductor, known as band bending. The nature of this band bending strictly depends on the position of the Fermi level in the semiconductor. Taking this into account four different situations may arise:[14,25]

Flat-Band potential (U_{fb}): When there is no excess of charges on the semiconductor side of the junction, an electric field is not generated, therefore the space-charge layer does not exist and band bending does not occur. This is known as the flat-band potential (Fig. 2-7a).

Accumulation layer: If an excess of positive (or negative) charges is adsorbed at the surface of an *n-type* (or *p-type*) semiconductor, a downward (or upward) bending of the *CB* and *VB* of the semiconductor occurs towards the interface due to the formation of an accumulation layer made of free majority carriers that compensate the charge (Fig. 2-7b).

Depletion layer: If an excess of positive (or negative) charges is transferred from the surface of an *n-type* (or *p-type*) semiconductor to the electrolyte, an upward (or downward) bending of the *CB* and *VB* of the semiconductor occurs towards the interface due to a diminishment of charges at the interface (Fig. 2-7c).

Inversion layer: If the number of adsorbed positive (or negative) charges is above the intrinsic level of the *n-type* (or *p-type*) semiconductor, the semiconductor behaves as a *p-type* (or *n-*

type) at the surface and *n-type* (or *p-type*) at the bulk, enhancing the downward (or upward) band bending of the *CB* and *VB* of the semiconductor (Fig. 2-7d).

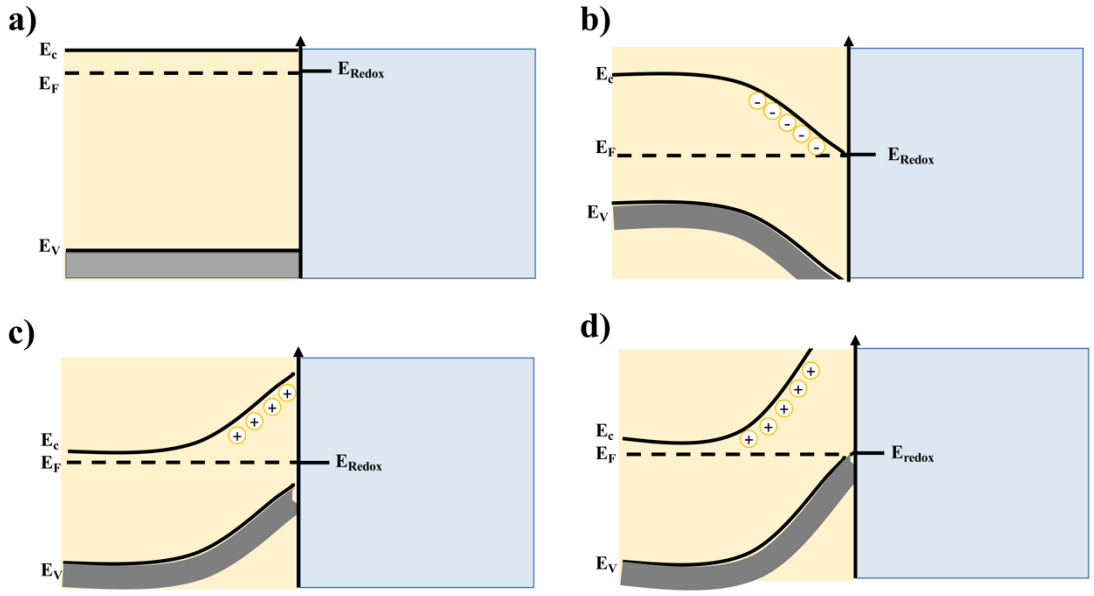

Fig. 2-7 Schematic diagram showing the electronic energy levels of a *n-type* semiconductor in contact with an electrolyte, where electrons are the mobile phase carrier. (a) flat band potential, (b) accumulation layer, (c) depletion layer and (d) inversion layer. The same situation applies for *p-type* semiconductors. However, band bending occurs towards the other direction and charges are the opposite. Adapted from ref.[25] Copyright 2001 Springer Nature.

In addition to all the possible situations regarding the space charges and band bending of semiconductors in contact with an electrolyte, one has to consider the effect that an applied bias and pH has on the band edges of a semiconductor.[14,29]

Typically, if the band edges of the semiconductor do not match the challenging required potentials to undertake the water reduction or oxidation reactions, an external voltage between the photoelectrode and counter electrode can be applied to compensate this potential deficiency. Under these circumstances, the charge distribution of the space charge region is modified, which in turn amends the band bending of the semiconductor. For instance, for an *n-type* semiconductor, a positive bias increases the depletion layer, facilitating an upward band bending of the semiconductor electronic bands, whereas a negative bias can bring the band bending to zero. The band edges of the semiconductor are also affected by the pH. Nevertheless, the reduction and oxidation potential of water also depend on the pH in the same way as the semiconductor-band positions. Therefore, simply changing the pH of the solution does not help meet the redox potential for the water splitting reactions.[14,30]

The oxidation and reduction potential of water as a function of pH changes according to the Nernst equation:

$$E_{red} = E_{red}^{0} - \frac{RT}{4F} ln\left(\frac{p_{H2}^{2}}{[H^{+}]^{4}}\right) = E_{red}^{0} - \frac{2.3RT}{F}(\log\left(p_{H2}^{\frac{1}{2}}\right) + pH) \quad 2\text{-}2$$

$$E_{ox} = E_{ox}^{0} + \frac{RT}{4F} ln(p_{O2}[H^{+}]^{4}) = E_{ox}^{0} + \frac{2.3RT}{F}(\log(p_{O2}) - pH) \quad 2\text{-}3$$

where equation 2-2 and equation 2-3 correspond to the reduction and oxidation of water, respectively.

This pH dependence implies that for an alkaline electrolyte (pH=14) the water redox reactions and potentials are as follows:

$$4H_2O + 4e^{-} \rightleftarrows 2H_2 + 4OH^{-} \;\; E_{red}^{0} = -0.828 \;\; V_{NHE} \quad 2\text{-}4$$

$$2H_2O + O_2 \rightleftarrows 4OH^{-} + 4h^{+} \;\; E_{red}^{0} = +0.401 \;\; V_{NHE} \quad 2\text{-}5$$

whereas in acidic electrolytes (pH=0), the water redox reactions and corresponding potentials are:

$$4H^{+} + 4e^{-} \rightleftarrows 2H_2 \;\; E_{red}^{0} = +0.000 \, V \; vs. NHE \quad 2\text{-}6$$

$$4H^{+} + O_2 \rightleftarrows 2H_2O + 4h^{+} \; E_{red}^{0} = +1.229 \, V \; vs. NHE \quad 2\text{-}7$$

2.3.2 PEC systems under illumination

In the previous section (Section 2.3.1) the main aspects affecting the electronic properties of the semiconductor involved in a PEC device have been reviewed. However, no attention has been given to the behavior of such semiconductors under illumination conditions (*i.e* non-equilibrium conditions). When a semiconductor electrode is illuminated with an energy equal to or greater than the E_g of the material, e^- are excited from the *VB* of the semiconductor to the *CB*, creating a h^+ in the *VB* as previously mentioned in Section 2.2. At this point, the system is no longer in equilibrium, especially at the space-charge region, and instead of having a single Fermi Energy level near the semiconductor-electrolyte interface *quasi-Fermi* levels both for e^- and h^+ appear. These *quasi-Fermi* levels are a measure of the concentration of electrons and holes near the interface and define the free energy of the photocarriers. In addition to that, under illumination conditions the band bending is reduced and Fermi level moves slightly upward or downward for an *n-type* or *p-type* semiconductor, respectively.[14,16]

All the processes taking place under dark and light conditions are summarized in Fig. 2-8. The left-hand side diagram of Fig. 2-8 shows a typical *n-type* semiconductor material under dark conditions. At this point, the system is in equilibrium, however, after light irradiation,

photogenerated e^- and h^+ are formed bringing the device to a non-equilibrium condition (Fig. 2-8, right).

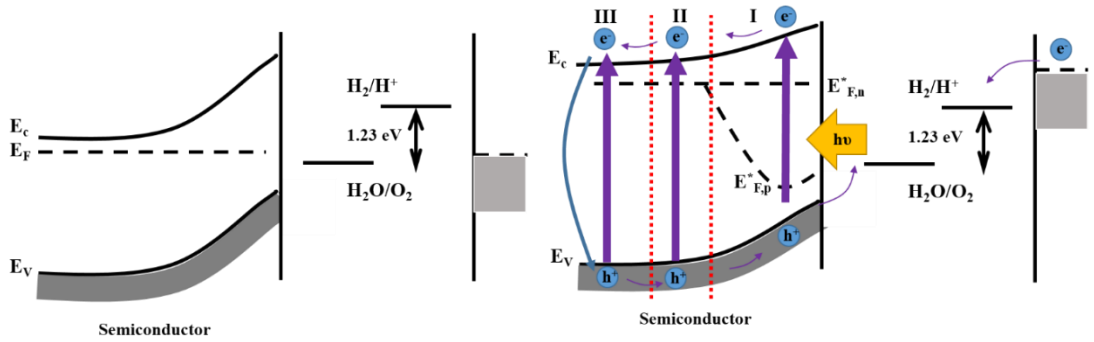

Fig. 2-8 Band diagram for a PEC cell based on an *n-type* semiconductor material under dark conditions (left) and illumination conditions (right) showing the main absorption regions. Adapted from ref.[14]

Under light conditions, three distinguished regions must be considered in the semiconductor material, where different processes take place: Region I (Fig. 2-8, right (I)) is the region where most of the light is absorbed by the semiconductor, charge separation occurs and photocarriers (e^- and h^+) are separated by a field called drift current. The efficiency of photocarriers generation and collection depends on the width of the space charge region, the penetration depth of the light incident on the surface of the photoelectrode and the minority carrier diffusion length. Ideally, the vast majority of these photocarriers migrate to the bulk of the semiconductor, whereas a small minority is driven to the surface. However, if 'surface-states' also known as defects are present on the surface of the semiconductor, electron-hole recombination can occur within the space-charge layer, avoiding the migration of carriers to either the semiconductor-electrolyte interface or back contact. In region II (Fig. 2-8, right (II)), light absorption also takes place, photocarriers are transported by diffusion and holes migrate to region I before recombining. Finally, in region III (Fig. 2-8, right (III)), mainly absorption and photocarriers recombination take place. However, this will strongly depend on the average diffusion length of each carrier (e^- or h^+) and their probability to migrate either to the back contact or to the space-charge region of the semiconductor.[14,15,31]

When a PEC system is immersed in an electrolyte solution, current *vs.* voltage curves provide a useful picture of their activity. Under dark conditions, the current generated under applied bias originates from the flowing of majority carriers along the PEC device. Alternatively, under illumination conditions, the photocurrent observed originates mainly from the minority carriers. Therefore, depending on the nature of the semiconductor, either *n* or *p-type*, the photocurrent derives either from holes or electrons, respectively, affecting the photoelectrochemical reaction at the interface of the photoelectrode. For instance, when an *n-type* semiconductor is used, photooxidation of water takes place, whereas in the case of a *p-type*, the photoreduction of water occurs. Fig. 2-9 shows a schematic representation of typical

current-potential curves (J-V) recorded under dark and light conditions for both *n* and *p-type* semiconductors.[15] The maximum photocurrent performance achieved will depend on the efficiency of the processes described in Fig. 2-8: photoabsorption, carrier separation and transport.

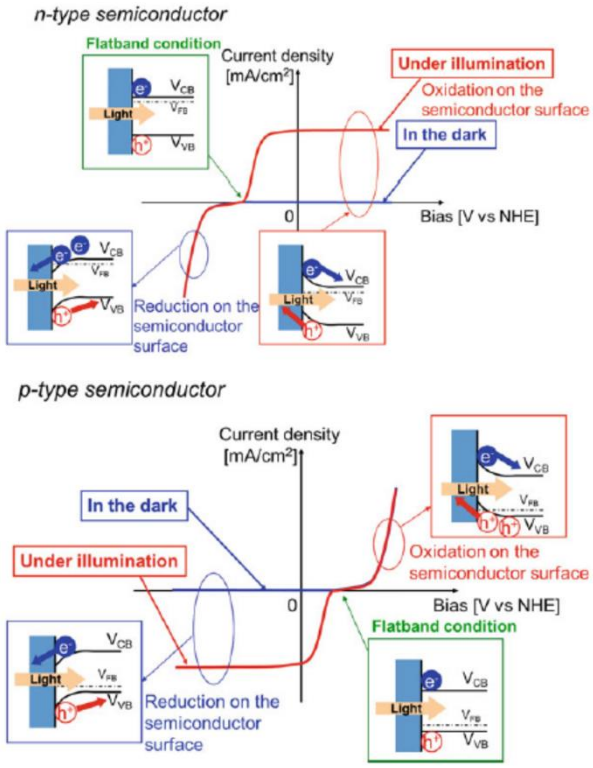

Fig. 2-9 Schematic current-voltage (*J-V*) characteristics for an *n-type* (upper) and *p-type* semiconductor (lower), both in the dark and light conditions. V_{CB}, V_{VB} and V_{FB} refer to conduction band, valence band and flat band potential. Reproduced from ref.[15]

2.3.3 Energy and quantum efficiencies in PEC devices

To advance in the PEC field there is a necessity to establish well-defined benchmark metrics of assessment, so that performances and efficiencies of PEC materials can be easily reported and compared with materials made and tested in labs across the globe. In general, the main measures of efficiency can be classified in two categories: (a) benchmark and (b) diagnostic efficiencies. Benchmark efficiencies encompass those mathematical expressions that are suitable for mainstream reporting of the water splitting capability of a device, whereas diagnostic efficiencies refer to those measurements used to understand and characterize materials performances.[32,33]

The foremost benchmark efficiency is the *solar-to-hydrogen conversion efficiency* (STH), which defines the overall efficiency of a PEC device when exposed only to solar light irradiation (AM 1.5G) with no applied bias. The STH efficiency is expressed as shown in equation 2-8:

$$STH = \left[\frac{r_{H2}(mmol\ H_2\ s^{-1}) \times (237{,}000\ J\ mol^{-1})}{P_{total}\ (mW\ cm^{-2}) \times Area\ (cm^2)}\right]_{AM\ 1.5\ G} \quad \text{2-8}$$

where 237,000 J mol^{-1} is the change in Gibbs free energy per mole (ΔG at 25 °C), r_{H2} is the rate of hydrogen production (mmol s^{-1}) measured by means of an analytical technique (*i.e.* gas chromatography), P_{total} is the incident light intensity (typically 100 mW cm^{-2}) and *Area* is the illuminated area of the photoelectrode (cm^2).

Alternatively, STH efficiency can also be calculated by taking into account the relation that power is the product of voltage, current and the Faradaic efficiency (η_F), as shown in equation 2-9:

$$STH = \left[\frac{|j_{sc}(\ mA\ cm^{-2})| \times (1.23\ (V_{RHE})) \times \eta_F}{P_{total}\ (mW\ cm^{-2})}\right]_{AM\ 1.5\ G} \quad \text{2-9}$$

where j_{SC} (mA cm^{-2}) is the short-circuit photocurrent density and 1.23 V_{RHE} (ΔE° at 25 °C) refers to the thermodynamic water splitting potential.

It must be noted that both equations are only valid in the absence of a scavenger, if the stochiometric ratio of H_2 and O_2 is confirmed and if reaction is of Faradaic unity.

A longer list of metrics is found under the 'diagnostic efficiencies' category. One of the first metrics included in the list is the *applied bias photon-to-current efficiency* (ABPE). Unlike STH, ABPE refers to the efficiency of a PEC device in which an external bias is applied to the system, therefore a true solar-to-hydrogen efficiency is not measured since an additional energy input (other than the sun irradiation) is supplied to the PEC device. The ABPE expression is described below (equation 2-10):

$$ABPE = \left[\frac{\left|j_{ph}(\ mA\ cm^{-2})\right| \times (1.23 - |V_b|\ (V)) \times \eta_F}{P_{total}\ (mW\ cm^{-2})}\right]_{AM\ 1.5\ G} \quad \text{2-10}$$

where j_{ph} is the photocurrent obtained at an applied bias V_b.

To account for an ABPE efficiency of the overall PEC device, the measurement must be performed in a 2-electrode system configuration (working and counter electrode). Performing the measurement in a 3-electrode configuration (working, counter and reference) results in an interface measurement instead, excluding the second half of the cell.

The most easily accessible figure of merit in diagnostic efficiencies is the *incident photon-to-current efficiency* (IPCE). Briefly, IPCE describes the photocurrent collected per incident photon flux as a function of illumination wavelength. Integration of the IPCE curve over AM 1.5G solar spectrum at zero bias conditions (2- electrode, short-circuit) results in an estimate

of the STH efficiency of the device. Alternatively, if IPCE is measured under applied bias, integration of the curve over AM 1.5G results in an estimation of the total photocurrent obtained at that specific potential.

IPCE is one of the most powerful figures of merit for material diagnostics because it takes into account three fundamental efficiencies involved in a PEC process: the amount of e^- and h^+ pairs generated per incident photon flux ($\eta_{e-/h+}$), charge transport to the solid liquid-interface ($\eta_{transport}$) and efficiency of interfacial charge transfer ($\eta_{interface}$). In this regard, IPCE can be described as follows (equation 2-11):

$$\mathrm{IPCE}\ (\lambda) = \frac{|\mathrm{j}\ (\mathrm{mA\ cm^{-2}})|\ \times 1239.8\ (\mathrm{V} \times\ \mathrm{nm})}{\mathrm{P_{mono}}\ (\mathrm{mW\ cm^{-2}}) \times\ \lambda\ (\mathrm{nm})} \qquad 2\text{-}11$$

where j_{ph} is the photocurrent measured at a wavelength λ, 1239.8 is the result of multiplying h (Planck constant) and c (speed of light) and P_{mono} is the monochromatic incident irradiation power.

Absorbed photon-to-current Efficiency (APCE) also known as *internal quantum efficiency (IQE)* measures the efficiency of a device based only on the amount of absorbed photons. Unlike in STH or IPCE, in APCE optical losses such as reflection or transmission of photons are subtracted. Therefore, APCE can be expressed as (equation 2-12):

$$\mathrm{APCE}\ = \frac{\mathrm{IPCE}\ (\lambda)}{A\ (\lambda)} = \frac{\mathrm{IPCE}\ (\lambda)}{A - R - T} \qquad 2\text{-}12$$

where A, R and T are the optical absorption, reflection and transmission of the film.

2.3.4 PEC cell configurations

PEC water splitting devices mainly consist of at least three different components: anode (or photoanode), cathode (or photocathode) and electrolyte along with a reference electrode (if necessary). Different PEC setups can exist depending on the photoelectrode configuration, grouped by Jiang *et al*. in six types, reprinted in Fig. 2-10.[33]

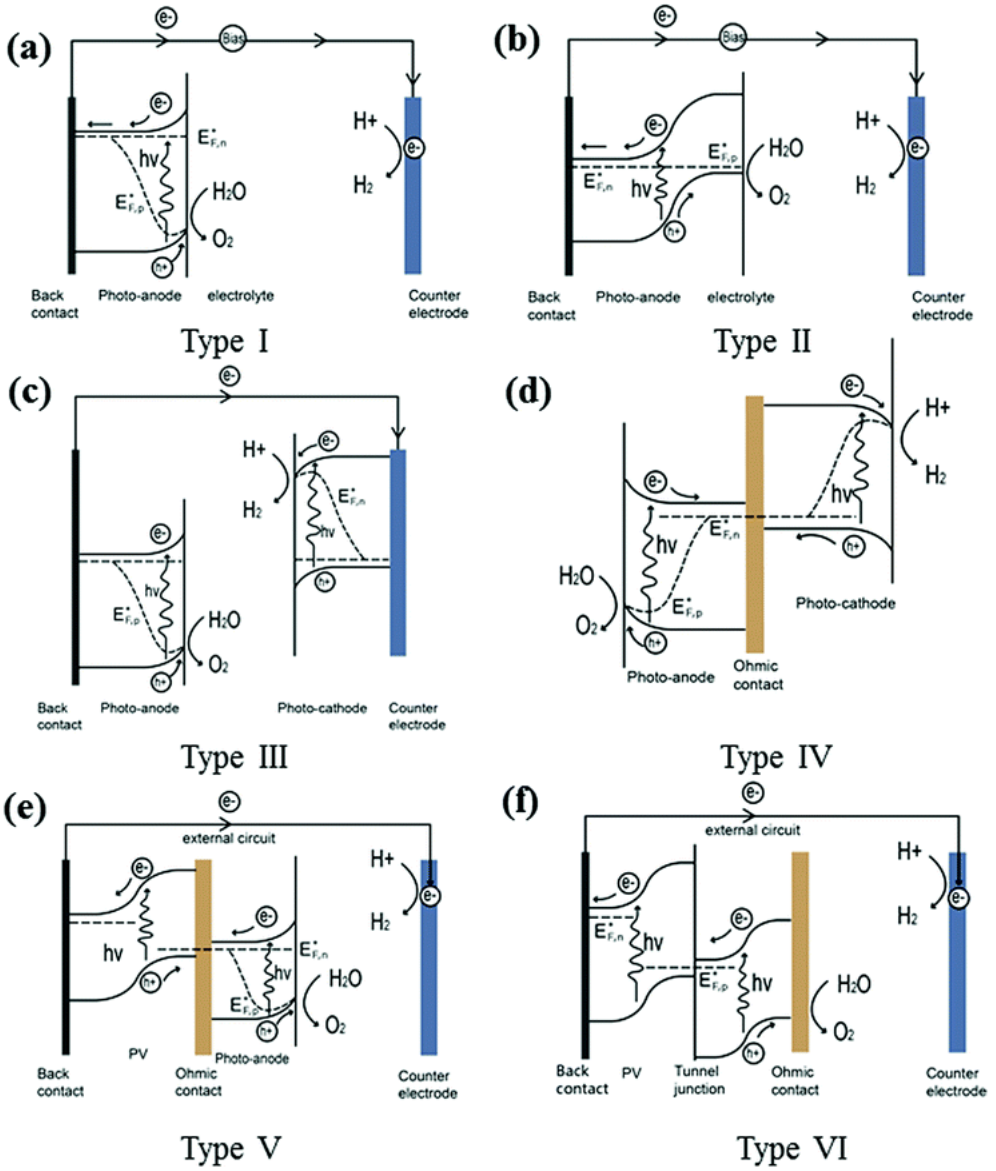

Fig. 2-10 PEC water splitting devices configurations: (a) type I, single light absorber. (b) type II, heterojunction photoelectrode. (c) type III, wired PEC tandem cell. (d) type IV, wireless PEC tandem cell. (e) type V, PV-PEC tandem cell. (f) type VI, PV-electrolyzer cell. Reproduced from ref.[33] Published by The Royal Society of Chemistry.

The simplest PEC cell configuration, denoted as type I, is shown in Fig. 2-10a. In this configuration only one semiconductor is mounted on the photoelectrode, which can be used either as a photoanode or photocathode in the water splitting reaction along with a metal counter electrode. In this configuration, an external bias is often applied to trigger the separation of photogenerated electron and hole pairs throughout the cell to undergo the water splitting reaction.

Heterojunction or type II PEC devices (Fig. 2-10b) refer to those systems in which two semiconductors are mounted in one photoelectrode to form a heterojunction. An example of heterojunction is between and *n-type* and *p-type* semiconductor. In this configuration, a space-charge layer is formed at the interface of both semiconductors inducing photocarrier diffusion

amongst them. Depending on the band alignment between the *n-type* and *p-type* semiconductor, photocarriers will diffuse differently. For instance, in the example shown in Fig. 2-10b electrons from the *CB* of the *p-type* material are transferred to the *CB* of the *n-type* semiconductor, whereas holes migrate from the *VB* of the *n-type* to the *VB* of the *p-type*. Overall, this system offers improved charge separation, longer charge carrier lifetimes, higher reaction rates and enhanced light absorption over simplest PEC configurations when satisfactory band alignment conditions are met.[34] Other types of heterojunctions will be further discussed in Section 2.3.6.1.

Tandem devices (type III and type IV) as the ones depicted in Fig. 2-10c-d consist of two semiconductors connected in series in which one acts as a photoanode and the other as a photocathode, for the oxidation and reduction of water, respectively. These systems can exist in either a wired configuration (Fig. 2-10c, type III), in which a conductive metal wire is used to connect both photoelectrodes or in a wireless setup (Fig. 2-10d, type IV), in which a transparent conductive substrate is used as an ohmic contact. The only key requirement of a tandem device is to ensure complementary light absorption by both materials. Briefly, when light is irradiated, the photons transmitted through the first material should be absorbed by the second material. To accomplish that the *CB* minimum of the photoanode must be more negative than the *VB* maximum of the photocathode.[33] Advantages of this tandem configuration include higher photovoltages to drive unbiased water splitting reactions and a wider selection of materials used.

A type V configuration includes devices consisting of a combination of a photovoltaic (PV) cell with a PEC device (Fig. 2-10e). In such configurations, the additional bias required for the water splitting reaction is supplied by the PV cell, so that a larger selection of semiconductor materials can be used. Furthermore, a transparent oxide layer (ohmic contact) is required between the PV and PEC cell for the recombination of electrons and holes coming from the photoelectrode and PV cell, respectively (for PV- n-type configuration).

Finally, a type VI configuration encompasses those devices in which a PV cell is combined with an electrolyzer. In these systems, the power is supplied by the PV cell and the electrolyzer performs the water splitting reaction. Although a PEC device is not technically employed in this configuration it can still be counted as a type of PEC system because the water splitting reaction is driven by solar light (Fig. 2-10f).

2.3.5 Photoelectrode materials in PEC devices

Forty-seven years later since the discovery of PEC water splitting some promising material candidates, such as Fe_2O_3 or $BiVO_4$ have been developed as potential materials for PEC devices. However, significant research efforts are still need it to find the adequate material for

the design of an efficient and stable PEC device utilizing visible light. This is mainly due to the difficulty of finding semiconductor materials able to fulfil the minimum requirements that need to be accomplished in order to bring these devices into large scale applications:[14,26,35]

i) Stability in the dark and under illumination in an aqueous electrolyte

A large amount of non-oxide semiconductors either dissolve or form a thin oxide layer at the surface of the electrode when in contact with the electrolyte limiting the charge transfer process across the semiconductor-electrolyte interface. Metal oxides are usually more stable in these conditions, but they can suffer from photocorrosion, in which photogenerated holes oxidize the material itself rather than the water. Some examples of metal oxides undergoing photocorrosion include Cu_2O, ZnO, PbO and $FeTiO_3$. However, many others such as TiO_2, Fe_2O_3, WO_3 are widely stable in solution and resistant to hole oxidation.[36]

ii) The band gap (Eg) should fall in the visible range of the spectrum to allow maximum absorption of the solar spectrum

It has been suggested that the optimal band gap of the semiconductor should fall within 1.9 and 3.1 eV, which corresponds to an absorption of 650 nm to 400 nm, respectively. This band gap range takes into account the energy required to split water (1.23 V_{NHE}) along with some thermodynamic losses and overpotentials ascribed to interfacial kinetics.[14,37] The theoretical maximum solar-to-hydrogen efficiency (STH) is determined by the band gap of the material. The lower the band gap, the higher STH efficiency due to larger absorption of the solar spectra.[26] Fig. 2-11 shows the maximum STH and theoretical photocurrent density values as a function of the material band gap. In Section 2.3.6, band gap engineering approaches to enhance visible light absorption will be discussed.

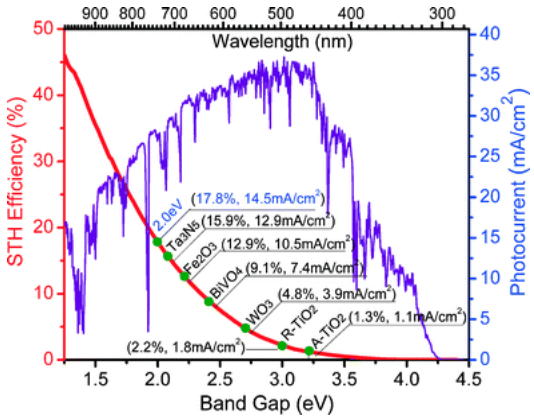

Fig. 2-11 Dependence of the theoretical maximum solar-to-hydrogen (STH) efficiency and the photocurrent density of photoelectrodes on the band gap under AM 1.5 G irradiation (100 mW cm^{-2}). Reproduced from ref.[26] with permission from The Royal Society of Chemistry.

iii) Efficient charge transport in the semiconductor

As previously stated, under light irradiation e^- and h^+ are generated in the semiconductor. Ideally, these photocarriers should possess a good and efficient transport mobility in order to avoid their recombination. The likelihood of photocarriers recombination is usually expressed in terms of either their carrier lifetime (τ_R) or their carrier diffusion length (L_D), as shown in equation 2-13. These two factors are related according to:

$$L_D \cong \sqrt{D\tau_R} \qquad 2\text{-}13$$

where D is the diffusivity of the free carriers. The L_D values can vary from several nanometers to hundreds of micrometers depending on the type of material, nanostructure, crystallinity and grain boundaries.

iv) The conduction and valence band edge positions must meet the redox potentials for the hydrogen and oxygen half reactions

Only a limited number of semiconductor materials straddle the redox potentials required for overall water splitting, which often requires materials with large band gap (Fig. 2-4). PEC technology offers the advantage that semiconductor materials can meet the requirements of only half of the water splitting reaction (either reduction or oxidation). In Sections 2.3.5.1 and 2.3.5.2 the most common materials employed for these reactions are reviewed.

v) Low overpotentials for the reduction/oxidation of water

Ideally, the materials employed should have low overpotentials, meaning that the interfacial charge transfer should be fast to avoid accumulation of charges at the surface that would lead to an increase in photocarrier recombination. To improve this, several electrocatalysts such as Co-based compounds and RuO_2 are usually deposited on top of the photoelectrode. More examples are reviewed in Sections 2.3.5.1 and 2.3.5.2.

vi) Materials must be of low-cost and environmentally friendly

Finally, materials used in PEC devices must be inexpensive, earth abundant and ideally prepared *via* a green synthetic route.

2.3.5.1 Photocathode materials

In PEC devices, photocathode materials are the responsible for the hydrogen evolution reaction and are usually *p-type* semiconductors. In these systems, the hydrogen evolution reaction occurs at the semiconductor-electrolyte interface and takes place when *CB* of the semiconductor is more negative than the reduction potential of H_2O to H_2.[29] A PEC diagram where the light absorbing material is a photocathode is shown in Fig. 2-12. Under these

circumstances, photogenerated e^- are directly transferred to the electrolyte solution where they react with water to produce hydrogen, whereas holes migrate to the counter electrode to undertake the oxidation reaction of water.

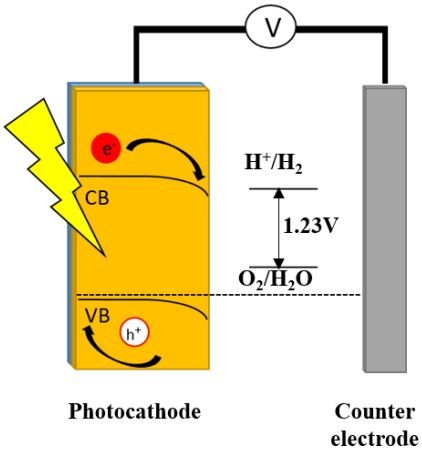

Fig. 2-12 One-step excitation PEC device consisting of a photocathode as the light absorbing material.

Only a limited amount of materials can be employed as photocathodes in PEC devices due their high instability and photocorrosion once in contact with the electrolyte solution and light exposure, respectively.[33] As stated earlier, metal oxides are often the most stable materials in electrolyte solutions at different pH. However, only a small amount of metal oxides are intrinsically *p-type*. The most common *p-type* metal oxide is Cu_2O, but it suffers from photocorrosion.[36] For this reason, most photocathodes require the deposition of a protective layer on top of the semiconductor, the choice of which also depends on the band position of the protective material in relation to the band positions of the photocathode.[38]

Cu_2O is one of the most highly used photocathode materials in PEC devices, due to its abundance and low toxicity. It has a direct band gap of 2.0 eV, which translates to a high theoretical photocurrent of *ca.* 15 mA cm^{-2} and potential STH efficiency of 18 % under solar light irradiation. However, its stability under electrolyte and light conditions is very poor since the reduction and oxidation potential of Cu_2O to Cu and CuO, respectively, falls within its band gap.[33,39] Therefore, in order to optimize the stability of this material several studies have been focusing on either depositing a protective layer such as another metal oxide on top of Cu_2O or by depositing an *n-type* semiconductor to form a p-n junction that will not only improve the stability but also charge transfer. For instance, in 2011, Paracchino *et al.*[40] reported a photocurrent density of -7.6 mA cm^{-2} at 0 V_{HRE} under simulated solar light conditions for a Cu_2O based photocathode. In this publication, they synthesized Cu_2O via an electrodeposition method and used atomic layer deposition (ALD) to coat the surface with Al-doped zinc oxide and titanium oxide (Al:ZnO/TiO_2). In addition, they also electrodeposited Pt nanoparticles to activate the hydrogen evolution reaction and overcome the overpotential that

was formed when the photocathode and electrolyte were in contact. Using this configuration, stable photocurrents were achieved for 1 h but rapidly decreased near zero values after that time. Similarly, Tilley *et al.* [41] reported in 2014 the use of the same Al:ZnO/TiO_2-Cu_2O using RuO_2 instead of Pt nanoparticles. By using this configuration, they considerably enhanced the stability of the system. After 8 h of irradiation the system was still stable. However, it was not until very recently (in 2018), where L. Pan *et al.* reported the best performing Cu_2O photocathode in general for photocatalytic hydrogen production known so far. The device, consisting of a nanostructured Cu_2O layer with Ga_2O_3 forming a p-n junction, a TiO_2 protective layer and a RuO_X as a hydrogen evolution catalyst, achieved benchmark photocurrent densities of -10 mA cm^{-2} at 0 V_{RHE}, a photovoltage of 1 V and a stability beyond 100 h.[42] An alternative approach to protect Cu_2O photocathodes is by depositing a protective layer of CuO on top of the Cu_2O. For instance, Zang and Wang reported an improved photocurrent performance and stability for CuO-Cu_2O composites than for bare Cu_2O.[43] This improvement was attributed to the inhibition of Cu_2O photocorrosion and to the decrease in photocarriers recombination for the final CuO-Cu_2O composite.

Other common *p-type* semiconductor materials found in literature are copper based chalcogenide semiconductors such as Cu(In,Ga)Se_2 (CIGS),and Cu_2ZnSnS_4 (CZTS).[38,39,44] The research of copper chalcogenide semiconductors for photocathodes in PEC devices was triggered after their great performance in photovoltaic applications which was ascribed due to their high absorption coefficients, narrow band gaps and good carrier transport properties. In 2004 and 2005, Valderrama *et al.* were one of the first authors to report the use of CIGS as a photocathode material in a PEC device for hydrogen production.[45,46] They found that the amount of hydrogen produced considerably increased under light conditions. Nevertheless, as for Cu_2O, these materials also require a protective layer to avoid photocorrosion and often a hydrogen evolution catalyst to minimize the overpotential between the electrode and electrolyte. For instance, Koo *et al.* reported the design of a photocathode consisting of CIGS/CdS/TiO_2/Pt where TiO_2 was acting as a protective layer.[47] Another type of chalcogenide material with relevant research interest is CZTS. Unlike CIGS, CZTS is also gaining research interest because their composition consists of more abundant and less toxic elements. A detailed explanation of these chalcogenide semiconductors in PEC devices is beyond the scope of this thesis but a full explanation and state of the art of these materials can be found in the reviews published by Chen *et al.* [48] and Wang *et al*.[49]

Silicon (Si) photocathodes are also of relevant interest in the scientific community due to the high abundance of this material on the Earth's surface and its use in industry. Si has a band gap (E_g=1.1 eV) capable of absorbing a large amount of the solar spectrum and adequate *CB* edge for the photoreduction reaction of water. Nevertheless, it also suffers from low stability

in electrolyte solutions and requires a co-catalyst for its successful application.[50,51] To overcome these limitations, several publications have reported the use of a TiO_2 protective layer on top of the Si material. The coating of Si surfaces, on the other hand, can also become an issue, since it can hinder the electron conduction at the semiconductor-electrolyte interface. In this regard, Seger *et al.*[52] successfully demonstrated that a 100 nm layer of TiO_2 protected the Si surface without limiting the electron transfer from the semiconductor to the electrolyte achieving a stability higher than 72 h. Along the same lines, Dai *et al.*[53] reported the deposition of Pt catalyst using ALD on the surface of silicon nanowires. They demonstrated an easy method of catalyst loading in nanowire particles and found that these materials had better photocatalytic performance and charge transfer improvement than planar Si due to an increase in surface area. In 2014, Choi *et al.* also demonstrated that protection of Si with a layer of Al_2O_3 deposited using ALD inhibited the oxidation of the Si photocathode and reduced the overpotential for the hydrogen evolution reaction.[54]

2.3.5.2 Photoanode materials

In a typical PEC device, the oxidation reaction of water (oxygen evolution reaction) takes place at the photoanode-electrolyte interface. These electrodes usually consist of *n-type* semiconductors in which their *VB* edge is more positive than the oxygen evolution reaction of H_2O to O_2.[29] A typical PEC device consisting of a photoanode as the light absorbing material is shown in Fig. 2-13. Under light irradiation, photogenerated h^+ accumulate at the surface of the electrode where they react with water to produce oxygen, whereas photogenerated e^- migrate across the external circuit to reach the counter electrode to undergo the hydrogen evolution reaction.[29]

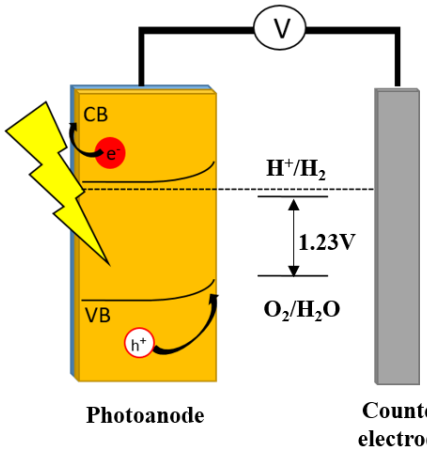

Fig. 2-13 One-step excitation PEC device consisting of a photoanode as the light absorbing material.

Unlike *p-type* semiconductor materials for photocathode applications, a larger amount of *n-type* materials can be employed in photoanode electrodes since they tend to be more stable

than *p-type* semiconductors. Among the different available materials, metal oxides such as Fe_2O_3, $BiVO_4$, WO_3 and TiO_2 are the most common materials used in these devices.[38,44,55]

Fe_2O_3 (hematite) photoanodes

Iron oxide has gained large scientific attention in the past years as a photoanode material for PEC devices owing to its high visible light absorption (E_g=2.0 eV), which translates into theoretical maximum photocurrents of 10.5 mA cm^{-2} under solar light conditions (STH= 12.9 %), non-toxicity, high abundance on the Earth surface (Fe is the 4th most abundant element on Earth), low-cost and high stability. All these numerous advantages make Fe_2O_3 a promising and excellent candidate material for PEC devices. In addition to these outstanding features, Fe_2O_3 also possesses several disadvantages that still limit the practical application of this material. Some of these disadvantages include: low conductivity and fast recombination of photocarriers, low electron mobility, large overpotential for water oxidation reactions and relatively low absorption coefficient.[38,56]

To overcome some of these limitations and improve the PEC performance of hematite, several approaches have been studied in the past years, including doping, fabrication of nanostructured devices and surface modifications.[38,56]

Hematite doping has been widely studied throughout the last years due to its potential to improve the structural, electronic and optical properties of hematite. Among the different elements that have been used for hematite doping, Sn^{4+} is currently one of the most promising ones to improve its PEC performance.[57] The first attempt of Sn^{4+} doped Fe_2O_3 was carried out in 1981 by Kennedy *et al.*[58] However, it was not until 2010 when a significant improvement in the PEC performance of Fe_2O_3 photoanodes was achieved, drawing a breakthrough in the field of hematite. K. Sivula *et al.* reported photocurrent density values of 0.56 mA cm^{-2} at 1.23 V_{RHE} reaching values higher than 1 mA cm^{-2} at 1.55 V_{RHE} when growing hematite on fluorine-doped tin oxide (FTO) substrates from a solution-based colloidal method.[59] The authors found that after 800 °C annealing treatment, Sn^{4+} from FTO substrate diffused onto the structure of hematite causing substitutional doping of Fe^{3+} for Sn^{4+} which resulted in a better absorption coefficient and improved carrier conductivity of the hematite, enhancing the photoactivity of the photoanode.

Alternatively, an approach to deal with the poor carrier mobility and facilitate efficient hole transportation to the hematite surface consists of designing nanostructured electrodes (*i.e* photoelectrodes with a certain morphology). This nanostructuring approach helps to overcome some of the main limitations encountered in metal oxides, such as poor absorption coefficients and minority carrier diffusion length. The main advantages of nanostructured materials over compact materials are reviewed in detail in Section 2.3.7. The vast availability and variety of

deposition techniques such as electrochemical deposition, spray pyrolysis and chemical vapor deposition have eased the design of such photoelectrodes.[56] One of the first publications that demonstrated the advantages of nanostructuring Fe_2O_3 photoanodes was published by A. Kay *et al.*[60] In this publication, a cauliflower-like Fe_2O_3 photoanode grown by atmospheric pressure chemical vapor deposition (APCVD) from $Fe(CO)_5$ and tetraethoxysilane achieving photocurrent density values of 2.2 mA cm^{-2} at 1.23 V_{RHE} was reported (Fig. 2-14). Such outstanding performance was attributed to the shorter pathway that photogenerated holes had to travel to reach the semiconductor-electrolyte interface, thanks to the characteristic dendritic morphology.

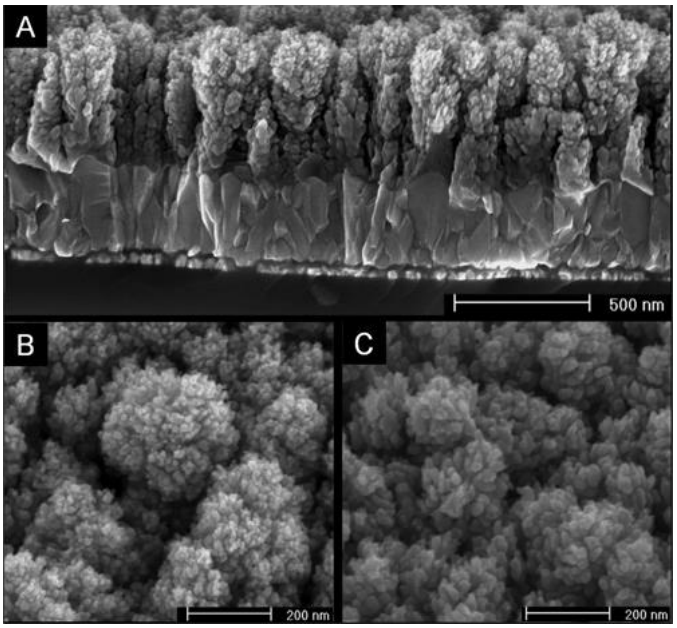

Fig. 2-14 Cauliflower-like Fe_2O_3 films grown by APCVD. Reprinted with permission from ref.[60] Copyright (2006) American Chemical Society.

A few years later, in 2013, a further optimization of the APCVD deposition process of the above mentioned Fe_2O_3 photoanodes, resulted in a significant enhancement of the PEC performance, reaching photocurrent values of 2.5 mA cm^{-2} at 1.23 V_{RHE} under 1 sun illumination.[61]

The large oxygen evolution overpotential typically encountered for hematite photoanodes has also been troublesome in hematite research. To overcome this limitation, researchers have been working on loading co-catalysts such as cobalt, cobalt-phosphate (Co-Pi), IrO_2 and FeOOH on the surface of hematite. The addition of such co-catalysts resulted successful in speeding up the water oxidation kinetics and lowering the onset potential of hematite photoanodes.[56,62] For instance, loading of Co into the cauliflower-like Fe_2O_3 resulted in an onset cathodic shift of 80 mV and a slight increase in photocurrent density values (2.7 mA cm^{-2} at 1.23 V_{RHE}, 1 sun).[60] Similarly, incorporation of Co-Pi shifted the onset potential by *ca.*

350 mV, from *ca.* 1.2 to 0.9 V_{RHE}, IrO_2 from 1.0 to 0.8 V_{RHE} and FeOOH from *ca.* 0. 13 to 0 V_{RHE} .[62–64]

Recently, iron titanates, hybrids of Fe_2O_3 and TiO_2 have also attracted scientific attention. These materials are typically formed *via* a solid-state reaction of Fe_2O_3 and TiO_2 in which, after thermal annealing various iron titanates such as Fe_2TiO_5, Fe_3TiO_4 and $FeTiO_3$ can be formed. Among the different configurations, Fe_2TiO_5 (iron titanate pseudobrookite) has been the most studied one as a photoanode material for PEC water splitting. Overall, Fe_2TiO_5 is an *n-type* semiconductor having a band gap of *ca.* 1.9-2.1 eV and showing better photocarrier separation efficiencies than their origin materials (Fe_2O_3 and TiO_2).[65] In addition, its *CB* and *VB* positions are well located in relation to the water splitting potential, as shown in Fig. 2-15. Although a promising material for PEC water splitting due to its inherent features, recent studies reveal poor PEC efficiencies and performances for the pure Fe_2TiO_5 phase.[66] This is mainly because its absorption coefficient is of *ca.* 4.6 x 10^4 cm^{-1} at a wavelength of 500 nm, requiring a film thickness of 650 nm to absorb 95 % of the incident light.[67] Thin films of pristine Fe_2TiO_5 have reported photocurrent density values of *ca.* 0.2 mA cm^{-2} at 1. 23 V_{RHE} (100 mW cm^{-2}, AM 1.5G) and onset potentials of 1.0 V_{RHE}.[66] Therefore, the challenge still relies on developing pristine nanostructured Fe_2TiO_5 films that would minimize the poor light absorption of this material. Nevertheless, it shows favorable activities when coupled to either TiO_2 or Fe_2O_3 to form heterojunctioned photoanodes.[68–70] For instance, the PEC improvement in Fe_2TiO_5-TiO_2 systems is mainly attributed to enhanced light absorption towards the visible region of the solar spectrum, whereas in Fe_2TiO_5-Fe_2O_3 heterojunctions the enhancement is ascribed to a combination of factors, such as passivation of Fe_2O_3 trapping surface states with Fe_2TiO_5 and improved charge separation efficiency due to favorable band alignment between both oxides.[65]

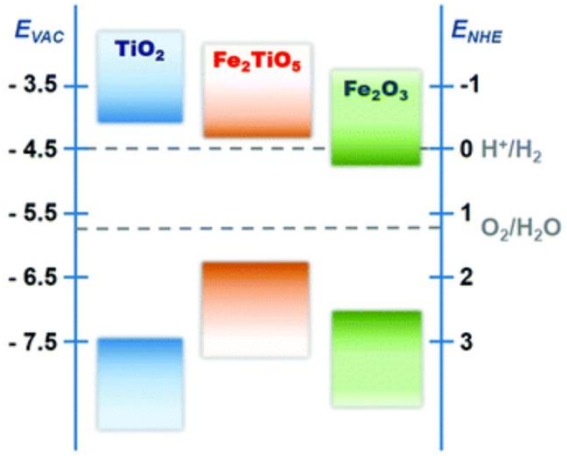

Fig. 2-15 Energy band structure of TiO_2, Fe_2TiO_5 and Fe_2O_3. Reproduced from ref.[65] with permission from The Royal Society of Chemistry.

$BiVO_4$ photoanodes

$BiVO_4$ is also an attractive material that has been widely studied as a photoanode in PEC devices. $BiVO_4$ can exist in three different polymorphs; monoclinic scheelite, tetragonal scheelite and tetragonal zircon structures. The band gap of such polymorphs falls within the range of 2.4 to 2.9 eV. Among the different polymorphs, monoclinic $BiVO_4$ is the most active one for photocatalytic water splitting applications, having a theoretical photocurrent density of 7.4 mA cm^{-2} at 1.23 V_{RHE} and STH efficiency of 9.1%.[33,71]

The first use of $BiVO_4$ as a photocatalyst was reported by Kudo *et al.* where they demonstrated its photocatalytic activity under visible light irradiation for O_2 evolution under aqueous media.[72] Since then, $BiVO_4$ has also been investigated as a promising candidate material for PEC water splitting. However, as many other metal oxides, $BiVO_4$ also suffers from several drawbacks: it has relatively low IPCE values at low potentials, suffers from fast photocarrier recombination due to short electron diffusion length and photocurrent stability is poor due to both dissolution of V^{5+} ions in the solution and surface reactions at the photoelectrode such as O_2 and H_2O_2, that act as recombination centres.[33,71]

Similar to hematite photoanodes, in order to overcome bottlenecks encountered in $BiVO_4$ photoanodes researchers are working on modifying its band structure and electronic properties by incorporating metal ions into the site of V in within the $BiVO_4$ lattice structure. Among the different doping elements that have been studied (Mo^{6+}, W^{6+}, Ta^{5+}, Zr^{4+}, Si^{4+}, Sr^{2+}, Zn^{2+} and Ag^{+}), mainly Mo^{6+} and W^{6+} reported an improvement in the PEC performance. Both metal ions (Mo^{6+} and W^{6+}) contributed to an increase in the carrier concentration promoting electron transfer from the film onto the substrate and thus giving rise to better PEC performance.[38,71] An interesting study of gradient doping of $BiVO_4$ with W for improved charge separation was published by F. F. Abdi *et al.*[73] In the study, they prepared gradient doped W-$BiVO_4$, starting from 1 % W at the interface with the back contact to 0 % W at the semiconductor electrolyte-interface *via* a spray pyrolysis method. This configuration resulted in band-bending over the entire film (bulk and surface) which increased drastically the charge carrier separation efficiency, from 38 to 60 % for a homogeneously W-doped and gradient W-doped $BiVO_4$ photoanode, respectively.

The poor surface kinetics encountered in $BiVO_4$ photoanodes is usually treated with the load of oxygen evolution catalysts. The incorporation of such catalysts reduces the e^- and h^+ recombination and lowers the onset potential of the system. Likewise hematite photoanodes, typical oxygen evolution catalysts for $BiVO_4$ also include Co_3O_4, RhO_2, Co-Pi and FeOOH/NiOOH.[71] The incorporation of these electrocatalysts in the system has successfully improved the IPCE performance, lowered the onset potential and improved the PEC

photostability of $BiVO_4$ photoanodes. In fact, one of the highest photocurrent responses for $BiVO_4$ achieved so far involved the use of FeOOH/NiOOH as an oxygen evolution catalyst.[74] In this article, Kim *et al.* reported a photocurrent performance of 1.7 mA cm^{-2} at 1.23 V_{RHE} under 1-sun illumination for undoped $BiVO_4$ photoanode, and a photocurrent performance of 4.5 mA cm^{-2} under the same conditions for $BiVO_4$ catalyzed with a dual layer of FeOOH/NiOOH as an oxygen evolution catalyst.[74] This enhancement in the PEC performance was attributed to a reduction of the e^- and h^+ recombination and shifting of flat band potential to lower values. More precisely, FeOOH reduced the interface recombination while NiOOH decreased the potential drop at the Helmholtz-layer shifting the flat band potential to lower values.

Enhancement of the e^- and h^+ separation efficiency giving rise to improved PEC performance has also been achieved by designing $BiVO_4$ composite heterojunctions. Some examples of these composites include WO_3-$BiVO_4$ and SnO_2-$BiVO_4$.[75,76]

One of the highest PEC performances found in literature for undoped and uncatalyzed $BiVO_4$ photoanodes was reported by Trzesniewski *et al.* in 2016.[77] In this publication, the authors reported a novel method for improving the PEC performance of undoped $BiVO_4$ photoanodes. They found that long exposure of $BiVO_4$ photoanodes under AM 1.5 illumination at the open circuit potential significantly improved the photoanode performance reaching photocurrent density values of 3.3 mA cm^{-2} at 1.23 V_{RHE} under 1-sun illumination, along with a cathodic shift in the onset potential and increased photovoltage. It was found that this method improved both surface and bulk properties of the photoanode, most likely due to passivation of surface states and photoreduction of V^{5+} to V^{4+}, respectively. In 2018, H. S. Han *et al.*[78] reported even higher PEC performances on $BiVO_4$ photoanodes by tailoring the surface of $BiVO_4$ so that a majority of {0 0 1} facets were exposed to the surface. The resultant photoanode exhibited a PEC performance of 3.9 mA cm^{-2} at 1.23 V_{RHE}, being 15.6 times higher than the PEC performance of a randomly oriented $BiVO_4$ photoanode. The PEC enhancement was ascribed to an improved charge transfer efficiency. Further improvement in PEC performance was achieved after an acid surface etching treatment and Co-Pi loading, obtaining PEC performances of 6.1 mA cm^{-2} at 1.23 V_{RHE}. Overall this publication demonstrated that facet engineering can boost significantly the PEC performance of $BiVO_4$ photoanodes.

WO_3 photoanodes

WO_3 has been intensively studied as a photoanode material for PEC devices owing to its attractive advantages including chemical stability at pH lower than 7, low band gap (E_g=2.5-2.8 eV) which accounts for approximately 12 % of the solar radiation on the Earth's surface, and stability against photocorrosion. Its theoretical photocurrent and STH are of 3.9 mA cm^{-2}

and 4.8 %, respectively. The *VB* of WO_3 is well located for the oxygen evolution reaction of water (2.8-3.1 V_{RHE}). However, its *CB* is placed at positive potentials (0.2-0.3 V_{RHE}), therefore an external bias is required to trigger the hydrogen evolution reaction.[26,38,79,80] An interesting feature of WO_3 is that it can crystallize in five different polymorphs as temperature increases: low temperature monoclinic ε-WO_3, triclinic δ-WO_3 (from -43 to 17 °C), room temperature monoclinic γ-WO_3 (from 17 to 330 °C) orthorhombic β-WO_3 (from 740 to 1400 °C) and tetragonal α-WO_3 (from 740 to 1400 °C).[81] One of its main disadvantages is that it possesses an indirect band gap (more energy is required to generate the electron-hole pair) which often requires the preparation of relatively thick films to absorb the maximum possible light. Usually, thick films suffer from higher recombination rates of photocarriers, resulting in lower efficiencies.[82] In order to address some of these issues, research in WO_3 photoanodes has also been triggered towards the development of new WO_3 morphologies, elemental doping, heterojunction design and addition of oxygen evolution electrocatalysts to lower the onset potential of the oxygen evolution reaction.[82]

A relatively easy approach for developing nanostructured WO_3 photoanodes is using electrochemical deposition methods such as electrochemical anodization and cathodic electrodeposition. These deposition methods are cost effective and a wide range of thin film WO_3 morphologies can be achieved by simply changing the experimental conditions such as precursors employed, electrode substrate and applied potential. For instance, in 2011 Fraga *et al.* reported a self-ordered W-WO_3 nonporous electrode prepared by anodization of W foil in NaF solution (Fig. 2-16a).[83] This photoelectrode achieved a photocurrent density of 17 mA cm^{-2} at 1.7 $V_{Ag/AgCl}$ under visible light irradiation (420-630 nm). A relevant publication combining the effect of nanostructured photoanodes and heterojunctions was reported by Lei and Sreekantan in 2013.[84] In this publication, however, they grew WO_3-TiO_2 nanotube photoelectrodes using electrochemical anodization for the growth of TiO_2 and a wet impregnation method for the addition of WO_3. Interestingly, the combination of WO_3 and the large surface area of WO_3-TiO_2 nanotubes resulted in a 1.5 increase in photocurrent performance in comparison with pure TiO_2 (Fig. 2-16b). Nevertheless, this article also highlights that excess of WO_3 loading can be detrimental for the PEC performance owing to aggregate formation that can act as recombination sites for photogenerated electrons and holes. A widely cited publication in the field of nanostructured WO_3 heterojunctions was published by Su *et al.* in 2011.[75] In this article the authors also reported the effect that a nanostructured $BiVO_4$-WO_3 photoanode had on the PEC performance over planar $BiVO_4$-WO_3 photoanodes and pure WO_3 and $BiVO_4$ (Fig. 2-16c). These composites were synthesized using a solvothermal method for the growth of WO_3 and spin coating for the deposition of $BiVO_4$. The outcomes of this publication are twofold: First, an enhancement in the PEC performance

for WO_3-$BiVO_4$ photoanodes over pure WO_3 was observed owing to a better visible light absorption for the composite. Second, WO_3-$BiVO_4$ photoanodes having a nanorod morphology revealed better IPCE performance (from 9.3% to 31%) and better PEC performance than planar photoanodes owing to the slower recombination rate of electron and holes and better charge transfer in the nanostructured photoanodes.

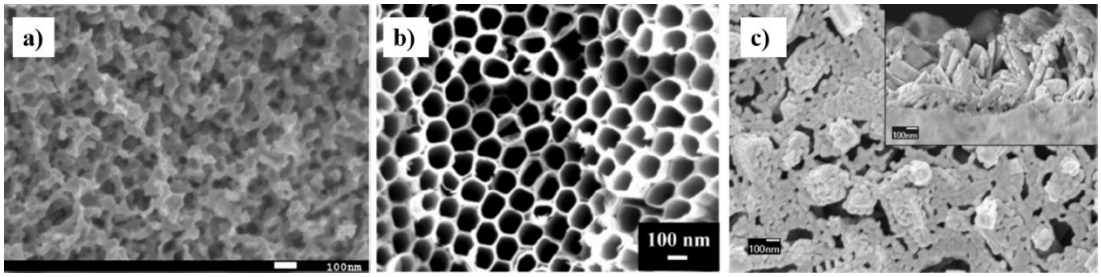

Fig. 2-16 Nanostructured photoanodes. (a) Nanoporous W-WO_3 photoanode, (b) WO_3-TiO_2 nanotubes and (c) WO_3-$BiVO_4$ nanorods. Adapted from (a) ref.[83], (b) ref.[84] Copyright (2012) Elsevier and (c) ref.[75] Copyright (2011) American Chemical Society.

As in the aforementioned semiconductor photocatalysts, another strategy to reduce the onset potential of the system and enhance the oxygen evolution reaction is by loading an oxygen evolution catalyst on the WO_3 photoanode. WO_3 is only stable in acid conditions, therefore the choice of the electrocatalyst must also meet this requirement. In line with this, typical oxygen evolution catalysts for these systems are manganese or cobalt based. In 2011 Liu *et al.* published the design of WO_3 photoanode grown by ALD and coated with a Mn-based electrocatalyst.[85] This coating improved both the stability of WO_3 photoanode in neutral pH by avoiding a direct contact of the WO_3 with the electrolyte and doubled the amount of oxygen produced during the water splitting reaction. An example of a cobalt-based electrocatalyst deposited on top of WO_3 photoanodes was reported by Seabold and Choi.[86] In this publication, the authors revealed how the loading of Co-Pi electrocatalyst both reduced the onset potential and enhanced the PEC performance of the photocatalyst. A common drawback of WO_3 photoanodes is that under light irradiation the photogenerated holes can also be used to form peroxo species that tend to accumulate at the surface of the photocatalyst and promote the electron and hole recombination which tends to lower the efficiency and stability of these photoanodes. However, loading of Co-Pi at the WO_3 photoanode favored the oxygen evolution reaction of water over the formation of peroxo species, which in turn resulted in a better photostability and PEC performance than a non-loaded WO_3 photoanode owing to the minimization of the electron and hole recombination.

The low O_2 Faradaic efficiency typically obtained in WO_3 photoanodes was investigated by J. C. Hill and K. Shin Choi.[87] They carried out a systematic investigation on the effect of using different electrolytes, containing different anions such as acetate, chloride, phosphate, perchlorate and sulfate, and cations (Li^+, Na^+ and K^+) at different pH (1, 3 and 5) for the

photooxidation of water. In particular, they studied how changing these conditions affected the portion of photogenerated holes used for the water oxidation reaction (i.e Faradaic efficiency). First, it was concluded that when acetate and chloride were present in the solution, oxidation of acetate and chloride took place, suppressing the O_2 evolution reaction. Alternatively, when a phosphate solution was used mainly O_2 and peroxo species coming from water oxidation were formed. The amount of O_2 evolved increased gradually with increasing pH. A similar trend was observed in perchlorate solutions, although the O_2 evolution Faradaic efficiency was much lower than in the case of phosphate solutions. When sulfate solutions were used, photo-oxidation of sulfate to persulfate competed also with O_2 evolution and peroxo species formation. Interestingly, as pH increased the O_2 Faradaic efficiency also increased, suggesting an improvement in the kinetics of the O_2 evolution reaction. The use of different cations also changed significantly the O_2 Faradaic efficiency. The highest values were obtained when K^+ ions were present in solution, whereas the lowest values when Li^+ was present. This was attributed to the much higher interaction of Li^+ to the WO_3 surface, which blocked active reaction sites for the O_2 evolution reaction to occur.

TiO_2 photoanodes

TiO_2 is an *n-type* semiconductor due to its intrinsic oxygen deficiency in the structure and one of the most popular semiconductor materials for water splitting applications. Since the discovery of TiO_2 as a suitable material for PEC water splitting in 1972 [28] great scientific interest and effort have been put in the development of both efficient and stable TiO_2 devices. TiO_2 has a large amount of advantages including good electronic properties, low cost, non-toxicity and chemical stability in both acid and basic conditions. These features not only make TiO_2 to be present in many current applications such as paint, tooth paste and sun cream for UV protection, but also to be highly appealing for applications in the energy and environmental field, such as photovoltaics and photochromic devices, sensing, photocatalysis, photocatalytic degradation of organic pollutants and construction materials aiming to oxidize the highly toxic nitrogen oxides (NO_x) to convert them to NO_3^-.[88–91]

TiO_2 can exist in three different crystalline polymorphs: anatase, rutile and brookite, although anatase and rutile are the most relevant in the photocatalysis field. The *CB* and *VB* edges for TiO_2 are well placed for the overall water splitting reaction of water being of -0.2 and +3.0 V_{RHE}, respectively.[92] Among the several advantages reported for TiO_2, this material is still far away from practical applications in PEC devices due to its low efficiency, which is commonly ascribed to photocarrier recombination, but mainly to the reduced use of the solar spectrum. The band gap of TiO_2 is about 3.2 eV (3.2 eV for anatase and 3.0 eV for rutile), therefore only UV light with wavelengths smaller than 380-390 nm can be utilized for photocarriers

generation. The UV light contribution of the solar radiation energy is only about 3-5 %, while the visible light accounts for 50 % of the spectrum. This implies that only a small fraction of the solar spectrum is currently used to activate TiO_2 photocatalyst, leading to theoretical photocurrent efficiencies of 1.1 and 1.8 mA cm^{-2}, for anatase and rutile, respectively, and STH of 1.3 % for anatase and 2.2 % for rutile.[26,92,94]

In the following section (Section 2.3.6), the main strategies of semiconductor band gap engineering to tackle the aforementioned limitations of TiO_2 photoelectrodes are reviewed.

2.3.6 Band gap engineering of metal oxides

Band gap engineering relies on the modification of the electronic energy structure of a semiconductor in order to promote the development and design of an active photocatalyst under visible light irradiation with better charge separation efficiency. There are two main strategies to control the electronic energy structure of photocatalysts: composite semiconductors (heterojunctions) and cation or anion doping. Although a band gap modification does not properly occur in a composite system, they are still described and considered in this section due to the enhanced utilization of the solar light that these systems can offer.

2.3.6.1 Composite semiconductors

Composite semiconductors also known as heterojunctions are a feasible alternative to create active visible-light photocatalysts as well as to reduce electron and hole recombination. Composite semiconductors consist of coupled photocatalysts with different band gap or *CB* and *VB* potentials.[88,95] Three main types of heterojunction architectures exist, as shown in Fig. 2-17: Type I (straddling), where the *CB* of SCII is higher than that of SCI and the *VB* of SCII is lower than SCI. Therefore, holes and electrons will travel to the *CB* and VB of component SCI, and accumulate there. In a type II (staggered) heterojunction, after excitation with light, photoexcited electrons will travel from the *CB* of component SCII to the *CB* of component SCI, whereas holes will travel from the *VB* of component SCI to the *VB* of component SCII. Finally, a type III (broken) heterojunction is the same as a type II but with a higher difference in *VB* and *CB* positions.[34]

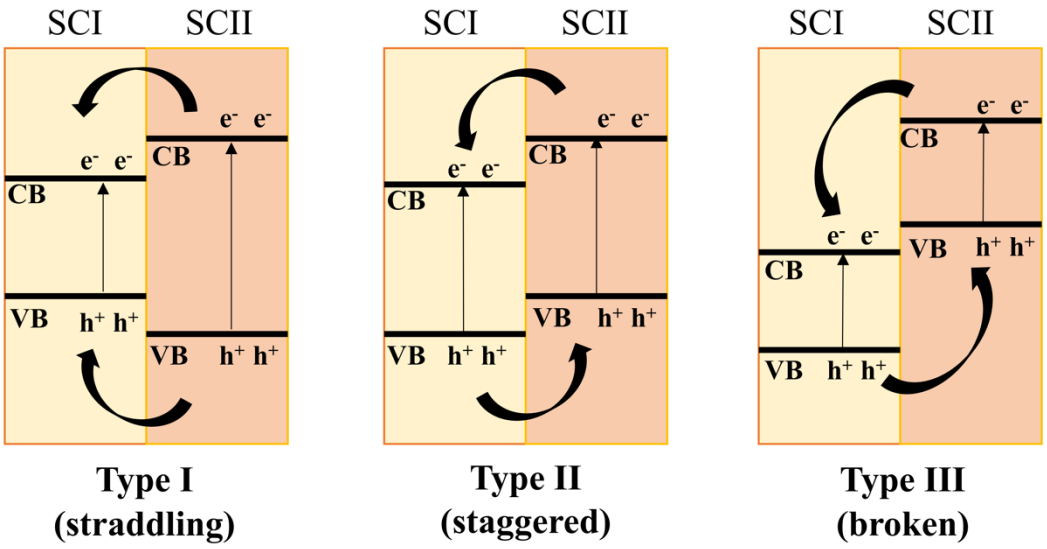

Fig. 2-17 Type I (straddling), II (staggered) and III (broken) heterojunction architectures. SCI refers to semiconductor 1 and SCII to semiconductor II. Semiconductors can be either p-type or n-type.

In the field of PEC water splitting, heterojunctions are an inherent feature of the process itself. In PEC devices, junctions between the electrolyte and the semiconductor material are always formed, whereby electron transfer takes place between the electrolyte and the semiconductor material resulting in equilibration of the Fermi Level and band bending of the semiconductor, as previously described in Section 2.3.1 and 2.3.2. Nevertheless, in this section, heterojunctions with enhanced visible light absorption and minimization of electron and hole recombination will be reviewed, with special attention to TiO_2 based heterojunctions.

A large amount of semiconductor materials with a smaller band gap than TiO_2 such as WO_3, Fe_2O_3, CeO_2, $BiVO_4$ and MoO_3 have successfully been coupled with TiO_2 to form heterojunctions that provide a synergic effect in improving both photocarriers charge separation and visible light absorption. For instance, in regard to WO_3-TiO_2 heterojunctions two relevant publications were reported by J.H Park *et al.* and W. Smith *et al.* [96,97] In 2006, TiO_2 nanotubes were grown using electrochemical anodization and were coated with WO_3 precursor using electrophoresis followed by calcination at 450 °C.[96] The resultant WO_3-TiO_2 nanotubes showed a significant improvement in visible light absorption owing to the presence of WO_3. In 2011, two types of nano-shell structures, consisting of WO_3 at the core and TiO_2 at the shell and viceversa, were synthesised.[97] These structured WO_3-TiO_2 photoanodes were grown on top of indium tin oxide (ITO) using an electron-beam evaporation system. In this study the authors found that the best sample was the one where WO_3 was at the core and TiO_2 at the shell, showing a much larger absorption in the visible range and better photocurrent performance.

A few publications have also been reported dealing with the coupling of TiO_2 with Fe_2O_3. For instance, a widely cited publication in this field was authored by S. Kuang *et al*.[98] In this work, TiO_2 nanotubes were prepared by anodization followed by deposition of $Fe(OH)_3$ using sequential chemical bath deposition to form Fe_2O_3-TiO_2 nanotubes. Maximum photocurrent density values of *ca.* 0.5 mA cm^{-2} at 0.1 V_{SCE} were achieved, which outperformed by a factor of five pristine TiO_2 samples. As in other heterojunctioned systems, this improved PEC performance was attributed to the delay in electron and hole recombination (photogenerated electrons travel from the *CB* of TiO_2 to the *CB* of Fe_2O_3) and improved visible light absorption.

The coupling of TiO_2 with CeO_2 has also proven to be successful in both reducing the band gap of the material and improving the PEC performance. Recently, Y. Tan *et al.* designed TiO_2 nanotubes using electrochemical anodization and incorporated Ce in the form of Ce_2O, CeO_2 and Ce.[99] The resultant photoanodes were able to split water at 0 V *vs*. E_{OCP} (open circuit potential). This great achievement was attributed to a better visible light absorption and improved electron-hole separation efficiency.

MoO_3-TiO_2 heterojunctions have also demonstrated better visible light absorption and improved photocatalytic performance over pristine TiO_2. For instance, M. Lu *et al.* reported an enhancement in photocatalytic activity towards photodegradation of Rhodamine B for MoO_3-TiO_2 heterojunction over pristine TiO_2.[100] M. Yang *et al.* also reported an enhancement in photocatalytic performance for MoO_3-TiO_2 nanotubes prepared using electrochemical anodization reaching a photocurrent performance of 200 μAcm^{-2} at 0.6 V_{AgCl}.[101] In 2016, H. Liu *et al*. also published an improvement in the photocatalytic performance of a MoO_3-TiO_2 heterojunction over pristine TiO_2 when used for photodegradation of Rhodamine B.[102]

2.3.6.2 Cation or anion doping

A well-known method for modifying the electronic structure of a semiconductor to extend its visible absorption range is doping, which consists of replacing some elements from the host material with external elements. Typically, doping of photocatalysts can be carried out either by cation (also known as metal doping) or anion doping and depending on the interaction of the external element with the host material, two main electronic band structure modifications may occur (Fig. 2-18).[26,88,91,95,103,104] In the first case (Fig. 2-18b), the band gap of the semiconductor is not modified, but doping introduces additional energy states below and above the *CB* and *VB*, respectively. Upon light irradiation, these impurity energy levels can extend the light absorption towards the visible region of the spectrum, showing an add-on shoulder on the absorbance spectrum (Fig. 2-18b) when compared to an un-doped intrinsic semiconductor (Fig. 2-18a). Alternatively, doping of a semiconductor can result in a modification of the *CB* and *VB* due to strong orbital overlap of the dopant with the states that

form the edge of the VB and CB, leading to an overall band gap reduction when compared to un-doped semiconductor (Fig. 2-18c). In this situation, a red shift is usually observed in the UV-Vis spectrum.[26]

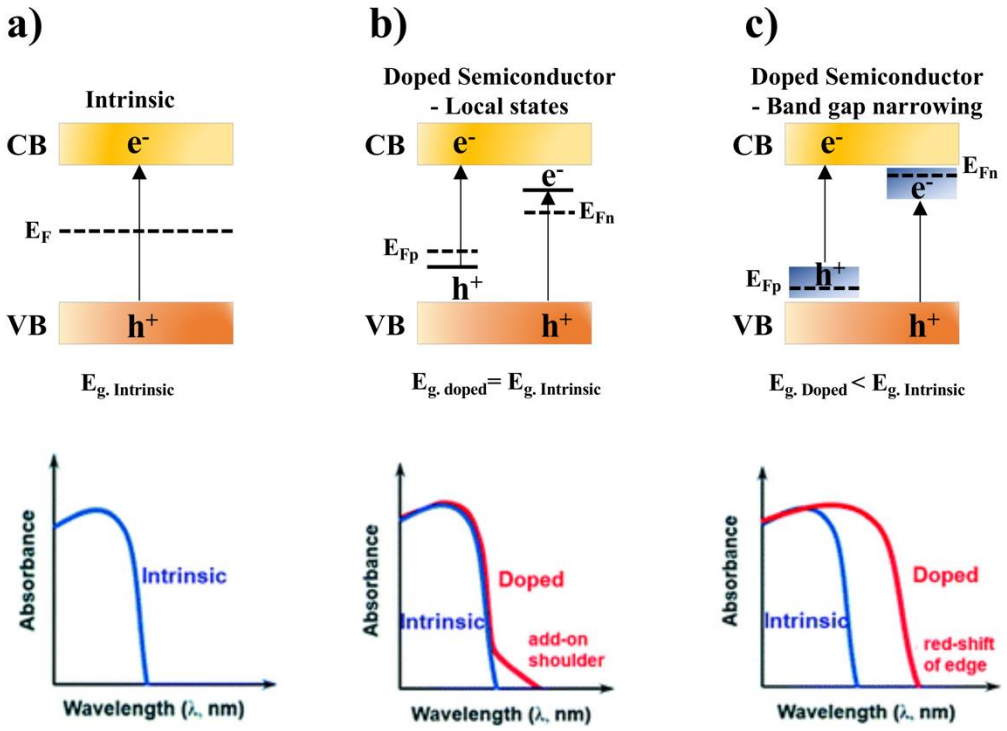

Fig. 2-18 Schematic of band gap engineering of doped semiconductors. (a) Intrinsic semiconductor, (b) doping-induced intraband energy states and (c) doping-induced band gap narrowing. Adapted and reproduced from ref.[26] with permission from The Royal Society of Chemistry.

Cation doping consists of the replacement of the metal ions present in the semiconductor with alternative metals. This metal substitution allows tuning the electronic structure of the photocatalyst since impurity energy levels are created within the band gap of the photocatalysts, which may result in a diminishment of the band gap facilitating absorption in the visible range (Fig. 2-18b,c).[95]

There is a bit of controversy in literature in determining whether or not cation doping can increase the photocatalytic response in comparison to pristine TiO_2. On one hand, cation doping can reduce the band gap of the material which helps maximize the light absorption of TiO_2 in the visible region of the solar spectrum, but on the other hand, cation doping might also contribute to the formation of recombination centers for photogenerated electrons and holes being detrimental for the photocatalytic performance of the photocatalyst.[26,88,95]

In the early 90's, W. Choi *et al.* reported the effects of cation doping for the photocatalytic activity of TiO_2 (colloidal TiO_2) using 21 different metals. The authors reported that for a better charge transfer of electrons and holes to the surface of the photocatalyst, metal ions should be doped near the surface of TiO_2 particles since a deep metal-ion doping promotes

electron and hole recombination owing to the difficulty for electrons and holes to migrate to the interface of the photocatalyst. Furthermore, they also noticed that the concentration of the doped metal as well as the ability to trap electrons and holes had a significant effect on the photocatalytic activity of doped TiO_2. Above an optimum concentration of doped metal, the photocatalytic activity decreased due to an increase in electron and hole recombination, whereas metals with the ability to trap both electrons and holes enhanced the photocatalytic activity. Based on these, among the 21 metals studied, it was found that only Cu and Fe ions could be recommended for an improvement of the photocatalytic activity.[105]

More recently, researchers argued that the reason behind the poor photocatalytic response of some metal-doped photocatalysts was that metals were not actually incorporated into the lattice of the photocatalysts (*i.e* TiO_2). Instead, they were impregnated on the surface of the semiconductor, resulting in the formation of recombination sites and blocking reaction sites.[92,106] The substitution of Ti atoms in the TiO_2 lattice structure with an external metal reduced the band gap of the material without compromising the surface of the photocatalyst.[106]

Metal doping of TiO_2 has proved to be relatively successful in both enhancing visible-light absorption and improving the PEC response for doped-TiO_2 photoanodes. For instance, Y. Yan *et al.* reported an enhancement of the PEC performance for photoanodes of Ta-doped TiO_2 nanotubes in comparison with pristine TiO_2. This enhancement in PEC performance was attributed to decreased band gap, lower charge transfer resistance and higher charge carriers density.[107] Along the same lines, W. Zhao *et al.* successfully demonstrated that Fe-doped TiO_2 also resulted in a better PEC performance than pristine TiO_2 which was attributed to a smaller band gap and thus better light absorption.[108] In 2014, C. Wang studied the effect that different metals such as Fe, Mn and Co had on the PEC performance of TiO_2 nanorods.[109] Among the different metals studied, the authors concluded that Fe-doped TiO_2 was the most successful, being five times higher than pure TiO_2, whereas Co-doped TiO_2 had the poorest activity, but still outperforming pure TiO_2. Metal doping of TiO_2 with Ni, Ga and Cu-Ni has also been recently published, all of them showing an improved photoresponse in comparison with non-doped TiO_2.[110–112] In all cases, the PEC improvement was mainly attributed to a decreased band gap that promoted better light absorption of the solar spectrum. Very few studies have reported Mo-doped TiO_2 for PEC water splitting applications. In 2015 T. Zhang *et al.* reported Mo-doped TiO_2 photoanodes using a two-step anodization process.[113] The authors also reported an improvement in PEC performance for Mo-doped TiO_2 photoanodes in comparison with pure TiO_2 attributed to a diminishment in the recombination of electrons and holes due to a mixed phase of anatase/rutile and better light absorption. Furthermore, a larger amount of studies dealing with Mo-doped TiO_2 have been focused on photodegradation of organic dyes, showing also better photocatalytic response for Mo-doped samples than pure TiO_2.[114–

[118] In all the aforementioned publications, the substitution of the corresponding metal with the Ti atoms in the TiO_2 lattice structure was confirmed by different characterization techniques such as XRD and XPS, where a shift in peaks ascribed to metal substitution was observed. A summary of the PEC performance for the above-mentioned semiconductors along with the preparation method is illustrated in Table 2-1.

Table 2-1 Reported photocurrent performances and preparation method of several metal doped TiO_2.

M-doped photoanode	**Preparation**	**Photocurrent density ($mA\ cm^{-2}$)***	**Reference**
$Ta:TiO_2$	TiO_2 nanotubes prepared by anodic oxidation, and Ta doping using magnetron sputtering	$Ta:TiO_2$: 0.11 at $0.6V_{RHE}$ TiO_2 : 0.07 at $0.6V_{RHE}$	107
$Fe:TiO_2$	Hydrothermal method	$Fe:TiO_2$: ~ 2.92 TiO_2 : ~ 0.56	109
$Co:TiO_2$	Hydrothermal method	$Co:TiO_2$: ~ 0.76 TiO_2 : ~ 0.56	109
$Mn:TiO_2$	Hydrothermal method	$Mn:TiO_2$: ~1.25 TiO_2 : ~ 0.56	109
$Ni:TiO_2$	Anodization	$Ni:TiO_2$: ~ 0.84 TiO_2 : ~ 0.47	110
Black-$Ni:TiO_2$	Anodization	Black-$Ni:TiO_2$: ~ 4.5 TiO_2 : ~ 0.47	110
$Gd:TiO_2$	Anodization	$Gd:TiO_2$: ~ 5.1 TiO_2 : ~ 3.3 (UV light, adjusted to 100 $mWcm^{-2}$)	111
Cu-$Ni:TiO_2$	Screen printed on FTO	Cu-$Ni:TiO_2$: ~ 2.3 TiO_2 : ~ 0.4	112
$Mo:TiO_2$	Anodization and hydrothermal synthesis	$Mo:TiO_2$: ~ 0.8 TiO_2 : ~0.4	113

* Reported photocurrent density value at 1.23 V_{RHE} under 1 sun illumination (AM 1.5G, 100 mW cm^{-2}) unless otherwise stated.

Anion doping is another alternative approach to form visible-light driven oxide photocatalysts. Typically, the top of the *VB* of an oxide photocatalysts consists of O 2p atomic orbitals coming from the oxide lattice structure. The substitution of some of these oxygens in the oxide lattice with anions such as N, S or C results in a mixing of O 2p orbitals with p states of doped anions that shifts the *VB* edge upward and narrows the band gap energy of the photocatalyst (Fig. 2-18c).[95] Alternatively, anion doping may also add additional energy levels in within the band gap of the semiconductor without altering the band gap of the host material, as demonstrated by J. Wang *et al.* in N-doped TiO_2 (Fig. 2-18b).[119] Unlike cation or metal doping, anions are less likely to form recombination centers and seem to be more effective to enhance the photocatalytic activity in the visible region of the spectrum.[91,95,103]

Like metal doping, anion doping has also been proved to be successful in the development of visible light semiconductors and in the enhancement of the PEC performance of TiO_2 photoanodes. One of the most common visible-light driven photocatalyst is nitrogen-doped (N) TiO_2 and it was first reported by S. Sato in the form of NO_x-doped TiO_2 in 1986.[120] However, it was not until 2001 when researchers started to consider N-doped-TiO_2 as a promising material in photocatalytic applications. In this year, R. Asahi *et al.* demonstrated an improvement in the photocatalytic activity of N-doped TiO_2 for photodegradation of methylene blue and gaseous acetaldehyde owing to band gap narrowing.[121] Although a large number of N-doped-TiO_2 publications dealt with powdered photocatalysts suspended in aqueous solutions, a certain amount of publications have also reported an improvement in N-doped-TiO_2 photoanodes for PEC water splitting applications over pristine TiO_2. For instance, in 2016 Y. Ding and P. Nagpal reported an enhancement in the PEC performance for N-doped TiO_2 and C-doped TiO_2 nanotubes in comparison with pure TiO_2 nanotubes attributed to a better light absorption and increased charge-transfer rate over pure TiO_2.[122] S. Hejazi *et al.* also concluded that N-doped-TiO_2 nanotubular photoanodes contributed to a better PEC performance over un-doped TiO_2.[123] Other publications by J. Cao *et al.*[124] and K. Ranganathan *et al.*[125] also proved a better PEC performance for N-doped-photoanodes. The PEC performance of some of these N-doped TiO_2 photoanodes along with their preparation method is listed in Table 2-2.

Similar to N doping, carbon (C) doping has also proved to improve the PEC performance of un-doped TiO_2 photoanodes. However, the number of publications is much smaller than N-doped TiO_2. A highly relevant and cited publication for C-doped TiO_2 was published by J. Park *et al.* in 2005.[126] In this publication the authors synthesized C-doped-TiO_2 nanotube arrays via the electrochemical anodization technique. For comparison, they also prepared un-doped TiO_2 nanotube arrays. It was found that C-doped TiO_2 nanotubes had a much higher PEC performance than un-doped TiO_2. The authors attributed this improvement to a combined effect of decreased band gap and morphology. A summary of PEC performances is listed in Table 2-2.

Table 2-2 Reported photocurrent performances and preparation method of several anion doped TiO_2.

A-doped photoanode	**Preparation**	**Photocurrent density (mA cm^{-2})***	**Reference**
N:TiO_2	Anodization	N:TiO_2 : ~ 0.17 TiO_2 : ~ 0.045	122
C:TiO_2	Anodization	C:TiO_2 : ~ 0.07 TiO_2 : ~ 0.045	122
N:TiO_2	Anodization	N:TiO_2 : ~ 0.8 TiO_2 : ~ 0.2	123
N:TiO_2	Pulsed laser deposition	N:TiO_2 : ~ 0.4 TiO_2 : ~ 0.1	124

$N:TiO_2$	Doctor Blading	$N:TiO_2$: 0.15 TiO_2 : ~ 0.06	[125]
$Ni\text{-}C\text{-}N:TiO_2$	Anodization	$Ni\text{-}C\text{-}N:TiO_2$: ~ 0.250 TiO_2 : ~ 0.01	[127]
$C:TiO_2$	Anodization	$C:TiO_2$: ~ 1.8 TiO_2 : ~ 0.8	[128]

*Reported photocurrent density value at 1.23 V_{RHE} under 1 sun illumination (AM 1.5G, 100 mW cm^{-2}) unless otherwise stated.

2.3.7 Nanostructured materials

Over the last decade, nanostructured materials have made important progress and many materials such as TiO_2 or Fe_2O_3 have shown significant improvements in their performance when compared to dense and flat films. In this section, the main advantages and disadvantages of nanostructured materials, with a special focus on TiO_2 photoanodes are reviewed.

Nanostructured materials offer *shorter pathways for charge carrier collection*. This means that upon light excitation, photogenerated carriers have to travel either to the semiconductor-electrolyte interface of the photoelectrode or to the back contact to reach the external circuit and perform the water splitting reaction. The longest distance that photocarriers have to travel to reach the surface (L), relies upon the depletion layer width (W) and the charge carrier diffusion distance (L_D). Therefore, if a nanostructure can be engineered so that L is shorter or equal to the sum of W and L_D the likelihood of photocarriers recombination reduces and the charge collection efficiency improves. Fig. 2-19 shows a schematic representation of a photoelectrode comparing a flat and compact surface (Fig. 2-19a) with a nanostructured one (Fig. 2-19b). In a flat film, only photocarriers generated close to the semiconductor-electrolyte interface will avoid recombination, whereas those formed far from the surface will most likely recombine before reaching the surface-electrolyte interface. Alternatively, in the case of nanostructured photoelectrodes, regardless of where the photocarriers are generated the distance to reach the surface-electrolyte interface will always be shorter or equal than L, minimizing the probability of photocarrier recombination and increasing the amount of photocarriers reaching the surface.[15,51,129]

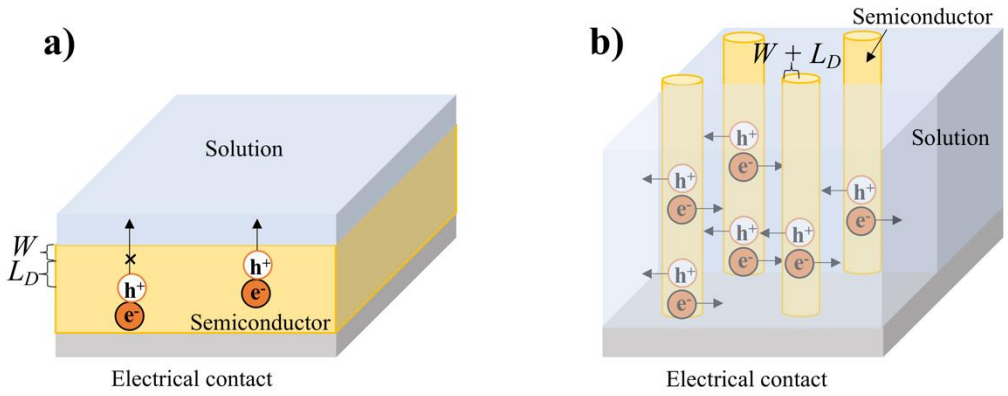

Fig. 2-19 Schematic diagram showing the photocarriers pathway in (a) flat film and (b) nanostructured film. *W* and L_D refer to the width of the space charge layer and the charge carrier diffusion length, respectively. Adapted from ref.[130] Copyright (2011) Elsevier.

An additional advantage of nanostructured over bulk or flat photoelectrodes is their *higher surface area*. If the surface area is high, a larger number of photocarriers reach the semiconductor-electrolyte interface, promoting enhanced charge transfer and maximizing the photocurrent performance of the devices. In other words, this allows water redox reactions to occur at much lower voltages which could potentially avoid the need of expensive co-catalysts.[51] Nevertheless, increasing the surface area might also imply an increase in the number of surface defects, that could eventually act as photocarrier recombination centers.

Additionally, since in a PEC process the reaction takes place at the semiconductor-electrolyte interface, tailoring the nanostructure of the material so that its most photocatalytically active facet is exposed at the surface could enhance, even more, the photocurrent performance of the device.[129] For instance, anatase TiO_2 crystals grow predominantly with {1 0 1} facets exposed, being the most stable surface, as shown in Fig. 2-20.[131] Recently, research has shown that the most photocatalytically active facets for anatase TiO_2 are {0 1 0} and {0 0 1}, therefore there are numerous research efforts in growing nanostructured anatase TiO_2 crystals with those specific facets exposed.[129,131–133]

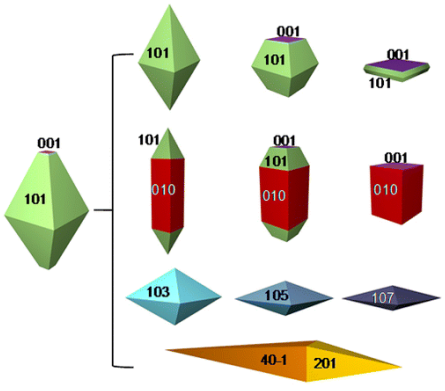

Fig. 2-20 Equilibrium shape of anatase TiO_2 crystals and evolved shapes. Reprinted with permission from ref.[131] Copyright (2014) American Chemical Society.

Another benefit of nanostructuring is the *higher light absorption*. Although the absorption coefficient (α^{-1}) of a material is independent of its nanostructure, the high aspect-ratio of nanostructured materials facilitates absorption of light that has been previously scattered from the material, as shown in Fig. 2-21b. Conversely, on a flat surface, the scattered light is lost due to direct reflection from the flat surface (Fig. 2-21a).

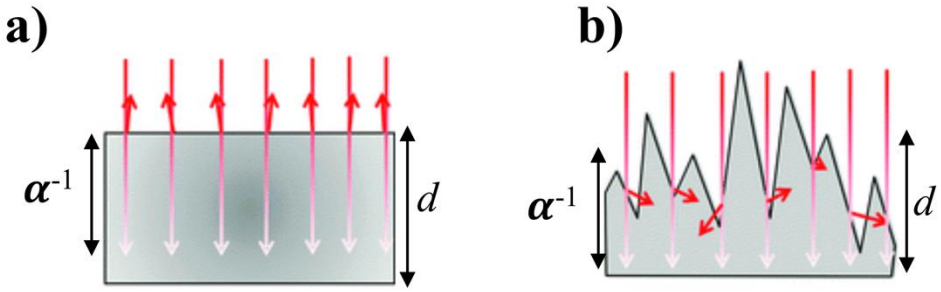

Fig. 2-21 Light distribution in (a) flat and (b) nanostructured film. *d* and α^{-1} refer to film thickness and optical penetration depth, respectively. *Short arrows* stand for scattered or reflected light. Reproduced from ref.[51] with permission from The Royal Society of Chemistry.

Finally, one of the main disadvantages of nanostructuring is the possibility of *reducing the depletion layer thickness* or space charge layer. Typically, to reduce photocarriers recombination, the space charge layer must be at its maximum. This is mainly because of the electric field formed within the space charge layer, which is responsible for triggering the photocarriers either at the surface or back contact of the photoelectrode for the water splitting reaction. Therefore, when engineering a nanostructure, if the nanomaterial is smaller than the depletion layer an increase of photocarrier recombination may be observed due to difficulty of charge separation.

Overall, even though some disadvantages may exist in nanostructured materials, their numerous advantages prevail and indeed have resulted successful in improving the PEC performance of many materials such as Fe_2O_3 and TiO_2. [56,134,135]

Table 2-3 lists characteristics of nanostructured TiO_2 photoanodes for PEC water splitting applications from some of the most relevant recent publications. The preparation method, the nanostructure obtained along with the corresponding figures of merit (photocurrent density and IPCE) are presented and summarized. The hydrothermal/solvothermal method is one of the most employed methods for the fabrication of nanostructured TiO_2 photoanodes, although mainly rutile TiO_2 is obtained. On the other hand, there is a lack of high-performing TiO_2 photoanodes prepared using CVD methods and variants, such as AACVD or MOCVD, for PEC applications. The mechanism and parameters influencing the morphology during an AACVD process will be discussed in detail in Chapter 3. The highest photocurrent density values are primarily obtained for both rutile TiO_2 and rutile/anatase TiO_2 heterojunctions

having nanorod/nanowire structures, where a PEC performance of ~ 2.6 mA cm^{-2} has been achieved. [136,137] The highest reported photocurrent density value for pure anatase TiO_2 is of 1.59 mA cm^{-2}, but it must be noted that IPCE values were not reported for this sample.[138]

Table 2-3 Summary of crystal phase, preparation method, nanostructure, photocurrent density and IPCE of pristine TiO_2 photoanodes reported in literature.

TiO_2 crystal phase	**Preparation**	**Nanostructure**	**Photocurrent density (mA cm^{-2})[a]**	**IPCE at 350 nm[b]**	**Reference**
Anatase and rutile	MOCVD	dendritic	~1.2[c]	85	[139]
Anatase	AACVD	cauliflower-structured	~0.16	n/a	[140]
Rutile	hydrothermal	branched nanorods	~ 0.85	~57 at 0.6V_{RHE}	[141]
Anatase and rutile	drop casting	nanowires	~ 2.6	~ 90	[136]
Anatase	electrochemical anodization	nanotubes	~ 0.90	~ 35	[142]
Rutile	hydrothermal	nanowires	~ 0.80	~ 90	[143]
Rutile (hydrogen treated)	hydrothermal	nanowires	~ 2.5	~ 100 at 0.4V_{RHE}	[137]
Rutile	hydrothermal	nanowires	~ 0.70	~ 40 at 1.5 V_{RHE}	[144]
Anatase	electron-beam evaporation	nanorods	~ 0.015	~ 79 at 1.6 V_{RHE}	[145]
Anatase	anodization	nanopore/nanotube	1.59	n/a	[138]
Rutile	hydrothermal	nanorods	0.98	n/a	[146]

[a] Reported photocurrent density value at 1.23 V_{RHE} under 1 sun illumination (AM 1.5G, 100 mW cm^{-2}) unless otherwise stated.

[b] IPCE measured at 1.23 V_{RHE} unless otherwise stated.

[c] Theoretical photocurrent calculated by integrating IPCE spectra.

2.3.8 Polyoxotitanium oxo/alkoxy clusters as TiO_2 precursors

Polyoxotitanium oxo/alkoxy (POT) clusters (also known as cages) are compounds of the type of $[Ti_xO_y(OR)_z]$ consisting of Ti_xO_y inorganic titanium oxide cores encapsulated within an organic alkoxy ligand periphery (OR).[147] These compounds are of great interest because they are considered both as models for studying the structural chemistry of bulk TiO_2 and as TiO_2 precursors after a controlled calcination process, as shown below:

$$[Ti_xO_y(OR)_z] \xrightarrow[-Z\ ROH]{H_2O} \xrightarrow{\text{calcination}} TiO_2 \qquad 2\text{-}14$$

Conversely to bulk TiO_2, they are very soluble in many organic solvents such as toluene and tetrahydrofuran (THF), facilitating its characterization *via* NMR or mass spectrometry techniques. Furthermore, they can be easily characterized by single-crystal X-Ray diffraction, which allows a simple correlation with the structural features of bulk TiO_2 (anatase and rutile).[148]

An additional advantage of these POT clusters is the facile modification of their chemical structure. For instance, a dopant metal can be easily incorporated into the POT structure to form metal-doped polyoxotitanium (HM-POT) cage/cluster also known as heterometallic polyoxotitanate cage. These HM-POT cages having the structure of $[Ti_XO_y(OR)_ZM_nX_m]$, where M is a metal and L an halide, are highly appealing for photocatalytic applications since they can act as a single source precursors (SSP) for metal-doped TiO_2 (TiO_2(M)) leading to the potential synthesis of active visible light photocatalysts.[147,149,150]

$$[Ti_xO_y(OR)_zM_nX_m] \xrightarrow[-Z\ ROH]{H_2O} \xrightarrow{\text{calcination}} TiO_2(M) \qquad 2\text{-}15$$

Two key concepts must be taken into account when dealing with the use of POT cages for the formation of TiO_2: The *condensation number*, which defines the ratio of the number of O_{oxo}:Ti atoms in the Ti_xO_y core (y/x) and measures the degree to which the Ti_xO_y core of a cage approximates to the composition of bulk TiO_2, and the *cage nuclearity*, which is the total number of Ti atoms in the structure.[147] Slightly modified definitions of the *condensation number* and *cage nuclearity* are used for the case of HM-POT cages. In these systems, the *condensation number* is defined as the ratio of the number of $[(O_{oxo})/(Ti+M)]$ atoms, whereas *cage nuclearity* refers to the total number of Ti + M atoms.[147] Therefore, the higher the condensation number and cage nuclearity the easier the synthesis of TiO_2 and TiO_2(M).

In 2014, P. Coppens *et al.* studied the relationship between the condensation number and cage nuclearity from a list of reported polyoxotitanium clusters with nuclearity values equal to or greater than 11 (Fig. 2-22). No clear trend was observed when plotting condensation *vs.*

nuclearity for the clusters studied (Fig. 2-22a).[148] However, when the plot was performed from classifying the different alkoxide ligands forming the cluster a relationship emerged (Fig. 2-22b). Clusters consisting of ethoxy (OEt) terminated clusters showed relatively low condensation numbers, whereas for clusters consisting of larger ligands such as isopropoxy (O^iPr), higher condensation numbers were achieved. The authors attributed this phenomenon to the effect of steric repulsion in the coordination shell of larger alkoxide ligands.[148]

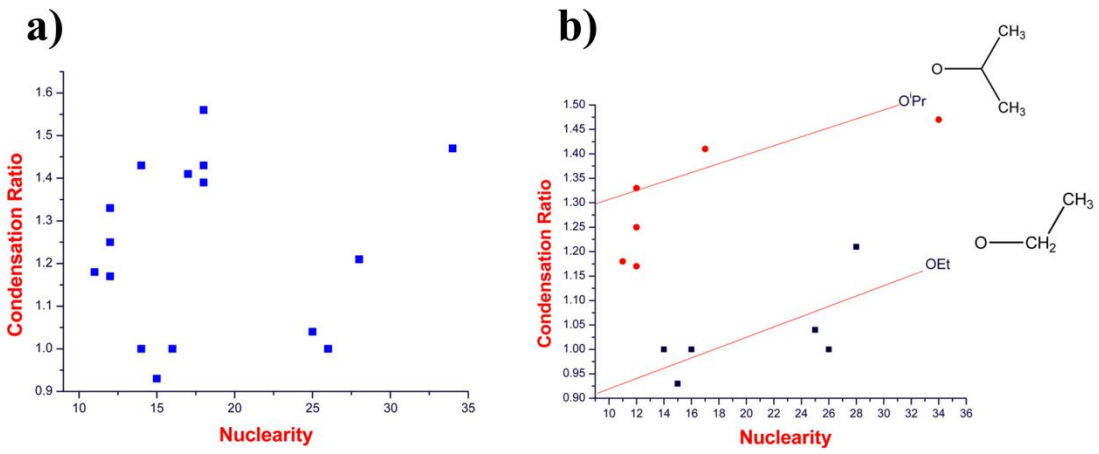

Fig. 2-22 Nuclearity *versus* condensation ratio for a list of polyoxotitanium clusters with nuclearity values ≥11. (a) No distinction between alkoxides groups and (b) for *ethoxy* and *isopropoxy*-substituted polyoxotitanate cluster. Reprinted with permission from ref.[148] Copyright (2014) American Chemical Society.

Nevertheless, a much clear correlation between the modified condensation number and metal nuclearity was observed in HM-POT clusters, as shown in Fig. 2-23.

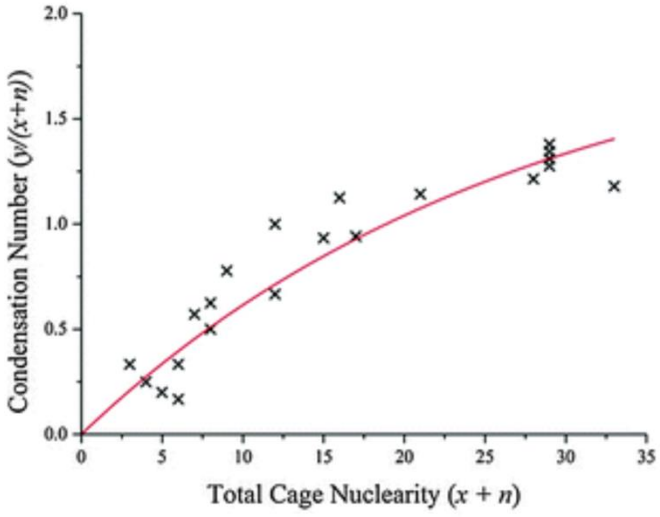

Fig. 2-23 Graph of number of metal atoms ($x + n$) in a structurally characterized HM-POT cages [$Ti_xO_y(OR)_zM_nX_m$] *vs.* the modified condensation number (y/ (x + n)). The best fit line (in red) has been drawn so that it tends to zero as the condensation number tends to 0 and tends to 2.0 as the condensation number tends to infinity. Reproduced from ref.[147] with permission from The Royal Society of Chemistry.

POT and HM-POT cages can be synthesized *via* either a sol-gel or solvothermal synthesis. Typically, a sol-gel approach involves a nucleophilic reaction of metal-alkoxides ($Ti(OR)_4$)

with H_2O. The water is usually supplied by adding traces of water to the reaction mixture or from a by-product of an esterification reaction of, for instance, acetic acid and ROH. A common reaction pathway proposed in the literature is described below, in which the degree of polymerization (*n*) depends on the initial $[H_2O]/Ti(OR)_4$ ratio.[148]

$$Ti(OR)_4 + H_2O \longrightarrow Ti(OR)_3OH + ROH \qquad 2\text{-}16$$

$$n\,Ti(OR)_3(OH)^+ \longrightarrow Ti_nO_m(OR)_{4n-2m} \qquad 2\text{-}17$$

The incorporation of additional functional groups into the titanium oxo cluster, to synthesize for example HM-POT cages *via* a sol-gel approach, is usually carried out in one pot synthesis or by grafting the ligand in a pre-formed cluster.[93]

Alternatively, POT and HM-POT cages can also be synthesized by solvothermally treating titanium (IV) alkoxides ($Ti(OR)_4$) in the presence of the corresponding alcohol (ROH) as a solvent (POT), or by adding a metal dopant precursor in the previous reaction mixture (HM-POT), as described below:[147]

$$Ti(OR)_4 \xrightarrow[D]{ROH} [Ti_xO_y(OR)_z] \qquad 2\text{-}18$$

$$Ti(OR)_4 \xrightarrow[MX_w\,D]{ROH} [Ti_xO_y(OR)_zM_nX_m] \qquad 2\text{-}19$$

These POT and HM-POT cages offer different nuclearities, spatial arrangements, and bond types depending on the precursors used during their solvothermal preparation, since they direct the path to obtain thermodynamically stable cages. The integrity and high purity obtained for these cages make them promising candidates as a single source precursor (SSP). Examples of the structure of some of these cages are shown in Fig. 2-24.

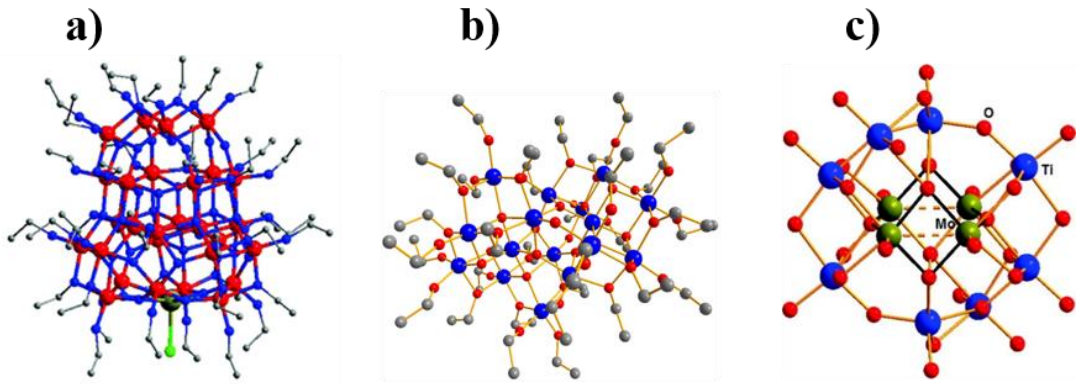

Fig. 2-24 Structures of (a) $[Ti_{28}O_{38}(OEt)_{38}(EtOH)_{1.4}CeCl]$, (b) $[Ti_{16}O_{16}(OEt)_{32}]$ and (c) $[\{Ti_4Mo_2O_8(OEt)_{10}\}_2]$. Adapted from (a) ref. [151] with permission from The Royal Society of Chemistry (b) ref.[152] Published by The Royal Society of Chemistry and (c) ref.[149] Copyright (2011) American Chemical Society.

POT and HM-POT cages as SSP have been mainly studied in the field of photodegradation of pollutants and photochemical water oxidation/reduction. In 2013 Y. Lv *et al.* reported the use of $[Ti_{28}O_{38}(OEt)_{38}(EtOH)_{1.4}CeCl]$, $[Ti_8O_7(HOEt)(OEt)_{21}Ce]$ and $[Ti_2O(OEt)_8(EtOH \cdot CeCl)]_2$ as SSP for ceria doped TiO_2 in the form of $TiO_2(Ce^{3+})$ and $Ce_2Ti_2O_7$ for photocatalytic degradation of Rhodamine B under visible light.[151] In their work, Ce-doped TiO_2 and $Ce_2Ti_2O_7$ particles were prepared by dissolving the corresponding cage in ethanol followed by calcination at 150 °C in air. Results indicated that the higher photocatalytic activity towards photodegradation of Rhodamine B was for the $Ce_2Ti_2O_7$ sample. This was attributed to a lower band gap that resulted in higher absorption in the visible region of the spectra. Recently, W. Luo and G. Ge reported the use of $Ti_6O_3(OOCCH_2COO)_2(OiPr)_{14}$ and $Ti_6O_3(OOCC_2H_4COO)_2(OiPr)_{14}$ POT cages for photodegradation of methyl orange under UV light with the assistance of H_2O_2.[153] The authors dispersed microcrystals in an aqueous solution of methyl orange. It was found that $Ti_6O_3(OOCC_2H_4COO)_2(OiPr)_{14}$ had the highest photocatalytic activity.

In 2013, Wu *et al.* reported for the first time two metal-phenanthroline substituted HM-POT cages, $[Ti_{17}O_{28}(OiPr)_{16}(Co^{II}phen)_2]$ and $[Ti_{17}O_{28}(OiPr)_{18}(Cd^{II}phen)_2]$ using a solvothermal process. These two cages were successfully deposited on indium tin oxide (ITO) coated glass by a solution coating method followed by evaporation at room temperature. Interestingly, PEC measurements of these films revealed a photocurrent of -0.4 µA for $[Ti_{17}O_{28}(OiPr)_{16}(Co^{II}phen)_2]$, whereas a much lower signal was obtained for $[Ti_{17}O_{28}(OiPr)_{18}(Cd^{II}phen)_2]$.[154] Along the same lines, HM-POT cages were also studied as SSP for the formation of CoO_x water oxidation electrocatalysts using $[Ti_{12}O_{15}(OiPr)_{17}]^+[(CoBr)_6Ti_{15}O_{24}(OiPr)_{18}(Br)]^-$ and $(CoI)Ti_{11}O_{14}(OiPr)_{17}$ cages.[155] Electrodes of these POT cages were prepared by a drop-casting method on top of FTO-coated glass. It was found that the performance of this Co-electrocatalyst was comparable to the well-known

water oxidation electrocatalyst (Co-Pi) reported by Nocera, and widely used for improving the PEC performance.[156] In 2014, Y. Lin *et al.* reported the use of $Ti_6O_4(OEt)_4(OPr^i)_4(OOCC_6H_5)_8$, $Ti_6O_4(OEt)_8[OOC(CH_3)_3]_8$ and $Ti_6O_4(OCH_3)_8[OOC(CH_3)_3]_8$ oxo cages for photocatalytic hydrogen production in water suspensions using methanol as a hole scavenger and UV irradiation.[157] These clusters achieved H_2 production rates of 383.6, 258 and 279.7 mmol h^{-1} g^{-1}, respectively. Similarly, in 2016 W. H. Fang *et al.* synthesized the largest titanium oxo cluster ever reported (3.6 nm), with a chemical formula of $Ti_{52}(\mu\text{-}OH)_2(\mu\text{-}O)_{14}(\mu_3\text{-}O)_{50}(\mu_4\text{-}O)_8(PA)_{34}(OiPr)_{28}$ (HPA= propionic acid).[158] This cluster was synthesized following a solvothermal reaction. Additionally, it showed good stability in both alkaline and acidic aqueous suspensions for at least 24 h. This high stability was most likely attributed to the protection effect of large organic ligands surrounding the core of the cluster. Once tested for photocatalytic H_2 production in the presence of a hole scavenger (methanol) and under UV light it reached H_2 production rates of 398 μmol h^{-1} g^{-1}.

A photoelectrode for water oxidation application using $[Ti_2(OEt)_9(NiCl)]_2$ cage was reported by Y. Lai *et al.* in 2013.[159] In this publication, the authors deposited $[Ti_2(OEt)_9(NiCl)]_2$ on top of a nanostructured WO_3 photoanode using a drop-casting method. Hydrolysis and polycondensation of the cage gave rise to amorphous TiO_2, which helped to stabilize WO_3 and NiO_x that was acting as an electrocatalyst for the system. Photocurrent measurements under solar light irradiation (1 sun, AM 1.5G) showed a photocurrent of around 200 μA cm^{-2} at 0.94 V_{RHE} for the photoanode. Along the same lines, J. Hou *et al.* synthesized two benzene dicarboxcylate (BDC) and salicylate (SAL) substituted POT cages $Ti_{13}O_{10}\text{-}(o\text{-}BDC)_4(SAL)_4(OiPr)_{16}$ and $Ti_{13}O_{10}(o\text{-}BDC)_4(SAL\text{-}Cl)_4(OiPr)_{16}$.[160] These POT cages were deposited on ITO-coated glass and annealed at three different temperatures; room temperature, 280 and 500 °C. The film prepared at room temperature had the same composition and structure as the starting cage, whereas at 280 °C the organic components of the cage were lost and at 500 °C the POT cage was transformed to anatase TiO_2. PEC studies indicated that the highest photocurrent was obtained for the sample annealed at 500 °C, reaching a photocurrent value of 5 μA cm^{-2} using a xenon lamp without any filter.

More recently, S. Eslava *et al.* reported the use of $Ti_{16}O_{16}(OEt)_{32}$ and graphene oxide (GO) for the synthesis of TiO_2 nanoflakes to be used for photocatalytic hydrogen production in aqueous suspensions using methanol as a hole scavenger.[152] These TiO_2 nanoflakes increased by a factor of five the amount of solar hydrogen produced in comparison to standard TiO_2 P25.

Chapter 3. Aerosol-assisted chemical vapor deposition: Processes and influence of deposition parameters on the morphology of the films

In this chapter, fundamentals and mechanisms of chemical vapor deposition (CVD) and aerosol-assisted chemical vapor deposition (AACVD) for thin films preparation are presented. A literature review highlighting the main deposition parameters of AACVD (precursor, temperature, solvent and substrate) with greatest influence on the final morphology and nanostructure of the film are discussed and reviewed in detail.

3.1 Fundamentals of CVD and AACVD systems

Chemical vapor deposition (CVD) is a deposition technique that has been widely used for the formation of thin solid films on substrate materials, since it offers good film uniformity, composition control and excellent step coverage. As its name suggests, this deposition method involves a chemical reaction of vapor-phase precursors, through several key steps, summarized in Fig. 3-1. First, precursor molecules are transported into a heated reaction chamber by means of either an inert carrier gas (argon or nitrogen) or vacuum (1). Once in the reaction chamber, weak physisorption of precursor molecules on the substrate surface' occurs along with gas-phase reactions to produce reactive intermediates and gaseous by-products (2-4). Further transport of atoms across the surface leads to nucleation and surface chemical reactions for film growth (5-6). Finally, desorption and mass transport of remaining decomposition by-products (7-9) allows the formation of films of the desired material.[161,162]

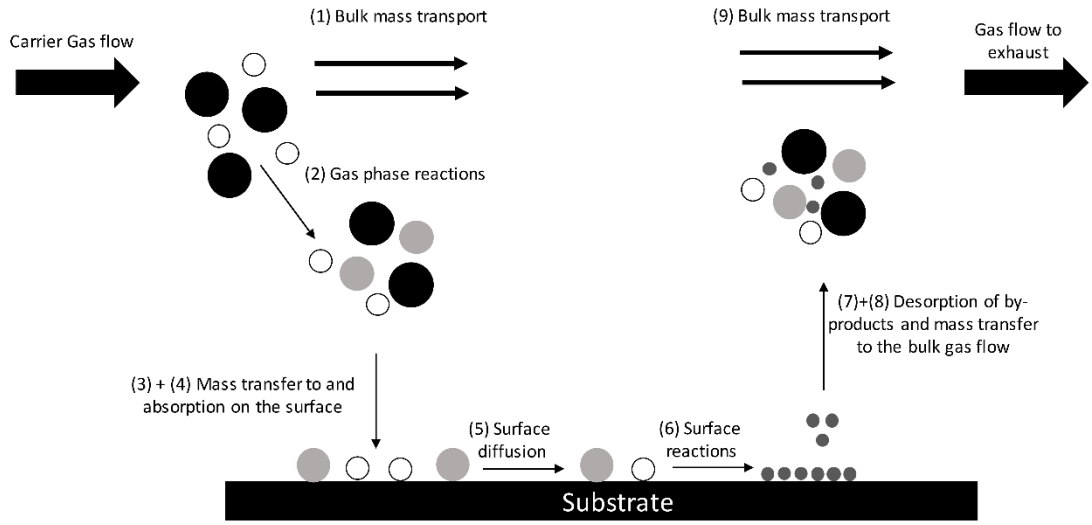

Fig. 3-1 Schematic diagram showing the main steps in a conventional CVD process. Adapted from ref.[163] Copyright 1969 Springer Nature.

The first industrial application of CVD was reported in 1893, where Lodyguine patented the deposition of W onto carbon lamp filaments.[164] Around that period, CVD processes were

widely used in industry, mainly in the field of extraction and pyrometallurgy for the production of high purity refractory metals such as Ti and Ni, as shown below:[165]

$$TiI_4 \xrightarrow{1200\,^{\circ}C} Ti + 2I_2 \quad (The\ Van\ Arkel\ process) \qquad 3\text{-}1$$

$$Ni(CO)_4 \xrightarrow{150^{\circ}C} Ni + 4CO\ (The\ Mond\ process) \qquad 3\text{-}2$$

However, it was not until the last 50 years that CVD technology took a new perspective and started to focus on the deposition rather than extraction process of metals. This new approach made CVD technology to become pioneer in coating technologies with a wide range of applications such as fabrication of electronic and optoelectronic devices, surface modification coatings, ceramic fibers and gas sensors.[162,165]

CVD technology has attracted great interest from the scientific community, especially in the semiconductor field due to its abundant advantages. It can produce highly dense and pure materials, and produced films are uniform with good reproducibility. Furthermore, surface morphology, crystallinity and orientation of the films can be easily controlled, facilitating to meet the targets for each specific application.[165] However, one of its main disadvantages is that only chemical precursors which are volatile and thermally stable can be used in conventional CVD process, limiting the range of precursors that can be investigated.[162,165,166] In this regard, several CVD variants such as plasma enhanced CVD (PECVD), atmospheric pressure CVD (APCVD), metal organic CVD and aerosol-assisted CVD (AACVD) have been developed in the past years, so that a wider span of materials and films could be deposited depending on the process employed.[165] In this chapter, AACVD will be the only technique reviewed, being the primary scope of this thesis.

In an AACVD process chemical precursors are dissolved in a solvent from which an aerosol is generated and transported to the reactor chamber by a carrier gas. This holds out the advantage that chemical precursors used do not need to be volatile, but soluble in any solvent from which an aerosol could be easily generated.[162,166] This benefit over conventional CVD systems allows a wider choice and availability of chemical precursors used for the production of high-quality thin films and facilitates the delivery and vaporization of precursors.[166] A schematic diagram of an AACVD process, summarizing the main steps is shown in Fig. 3-2.

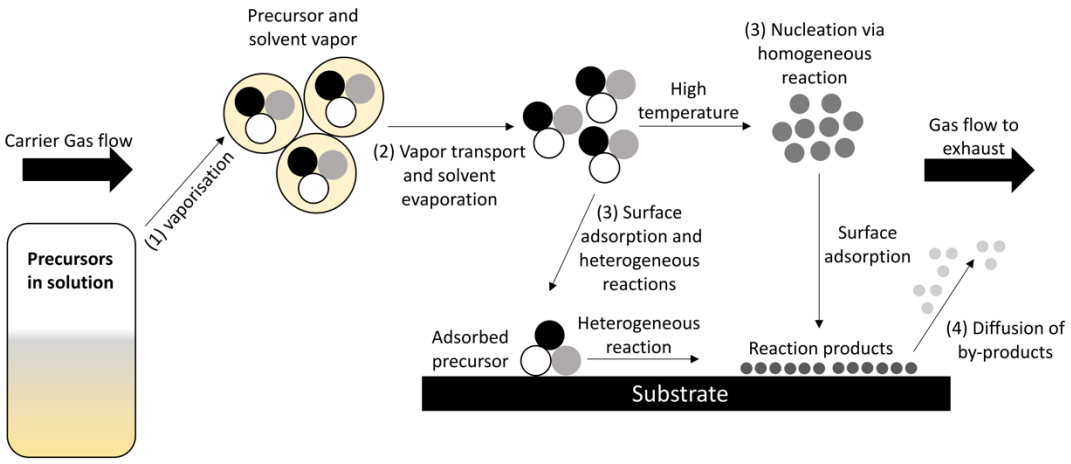

Fig. 3-2 Schematic diagram summarizing the main steps and process involved in AACVD. Adapted from ref.[162] with permission from The Royal Society of Chemistry.

Briefly, in an AACVD deposition process the chemical precursors are dissolved in a solvent from which an aerosol is generated *via* either an ultrasonic aerosol generator, pneumatic aerosol Jet or electrostatic aerosol atomizer.[166] The 'precursor mist or aerosol' is then transported to the heated reactor chamber by a carrier gas, usually argon or nitrogen, although compressed air can also be used for the deposition of some oxide products.[166] Once the 'precursor mist' is in the heated reactor chamber, the solvent undergoes rapid evaporation/decomposition (1-2), leaving the vaporized precursor in its gaseous state, which decomposes/react to form the desired film (3). The film can be formed either *via* a heterogeneous or homogeneous reaction or a combination of both (3). Typically, in a heterogeneous reaction system the vaporized precursor suffers from preliminary decomposition in the gas phase. The resultant intermediate products are then adsorbed on the surface of the heated surface undergoing chemical reactions/decomposition to form the desired film. Alternatively, homogeneous reaction processes occur when the temperature of the reactor chamber is too high. Under these conditions, vaporized precursor decomposes/reacts primarily in the gas phase giving rise to the formation of films with very fine particles and structures. [162,166] Finally, diffusion of by-products to the exhaust system occurs (4).

3.2 Influence of deposition parameters on the morphology of the films

AACVD is a versatile technique in which film growth can be easily controlled by varying different experimental parameters such as precursor, temperature, solvent and substrate used. By changing these parameters, deposition conditions are modified giving rise to thin films with different morphologies, nanostructures and eventually material properties. This control over the morphology of the films is of special interest in PEC applications, in which nanostructured devices tend to offer better performances than flat films, as briefly discussed in Chapter 2.[51,167] In this regard, AACVD emerges as a promising deposition method for the

design of efficient nanostructured thin films for PEC applications. In the following sections, the main four parameters affecting the morphology and growth of the films will be discussed along with relevant examples.

3.2.1 Precursor

The choice of the chemical precursor plays an important role in the final morphology of the film. AACVD of different precursors under the same experimental conditions (*i.e* same deposition temperature, substrate, flow and carrier solvent) leads to films with different morphologies due to different reaction/decomposition paths of each chemical precursor during the deposition process. For instance, S. Basharat *et al.* demonstrated that when preparing Ga_2O_3 from a mixture of $[Ga(NMe_2)_3]_2$ and ROH (R = $CH_2CH_2NMe_2$, $CH(CH_2NMe_2)_2$, $CH(CH_3)CH_2NMe_2$, CH_2CH_2OMe and $C(CH_3)_2CH_2OMe$)) in toluene at 550 °C different morphologies were obtained.[168] When a mixture of $[Ga(NMe_2)_3]_2$ with $HOCH(CH_2NMe_2)_2$ was deposited spherical particles were obtained (Fig. 3-3a) whereas when $HOCH(CH_3)CH_2NMe$ was used a snowflake-like morphology was observed (Fig. 3-3b). Post-annealing in air at 600 °C for 24 h ($[Ga(NMe_2)_3]_2$ with $HOCH(CH_2NMe_2)_2$) resulted in films with similar morphology but larger particle size (Fig. 3-3c,d).

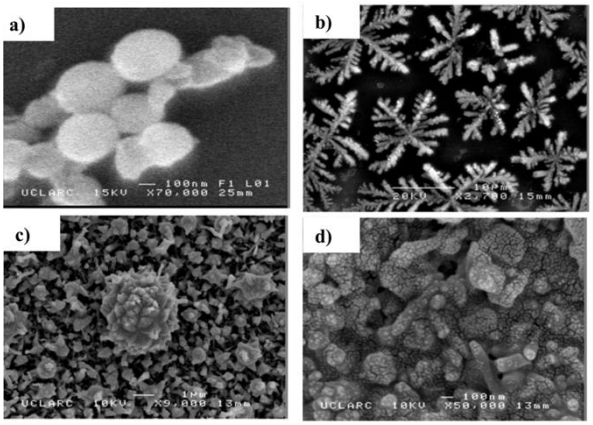

Fig. 3-3 SEM micrographs of as-deposited Ga_2O_3 films deposited at 550 °C in toluene on a SiCO coated float-glass substrate. Films were deposited from a mixture of $[Ga(NMe_2)_3]_2$ with (a) $HOCH(CH_2NMe_2)_2$ and (b) $HOCH(CH_3)CH_2NMe$. SEM micrographs of post-annealed film at 600 °C for 24 h of $[Ga(NMe_2)_3]_2$ with $HOCH(CH_2NMe_2)_2$ at (c) 9,000 and (d) 50,000 magnification. Adapted and reproduced from ref.[168] with permission from The Royal Society of Chemistry.

Likewise, H. Kim *et al.* reported that when using different WO_x precursors completely different morphologies were achieved.[169] Fig. 3-4 shows SEM micrographs of $W_{18}O_{49}$ films prepared using $WO(OCH_3)_3$(acac) and $WO(OCH_2C(CH_3)_3)_3$(dpm) as WO_x precursors under the same experimental deposition conditions. It was found that when using $WO(OCH_3)_3$(acac) nanorod-like structures were formed (Fig. 3-4a-b), whereas when $WO(OCH_2C(CH_3)_3)_3$(dpm) was used a combination of nanorods and 3D-dendritic like structures were obtained (Fig. 3-4 c-d), suggesting the presence of nucleation sites along the nanorods.

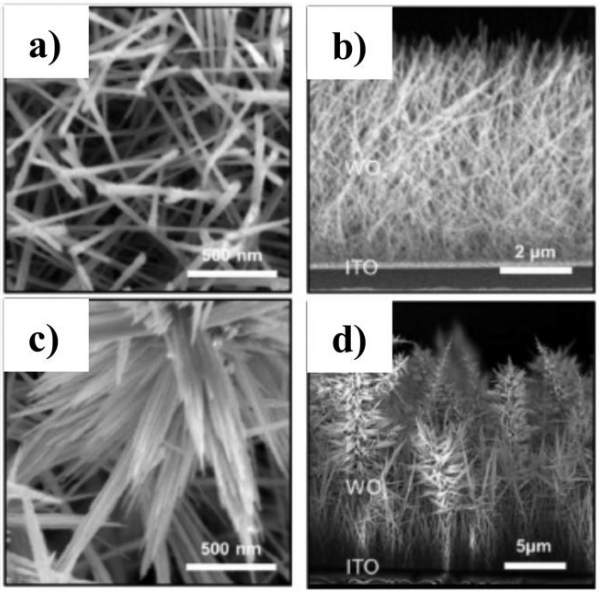

Fig. 3-4 SEM micrographs of $W_{18}O_{49}$ films deposited from (a-b) $WO(OCH_3)_3(acac)$ and (c-d) $WO(OCH_2C(CH_3)_3)_3(dpm)$ at 550 °C in diglyme. Adapted and reproduced from ref.[169] Copyright 2012 Electrochemical Society.

As for WO_x precursors, when a variety of PbS precursors were used for AACVD deposition of PbS films, different nanostructures were attained (Fig. 3-5).[170] For instance, when $[Pb(S_2CNMeBenzyl)_2]$ was used large cubes and rods of *ca.* 10 μm were obtained (Fig. 3-5a), whereas when $[Pb(S_2CNMehep)_2]$ was used plate-like morphologies of *ca.* 8 μm were formed (Fig. 3-5b).

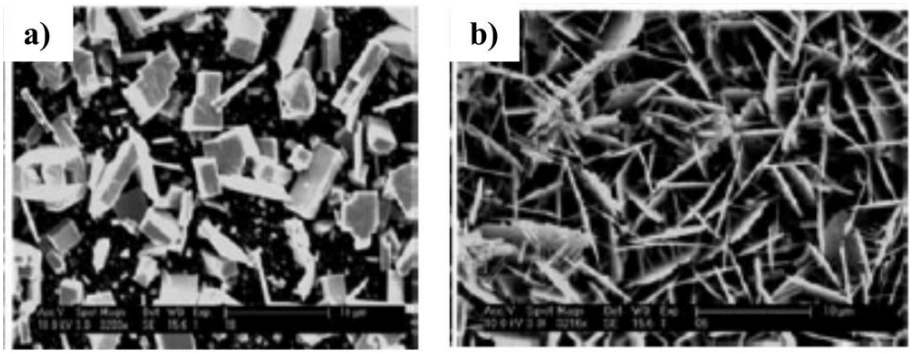

Fig. 3-5 SEM micrographs of PbS thin films deposited from (a) $[Pb(S_2CNMeBenzyl)_2]$ and (b) $[Pb(S_2CNMehep)_2]$ at 525 °C in toluene. Adapted and reproduced from ref.[170] with permission from The Royal Society of Chemistry.

AACVD has also been widely used for the synthesis of doped metal oxides, such as Mg or W-doped TiO_2.[171,172] To achieve that, a mixture of chemical precursors containing the chemical precursor of the desired metal oxide along with small amounts of the dopant precursor were added into the reactor chamber to obtain (un)doped-metal oxide thin film. In this regard, since the mixture involves different precursors, different morphologies were usually obtained for the doped and undoped metal oxide films due to different reaction/decomposition paths of the

mixture. For instance, S. Shakir *et al.* reported Mg-doped TiO_2 photoanodes grown by AACVD.[171] The authors found that when Mg precursor was added in the reaction mixture films were significantly more porous than undoped TiO_2 films (Fig. 3-6).

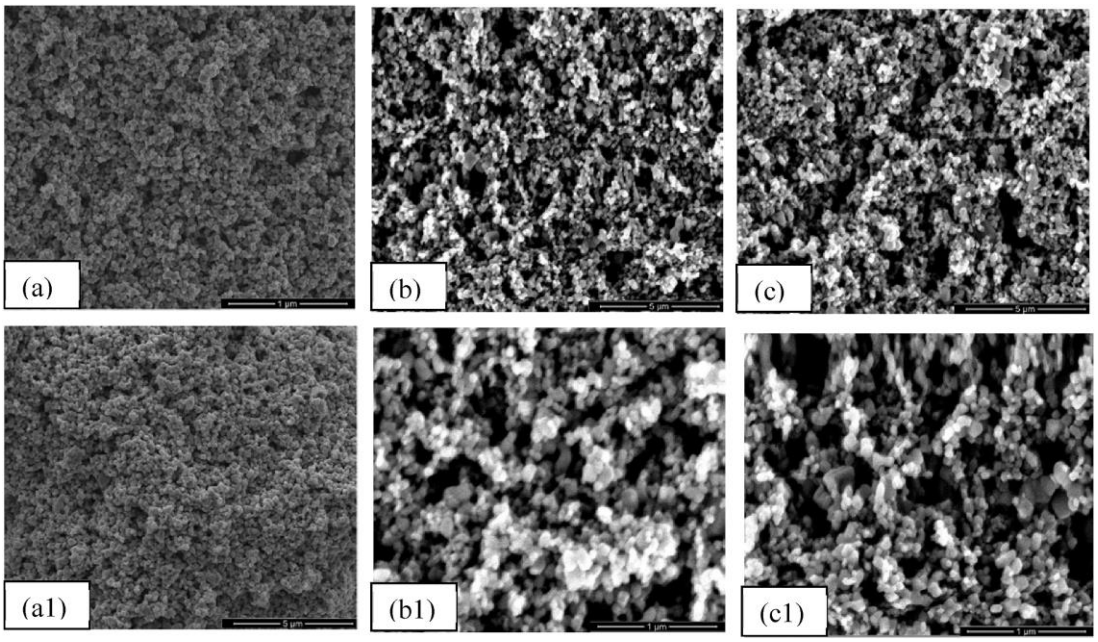

Fig. 3-6 Low (a-c) and High (a1-c1) resolution SEM micrographs of (a, a1) un-doped TiO_2, (b, b1) 1 % mol Mg-doped TiO_2 and (c, c1) 2 % mol Mg- doped TiO_2. All films were deposited at 450 °C for 2 h from a mixture of titanium isopropoxide and $Mg(NO_3)_2$. $6H_2O$ (dopant source) in methanol. Reproduced from ref.[171] Copyright 2017 Elsevier.

Similarly, when adding $W(OEt)_5$ in a solution of $Ti(OEt)_4$ for the preparation of W-doped TiO_2 films, films consisting of compact domes (Fig. 3-7a) that gradually transformed to pyramidal-like features (Fig. 3-7b-f) after incorporation of $W(OEt)_5$ in the reaction mixture were formed.[172]

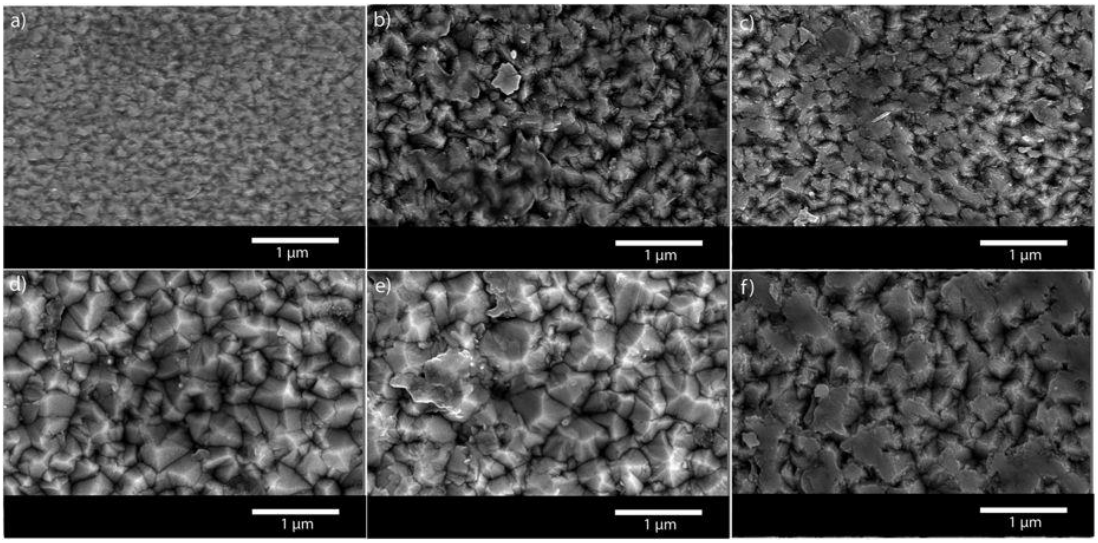

Fig. 3-7 SEM micrographs of (a) un-doped TiO_2 and (b-f) W-doped TiO_2 with varying atomic percentages of W, from 0.63 to 4.65 %. All films were deposited from a mixture of $Ti(OEt)_4$ with dopant amounts of $W(OEt)_5$ in toluene. Deposition was performed at 500 °C for 45 min. Reproduced from ref. [172] by Scientific Reports.

3.2.2 Temperature

The deposition temperature during an AACVD process can also affect significantly the microstructure of the film due to different decomposition/reaction paths of the chemical precursor. As mentioned in Section 3.1, if deposition temperature is too high films usually tend to form primarily due to homogeneous nucleation of particles giving rise to films with finer structures and porosity. Conversely, at lower deposition temperatures films tend to be formed mainly *via* heterogeneous reactions and larger microstructures are usually observed. For instance, different morphologies and microstructures were observed when depositing titanium isopropoxide at deposition temperatures of 400, 500 and 550 °C.[173] SEM micrographs of these films revealed that at 400 °C films were mainly amorphous with no characteristic morphology (Fig. 3-8a) whereas at 500 and 550 °C, angular crystallites with well-defined shape were formed (Fig. 3-8b,c). The different deposition temperature also affected the TiO_2 crystalline phase obtained: at a deposition temperature of 400 °C, only tetragonal anatase TiO_2 was observed; at 500 °C an equal mix of both anatase and rutile was present; whereas at 550 °C mainly rutile TiO_2 with small traces of anatase existed.

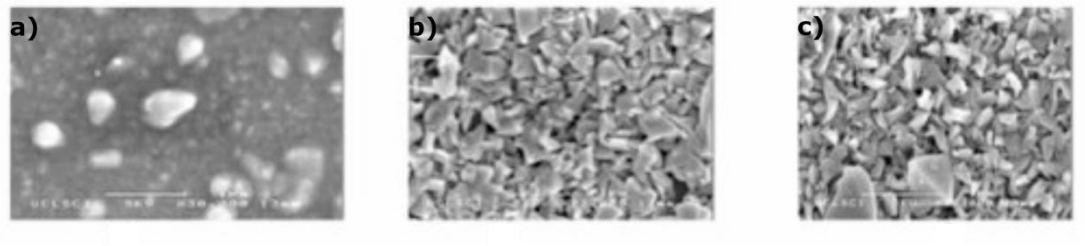

Fig. 3-8 SEM micrographs of TiO_2 films deposited by AACVD from titanium isopropoxide and methanol on glass substrates at (a) 400, (b) 500 and (c) 550 °C. Adapted and reproduced from ref. [173] Copyright 2011 Wiley.

Similarly to these TiO_2 films, A. Tahir *et al.* also observed significant differences in the microstructure when TiO_2 films prepared from a solution of titanium isopropoxide in toluene:ethanol where deposited at 350 and 400 °C.[140] At 350 °C, TiO_2 films showed rod-like features (Fig. 3-9a) whereas at 400 °C granular morphologies forming cauliflowers-like structures were observed (Fig. 3-9b). In both cases, the films consisted of pure anatase TiO_2.

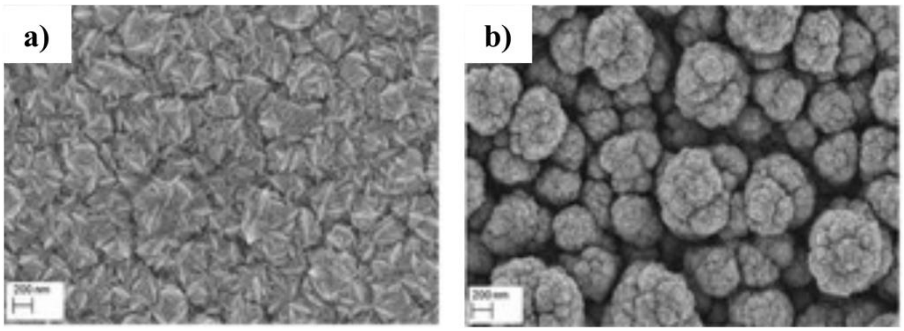

Fig. 3-9 SEM micrographs of TiO_2 films deposited by AACVD from titanium isopropoxide in a mixture of toluene and ethanol (4:1 volume ratio) grown at (a) 350 and (b) 400 °C on FTO-glass substrates. Adapted and reproduced from ref.[140] Copyright 2012 Wiley.

The growth of composites of TiO_2 by AACVD also exhibited different morphologies as a function of deposition temperature. For instance, M. Ehsan *et al.* reported the growth of CeO_2-TiO_2 composites from the reaction product of $Ce(OAc)_3 \cdot xH_2O$ and $Ti(iPro)_4$ in methanol by AACVD. [174] SEM micrographs of the obtained films presented different surface morphologies at deposition temperatures of 550 and 600 °C (Fig. 3-10). Both samples exhibited similar morphologies consisting of spherical-shaped particles. Nevertheless, the sample prepared at 550 °C (Fig. 3-10a, a1) showed a rougher surface comprising mesoporous microspheres with a pore size range of 10-28 nm, whereas at 600 °C (Fig. 3-10 b,b1) smoother surfaces with finer nanostructures were obtained.

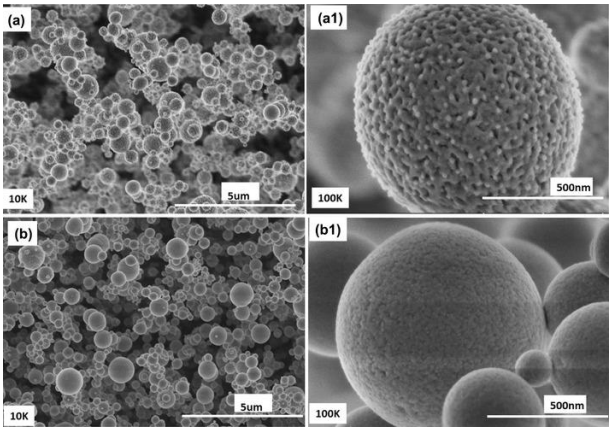

Fig. 3-10 SEM micrographs of CeO_2-TiO_2 composites prepared by AACVD on FTO-glass grown at (a, a1) 550 and (b, b1) 600 °C. Reproduced from ref.[174] Copyright 2018 Springer Nature.

A significantly greater change in morphology as deposition temperature increased was observed in Mn_2O_3-TiO_2 composites deposited from a trinuclear molecular complex with the chemical structure of $[Mn_2Ti(\mu3\text{-}O)\ (TFA)_6\ (THF)_3]$ (TFA=trifluoroacetato and THF=tetrahydrofuran).[175] Compact structures with irregular-shaped agglomerates (Fig. 3-11a), rectangular-shaped rod crystallites (Fig. 3-11b), spinal columns growing vertically from the substrate (Fig. 3-11c) and square-shaped particles forming agglomerated rectangular blocks (Fig. 3-11d) were formed at 400, 450, 500 and 550 °C, respectively. It is believed that the drastic change in morphology as deposition temperature increases was most likely attributed to the different decomposition/reaction path of the chemical precursor. At the highest deposition temperatures, the precursor was most likely undergoing a combination of homogeneous and heterogeneous reactions which led to the formation of more porous films.

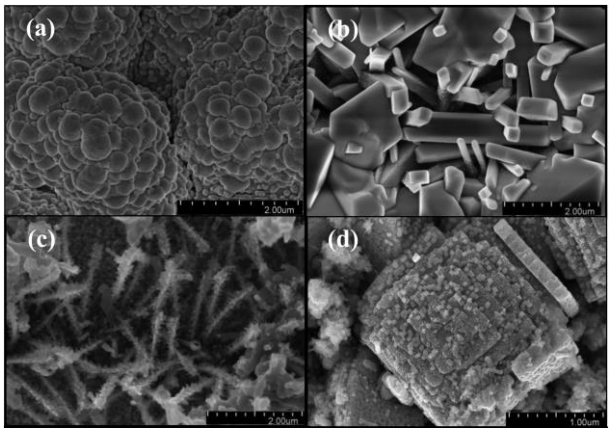

Fig. 3-11 SEM micrographs of Mn_2O_3-TiO_2 composite films prepared by AACVD at deposition temperatures of (a) 400, (b) 450, (c) 500 and (d) 550 °C. Adapted and reproduced from ref.[175] Copyright 2016 Elsevier.

Likewise, Fig. 3-12 shows SEM micrographs of $W_{18}O_{49}$ deposited from $WO(OCH_2C(CH_3)_3)_3(dpm)$ at a range of temperatures (250- 550 °C).[169] Compact and thin films were grown at low temperatures (250 and 350 °C) whereas nanostructured morphologies

consisting of nanorods (450 °C) and 3D-dendritic like structures (550 °C) were formed at higher temperatures.

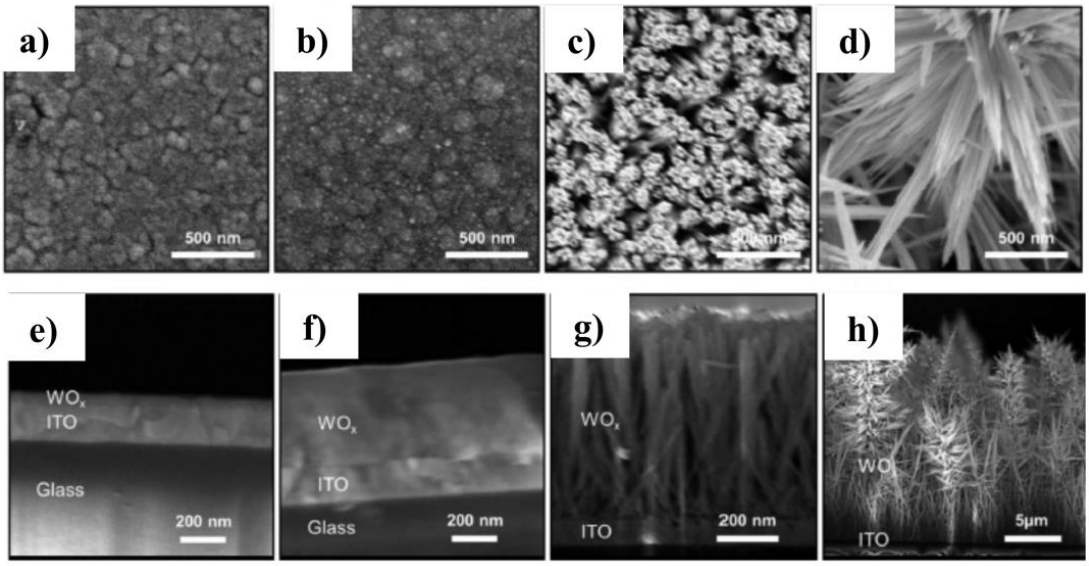

Fig. 3-12 SEM micrographs of $W_{18}O_{49}$ films deposited from $WO(OCH_2C(CH_3)_3)_3(dpm)$ at deposition temperatures of (a,e) 250, (b,f) 350, (c,g) 450 and (d,f) 550 °C. (a-d) Top-view SEM micrographs. (e-h) Cross-sectional micrographs. Adapted and reproduced from ref.[169] Copyright 2012 Electrochemical Society.

The morphology of PbS thin films was also easily tuned by changing the deposition temperature in the AACVD process. For instance, J. Akhtar *et al.* reported morphologies consisting of cubes and rectangles, snowy flakes, long strips and feather-like crystallites at 350, 400, 450 and 500 °C, respectively (Fig. 3-13).[170]

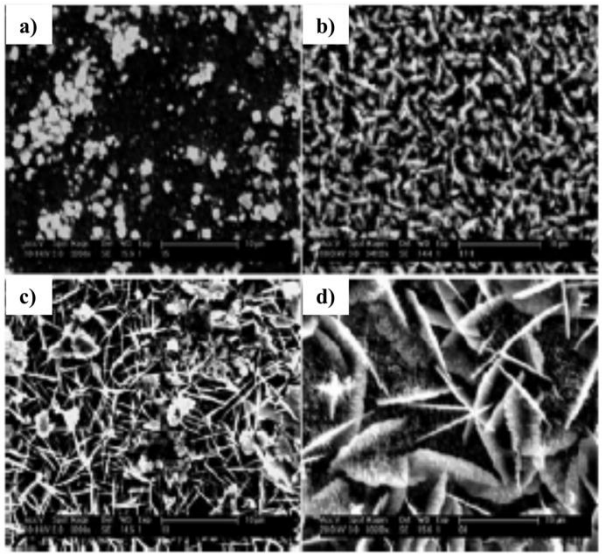

Fig. 3-13 SEM micrographs of PbS films deposited from $[Pb(S_2CNOct_2)_2]$ at deposition temperatures of (a) 350, (b) 400, (c) 450 and (d) 500 °C. Reproduced from ref.[170] with permission from The Royal Society of Chemistry.

In spite of the main homogeneous and heterogenous reactions taking place at the reactor chamber, different surface growth mechanisms can also alter the nanostructure of the as-deposited films. A detailed study on the growth mechanism of WO_x as a function of substrate temperature along the AACVD reactor was published by M. Ling and C. Blackman.[176] Fig. 3-14 shows SEM micrographs of the different WO_x morphologies obtained along the AACVD reactor as a function of reactor distance and substrate temperature. Within the first 25 mm of the AACVD reactor, where the substrate temperature was below 351°C, dense and planar films were formed. However, at a distance of 25 to 45 mm from the reactor inlet, where the substrate temperature was of 358 °C nanorod morphologies were formed.

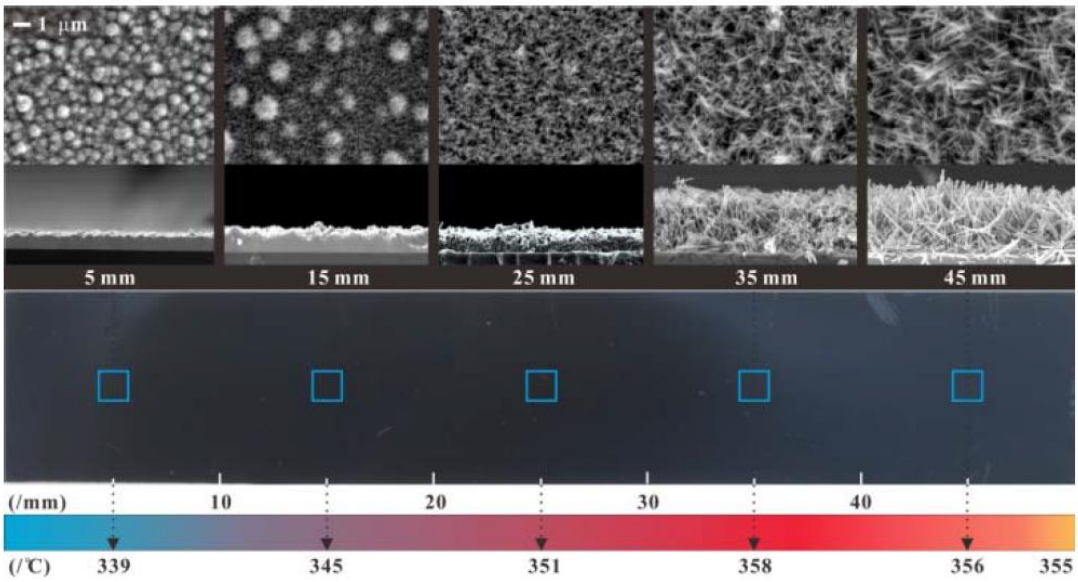

Fig. 3-14 SEM micrographs showing variation in morphology of WO_x thin films with structures that vary from planar to NRs as a function of distance from the reactor inlet and the corresponding substrate surface temperature. Reproduced from ref.[176] Copyright 2015 Wiley.

The authors ascribed these morphological changes to the competition of different growth mechanisms that occurred on the substrate surface, as shown in Fig. 3-15. For instance, at the lowest deposition temperature and close to the reactor inlet a layer-by-layer growth mechanism mostly occurred, giving rise to dense and planar films. Further away from the reactor inlet and at high deposition temperatures, a layer plus island growth took place, whereas at the highest substrate temperature mainly island growth occurred, which promoted the nanorod morphology.

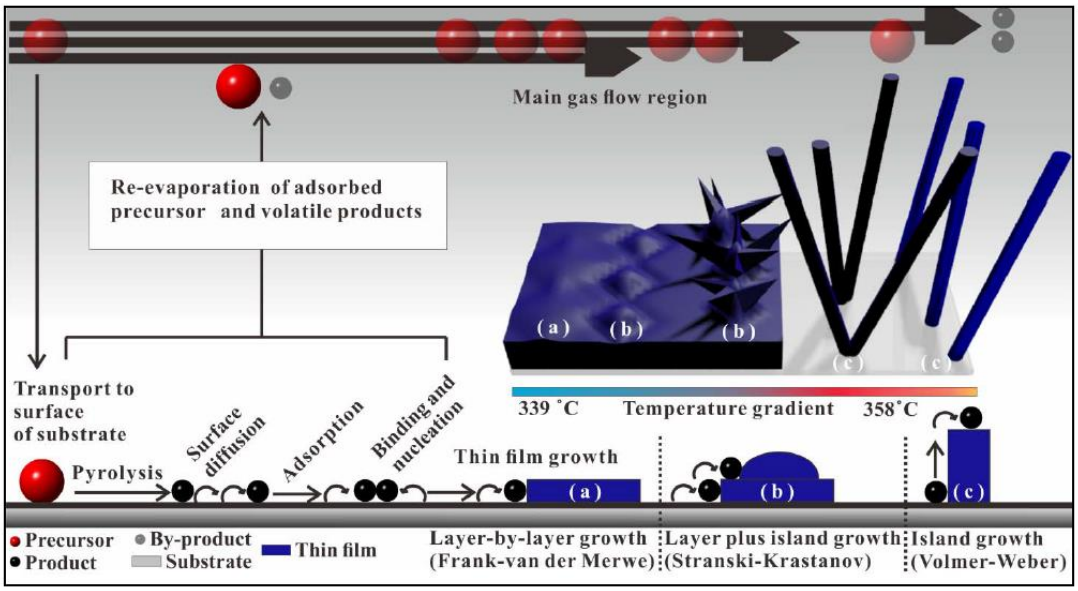

Fig. 3-15 Representative atomistic processes during thin film growth via AACVD with three growth modes: (a) layer-by-layer growth, (b) layer plus island growth and (c) island growth corresponding to various structures from planar to nanorod of WO_x. Reproduced from ref.[176] Copyright 2015 Wiley.

3.2.3 Solvent

Solvents can play a key role in tuning the morphology of an AACVD process and their influence on the final morphology is dependent upon the materials deposited and the chemical precursors used. The different inherent features of solvents, such as volatility or solubility with the precursor used can alter delivery rates and mass-transport properties of the solution in the reaction system and thus, modify the reaction pathways of chemical precursors in the gas phase. Modification of such reaction pathways leads to the formation of different reaction intermediates that can result in films with diverse morphologies and crystalline phases.[162,177] For instance, C. Edusi *et al.* reported that when depositing titanium (IV) isopropoxide using a variety of solvent compositions different morphologies and crystalline phases (anatase or rutile) were obtained.[178] Fig. 3-16 shows SEM micrographs of TiO_2 films deposited using different composition mixtures of ethanol and methanol. When only ethanol (Fig. 3-16a) was used as a carrier solvent mainly plate-like sheets morphologies were obtained, whereas needle-shaped structures were observed when methanol was used as a carrier solvent (Fig. 3-16b). In contrast, a mixture of both solvents led to films with pyramidal and rectangular-shaped crystallites (Fig. 3-16c,d). XRD analysis of these TiO_2 films indicated that films deposited using pure methanol as a carrier solvent consisted of TiO_2 rutile, whereas films deposited with ethanol were pure anatase TiO_2. When the composition ratio between these solvents was amended changes in the crystalline structure and composition were also observed. For instance, films prepared with a solvent ratio of ethanol/methanol of 50:50 and 75:25 were composed of TiO_2 rutile, whereas when the solvent ratio was 99:1, pure anatase was obtained. In contrast, when the solvent ratio was of 90:10 a mixture of rutile and anatase was achieved.

From these results it was inferred that methanol was the driving force for the formation of rutile TiO_2. Additional experiments with non-alcohol solvents, such as dichloromethane and hexane as carrier solvents also gave rise to films with a TiO_2 anatase crystal structure.

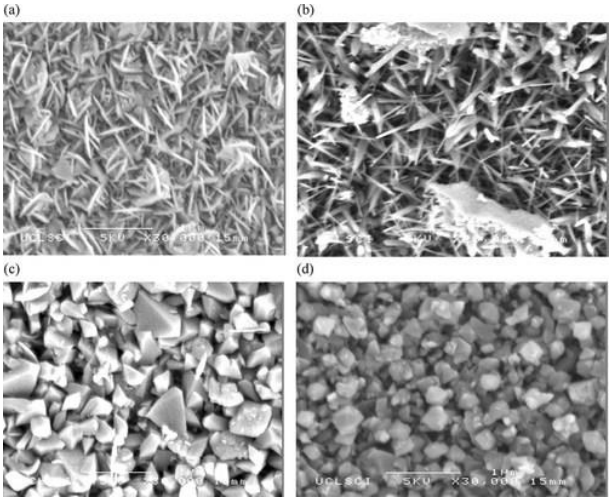

Fig. 3-16 SEM micrographs of TiO_2 films deposited at 550 °C on steel substrates by AACVD using different carrier solvents. (a) ethanol 100 %, (b) methanol 100 %, (c) 10 % methanol and 90 % ethanol and (d) 25 % methanol and 75 % ethanol. Reproduced from ref.[178] Copyright 2012 Wiley.

Similar examples were found in literature when preparing Al-doped ZnO films *via* AACVD. In this publication, D. Potter *et al.* carried out a systematic study for the deposition of Al-doped ZnO using a range of carrier solvents mixed with methanol.[179] Different morphologies were obtained when different solvent compositions were used, as shown in Fig. 3-17.

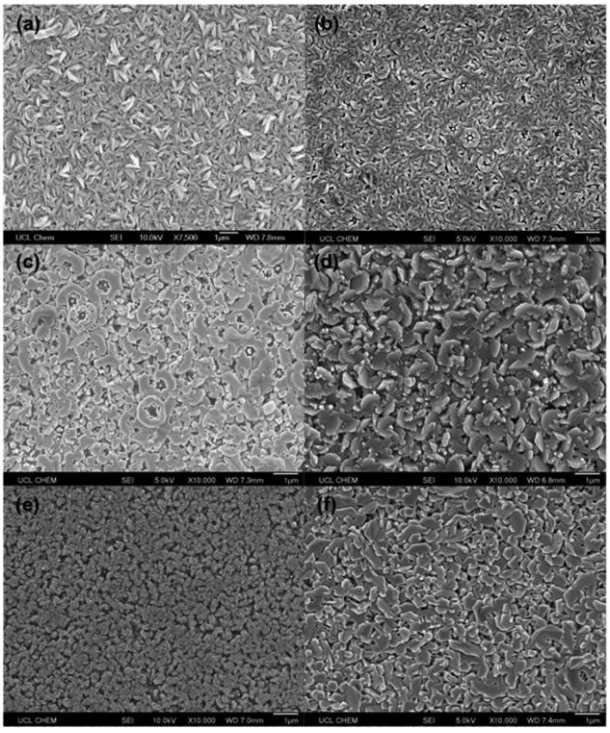

Fig. 3-17 SEM micrographs of 10 % mol Al-doped ZnO films deposited *via* AACVD at 450 °C using (a) methanol, (b) methanol and toluene, (c) methanol and tetrahydrofuran, (d) methanol and n-hexane, (e) methanol and

cyclohexane and (f) methanol and ethylacetate as carrier solvents. All mixtures consist of a 1:1 volume ratio. Reproduced from ref.[179] Published by the Royal Society of Chemistry.

All films were polycrystalline with plate-like grains of different sizes. In particular, films prepared using methanol mixed with tetrahydrofuran, n-hexane and ethylacetate exhibited the largest grains (Fig. 3-17c, d, f). The crystal structure of all samples was the same regardless of the solvent used, although preferential growth along the (0 0 2) diffraction plane was enhanced as the polarity of the solvent increased. This trend was correlated with the polar crystal structure of Wurtzite ZnO along the c-axis. The higher the polarity of the solvent, the stronger the interactions with the (0 0 2) surface and the solvent, promoting crystal growth along that direction.

The influence of carrier solvent on the morphology and crystal structure was also well studied in the deposition of fluorine-doped SnO_2 thin films.[180] Fig. 3-18 shows SEM images of fluorine-doped SnO_2 thin films prepared using either propan-2-ol (Fig. 3-18a-c) or ethanoic acid (Fig. 3-18d-f) at different deposition temperatures. As discussed in Section 3.2.2, the deposition temperature has an important influence on the morphology obtained as well as the carrier solvent used. When propan-2-ol was used particles had a pyramidal-shaped morphology (Fig. 3-18a-c), whereas when ethanoic acid was used, granular and spherical morphologies were obtained (Fig. 3-18d-f). No changes were observed in the crystal structure regardless of the solvent used and very similar crystallite sizes in the range of 30 nm were calculated when both solvents were used.

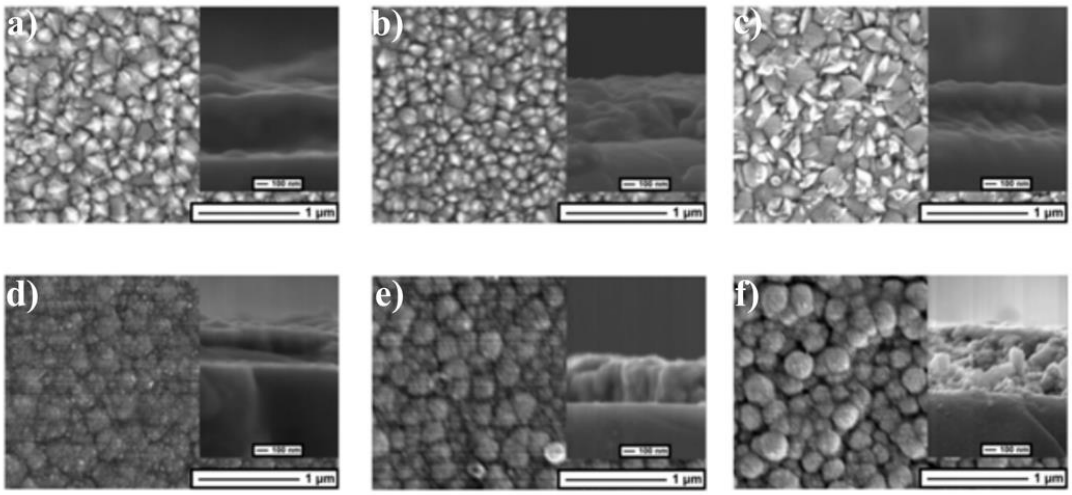

Fig. 3-18 SEM micrographs of fluorine-doped SnO_2 deposited *via* AACVD at a deposition temperature of (a-d) 500, (b-e) 550 and (c-f) 600 °C using (a-c) propan-2-ol and (d-f) ethanoic acid as carrier solvents. Adapted and reproduced from ref.[180] with permission from The Royal Society of Chemistry.

The change of solvent did not affect significantly the final morphology of $W_{18}O_{49}$ films prepared by AACVD at 350 °C.[177] Fig. 3-19 shows $W_{18}O_{49}$ films prepared using either benzonitrile, dimethoxymethane or toluene as carrier solvents. In all cases, nanorod

morphologies were obtained, although depending on the solvent used different sizes and thicknesses of nanorods were formed. For instance, the thickest and thinnest nanorods were formed when benzonitrile and toluene were used as carrier solvent, respectively.

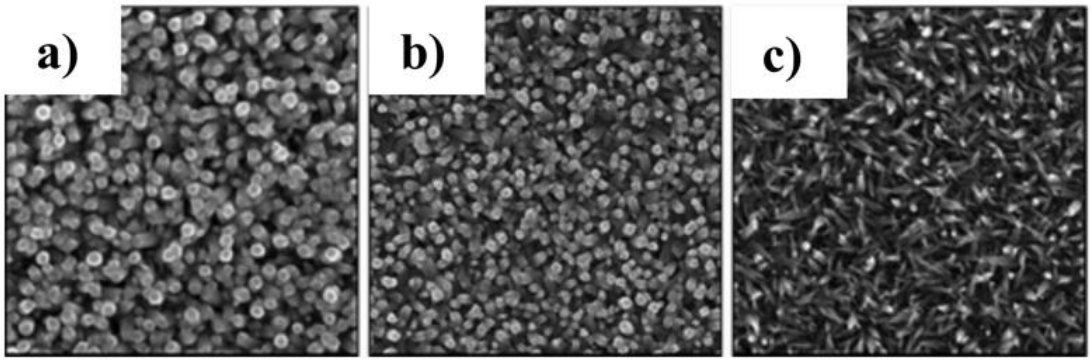

Fig. 3-19 SEM micrographs of $W_{18}O_{49}$ deposited *via* AACVD at 350 °C using (a) benzonitrile, (b) dimethoxymethane and (c) toluene as carrier solvents. Adapted with permission from ref.[177] Copyright (2015) American Chemical Society.

A detailed morphological study upon changing the ethanol carrier solvent concentration for $ZnFe_2O_4$ films prepared *via* AACVD was carried out by A. Tahir *et al.*[181] In this study, the authors reported significant structural changes from compact to rod-like morphologies when increasing the amount of ethanol in a carrier solvent mixture consisting of ethanol and methanol (Fig. 3-20). When no ethanol was added into the carrier solvent solution, films consisted of compact films with hexagonal-shaped crystallites (Fig. 3-20a). As the amount of ethanol increased, from 10 to 50 % vol. the size of the hexagonal-shaped crystallites also increased (Fig. 3-20b-f). At a higher concentration of ethanol (50 – 80 % vol.) a drastic change in morphology from hexagonal compact to plate-like structures was observed (Fig. 3-20g-i) until concentrations of 90 – 100 % vol. of ethanol where nanorods morphologies were obtained (Fig. 3-20j-k). These pronounced structural and morphological changes upon increasing the concentration of ethanol were attributed to different reaction/decomposition pathways, from heterogeneous to homogeneous as the amount of ethanol increased. Ethanol has a higher exothermic enthalpy of combustion than methanol (-1277.17 vs. -676.15 KJ mol^{-1}), implying that as the solution approaches the heated reactor chamber, the precursor primarily decomposes in the gas phase following a homogenous reaction pathway giving rise to highly structured films.[181]

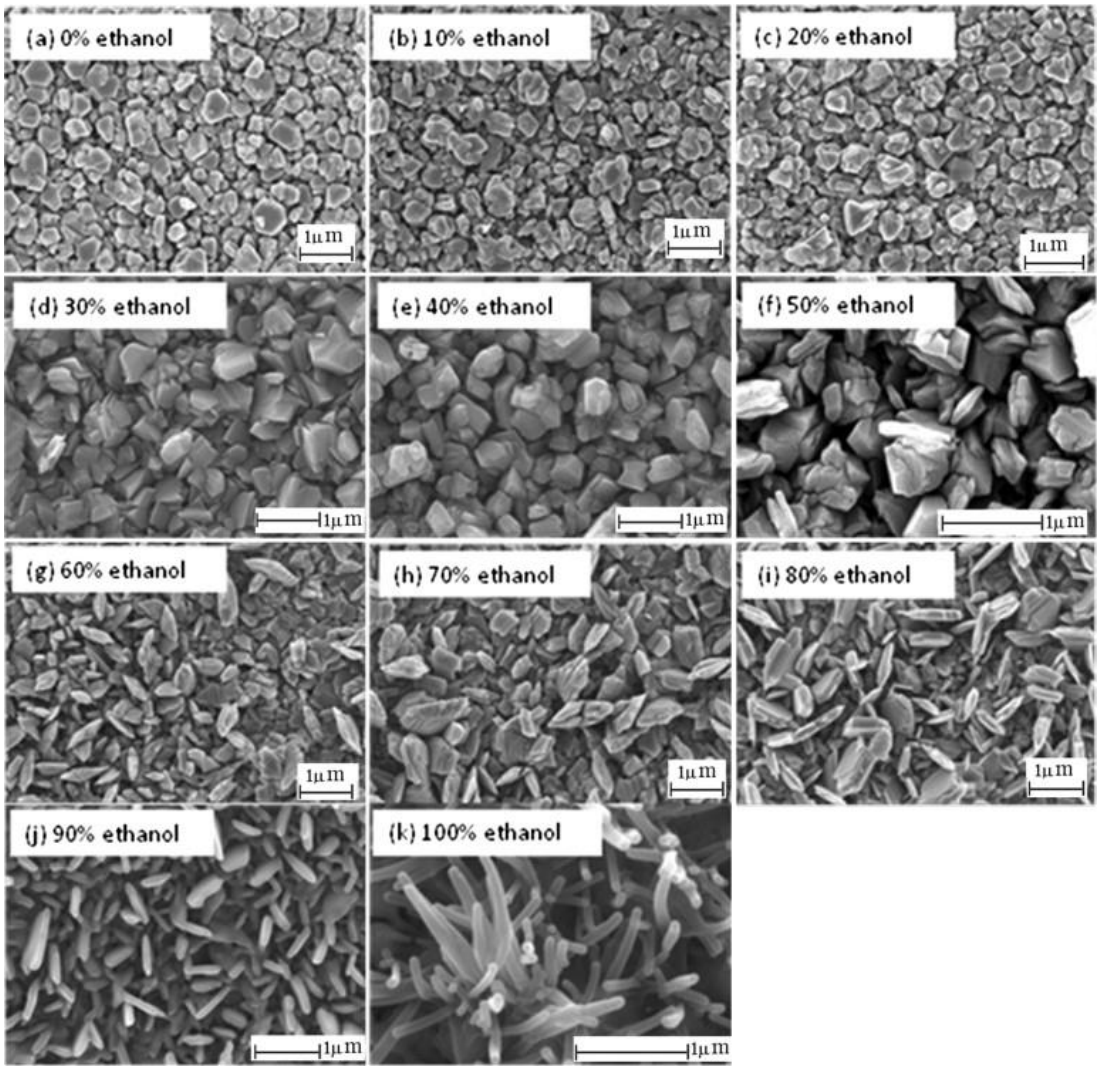

Fig. 3-20 SEM micrographs of $ZnFe_2O_4$ deposited *via* AACVD at 450 °C using ethanol and methanol as carrier solvents. (a) SEM micrograph of $ZnFe_2O_4$ using only methanol and (k) using only ethanol. (b-j) SEM micrographs of $ZnFe_2O_4$ films obtained when changing vol.% of ethanol in 10 % increments. Reproduced from ref.[181] Copyright 2013 Elsevier.

3.2.4 Substrate

The use of different substrates, much less studied than the influence of the precursor, deposition temperature and solvent, has also been reported to impact on the morphology and crystal structure of the films during an AACVD deposition process. For instance, C. Edusi *et al.* reported a substrate-selective deposition towards morphology and crystal structure when titanium (IV) isopropoxide was deposited on glass, steel and titanium substrates.[173] SEM micrographs of TiO_2 films deposited at different temperatures (400, 500 and 550 °C) and on different substrates (glass, titanium and steel) are shown in Fig. 3-21. At deposition temperatures of 400 °C, TiO_2 films deposited on glass were mainly amorphous (Fig. 3-21a) whilst angular and rectangular-shaped crystallites were formed on both titanium and steel substrates (Fig. 3-21d,g). Similar tendencies were observed at higher deposition temperatures. For instance, at 500 °C , compact angular-shaped crystallites were formed on glass (Fig. 3-21

b) whereas nanorods-like structures pointing out the substrate were formed on both titanium and steel (Fig. 3-21e,h). Likewise, when the deposition temperature was increased to 550 °C, nanorod-like structures were formed on both glass and titanium (Fig. 3-21c,f) whereas needle-like morphologies were formed on steel (Fig. 3-21i). Furthermore, XRD patterns also revealed changes in the crystal structure obtained depending on the substrate used. For instance, at a deposition temperature of 400 °C, only anatase TiO_2 phase was formed on glass, whereas pure rutile was obtained on both steel and titanium substrates. Similarly, at deposition temperatures of 500 and 550 °C, a mixture of anatase and rutile was obtained on glass substrates and pure TiO_2 rutile was only observed in both steel and titanium.

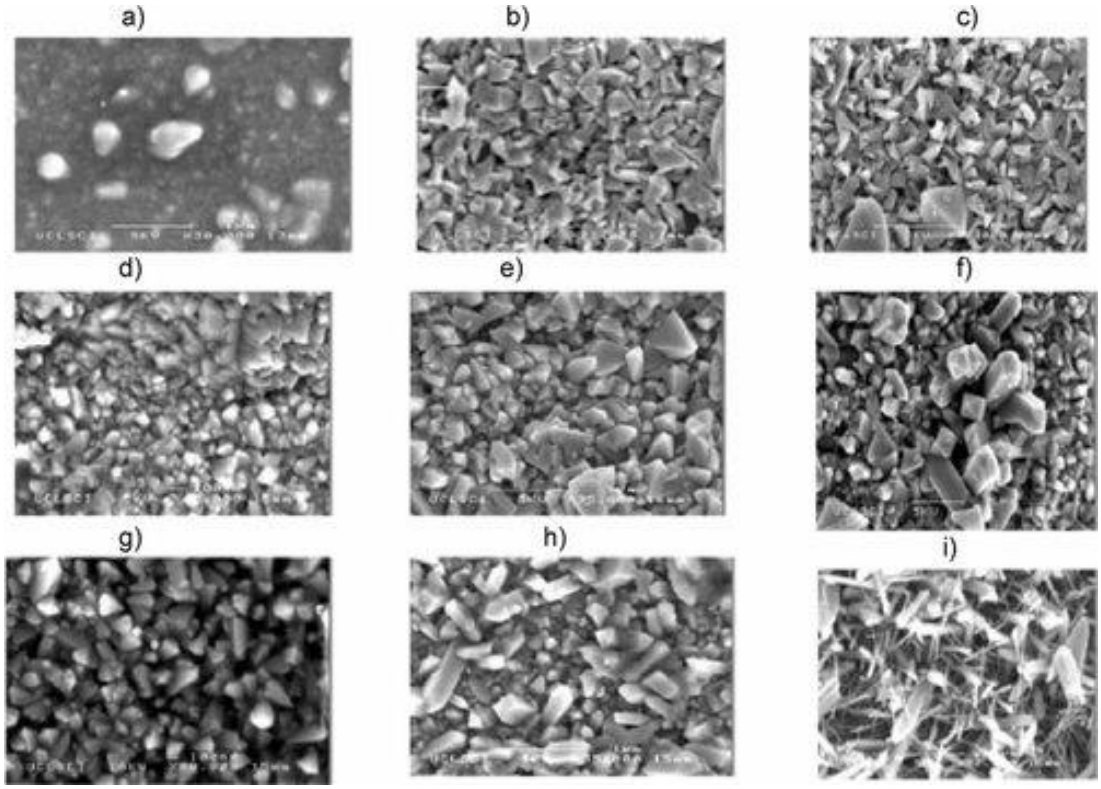

Fig. 3-21 SEM micrographs of TiO_2 deposited *via* AACVD on (a) glass at 400 °C, (b) glass at 500 °C, (c) glass at 550 °C, (d) titanium at 400 °C, (e) titanium at 500 °C, (f) titanium at 550 °C, (g) steel at 400 °C, (h) steel at 500 °C and (i) steel at 550 °C. Reproduced from ref. [173] Copyright 2011 Wiley.

Substrate-selective deposition was also observed in CdS films deposited from $Cd[S_2CNCy_2]_2$.py (py=pyridine) on both FTO and soda-glass substrates at a range of deposition temperatures (350, 400 and 450 °C), as shown in Fig. 3-22.[182]

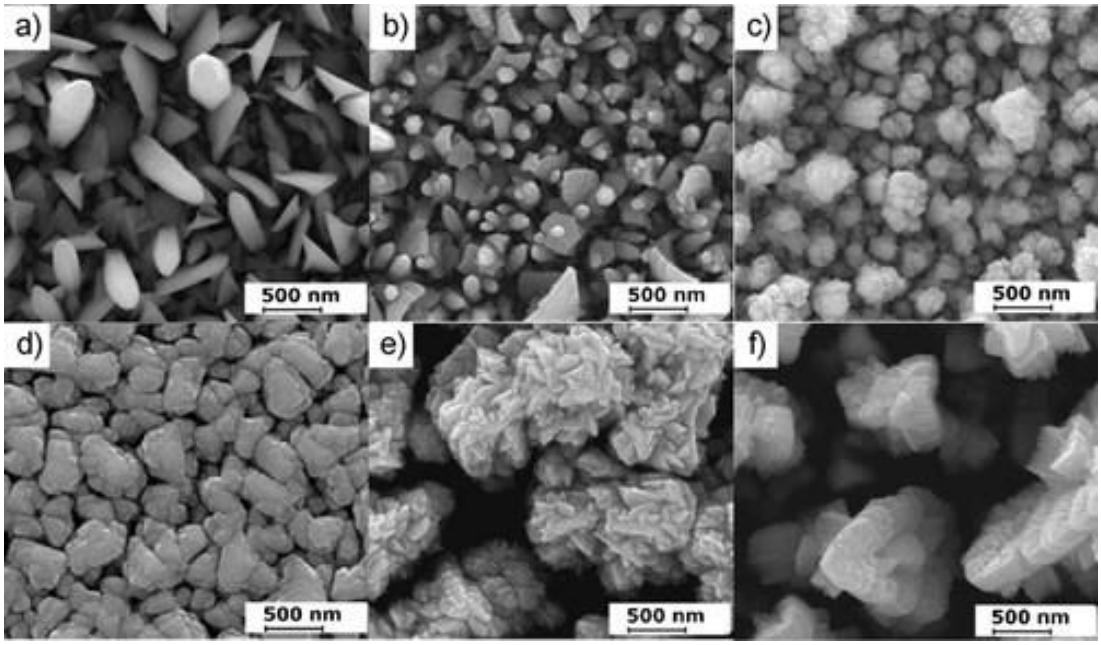

Fig. 3-22 SEM micrographs of CdS thin films deposited on (a-c) FTO and (d-f) soda glass at 350, 400 and 450 °C from THF solution, respectively. Reproduced from ref.[182] Copyright 2012 Wiley.

At 350 °C, films deposited on FTO, presented a combination of well-defined plate-like and nanorods morphologies (Fig. 3-22a), whilst films on soda-glass consisted of compact agglomerates of crystallites randomly distributed on the glass substrate (Fig. 3-22d). At 400 °C, films consisted of particulate pillars deposited on FTO (Fig. 3-22b) whereas dendritic flower-like assemblies were formed on glass-soda (Fig. 3-22e). Finally, at 450 °C heaps of agglomerated particles were formed on FTO substrates (Fig. 3-22c) whereas flake like structures were formed on soda-glass substrates (Fig. 3-22f).

Chapter 4. Mo-doped TiO_2 photoanodes prepared from a bimetallic oxo cage

4.1 Publication: Mo-doped TiO_2 photoanodes using $[Ti_4Mo_2O_8(OEt)_{10}]_2$ bimetallic oxo cages as a single source precursor

4.1.1 Preface

As discussed in previous chapters, TiO_2 is one of the most studied metal oxides in the field of PEC water splitting. Nevertheless, its limited visible-light absorption due to large band gap (3.2 eV for anatase and 3.0 eV for rutile) is still troublesome for its practical application in a water splitting device, since only a small portion of the solar spectrum can be used. During the last decade, research efforts have been put into trying to engineer the electronic band structure of TiO_2 towards the visible range, so that a larger portion of the solar spectrum could be absorbed. Among the different approaches, doping of TiO_2 has resulted in some cases successful in increasing visible light absorption and hence, improving its PEC performance, as reviewed in Chapter 2.

In this work, we demonstrate an effective approach to deposit molybdenum-doped titania (Mo-doped TiO_2) photoanodes from a heterometallic polyoxotitanate oxo/alkoxy cage with the chemical formula of $[Ti_4Mo_2O_8(OEt)_{10}]_2$ using a spray pyrolysis method. Systematically preparing films at different temperatures, we demonstrate that Mo atoms not only dope TiO_2 but also work as a pore agent. It evaporates during the calcination increasing the porosity in the films and helping in their nanostructuring. Furthermore, we also show that the PEC performance of Mo-doped TiO_2 photoanodes is highly dependent on the annealing temperature employed, 700 °C being the optimized annealing temperature. Extensive characterization of the optimized sample including EPR, SEM, TEM, XRD, XPS, EIS, and UV-Vis spectroscopy helped to understand the improved performance of Mo-doped TiO_2 annealed at 700 °C. Briefly, at this temperature there is a significant reduction in the band gap, from *ca.* 3.1 eV for pristine TiO_2 to 2.6 eV for Mo-doped TiO_2, the sample exhibits the highest surface area and substitutional doping occurs mainly in rutile TiO_2.

In summary, this works highlights the benefits of using a heterometallic polyoxotitanate oxo/alkoxy cluster as a single source precursor for the preparation of cation-doped TiO_2 photoanodes, and the importance that the cation, in this case molybdenum, has on both the film morphology and electronic structure of TiO_2 for PEC water splitting applications. Moreover, we expect that these results will stimulate new research on the production of sustainable solar fuels using polyoxotitanium oxo clusters.

4.1.2 Declaration of authorship

This declaration concerns the article entitled:				
Mo-doped TiO_2 photoanodes using $[Ti_4Mo_2O_8(OEt)_{10}]_2$ bimetallic oxo cages as a single source precursor				
Publication status (tick one)				
Draft manuscript	**Submitted**	**In review**	**Accepted**	**Published** X
Publication details (reference)	M. Regue, K. Armstrong, D. Walsh, E. Richards, A. L. Johnson and S. Eslava, *Sustainable Energy Fuels*, 2018, **2**, 2674-2686 **DOI:** 10.1039/C8SE00372F			
Copyright status (tick the appropriate statement)				
I hold the copyright for this material X		Copyright is retained by the publisher, but I have been given permission to replicate the material here		
Candidate's contribution to the paper (provide details, and also indicate as a percentage)	• Formulation of ideas: 80% The candidate considerably contributed to the formulation of the ideas. • Design of methodology: 90% The candidate was responsible for designing the methodology with few suggestions from co-authors. Katherine Armstrong and Emma Richards designed all the EPR experiments. • Experimental work: 80% The candidate performed most of the laboratory work, including material synthesis, deposition and characterization. The candidate participated in acquisition of TEM and SEM images by the Material and Chemical Characterization facility (MC^2). XPS depth profiling was acquired by the Cavendish Laboratory at the University of Cambridge. EPR data acquisition and interpretation was performed by Katherine Armstrong and Emma Richards from the EPR and ENDOR spectroscopy Unit at the Cardiff University.			

	• Presentation of data in journal format: 80% The candidate collected the data and drafted all the manuscript. The manuscript was then revised and edited by S. Eslava and approved by co-authors.		
Statement from Candidate	This paper reports on original research I conducted during the period of my Higher Degree by Research candidature.		
Signed		**Date**	23/09/2019

4.1.3 Copyright agreement

4.1.4 Published article

Mo-doped TiO_2 photoanodes using $[Ti_4Mo_2O_8(OEt)_{10}]_2$ bimetallic oxo cages as a single source precursor

Miriam Regue,[a,b] Katherine Armstrong,[c] Dominic Walsh,[b] Emma Richards,[c] Andrew Johnson, [a,d] and Salvador Eslava[*a,b]

[a]*Centre for Sustainable Chemical Technologies, University of Bath, Claverton Down, Bath, BA2 7AY, UK*

[b]*Department of Chemical Engineering, University of Bath, Claverton Down, Bath, BA2 7AY, UK*

[c]*EPR and ENDOR Spectroscopy, School of Chemistry, Cardiff University, Cardiff, CF10 3AT*

[d]*Department of Chemistry, University of Bath, Claverton Down, Bath, BA2 7AY, UK*

Received 23rd July 2018

Accepted 18th September 2018

First published on 19th September 2018

Abstract

Photoelectrochemical solar water splitting is a promising and sustainable technology for producing solar fuels such as clean hydrogen from water. A widely studied photoanode semiconductor for this application is TiO_2, but it suffers from a large band gap (3.2 eV) and fast recombination of electrons and holes. Herein, we present a novel, facile and rapid strategy to develop Mo-doped TiO_2 (Mo:TiO_2) mixed anatase-rutile photoanodes using $[Ti_4Mo_2O_8(OEt)_{10}]_2$ bimetallic oxo cages as a single source precursor. These cages dissolved in tetrahydrofuran deposit by spray pyrolysis at 150 °C forming films with hierarchical porosity on the micrometer and nanometer scale. XPS, EDXS and UV-Vis spectroscopy reveal Mo atoms evaporate during annealing in air at temperatures 650-800 °C, contributing to the formation of nanostructures and porosity. XPS depth profiling, XRD, EDXS, Raman, and electron paramagnetic resonance indicate that remaining Mo atoms are well spread and incorporated in the TiO_2 lattice, at interstitial or substitutional sites of the rutile or anatase phases depending on the annealing temperature. Photocurrent measurements show that Mo:TiO_2 photoanodes optimized at 700 °C outperform a TiO_2 photoanode prepared in a similar manner by a factor of two at 1.23 V_{RHE}. Finally, UV-Vis spectroscopy, conduction and

valence band calculations, and incident-to-photon efficiency measurements show these Mo:TiO_2 photoanodes possess a narrower band gap than TiO_2 and higher efficiency in the visible light range (5 % at 400 nm). These outcomes open a new avenue in the exploitation of titanium oxo cages and advance the development of photoelectrodes for water splitting and energy applications.

Introduction

The abundant solar energy, 1.3 x 10^5 TW $year^{-1}$ reaching the Earth's surface, can be utilized to produce hydrogen fuel by splitting water, offering an excellent and sustainable alternative to fossil fuels. Among solar absorber candidates in photoelectrochemical (PEC) solar water splitting devices, TiO_2 is one of the most promising ones due to its chemical and thermal stability, long durability, excellent optical and electronic properties, low cost and non-toxicity.[88,94,183] However, TiO_2-based PEC cells are still far from commercialization mainly due to both fast recombination of photogenerated electrons and holes in TiO_2 and its large band gap (3.2 eV for the anatase phase) that results in a reduced use of the solar spectrum. One strategy to overcome its limitations is doping it with transition metals. The metal doping increases the solar light absorption of TiO_2 and performance by incorporating additional energy levels within the band gap of the semiconductor.[95,184] Nevertheless, this only seems to occur when there is an actual substitution of Ti atoms in the TiO_2 lattice structure with the external metal (known as substitutional doping), that reduces the band gap of the material without compromising the surface of the photocatalyst.[106] Otherwise, if metals are simply impregnated on the surface of the semiconductor they may result in electron-hole recombination and blocking of reaction sites.[92,106]

Research on metal doping of TiO_2 with Ta, Fe, Co, Mn, and Ni is abundant and has proved to be successful in both reducing the band gap and improving the photoelectrochemical performance (PEC).[107–110] For instance, Yan *et al.* reported an enhancement in the PEC performance for Ta-doped TiO_2 nanotube photoanodes in comparison to pristine TiO_2.[107] This enhanced PEC performance was attributed to a decrease in the band gap, lower charge transfer resistance and higher charge carrier density. Similarly, Zhao *et al.* successfully demonstrated that Fe-doped TiO_2 results in a better PEC performance than pristine TiO_2, attributed to a smaller band gap and thus a better light absorption.[108] However, very few studies have been reported for Mo doping of TiO_2 and the few ones were mainly focused on photodegradation of organic dyes, not PEC water splitting.[114–118] In 2015 Zhang *et al.* reported Mo-doped TiO_2 photoanodes prepared using two steps of Ti foil anodization and a third one of hydrothermal doping, obtaining an improved PEC performance over pure TiO_2 photoanodes.[113] The

improvement was attributed to a decrease in the recombination of electrons and holes in the mixed phase of anatase and rutile and to better light absorption.

Heterometallic titanium oxo (HMTO) cages such as $[Ti_xO_y(L)_zM_nX_m]$, where *L* is a ligand, *M* a metal and *X* a halide, can be prepared with a wide range of metal compositions (e.g. with *M* = Co, Ni, and Mo), nuclearities, spatial arrangements, and functionalities via simple solvothermal methods and isolated by crystallization.[147,151,155,156,159,160] Some of these cages, also called clusters, have successfully been used as precursors for photocatalysts or electrocatalysts, for example using graphene oxide as a sacrificial template or impregnating WO_3 photoanodes.[152,159] However, their wide adoption as single source precursors still requires finding facile and effective approaches that overcome their instability in water or humid environments.

In this publication, we report for the first time a facile and rapid synthesis of porous Mo-doped TiO_2 photoanodes using a $[Ti_4Mo_2O_8(OEt)_{10}]_2$ HMTO cage as a single source precursor. Stability of the cages during the deposition is ensured using anhydrous tetrahydrofuran as solvent and spray pyrolysis as deposition method. We reveal that upon deposition, the calcination at temperatures above 600 °C induces sublimation of Mo atoms adding porosity and nanostructured features to remaining TiO_2, while the rest of Mo atoms effectively occupy substitutional or interstitial sites in the TiO_2 lattice. The resulting Mo:TiO_2 photoanode optimized at 700 °C outperforms by a factor of two a pure TiO_2 photoanode prepared in a similar manner in PEC solar water splitting. The results herein presented therefore reveal new strategies to develop efficient photoelectrodes for water splitting applications using Mo as both a sacrificial agent and dopant and opens an avenue to exploit HMTO cages as single source precursors using spray pyrolysis.

Experimental

Materials

Titanium (IV) ethoxide $[Ti(OEt)_4]$, anhydrous molybdenum (V) chloride ($MoCl_5$, 99.99%), anhydrous tetrahydrofuran (≥99.9 %, inhibitor free), anhydrous ethanol (<0.0003% water), titanium isopropoxide (TTIP, 97%), acetylacetone (AcAc) , cobalt nitrate ($Co(NO_3)_2$), iron chloride hexahydrate ($FeCl_3.6H_2O$), sodium acetate (NaOAc) and tetrabutylammonium hexafluorophosphate (TBAPF6) were provided by Sigma Aldrich. Cobalt (II) chloride ($CoCl_2$, anhydrous 97%) was provided by Alfa Aesar. Aluminoborosilicate glass (ABS) coated with fluorine-doped tin oxide (FTO) transparent conductive layer (8Ω sq^{-1}) was provided by Solaronix, CH. These FTO-ABS substrates were cleaned ultrasonically in a 2% aqueous Hellmanex III solution followed by dipping in deionized water, acetone and isopropyl alcohol,

ultrasonicating in each step for 3min. Finally, the substrates were rinsed with deionized water and dried with compressed air.

Synthesis of $[Ti_4Mo_2O_8(OEt)_{10}]_2$

$[Ti_4Mo_2O_8(OEt)_{10}]_2$ oxo cages (Fig. 4-1) were synthesized using a solvothermal process as described in a previous article by Eslava *et al.*[149] Briefly, $Ti(OEt_4)$ (14 mL, 66.8 mmol), $MoCl_5$ (1.128g, 4.12 mmol) and anhydrous ethanol (14 mL) were carefully mixed in a 45 mL Teflon-lined stainless steel autoclave and heated to 150 °C for 24 hours. The autoclave was left overnight to cool down to room temperature and mm size brown-red crystals were obtained (88% yield). Elemental analysis (%) calculated for $C_{40}H_{100}Mo_4O_{36}Ti_8$: C 25.7, H 5.3; found: C 25.6, H 5.3. Due to the humidity sensitive nature of these reactants, all manipulations were carried out in an air-free atmosphere involving the use of a glove box and Schlenk line when necessary.

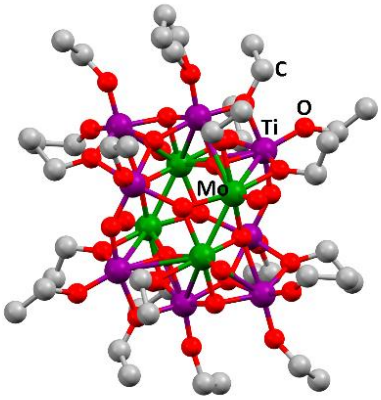

Fig. 4-1 Ball and stick drawing of $[Ti_4Mo_2O_8(OEt)_{10}]_2$ represented from CCDC no. 812604.[149] Mo: green; Ti: purple; O: red; C: grey.

Preparation of Mo:TiO_2 and TiO_2 films

Mo-doped TiO_2 (abbreviated as Mo:TiO_2) and pure TiO_2 films to be studied as photoanodes were prepared using a manual spray-pyrolysis system (Clarke CAB3P) on FTO-ABS. The solutions employed for the spray pyrolysis deposition were prepared in an argon atmosphere using a Schlenk line. Nevertheless, the actual spray pyrolysis deposition process was conducted in air, but vessels were kept closed when possible. The precursor solution for the Mo:TiO_2 photoanodes was prepared by dissolving $[Ti_4Mo_2O_8(OEt)_{10}]_2$ (0.96g) in anhydrous tetrahydrofuran (20 mL). The precursor solution for the preparation of pure TiO_2 was carried out following an established method.[185] Briefly, a 0.2M solution of TTIP was prepared by

diluting TTIP and AcAc in a 3:2 volumetric ratio and topping up with absolute ethanol in order to obtain 0.2M solution of TTIP.

The spray pyrolysis deposition of previous precursor solutions to prepare Mo:TiO_2 and TiO_2 photoanode films was conducted as follows. In a first stage, FTO-ABS was pre-heated on a hot plate at 150 °C. Secondly, the as-prepared precursor solutions were sprayed on top of the pre-heated FTO-ABS, at a constant distance of *ca*. 5 cm from the surface of the FTO-ABS to the spray pyrolysis nozzle. Three deposition layers were performed per sample. Finally, the as-prepared Mo:TiO_2 and TiO_2 films were annealed at different temperatures between 450 and 800 °C for 2h in air at a ramp rate of 10 °C min^{-1}. This range of temperatures was chosen to ensure full conversion of the precursor to the metal oxide and to evaluate the effect that different annealing conditions might have on the photoanode performance. The resultant photoanodes were denoted as Mo:TiO_2-### and TiO_2-###, where ### is the corresponding annealing temperature (°C).

Cobalt phosphate (Co-P_i) loading on Mo:TiO_2-700 photoanodes was carried out by photo-electrodeposition.[186,187] The electrolyte consisted of 0.5mM of cobalt nitrate in 0.1M potassium phosphate buffer (pH=7) and the applied potential 1 V_{RHE} was kept for 20s under simulated sunlight (AM 1.5G, 100 $mWcm^{-2}$) from a filtered 300W Xenon lamp source. Illumination was directed towards the back of the FTO-ABS working electrode. $CoFeO_x$ was deposited on Mo:TiO_2-700 by electrodeposition.[188] The electrolyte consisted of 10mM $FeCl_3 \cdot 6H_2O$, 16mM $CoCl_2$ and 0.1M NaOAc dissolved in deionized water. The pH of the solution was 4.90. The deposition was carried out by positively sweeping the voltage from 1.1 to 1.4 $V_{Ag/AgCl}$ three times. In both depositions, a Compactstat. potentiostat (Ivium Technologies) was used and an electrochemical cell consisting of a Pt counter electrode, a silver chloride (Ag/AgCl/3.5M KCl) reference electrode, and a Mo:TiO_2-700 photoanode as working electrode.

Characterization

^{13}C {H} NMR was conducted at room temperature using a 500 MHz Agilent Propulse spectrophotometer. Samples were dissolved in dried deuterated benzene (C_6D_6). CHN elemental analysis was performed on a Carlo Erba Flash 2000 Elemental Analyser. Field emission scanning electron microscopy images (FE-SEM) were acquired using a JEOL FESEM6301F and energy dispersive X-ray spectroscopy (EDXS) was carried out in a SEM 6480LV equipped with a high sensitivity Oxford INCA X-Act SDD X-ray detector. X-Ray diffraction (XRD) patterns were collected in the 2 Theta range 10-80° with a Bruker AXS D8 Advance using Cu Kα (0.154 nm) radiation with a total integration time of 960 s. Raman spectroscopy was carried out on a Renishaw inVia system using a 532 nm diode-pumped solid

state laser (DPSS) manufactured by Cobolt. The laser beam was focused onto the sample using a 50x long distance objective. X-Ray photoelectron spectroscopy (XPS) depth profiling was performed using a ESCALAB 250 Xi instrument manufactured by Thermo Fisher Scientific. Measurements were carried out using a monochromated Al Kα X-Ray source with an energy of 1486.68 eV. The X-Ray spot size was of 900 μm and the pass energy for the high resolution scans was of 50 eV. The depth profile for the sample was obtained by etching the surface of the sample with an Ar^+ ion gun (2000 eV, high current) for different times (0, 60, 180 and 420 s). C 1s XPS spectra was used as an internal charge correction. Samples studied via electron paramagnetic resonance (EPR) spectroscopy were evacuated at 393 K for over 12 h to reduce the influence of physisorbed water. Samples were maintained under static vacuum (10^{-5} mbar) for the duration of the experiments. For EPR analysis, powder samples were prepared by drying and calcining in air at 650, 700 and 800°C in a porcelain dish a solution of 0.96 g of $[Ti_4Mo_2O_8(OEt)_{10}]_2$ in 20 ml of anhydrous tetrahydrofuran. High resolution transmission electron microscopy (HRTEM) images were obtained using a JEOL JEM-2100Plus microscope. Ultraviolet-visible (UV-Vis) spectra were collected in a Cary 100 diffuse reflectance UV-Vis spectrophotometer.

(Photo)electrochemical measurements

(Photo)electrochemical performance of photoanodes was evaluated using a CompactStat. potentiostat (Ivium Technologies). Photocurrents were measured under simulated sunlight (AM 1.5G, 100 $mWcm^{-2}$) from a filtered 300W Xenon lamp source (Lot Quantum Design) or under UV illumination (365 nm, 3.6 $mWcm^{-2}$) from a ModuLight IM3412 LED light (Ivium Technologies). PEC cells consisted of three electrodes with Pt as the counter electrode, silver chloride (Ag/AgCl/3.5M KCl) as the reference electrode and as-prepared photoanodes as the working electrodes.

Electrochemically active surface area (ECSA) of photoanodes was investigated using cyclic voltammetry (CV), scanning from 0 to 0.17 $V_{Ag/AgCl}$ at scan rates between 10 and 250 mV s^{-1}, in 1M KOH solution (pH=13.7). ECSA is proportional to the double layer capacitance (C_{dl}), which is estimated from the slope of the plot Δj *vs.* scan rate and dividing by two.[189] Δj is equal to $(j_a - j_c)$, where j_a and j_c are the anodic and cathodic current densities, respectively, in this case taken at $0.1V_{Ag/AgCl}$ in the CV scans.[190]

Conduction and valence band (CB & VB) positions were measured from CV curves recorded in acetonitrile containing 0.1M of tetrabutylammonium hexafluorophosphate (TBAPF6) at a scan rate of 50 mV s^{-1} and using the following formula:[191–193]

$$CB\ (or\ VB)\ (eV) = -4.8 - \left(E - E_{1/2}\right) \quad 4\text{-}1$$

where E is the onset of the redox potential and $E_{1/2}$ is the formal potential of F_c/F_c^+ system (0.43 $V_{Ag/AgCl}$).[194]

Photoelectrochemical performances of photoanodes were carried out in a 1M KOH (pH=13.7) electrolyte solution. Illumination was directed towards the back of the FTO-ABS working electrode and a mask was placed on top of the photoelectrode to define the illuminated area. Photocurrent-time curves were performed at an applied bias of 1.23 V *vs* the reversible hydrogen electrode (V_{RHE}). Photocurrent-potential curves were recorded at a scan rate of 20 mV s^{-1}. The measured Ag/AgCl potentials ($E_{Ag/AgCl}$) were converted to RHE potentials ($E°_{RHE}$) following the Nernst equation:

$$E^0_{RHE} = E^0_{Ag/AgCl} + E_{Ag/AgCl} + 0.059pH \quad 4\text{-}2$$

where $E°_{Ag/AgCl}$ is 0.205 V at 25°C (3.5M KCl). Photoelectrochemical impedance spectroscopy (PEIS) was carried out under simulated sunlight (AM 1.5G, 100 mWcm^{-2}) at a direct current (DC) potential of 1.23 V_{RHE} and an alternating current (AC) potential frequency range of 100000-0.01 Hz with an amplitude of 5 mV. Incident photon-to-current efficiency (IPCE) measurements were calculated using the same Xe light source and a triple grating Czerny-Turner monochromator. The intensity of monochromatic light was measured at the working electrode position with SEL033/U photodetector (International Light Technologies). The following equation was used to calculate the IPCE values:[32]

$$IPCE\ (\lambda) = \frac{|j\ (mA\ cm^{-2})|\ \times 1239.8\ (V\ nm)}{P_{mono}\ (mW\ cm^{-2}) \times\ \lambda\ (nm)} \quad 4\text{-}3$$

where j is the photocurrent density measured under single wavelength (λ) light illumination and P_{mono} is the incident irradiation power. Oxygen (O_2) measurements were conducted using a Pyroscience FireStingO2 fibre-optic oxygen meter combined with a TROXROB10 oxygen probe, together with a TDIP temperature sensor to give automatic compensation for minor fluctuation in the PEC cell temperature. O_2 readings were recorded every 10 min for *ca.* 410 min. The probe was fitted into the headspace of the airtight PEC cell. The PEC cell was purged with a N_2 flow to ensure air O_2 removal before the irradiation started. The measurements were carried out under simulated sunlight (AM 1.5G, 100 mW cm^{-2}) with an applied bias of 1.23 V_{RHE}. Light was irradiated for 340 min. The Faradaic efficiency was calculated by dividing the measured amount of evolved O_2 by the theoretical amount of expected O_2 for measured

photocurrents (assuming 100% Faradaic efficiency). See more details in Supporting Information.

Results and Discussion

The synthesis of $[Ti_4Mo_2O_8(OEt)_{10}]_2$ cages was successfully performed using a solvothermal synthesis. The ^{13}C {H} NMR spectra of the product showed the ten characteristic sharp resonances of the cage at δ 75.24, 75.12, 73.80, 73.49, 73.38, 73.30, 72.65, 71.67, 71.22 and 70.06 ppm belonging to the different $–OCH_2–$ environments in the structure, in agreement with literature (Fig. 4-2).[149] In addition, CHN elemental analysis further confirmed the successful formation of $[Ti_4Mo_2O_8(OEt)_{10}]_2$ (wt % calculated for $C_{40}H_{100}Mo_4O_{36}Ti_8$: C 25.7, H 5.3; found: C 25.6, H 5.3). Fig. 4-1 shows a ball and stick model of the cage, which highlights a heterometallic oxo core with four Mo^V atoms in a rectangle and eight Ti^{IV} atoms. Mo and Ti atoms bridge together by a combination of μ_3-, μ_4-O and μ_2-OEt (CCDC no. 812604).

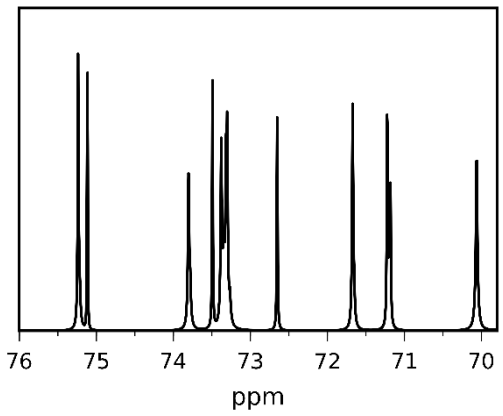

Fig. 4-2 ^{13}C {H} NMR spectra of the $–OCH_2–$ resonance region of $[Ti_4Mo_2O_8(OEt)_{10}]_2$, in agreement with literature [149].

Spray pyrolysis was used to deposit solutions of $[Ti_4Mo_2O_8(OEt)_{10}]_2$ cages or titanium isopropoxide-acetylacetone (TTIP-AcAc), respectively. The as-deposited films were then annealed in air at temperatures between 450 and 800 °C for 2 hours and allowed to cool to room temperature. The morphology of the as-prepared films was evaluated using SEM. Fig. 4-3 shows SEM images at different magnifications of Mo:TiO_2 prepared at different annealing temperatures (650, 700 and 800 °C), along with a film prior to calcination for comparison (i.e. a film of $[Ti_4Mo_2O_8(OEt)_{10}]_2$ cages deposited by spray pyrolysis at 150 °C). At lower magnification (Fig. 4-3, 1st row), all Mo:TiO_2 films, even the un-annealed sample, exhibit almost the same morphology, showing aggregated islands evenly distributed on top of FTO-ABS support. At slightly higher magnification (Fig. 4-3, 2nd row), a large amount of micrometer cavities on Mo:TiO_2 films are observed. These cavities contribute to an increase

of surface area, which in turn must result in more active sites for the PEC oxygen evolution reaction. At even higher magnification (Fig. 4-3, 3rd row), it can be observed that well-defined nanostructures form as the annealing temperature increases. A highly smooth and fine surface is present before calcination (Fig. 4-3i), but after calcination, grain-rice-shaped nanostructures appear creating nanometer-size porosity and extra surface area (Fig. 4-3j-l).

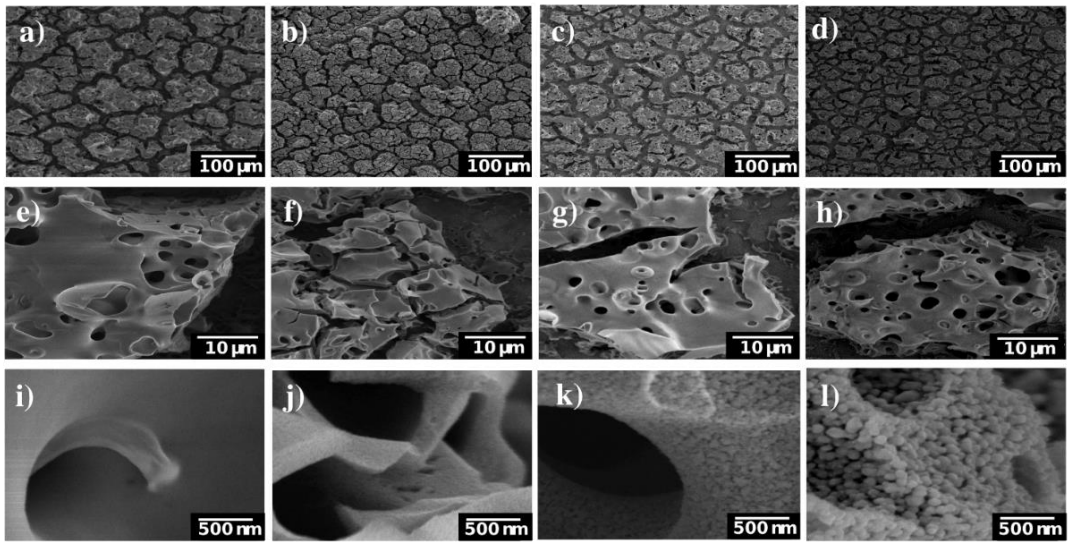

Fig. 4-3 SEM images of Mo:TiO_2 at different magnifications. (a,e and i) Film after spray-pyrolysis deposition at 150 ºC, (b,f, and j) Mo:TiO_2-650, (c,g and k) Mo:TiO_2-700 and (d,h and l) Mo:TiO_2-800.

SEM images of the pure TiO_2 film at different magnifications are shown in Fig. 4-4. Unlike Mo:TiO_2 films, TiO_2-650 (prepared with TTIP-AcAc) do not show neither the presence of cavities nor nanostructures.

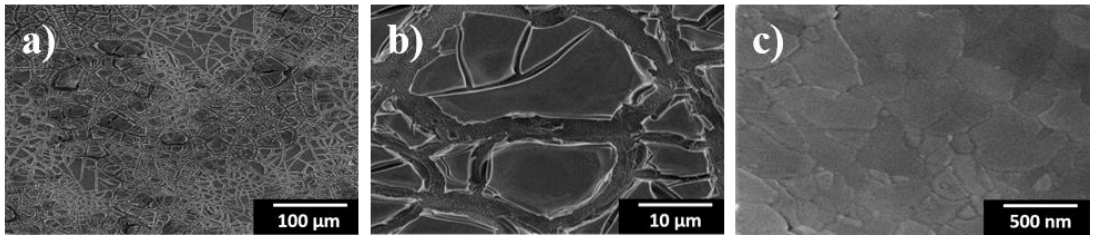

Fig. 4-4 SEM images of TiO_2-650 photoanode.

This comparison therefore reveals the benefits of using $[Ti_4Mo_2O_8(OEt)_{10}]_2$ cages as a precursor. Their decomposition and transformation to Mo-doped TiO_2 during the spray pyrolysis and posterior calcination leads to the formation of cavities, nanostructures and porosity. Cavities must result from the drying step upon spray pyrolysis at 150 °C. More cavities may form during the calcination and oxidation of the cages' carbon content up to 400-500 °C. Above this temperature, the grain rice shaped nanostructures and its associated porosity must result from the sintering of TiO_2 and especially from the very likely sublimation of Mo atoms. Previous reports have shown that MoO_3 sublimes above 700 °C.[195] The

sublimation of Mo atoms was confirmed by atomic quantification from XPS data (Fig. 4-5a). The amount of Mo in the films decreased with temperature. For example, at the top surface (XPS-etching time 0 s) it went from 10.6 at% for Mo:TiO_2-650 to 4.9 and 4.3 at% for Mo:TiO_2-700 and Mo:TiO_2-800, respectively, indicating Mo sublimes within the temperatures of study. Accordingly, the percentage of carbon (C) decreases with temperature and that of Ti increases. Carbon is present from solvents and cage ethoxides and deposition of volatile organic compounds during storage. The Mo sublimation was further confirmed by an experiment of simply heating $MoCl_5$ up to 700°C in air, which showed its complete sublimation. Therefore, Mo atoms work as pore formers, sacrificial agents that increase the porosity in the films and allow their nanostructuring.

The XPS depth profiling indicated that Mo is homogeneously distributed at different depths, but some gradient is formed at highest temperatures of 700 and 800 °C, with more C and Mo present at the surface (Fig. 4-5a). This may result from the gasification and sublimation taking place and accumulation at the top during the process. Corresponding XPS depth profiling for Mo-TiO_2 at different temperatures are shown in Fig. 4-18 (Supporting information).

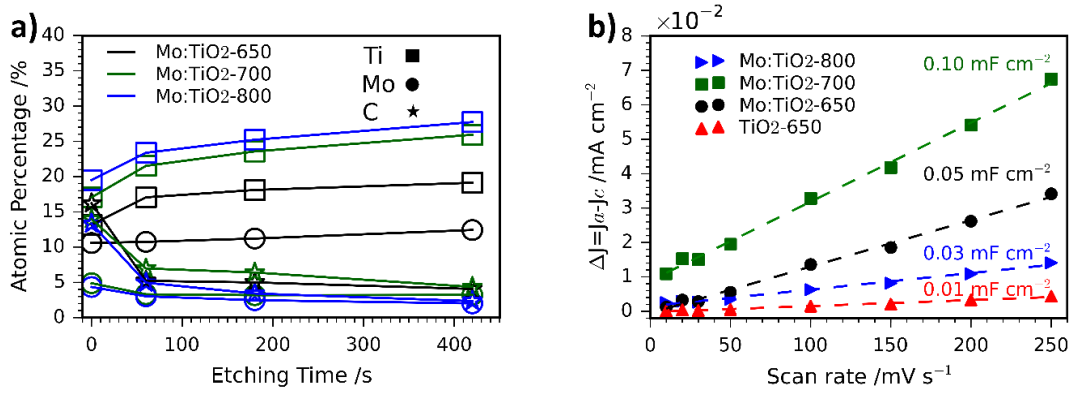

Fig. 4-5 (a) Atomic percentage (at %) distribution of Ti, Mo and C obtained *via* XPS depth profiling. (b) Capacitive current *Δj* versus scan rate curves of Mo:TiO_2 and TiO_2-650.

ECSA measurements are shown in Fig. 4-5b and the corresponding CV curves in Fig. 4-19 (Supporting information). In such measurements, the slope of the current density *vs.* scan rate can be related to the double layer capacitance, which is directly proportional to the ECSA.[190] Based on the obtained results, Mo:TiO_2-700 possess the highest surface area (C_{dl}=0.10 mF cm^{-2}), whereas TiO_2-650 is the sample with the smallest surface area (C_{dl}=0.01 mF cm^{-2}). These results agree well with SEM images, where grain-rice-shaped nanostructures and porosity are observed for Mo:TiO_2-700 (Fig. 4-3k) and very flat films for TiO_2-650 (Fig. 4-4). Among all Mo:TiO_2 photoanodes, Mo:TiO_2-800 is the sample with the smallest surface area, due to the largest grains formed at highest temperature (Fig. 4-3l).

SEM-EDXS analysis was also carried out to evaluate the distribution of Ti, O and Mo atoms at the surface of the films. Fig. 4-6 reveals a uniform distribution of Ti and Mo atoms at the surface of Mo:TiO_2-650 and Mo:TiO_2-700. The amount of Mo atoms at the surface of Mo:TiO_2-800 is considerably lower supporting the hypothesis that Mo species sublime during the calcination.

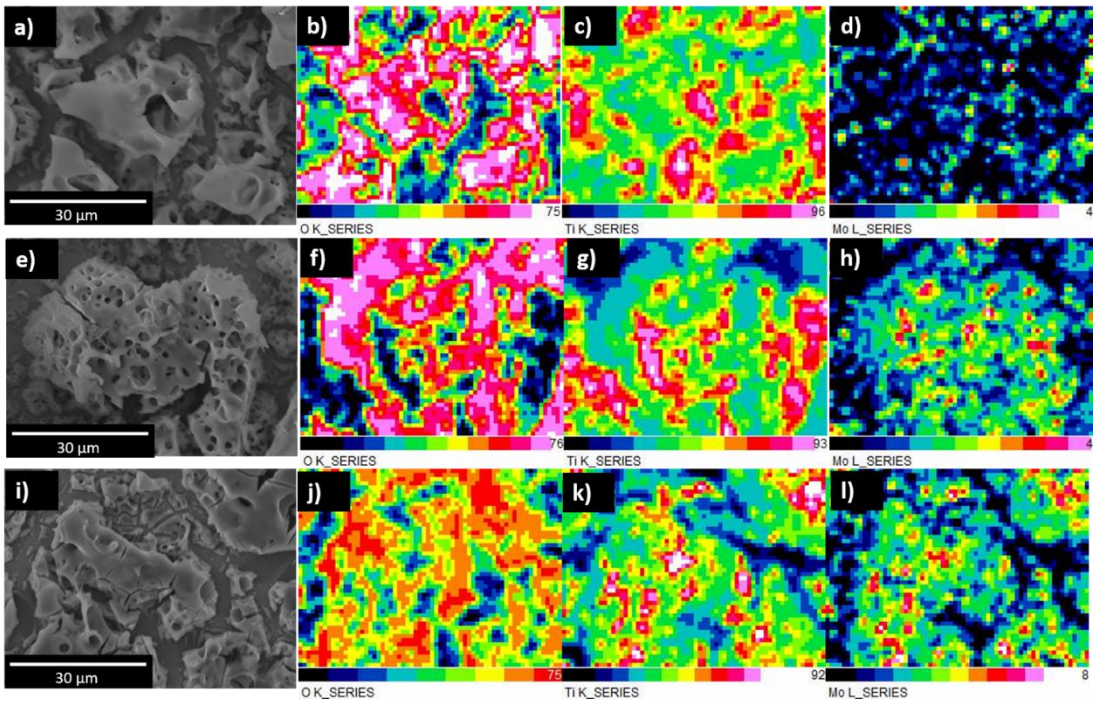

Fig. 4-6 SEM-EDXS images of Mo:TiO_2 photoanodes. (a-d) Mo:TiO_2-800, (e-h) Mo:TiO_2-700 and (i-l) Mo:TiO_2-650.

Fig. 4-7a and Fig. 4-7b show the XRD patterns of the resulting Mo:TiO_2 and TiO_2 films on FTO-ABS. Mo:TiO_2-650 and Mo:TiO_2-700 exhibit diffraction peaks corresponding to both anatase TiO_2 and rutile TiO_2. The diffraction peaks at 2θ 25.3 and 48.0° are indexed to the diffraction planes (1 0 1) and (2 0 0) of anatase TiO_2, respectively (ICDD-JCPDS no. 75-1537). The diffraction peaks at 2θ 27.4, 36.1, 39.2, 44.0, 54.3, 69.0 and 69.8° correspond to (1 1 0), (1 0 1), (2 0 0), (2 1 0), (2 1 1), (3 0 1) and (1 1 2) diffraction planes, resp., of rutile TiO_2 (ICDD-JCPDS no. 88-1173). The diffraction intensity of the rutile phase increases and that of anatase decreases with annealing temperature (Fig. 4-7a), indicating that the conversion of anatase to rutile was promoted at highest temperatures.[196] Actually, Mo:TiO_2-800 only shows diffraction peaks indexed to rutile TiO_2, due to the high calcination temperature employed. No diffraction peaks corresponding to any Mo phase such as MoO_3 are observed in any of the samples, which suggests that $Mo^{6+/5+}$ could be incorporated into the lattice of TiO_2. MoO_2 was unlikely to be formed since phase transformation from tetragonal MoO_2 to orthorhombic MoO_3 occurs at temperatures above 350°C.[100]

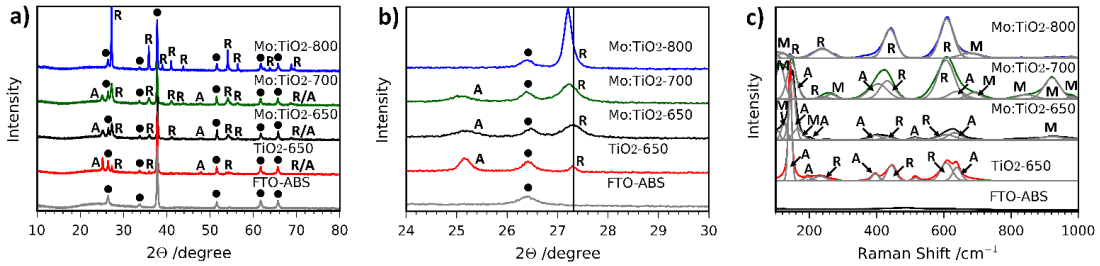

Fig. 4-7 (a) XRD patterns and (b) XRD diffraction profiles on (1 0 1) plane of anatase TiO_2 and (1 1 0) plane of rutile TiO_2 of Mo:TiO_2, TiO_2-650 and FTO-ABS substrate. A: anatase, R: rutile and black dot: FTO. (c) Raman spectra from 100 to 1000 $cm^{-1}$of Mo:TiO_2, TiO_2-650 and FTO-ABS substrate. A: anatase, R: rutile, M: Mo.

In Fig. 4-7b an expansion of the (1 0 1) and (1 1 0) diffraction peaks of anatase and rutile, respectively, of the different Mo:TiO_2 and pure TiO_2 films is shown. A shift of the anatase and rutile diffraction peaks towards lower angles for Mo:TiO_2-700 and Mo:TiO_2-800 in comparison to pure TiO_2 is observed, which indicates incorporation of Mo^{6+} or Mo^{5+} atoms in the TiO_2 lattice structure upon exposure to those temperatures.[115] The reported ionic radius for Mo^{6+} and Mo^{5+} are 0.0620 and 0.0610 nm, respectively, whereas the Ti^{4+} ionic radius is 0.0605 nm.[115,197,198] The similarity in the ionic radius of these ions facilitates the aliovalent substitution of Ti^{4+} atoms for $Mo^{6+/5+}$ in the TiO_2 lattice, and due to the slightly larger size of $Mo^{6+/5+}$ in comparison to Ti^{4+} a shift in the diffraction pattern towards lower angles is observed. However, Mo:TiO_2-650 shows a smaller shift towards lower angles, suggesting that at lower temperatures the majority of $Mo^{6+/5+}$ atoms are not occupying Ti^{4+} sites in the TiO_2 lattice structure. Instead, $Mo^{6+/5+}$ must be distributed on the surface of TiO_2 or occupying interstitial sites within the TiO_2 lattice, without distorting the crystal structure of either anatase or rutile TiO_2. In fact, this may also suggest that Mo^{6+} atoms could be present in the form of MoO_3 that could be either highly dispersed on the TiO_2 surface or of amorphous structure, and therefore not detectable by XRD analysis.

Raman spectroscopy was also carried out to further verify the presence of rutile TiO_2, anatase TiO_2 and the substitution of Mo for Ti atoms in the lattice structure of TiO_2. Fig. 4-7c shows the Raman spectra of all films. The presence of anatase-TiO_2 and rutile-TiO_2 is confirmed by the sharp peaks observed in all Raman spectra, with the exception of Mo:TiO_2-800 for which only rutile TiO_2 is observed, in agreement with the XRD patterns (Fig. 4-7a and Fig. 4-7b). The sharp bands at *ca.* 145, 395, 515 and 635 cm^{-1} correspond to Raman active modes of anatase TiO_2 and bands at 230, 445 and 610 cm^{-1} to Raman active modes of rutile TiO_2.[199,200] Interestingly, some bands ascribed to the presence of Mo are also observed. For instance, in the region between 870-970 cm^{-1} there are bands belonging to hydrated terminal Mo-O and Mo-O-Mo vibrations.[201,202] The presence of crystalline MoO_3 can be discarded since its characteristic main bands at 996, 820 and 666 cm^{-1} are not observed, which is in accordance

with XRD analysis. Moreover, the weak bands observed in the range 100-200 cm^{-1} are attributed to bending modes of Mo-O-Mo.[203] This verifies the incorporation of Mo atoms into the lattice of TiO_2, suggesting the presence of Ti-O-Ti, Mo-O-Mo and Mo-O-Ti bonds in Mo:TiO_2.[204] The Mo Raman vibrations are most evident for Mo:TiO_2-700 and drastically decrease for Mo:TiO_2-800, indicating that at 700 °C the Mo incorporation into the oxide crystalline structure is at its maximum. This temperature dependence is attributed to evaporation of the Mo species, which as previously shown, sublime at relatively low temperatures. Along the same lines, the Mo Raman vibrations for Mo:TiO_2-650 are relatively weak, which further confirms that the vast majority of Mo atoms are not incorporated in the TiO_2 lattice structure, instead they are impregnated on the surface of TiO_2 or distributed in interstitial sites of the TiO_2 structure, which agrees well with XRD patterns.

The composition and chemical state of Mo:TiO_2 films were further characterized by XPS. Fig. 4-8 shows the XPS high resolution spectra at the surface of Mo:TiO_2 samples. Ti 2p resolution spectra show the two characteristic peaks of Ti^{4+} in TiO_2 at 458 and 464 eV in the Mo:TiO_2 films.[199,205] The O 1s spectra for Mo:TiO_2 films are shown in Fig. 4-8b. The peak at lower binding energies mainly corresponds to crystal lattice oxygen O-Ti^{4+}, whereas the smaller peaks at higher binding energies correspond to hydroxyl groups or adsorbed water on the surface *i.e.* Ti-OH or Mo-OH.[199,205] Fig. 4-8c shows the high-resolution XPS surface spectra of Mo 3d. Surface Mo 3d spectra of all Mo:TiO_2 films show the characteristic peaks of Mo^{6+} situated at binding energies at 232 and 235 eV.[206–208] An additional doublet appears at lower binding energies for all Mo:TiO_2 films, attributed to the presence of some Mo^{5+} centers in the films.[209] XPS O 1s and Ti 2p spectra of TiO_2-650 are shown in Fig. 4-9. The binding energies for Ti 2p and O1s are in agreement with Mo:TiO_2 samples.

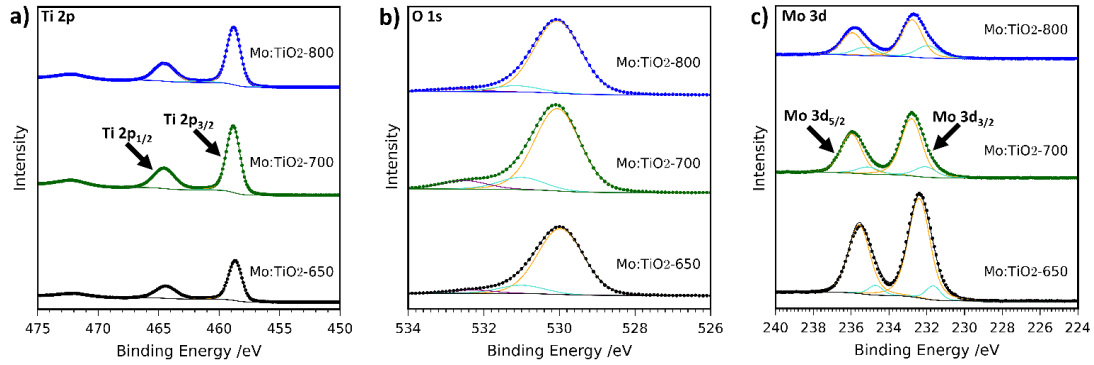

Fig. 4-8 XPS spectra of (a) Ti 2p, (b) O 1s and (c) Mo 3d of Mo:TiO_2. Scattered points correspond to raw data acquired in the measurements and solid lines to the fitted values.

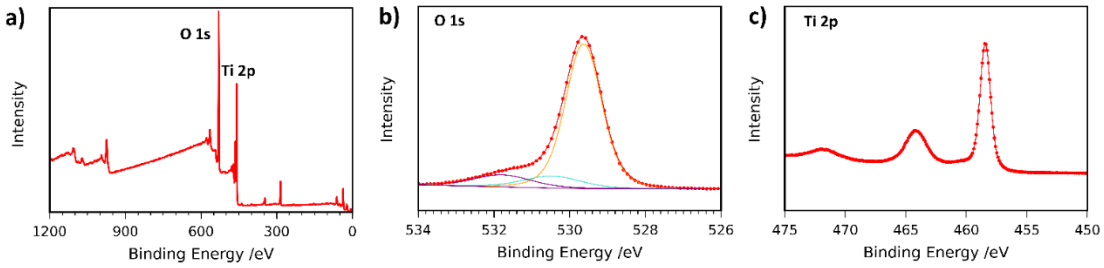

Fig. 4-9 XPS spectra of TiO_2-650. (a) Survey, (b) O 1s and (c) Ti 2p.

Electron paramagnetic resonance (EPR) spectroscopy was undertaken (at 120 K) to investigate the nature of the Mo doping within the series of TiO_2 lattice structures. EPR spectroscopy only detects the presence of paramagnetic species, thus the Mo^{5+} species are observed whereas there is no detection of Mo^{6+} centers. The EPR data (Fig. 4-10) indicate the presence of Mo^{5+} in all the films, in agreement with the XPS analysis. Variation in *g* values for the different samples demonstrated the existence of multiple Mo^{5+} species. As an example, the EPR spectrum of Mo:TiO_2-650 indicated the presence of MoO^{3+} species on the surface, characterized by an axial g-tensor ($g_\perp$ = 1.932 and $g_\parallel$ = 1.886) and corresponding weak hyperfine satellite lines originating from coupling of the unpaired electron to the two nuclear spin active isotopes of molybdenum (^{95,97}Mo, both with spin I = 5/2 and total natural abundance of 25.5%; $A_\perp$ = 112 MHz and unresolvable A||). Additional contributions from bulk Mo^{5+} (g_1 = 1.944, g_2 = 1.944, g_3 = 1.839; A_1 = 198, A_2 = 75 and A_3 = 93 MHz) and a small contribution from Mo^{5+} in substitutional anatase lattice positions (g_1 = 1.917, g_2 = 1.828, g_3 = 1.828) was also detected in the Mo:TiO_2-650 sample. In contrast, the EPR spectra obtained for both the Mo:TiO_2-700 and Mo:TiO_2-800 samples confirmed the existence of substitutional and interstitial doping in the TiO_2 rutile lattice. The variation in Mo sites displayed via EPR for Mo:TiO_2-650 and both Mo:TiO_2-700 and Mo:TiO_2-800 confirms that substitutional doping mainly occurs in rutile TiO_2.

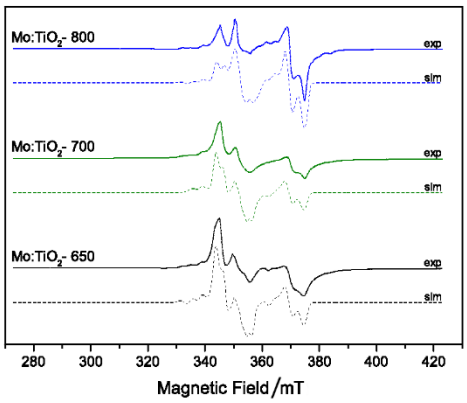

Fig. 4-10 CW X-Band EPR spectra of degassed samples at 393K of Mo:TiO_2, experimental (solid line) and simulation (dashed-line).

The particle size and crystallinity of Mo:TiO_2 were evaluated using TEM and SAED-TEM. Fig. 4-11 shows the corresponding SAED diffraction patterns, bright-field TEM and HRTEM images of Mo:TiO_2. To perform these analysis, a few milligrams of film deposited on FTO-ABS was scratched and dispersed in ethanol followed by TEM grid loading.

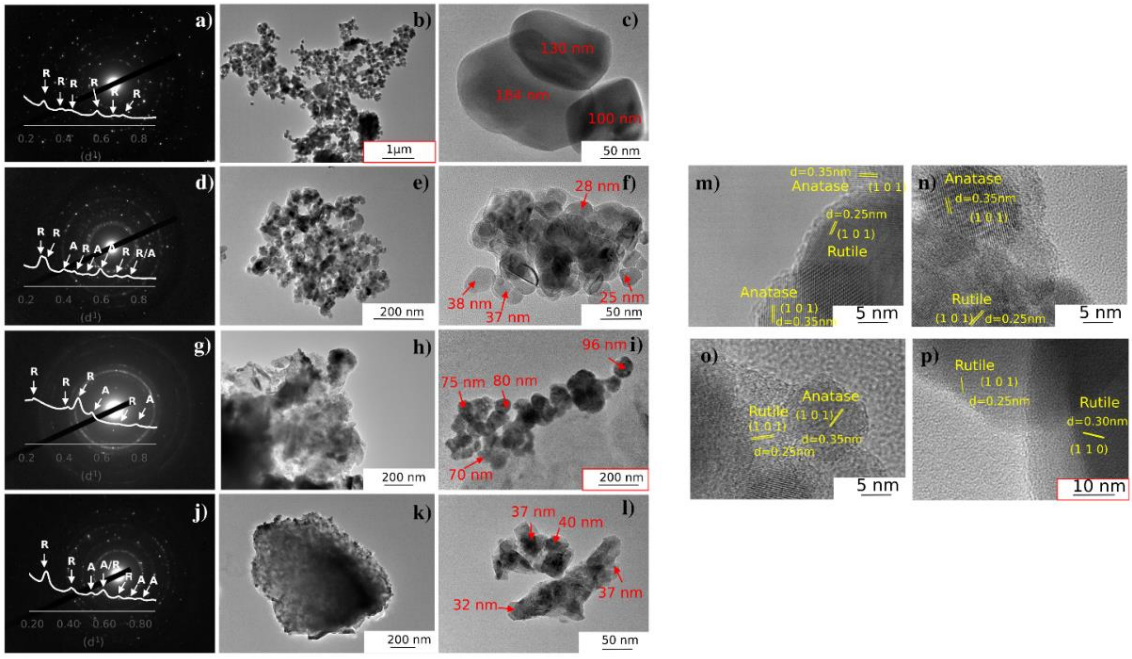

Fig. 4-11 SAED-TEM diffraction patterns, TEM and HRTEM images: (a-c) Mo:TiO_2-800, (d-f) Mo:TiO_2-700, (g-i) Mo:TiO_2-650, (j-l) TiO_2-650, (m) TiO_2-650, (n) Mo:TiO_2-650, (o) Mo:TiO_2-700 and (p) Mo:TiO_2-800. For clarity, images (b), (i) and (p) do not have scales consistent with the rest.

The SAED-diffraction patterns (Fig. 4-11, 1st column) indicate a high polycrystalline character of these Mo:TiO_2 and TiO_2 particles. The corresponding diffraction pattern along with peak identification is shown in the inlet of these figures. These data agree well with XRD where diffraction peaks corresponding to TiO_2 anatase and rutile are shown in Mo:TiO_2-650,

Mo:TiO_2-700 and pure TiO_2, whereas only TiO_2 rutile is observed in Mo:TiO_2-800. Particle size distributions are shown in Fig. 4-12. In all Mo:TiO_2 samples, the particles possess a well-defined particle shape in comparison to pure TiO_2. Nevertheless, a large variability of particle sizes is observed in Mo:TiO_2-650 suggesting an insufficient annealing temperature for the formation of uniform particles. Mo:TiO_2-800 has the highest particle size due to aggregation and sintering of particles at high calcination temperatures.[210,211]

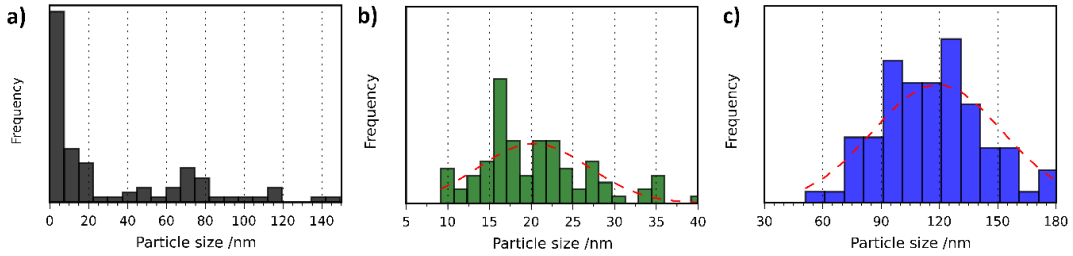

Fig. 4-12 Particle size distributions. (a) Mo:TiO_2-650, (b) Mo:TiO_2-700 and (c) Mo-TiO_2-800.

HRTEM images are shown in Fig. 4-11m-p. These images also reveal the highly crystalline character of Mo:TiO_2 and pure TiO_2. The measured lattice spacing for the TiO_2-650 sample agrees well with XRD analysis, since lattice spacings corresponding to the (1 0 1) diffraction plane of TiO_2 anatase and (1 0 1) of TiO_2 rutile are observed. In line with this, lattice spacings for Mo:TiO_2 also agree well with XRD and Raman analysis. More precisely, Mo:TiO_2-650 and Mo:TiO_2-700 show diffraction planes corresponding to both TiO_2 rutile and anatase crystalline phases, whereas only rutile TiO_2 particles are observed in Mo:TiO_2-800.

UV-Vis spectroscopy Tauc plots of Mo:TiO_2 and pure TiO_2 films are depicted in Fig. 4-13a and the corresponding absorption spectra are shown in Fig. 4-13b. All Mo:TiO_2 samples exhibit lower band-gap energy values ranging from 2.6 to 2.7 eV compared to TiO_2-650, *ca.* 3.1 eV, being in accordance with literature reports.[92] The overall band-gap reduction for all Mo:TiO_2 is attributed to the incorporation of $Mo^{6+/5+}$ centers in the TiO_2 lattice structures, contributing to the formation of a shallow donor energy level below the CB of TiO_2.[204,212] Two distinguished slopes are observed for Mo:TiO_2-800. The higher energy one is related to the band gap, while the lower one we assign it to an Urbach tail caused by sample disorder (i.e Ti-O, Ti-O-Mo bond breaking due to anatase transformation to rutile and Mo sublimation).[213] This sample disorder extends visible light absorption.

The CB and VB position of TiO_2-650 and Mo:TiO_2 photoanodes were determined using CV curves (Fig. 4-15). Detailed information of the electrochemical characteristics of TiO_2 and Mo:TiO_2 are shown in Table 4-1. A schematic diagram of the relative position of CB and VB energy levels for TiO_2-650 and Mo:TiO_2 samples is shown in Fig. 4-14. Interestingly, in all Mo:TiO_2 samples the CB offset is narrowed down from approximately -3.01 eV for TiO_2- 650

to *ca*. -4.2 eV for Mo:TiO_2. This further confirms that the incorporation of $Mo^{5+/+6}$ atoms at the TiO_2 lattice structure reduces the overall band-gap of TiO_2. The electrochemical band gap values obtained from CV curves are also shown in Table 4-1. The difference between the electrochemical band gap and optical band gap of TiO_2 and Mo:TiO_2 photoanodes is of 0.1-0.5 eV, which falls within the range of error.[214]

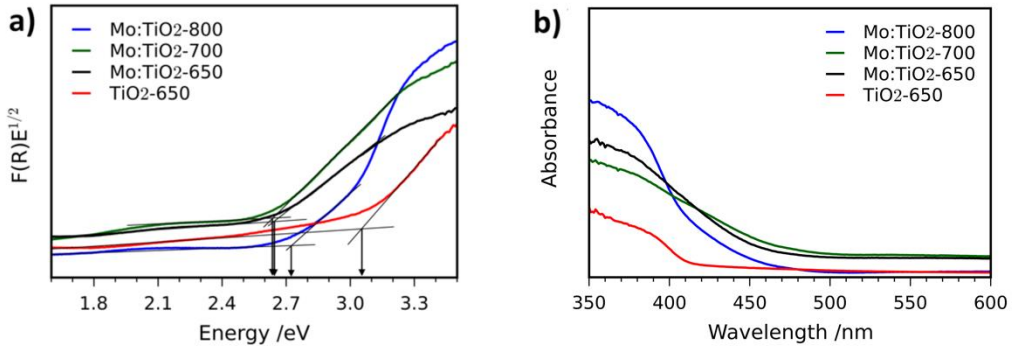

Fig. 4-13 Tauc plots of Mo:TiO_2-650, Mo:TiO_2-700, Mo:TiO_2-800 and pure TiO_2-650 photoanodes measured via diffuse reflectance UV-Vis spectroscopy. (b) Diffuse reflectance UV-Vis absorption spectra of Mo:TiO_2-650, Mo:TiO_2-700, Mo:TiO_2-800 and pure TiO_2-650 photoanodes.

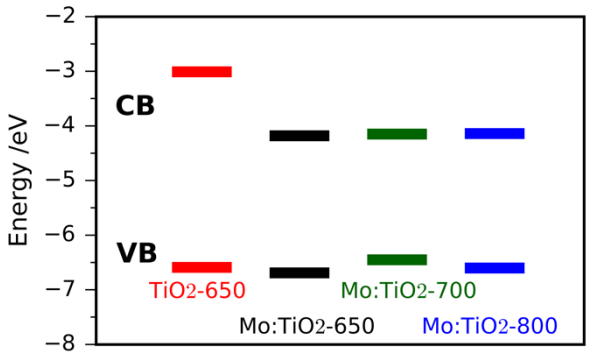

Fig. 4-14 Schematic diagram of CB and VB energy levels obtained by CV of Mo:TiO_2 and TiO_2 photoanodes.

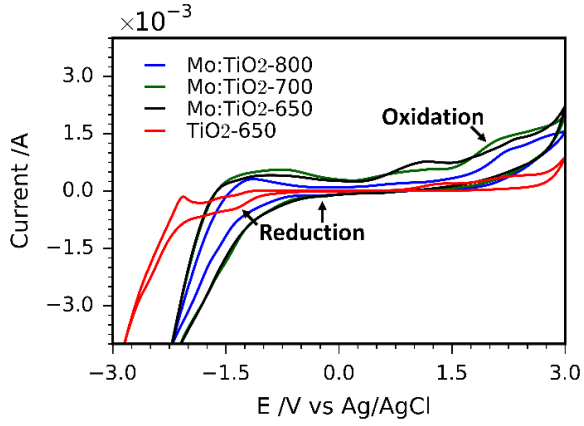

Fig. 4-15 Cyclic Voltammetry curves of TiO_2-650 and Mo:TiO_2 photoanodes in acetonitrile containing 0.1M of $TBAPF_6$ at a scan rate of 50 mv s^{-1}.

Table 4-1 Electrochemical characteristics of the bare TiO_2 and Mo:TiO_2 photoanodes.

Sample	E^{ox}_{peak} (V)/ VB (eV)	E^{red}_{peak} (V)/ CB (eV)	Eg (eV)
Mo:TiO_2-650	2.32 / -6.69	-0.19 / -4.18	2.51
Mo:TiO_2-700	2.08 / -6.45	-0.22 / -4.15	2.30
Mo:TiO_2-800	2.23 / -6.60	-0.23 / -4.14	2.46
TiO_2-650	2.22 / -6.59	-1.36 / -3.01	3.58

The photocurrent density (at 1.23 V_{RHE}) as a function of annealing temperature for front illumination (via the electrolyte-film interface) and back illumination (via the ABS) was evaluated for Mo:TiO_2 and pure TiO_2 films and the results are shown in Fig. 4-16a. Photocurrent performances are higher when films are illuminated from the back, which indicates the porous photoanodes have a sufficient thickness. Fig. 4-16a also indicates that the optimal annealing temperature for pure TiO_2 is 650 °C (and for Mo:TiO_2 is 700 °C). In view of these results, all the following photoelectrochemical experiments were carried out directing the light towards the back of the photoelectrode (via the ABS) and using TiO_2-650 as a benchmark against Mo:TiO_2 films.

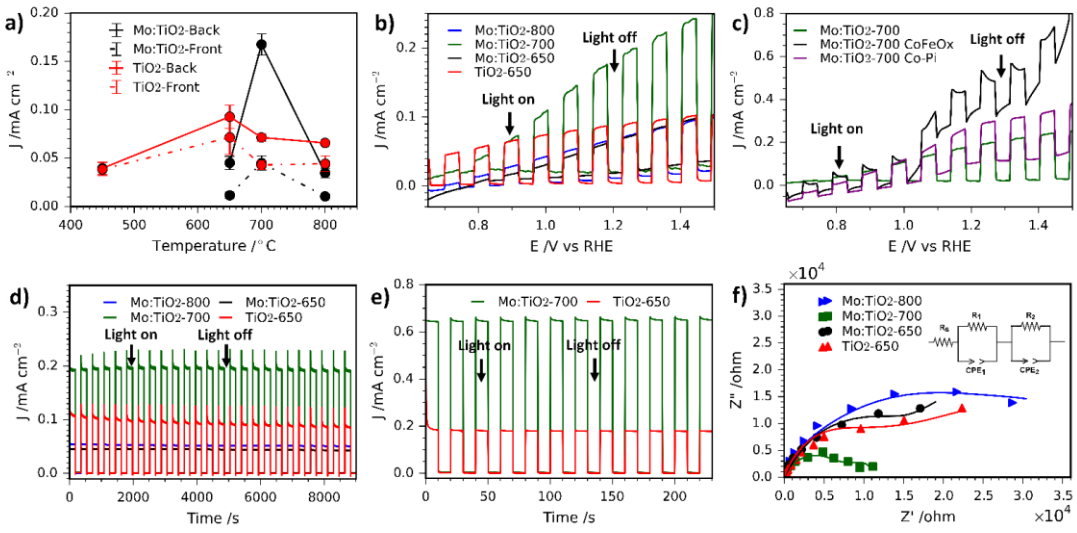

Fig. 4-16 (a) Variation of photocurrent density as a function of annealing temperature for Mo:TiO_2 and pure TiO_2 (at 1.23 V_{RHE}). Solid lines correspond to photoanodes where illumination was directed towards the back of the FTO-ABS and dashed-lines where illumination was directed towards the front of the working electrode. Error bars indicate standard error above and below the mean. (b) Photocurrent-potential curves of Mo:TiO_2 and pure TiO_2. (c) Photocurrent potential curves of Mo:TiO_2-700, Mo:TiO_2-700-CoFeOx and Mo:TiO_2-700-Co-Pi. (d) Photocurrent-time curves for 9,000s of Mo:TiO_2 and pure TiO_2 at an applied bias of 1.23 V_{RHE}. (e) Photocurrent-time curves for 250s of Mo:TiO_2 and TiO_2-650 at an applied bias of 1.23 V_{RHE} under UV illumination (365 nm, 3.6 mW cm^{-2}). (f) Nyquist plots of Mo:TiO_2 and pure TiO_2 in 1M KOH. DC of 1.23 V_{RHE}; AC potential frequency range 10^5-0.01 Hz with an amplitude of 5 mV. The inset of the figure shows the equivalent circuit used to fit the data (solid lines). All electrochemical measurements were carried out in 1M KOH aqueous electrolyte. All were irradiated with simulated sunlight (AM 1.5G, 100 mWcm^{-2}) except (e).

Photocurrent-potential (*J-V*) and photocurrent-time (*J-t*) curves are also shown in Fig. 4-16. *J-V* curves (Fig. 4-16b) under chopped simulated solar light indicate that Mo:TiO_2-700 outperforms the rest by almost a factor of two, reaching about 0.20 mA cm^{-2} at 1.23 V_{RHE}. This suggests that the annealing temperature has a significant effect. We assign this enhancement to a combination of (i) a smaller band gap, able to capture a higher fraction of the solar spectrum; (ii) higher surface area, as evidenced by FE-SEM and ECSA measurements (Fig. 4-3 & Fig. 4-5b); and (iii) to the presence of an anatase-rutile type-II heterojunction, that lowers the electron and hole recombination rate.[200,215–217] The slightly lower photocurrent observed for Mo:TiO_2 samples at lower applied bias in comparison to TiO_2-650 might arise from the different charge distribution at the space-charge region of Mo:TiO_2 that can affect the band-bending properties of the as-prepared photoanodes.[32] In fact, Z-potential measurements of powdered suspensions of Mo:TiO_2 particles revealed a highly negatively charged surface at a broad pH range (pH 1-14). This highly negative surface may lead to the formation of an accumulation layer when the Mo:TiO_2 films are in contact with the electrolyte, requiring a larger applied bias to switch to a depletion layer and promote the migration of photocarriers.[32]

Two different co-catalysts, cobalt phosphate (Co-P_i) and $CoFeO_x$ have been evaluated in order to reduce the onset potential of Mo:TiO_2-700. Previous reports have shown that both co-catalysts are excellent candidates for reducing the on-set potential owing to the decrease in electron-hole recombination at the electrode/electrolyte interface and reduction of surface charge recombination.[186,188,218] Fig. 4-16c shows the *J-V* curves for Mo:TiO_2-700 without co-catalyst and with either Co-Pi or $CoFeO_x$. Optimal deposition conditions were found to be 20s of deposition time for CoP_i loading and 3 cycles for $CoFeO_x$ (positively sweeping the voltage from 1.1 to 1.4 $V_{Ag/AgCl}$). Interestingly, both co-catalysts show a similar behaviour, where an enhancement in photocurrent is observed at low bias. At higher bias the driving force for the electron-hole separation comes from the higher bias applied itself rather than the co-catalyst, so main improvements with co-cotalyst addition are only seen at low bias.[186]

Photocurrent-time curves at 1.23 V_{RHE} also confirm that Mo:TiO_2-700 exhibits a twofold increase in photocurrent performance and reveals better photostability in comparison to TiO_2-650 (Fig. 4-16d). The photostability for Mo:TiO_2 and TiO_2-650 photoanodes was quantified as the percentage of the photocurrent performance at the end of the last illuminated cycle (*J*) against the photocurrent performance at the end of the first illumination cycle (J_0), as previously reported by Paracchino *et al*.[40] After 9,000s of chopped light irradiation, Mo:TiO_2-700 presented the best photostability with a J/J_0 of 99.0%, followed by Mo:TiO_2-650 (J/J_0=95.7%), Mo:TiO_2-800 (J/J_0=93.5%) and finally TiO_2-650 (J/J_0=81.7%). Interestingly, all Mo:TiO_2 photoanodes resulted in an enhancement in the photostability in comparison to pure

TiO_2, although only Mo:TiO_2-700 showed an improvement in the photocurrent performance over TiO_2-650. Unlike Mo:TiO_2-700, Mo:TiO_2-800 exhibits a lower photocurrent than TiO_2 at an applied bias of 1.23 V_{RHE}. This lower photocurrent performance is attributed to a combination of plausible reasons: First, Mo:TiO_2-800 only exhibits rutile TiO_2 in its composition due to the high annealing temperature employed for the preparation, as depicted in XRD and Raman experiments. Rutile TiO_2 is known to be less active than the anatase one, despite having a narrower band gap.[219] Second, unlike a rutile-anatase heterojunction where electrons and holes separate, the single phase rutile Mo:TiO_2-800 must suffer from higher electron-hole recombination.[200,215–217] Third, SEM images (Fig. 4-3) and ECSA measurements (Fig. 4-5b) also indicate a smaller surface area for Mo:TiO_2-800 with larger grains compared to Mo:TiO_2-700. Finally, many other factors such as particle size, aggregate shape and size may also influence the final photoelectrochemical performance of the Mo:TiO_2-800 film. In fact, TEM images showed higher particle size and aggregation for the Mo:TiO_2-800 photoanode, mainly due to the high annealing temperature employed.

Unlike Mo:TiO_2-800, Mo:TiO_2-650 shows both anatase and rutile TiO_2 crystalline phases, as demonstrated by XRD analysis and Raman spectroscopy and the measured band gap is considerably lower than pure TiO_2. Therefore, the poorer photoresponse behavior of Mo:TiO_2-650 must be due to the type of Mo doping and to the film morphology. As shown in SEM-EDXS and XPS analyses, Mo:TiO_2-650 possesses the highest amount of Mo amongst the Mo:TiO_2 photoanodes and XRD analysis shows a small shift towards lower angles. This fact suggests that the clear majority of $Mo^{6+/5+}$ atoms are dispersed around the surface or occupying interstitial sites of the TiO_2 lattice structure, rather than being occupying Ti^{4+} positions in the TiO_2 lattice structure. The presence of larger quantities of $Mo^{6+/5+}$ atoms on the surface of TiO_2 can reduce the photocurrent performance by creating recombination sites and blocking reaction sites.[92,106] Morphology and surface area can also play an important role in the photocurrent performance of photoanodes. As shown in the SEM images (Fig. 4-3j), very fine and poorly defined nanostructures are observed, which results in less surface area exposed for the water oxidation. This is further confirmed with ECSA measurements (Fig. 4-5b), where Mo:TiO_2-650 shows a significantly smaller surface area in comparison to Mo:TiO_2-700.

Photocurrent-time curves of Mo:TiO_2-700 and TiO_2-650 photoanodes at 1.23 V_{RHE} were also recorded using a UV lamp (365 nm, 3.6 mW cm^{-2}) and are shown in Fig. 4-16e. Under these conditions, Mo:TiO_2-700 also outperforms the performance of pure TiO_2, reaching a photocurrent value of *ca.* 0.65 mA cm^{-2} compared to *ca.* 0.2 mA cm^{-2}, respectively.

In order to further understand the enhancement in photoresponse for the Mo:TiO_2-700 photoanode, the charge transfer properties of photogenerated electrons and holes were studied

using PEIS. Fig. 4-16f shows Nyquist plots of the as-prepared photoanodes recorded at a DC potential of 1.23 V_{RHE} under illumination and AC potential frequency range of 100000-0.01 Hz. The inset of Fig. 4-16f shows the equivalent circuit used to fit the Nyquist plots. It consists of an ohmic resistance and two RC elements in series, where R_s corresponds to the resistance of the cell, R_1 to the resistance of the electronic process in the bulk semiconductor along with Constant Phase Element 1 (CPE_1), and R_2 to the resistance of the interfacial charge transfer between the electrolyte and the photoanode along with CPE_2.[220] The corresponding fitted resistance values are listed in Table 4-2.

Table 4-2 Calculated resistance parameters from EIS data.

Sample	R_s (Ω)	R_1 (Ω)	R_2 (Ω)
Mo:TiO_2-650	11.99	10,098	64,870
Mo:TiO_2-700	13.11	1,512	9,902
Mo:TiO_2-800	12.07	10,098	36,055
TiO_2-650	11.77	6,931	34,431

As expected, the resistance values of the Mo:TiO_2-700 photoanode are smaller than that of Mo:TiO_2-650, Mo:TiO_2-800 and TiO_2-650, suggesting a better separation efficiency and faster transfer rate of photogenerated electrons and holes. This enhancement in the charge transfer properties of the Mo:TiO_2-700 photoanode agrees well with the *J-t* curves (Fig. 4-16d), that showed better photostability and a twofold photocurrent increase. This improvement is attributed to the presence of oxygen vacancies, formed to balance charges after partial doping with $Mo^{6+/5+}$. Oxygen vacancies are known to improve the electrical conductivity and charge transportation of TiO_2.[137,221] Since Mo:TiO_2-700 shows an optimal substitutional doping of Mo atoms into TiO_2, an enhancement in electron conductivity and charge transportation occurs, giving rise to higher photocurrents and stability.[137,221]

IPCE measurements for Mo:TiO_2-700 and pure TiO_2 photoanodes are shown in Fig. 4-17a. Pure TiO_2 values slowly increase from 0% at 500 nm to 1.4% at 400 nm and reach a maximum of 35% at 320nm. However, Mo:TiO_2-700 IPCE values increase from 0% at 500 nm to 5% at 400 nm and reach a maximum of 40% at 330nm. These IPCE results with monochromatic light confirm the superior performance of Mo:TiO_2-700 over pure TiO_2 on absorbing and utilizing visible light, and corroborate the photocurrent results and impedance analysis with polychromatic solar light.

O_2 evolution and photocurrent measurements were performed on Mo:TiO_2-700 at 1.23 V_{RHE} under 1 sun illumination for 340 min (Fig. 4-17b). The amount of O_2 in the headspace of the PEC cell increased linearly with time during irradiation. Using the photocurrent-time curve obtained (Fig. 4-20, Supporting Information), the theoretical amount of O_2 expected for a

water oxidation reaction with 100% Faradaic efficiency was calculated and also represented in Fig. 4-17b. Comparison between values indicated that Mo:TiO_2-700 photoanode has a Faradaic efficiency of approx. 60% (details of calculations are shown in Supporting Information). Similar efficiency values have been obtained on bare photoanodes without oxygen evolution electrocatalysts.[86]

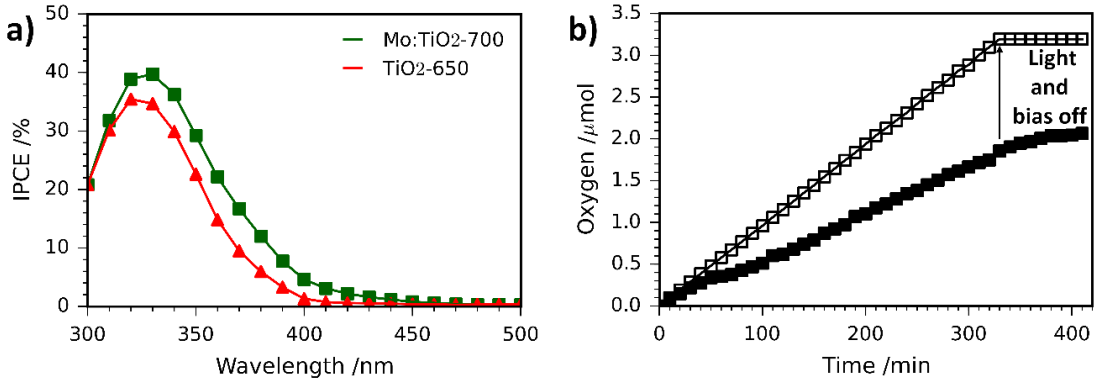

Fig. 4-17 (a) IPCE spectra at 1.23 V_{RHE} of Mo:TiO_2-700 and pure TiO_2. (b) Amount of O_2 gas evolved at 1.23 V_{RHE} under simulated sunlight (AM 1.5G, 100 mW cm^{-2}). The amount of O_2 quantified with a fluorescence probe is represented by solid markers, whereas the theoretical amount of O_2 calculated assuming a 100% Faradaic efficiency is shown with empty markers.

Conclusions

In this work a facile and rapid approach for the design of Mo:TiO_2 photoanodes using a heterometallic oxo cage of the type $[Ti_4Mo_2O_8(OEt)_{10}]_2$ as a single source precursor has been demonstrated. The performance of the resultant photoanodes is highly reliant on the annealing temperature employed owing to its effects on the crystallinity, morphology and doping of TiO_2, being 700 °C the optimal annealing temperature. At this temperature, the Mo:TiO_2 photoanode (Mo:TiO_2-700) presents better photostability and a two-fold increase in photocurrent performance (0.20 mA cm^{-2} at 1.23 V_{RHE}) in comparison to a TiO_2 photoanode (0.10 mA cm^{-2} at 1.23 V_{RHE}). This improvement both in the photocatalytic performance and stability is attributed to a combination of several factors that become optimized at 700 °C: First, Mo:TiO_2-700 exhibits the presence of anatase TiO_2 and in minor amount rutile TiO_2, forming a heterostructure that is known to reduce the electron and hole recombination rate. Second, Mo:TiO_2-700 has a smaller band gap than the obtained at different temperatures or without Mo doping, which allows for a better use of the solar spectrum and higher efficiencies (IPCE: 5% at 400nm). Third, in Mo:TiO_2-700 there is preferred substitutional doping of $Mo^{6+/5+}$ atoms for Ti^{4+} atoms in the TiO_2 lattice structure, causing the presence of oxygen vacancies which improve the electrical conductivity and charge transportation of the film. Fourth, Mo:TiO_2-700 shows a large amount of cavities, porosity and well-defined

nanostructures, resulting in the photoanode with the highest surface area. This characteristic morphology is associated to the spray pyrolysis deposition of $[Ti_4Mo_2O_8(OEt)_{10}]_2$ and to the partial sublimation of Mo species during the annealing process. On balance, these results clearly demonstrate a simple and effective methodology for preparing Mo-doped TiO_2 photoanodes with tuned electronic band properties and morphology and reveal the crucial parameters that allow the exploitation of heterometallic oxo cages in thin films for energy applications. These results open up the possibility for exploring a wide range of different heterometallic oxo cages for the fabrication of metal oxides photoanodes.

Conflicts of interest

There are no conflicts to declare.

Acknowledgements

The authors would like to acknowledge both EPSRC for funding the Centre for Doctoral Training in Sustainable Chemical Technologies at the University of Bath (EP/L016354/1), the microscopy and analysis (MAS) suite at the University of Bath and the Cavendish Laboratory from the University of Cambridge. SE would like to acknowledge the financial support from EPSRC (EP/P008097/1).

All data created during this research are openly available from the University of Bath data archive at https://doi.org/10.15125/BATH-00437.

4.1.5 Supporting information

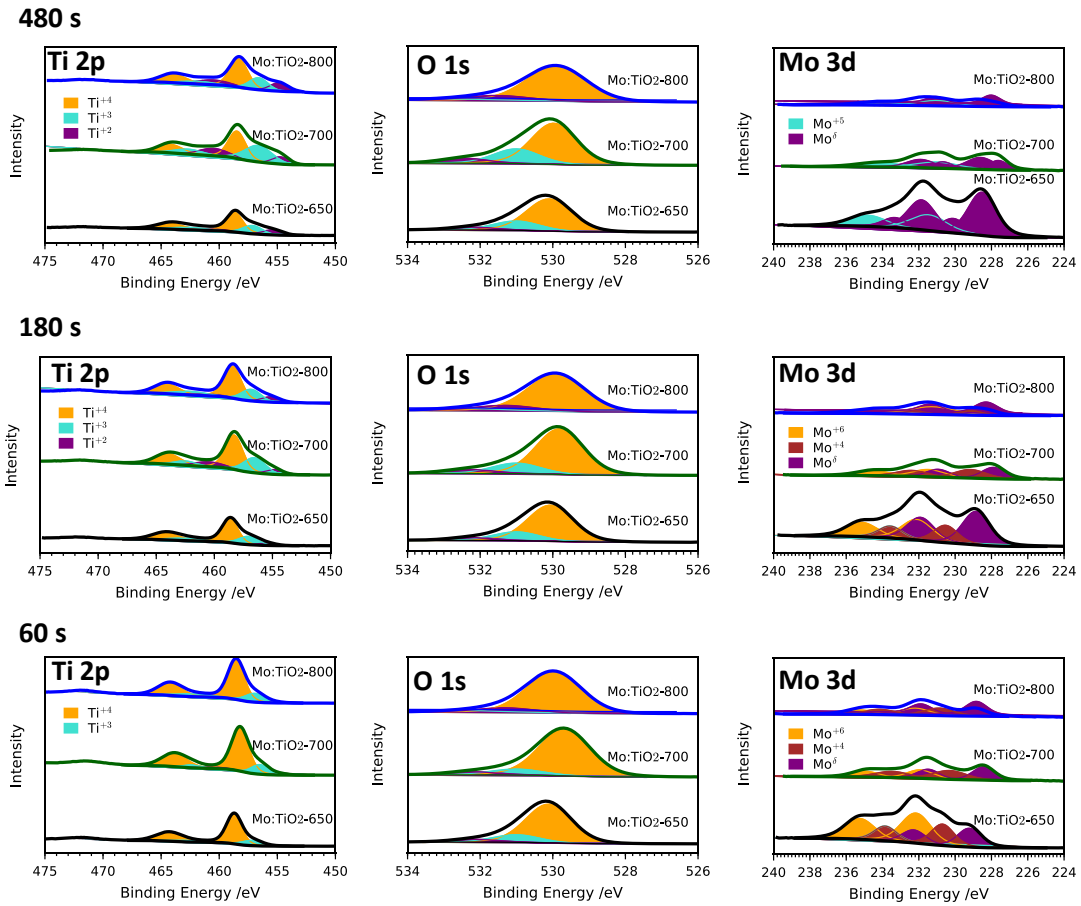

Fig. 4-18 Ti 2p, O 1s and Mo 3d XPS spectra of Mo:TiO_2 photoanodes at different etching times. Additional peaks at Ti 2p and Mo 3d XPS spectra appear at different etching times due to reduced Ti and Mo species, respectively caused by Ar bombardment.

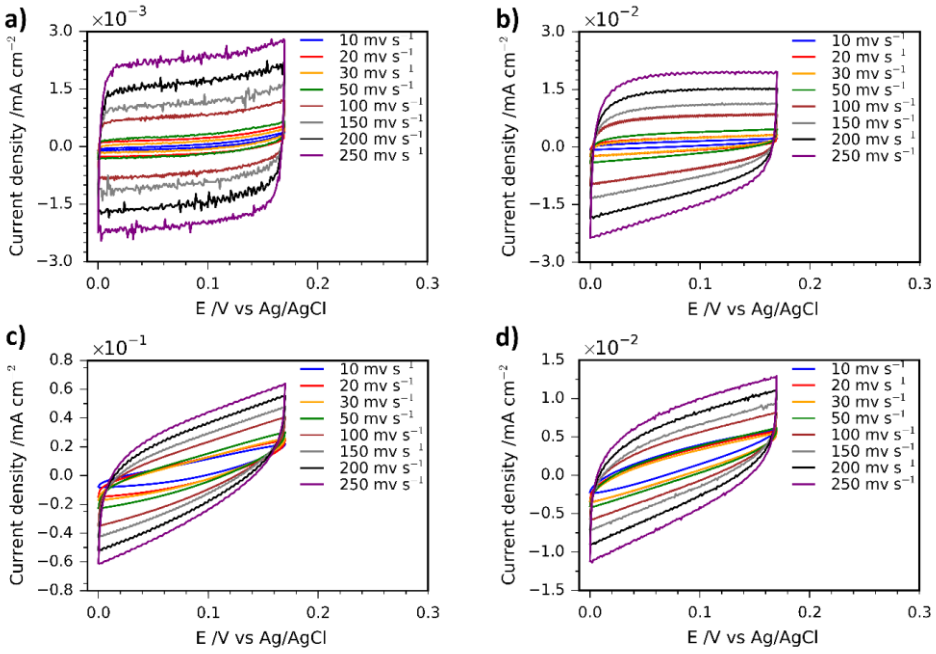

Fig. 4-19 Cyclic voltammetry curves for (a) TiO_2-650, (b) Mo:TiO_2-650, (c) Mo:TiO_2-700 and (d) Mo:TiO_2-800

Faradaic efficiency calculation

To calculate the Faradaic efficiency, first the amount of O_2 evolved in the headspace of the PEC cell was calculated using the ideal gas law and the % O_2 measurements. Next, the theoretical amount of O_2 expected for a water oxidation reaction with 100 % Faradaic efficiency was calculated. The following equation was used:

$$Q = n(e^-) * F$$

where *Q* is the charge in C, obtained from the photocurrent-time curve (Fig. 4-20); *n* (e^-) is the number of electrons in mol; and *F* is the Faraday constant (96485.3329 C mol^{-1}). The theoretical amount of O_2 generated was calculated by dividing *n* (e^-) by four, which is the number of electrons involved in the oxidation of water. Finally, the Faradaic efficiency was calculated by dividing the amount of O_2 evolved in the headspace by the theoretical amount of O_2 expected for 100 % Faradaic efficiency (µmol/µmolx100).[86]

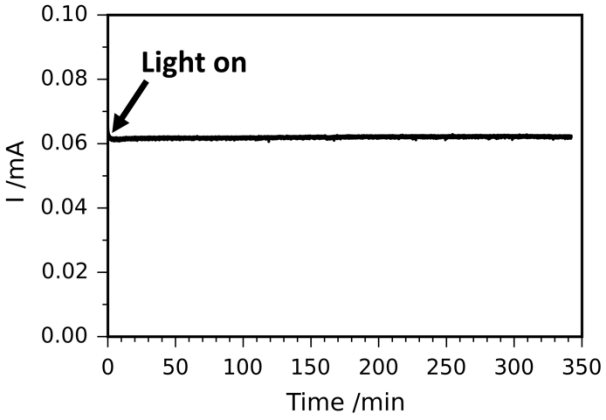

Fig. 4-20 Photocurrent-time curve of Mo:TiO_2-700 obtained during the O_2 measurement experiment at 1.23 V_{RHE}.

4.1.6 Commentary

4.1.6.1 Calculation of crystal lattice parameters

In the manuscript, we stated that substitutional doping of $Mo^{6+/5+}$ atoms for Ti^{4+} atoms in the TiO_2 lattice structure occurs, and this has been proven by a shift in the XRD pattern towards lower angles and by means of EPR spectroscopy. Even though the ionic radii of Mo^{6+} and Mo^{5+} are very similar with the Ti^{4+} ionic radius small changes in the lattice structure parameters (*a* and *c*) can occur which may further confirm the substitutional doping. Due to the slightly larger size of $Mo^{6+/5+}$ atoms in comparison to Ti^{4+}, it is expected that both lattice parameters and volume cell will increase as substitutional doping increases. In line with this, calculated cell parameters for Mo:TiO_2 samples are shown in Table 4-3. It should be noted that these parameters have been calculated only from the rutile (TiO_2) phase which is the common phase at the three annealing temperature studied (650, 700 and 800 °C). Rutile TiO_2 (but also anatase) has a tetragonal crystal structure, and the lattice parameters can be calculated according to:[222]

$$\frac{1}{d} = \frac{h^2 + k^2}{a^2} + \frac{l^2}{c^2} \qquad 4\text{-}4$$

Table 4-3 Calculated lattice parameters of Mo:TiO_2 photoanodes from TiO_2 rutile crystal phase.

Sample	*a* (Å)	*c* (Å)	Cell Volume (Å^3)
Mo:TiO_2-650	4.609	2.962	62.9
Mo:TiO_2-700	4.615	2.970	63.2
Mo:TiO_2-800	4.615	2.976	63.4

From Table 4-3 it can be observed how lattice parameters are quite similar for both Mo:TiO_2-700 and Mo:TiO_2-800, and slightly different for Mo:TiO_2-650 sample. In fact, Mo:TiO_2-650 has the smallest lattice parameters which is in agreement with XRD and EPR data shown in the manuscript, where substitutional doping in rutile TiO_2 was mainly confirmed for Mo:TiO_2-700 and Mo:TiO_2-800. The smallest cell volume is also found in Mo:TiO_2-650 sample. One might argue that the difference in the lattice parameters might also arise from the different annealing temperatures employed in each sample. In this regard, V. Štengl *et al.* reported a linear increase for both *a* and *c* parameters in rutile TiO_2 when a Mo-doped TiO_2 sample was annealed at different temperatures.[118] Conversely, B. Yarmand *et al.* reported that for rutile TiO_2 films both *a* and *c* lattice parameters decrease as annealing temperature increase.[223] In any case, our samples show neither a linear increase nor a decrease of *a* and *c* lattice parameters. All this along with XRD patterns and EPR studies further confirms that $Mo^{6+/5+}$ atoms are occupying substitutional positions mainly in Mo:TiO_2-700 and Mo:TiO_2-800 samples. This substitutional doping most likely induces the presence of oxygen vacancies to

compensate charge imbalance, as described with the Kröger-Vink notation used to describe different situations in doped metal oxides:[14,118]

$$MoO_3 \leftrightarrow Mo_{Ti}^{\cdot\cdot} + V_O^{\circ\circ} + 2O_O \qquad 4\text{-}5$$

where Mo_{Ti} is a molybdenum ion (Mo^{6+}) at a titanium lattice site, O_O is oxygen occupying an oxygen lattice site and V_O is an oxygen vacancy. The $(^{\cdot\cdot})$ and $(^{\circ\circ})$ represents the excess and deficiency of the charges, respectively.

4.1.6.2 Integration of IPCE curve over AM 1.5G solar spectrum

In the manuscript we did not report the product of integrating the calculated IPCE curves over AM 1.5G solar spectrum. The result of this integration gives an estimation of the photocurrent density values obtained at the measured potential of the IPCE curve. In this regard, integration of IPCE curves for TiO_2-650 and Mo:TiO_2-700 results in estimated photocurrent density values of *ca*. 0.2 and *ca*. 0.3 mA cm^{-2} at 1.23 V_{RHE}, respectively. These values are slightly higher than the *ca*. 0.1 and 0.2 mA cm^{-2} obtained in *J-V* curves at 1.23 V_{RHE} for TiO_2-650 and Mo:TiO_2-700, respectively. This variation is attributed to spectral mismatch between the simulated solar light (filtered Xe light) and the real AM 1.5G solar spectrum used in the integration.[224]

Furthermore, it should be noted the gradual decrease in IPCE values at wavelengths below 340 nm for both samples. This decrease is due to light being absorbed by the FTO-ABS substrate at these wavelengths (we are performing back-side IPCE), as demonstrated in transmittance measurements of the substrate (Fig. 4-21):

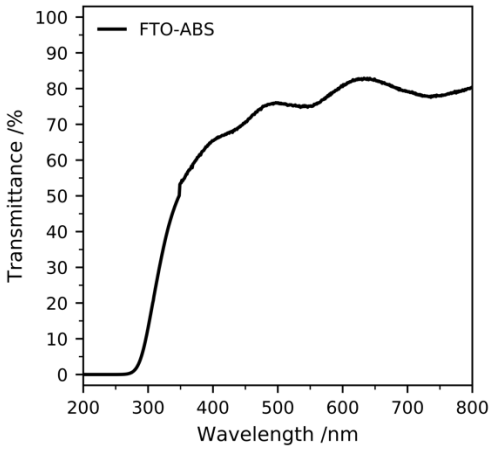

Fig. 4-21 UV-Vis spectrum of FTO-ABS substrate.

Chapter 5. Nanostructured TiO_2 photoanodes grown by aerosol-assisted chemical vapor deposition

5.1 Publication: TiO_2 photoanodes with exposed {0 1 0} facets grown by aerosol-assisted chemical vapor deposition of a titanium oxo/alkoxy cluster

5.1.1 Preface

TiO_2 was the first material that was used for photoelectrochemical water splitting applications and hence it has been widely studied throughout the last 50 years. As mentioned along this thesis, TiO_2 suffers from some limitations such as a wide band gap (3.2 eV for anatase and 3.0 for rutile) and fast recombination of electron and holes, which limits its practical applications. In Chapter 4, we have shown how doping TiO_2 can overcome some of these limitations and improve PEC performances. Alternatively, growing nanostructured TiO_2 photoanodes has also proved effective for improving its PEC performance mainly due to its higher surface area that promotes charge transfer across larger solid-liquid interfaces, shortened photo carriers pathways and induced light scattering which facilitates the generation of multiple electron and hole pairs, as discussed in detail in Chapter 2.[51] Among the different polymorphs in which TiO_2 exists, anatase TiO_2 is known to be the most photocatalytic active one. Therefore, an approach to enhance even more the performance of nanostructured TiO_2 is by preparing anatase TiO_2 films with high-energy facets such as {0 1 0} or {0 0 1} exposed on the surface of the TiO_2 nanostructure. These facets, specially {0 1 0} have been reported to be the most photoactive facet owing to its favorable surface atomic and electronic structure.[132]

There is plenty of interest in the scientific community to prepare high – temperature stable anatase TiO_2, not only in the field of photoelectrochemistry, but also in the smart tile ceramic industry, where anatase TiO_2 is used as a functional coating for antibacterial and self-cleaning properties due to its better photocatalytic activity over other TiO_2 polymorphs, such as rutile and brookite.[225]

In this publication, we report for the first time the formation of nanostructured anatase TiO_2 photoanodes having the morphology of 'desert-roses' with a majority of {0 1 0} facets exposed. This preferential growth orientation is achieved by a unique combination of aerosol-assisted chemical vapor deposition and the use of a titanium oxo/alkoxy cluster as precursor. In addition, a set of temperature studies reveal that these nanostructured TiO_2 films keep the metastable anatase TiO_2 films up to 900 °C (~ 200 °C above the conventional anatase-rutile phase transformation), with a gradual conversion to rutile phase above 1000 °C, which would also find applications in the smart-tile ceramic industry. Overall these nanostructured TiO_2 photoanodes achieved high photocurrent efficiencies (~ 0.67 mA cm^{-2} at 1.23 V_{RHE}, 1 sun illumination) and IPCE of ~ 100 % at 350 nm. Characterization techniques such as SEM, TEM

and time-resolved measurements reveal the unique advantages of this highly nanostructured anatase TiO_2 photoanode.

5.1.2 Declaration of authorship

<table>
<tr><td colspan="2">This declaration concerns the article entitled:</td></tr>
<tr><td colspan="2">TiO_2 photoanodes with exposed {0 1 0} facets grown by aerosol-assisted chemical vapor deposition of a titanium oxo/alkoxy cluster</td></tr>
<tr><td colspan="2">Publication status (tick one)</td></tr>
<tr><td colspan="2">Draft manuscript | Submitted | In review | Accepted | <u>Published</u> X</td></tr>
<tr><td>Publication details (reference)</td><td>M. Regue, S. Sibby, I. Y. Ahmet, D. Friedrich, F. F. Abdi, A. L. Johnson and S. Eslava, J. Mater. Chem. A, 2019, 7, 19161–19172.
DOI: 10.1039/C9TA04482E</td></tr>
<tr><td colspan="2">Copyright status (tick the appropriate statement)
I hold the copyright for this material [X] | Copyright is retained by the publisher, but I have been given permission to replicate the material here [ ]</td></tr>
<tr><td>Candidate's contribution to the paper (provide details, and also indicate as a percentage)</td><td>• Formulation of ideas: 90%
The candidate considerably contributed to the formulation of the ideas.
• Design of methodology: 85%
The candidate was responsible for designing the methodology with few suggestions from co-authors, mainly S. Eslava and A. L Johnson. I. Y. Ahmet, D. Friedrich and F.F. Abdi designed the time-resolved Microwave conductivity measurements (TRMC), although the candidate also participated in the design and data acquisition.
• Experimental work: 90%
The candidate performed most of the laboratory work, including material synthesis, deposition and characterization. The candidate participated in acquisition of TEM and SEM images by the Material and Chemical Characterization facility (MC^2) and XPS at the Harwell EPSRC National facility. The candidate also participated in the acquisition of TRMC data, at Helmholtz Zentrum Berlin along with I. Y. Ahmet and D. Friedrich.</td></tr>
</table>

	• Presentation of data in journal format: 80% The candidate collected the data and drafted most of the manuscript. The TRMC section was mainly drafted by I. Y. Ahmet, D. Friedrich and F.F. Abdi. The manuscript was then revised and edited by S. Eslava and approved by all co-authors.		
Statement from Candidate	This paper reports on original research I conducted during the period of my Higher Degree by Research candidature.		
Signed		**Date**	23/09/2019

5.1.3 Copyright agreement

5.1.4 Published article

TiO_2 photoanodes with exposed {0 1 0} facets grown by aerosol-assisted chemical vapor deposition of a titanium oxo/alkoxy cluster

Miriam Regue, [a,b] ***Sandra Sibby,*** [b] ***Ibbi Y. Ahmet,*** [c] ***Dennis Friedrich,*** [c] ***Fatwa F. Abdi,*** [c] ***Andrew L. Johnson**** [a,d] ***and Salvador Eslava*** [*a,b]

[a]*Centre for Sustainable Chemical Technologies, University of Bath, Claverton Down, Bath, BA2 7AY, UK*

[b]*Department of Chemical Engineering, University of Bath, Claverton Down, Bath, BA2 7AY, UK. E-mail: s.eslava@bath.ac.uk*

[c]*Helmholtz-Zentrum Berlin für Materialien und Energie Gmbh, Institute for Solar Fuels, Hahn-Meitner-Platz 1, Berlin 14109, Germany*

[d]*Department of Chemistry, University of Bath, Claverton Down, Bath, BA2 7AY, UK*

Received 29th April 2019

Accepted 25th July 2019

First published on 29th July 2019

Abstract

Photoelectrochemical water splitting is a promising technology for the development of solar fuels. Titanium dioxide (TiO_2) is one of the most studied metal oxides in this field as a photoanode. Achieving its full potential requires controlling its morphology and crystallinity and especially the exposure of its most active crystal facets. Herein, we present the formation of nanostructured TiO_2 photoanodes with anatase phase and high exposure of the {0 1 0} facet, the most active TiO_2 phase and facet. TiO_2 photoanodes were prepared from a $Ti_7O_4(OEt)_{20}$ titanium oxo/alkoxy cluster solution using aerosol-assisted chemical vapor deposition. Characterization techniques such as SEM and TEM reveal that these TiO_2 photoanodes consist of morphologies resembling the crystals of gypsum, sand and water found in nature, also known as desert roses. Furthermore, TEM and XRD analysis also reveal that the metastable anatase TiO_2 phase is maintained up to 1000 °C and exceeds the typical anatase-to-rutile phase-transition temperature of 500-750 °C, a feature that could be exploited in the smart ceramics industry. Photoelectrochemical measurements show that these desert-rose TiO_2 photoanodes achieve excellent photocurrent densities with an incident photon-to-current efficiency of ~100% at 350 nm and a faradaic efficiency for oxygen evolution of ~90%.

Introduction

A key approach to reduce global warming is to change and decarbonize the current energy portfolio, highly based on fossil fuels, to a more sustainable one.[4] The abundant solar energy reaching the Earth's surface (1.3×10^5 TW year^{-1}) provides a clean alternative and can be used to produce clean hydrogen from water via photoelectrochemical (PEC) water splitting. Among the different light harvesting materials used as photoanodes in PEC cells, TiO_2 is the most studied material owing to its good properties such as chemical and thermal stability, low cost, electronic properties and long durability.[88,183] Moreover, TiO_2 also finds applications in the decomposition of organic pollutants, photovoltaics, self-cleaning coatings, electrochromic display devices, Li-ion batteries and biomedical devices.[183,226] Nevertheless, it suffers from a few disadvantages, such as the large band gap and fast recombination of electrons and holes, which can limit its practical application, especially in PEC devices.[129] An approach to overcome some of these limitations is by designing nanostructured TiO_2 crystals with most active facets exposed, since they can offer more available active surface area for the charge transfer process at the photocatalyst-electrolyte interface.[51] Under equilibrium conditions, anatase TiO_2 crystals typically grow with a majority of {1 0 1} facets exposed that have one of the lowest surface energy (0.44 J m^{-2}) and poor PEC or photocatalytic activity.[131] In this regard, there is a great scientific interest in growing anatase TiO_2 crystals with high energy facets exposed, such as {0 1 0} and {0 0 1}, which are known to be the most active ones for photocatalytic or PEC applications, especially the {0 1 0} facet.[132,227–229]

Nowadays, the hydrothermal method is the most employed method for the fabrication of nanostructured TiO_2 photoanodes and a wide range of different morphologies have been achieved so far, such as nanotubes,[230] nanorods,[231] nanowires,[232] nanobelts[233] and even flower-like nanostructures.[234] Chemical vapor deposition (CVD) is an alternative method for the preparation of nanostructured TiO_2 films. This method allows the fabrication of robust films with a relatively low processing cost, facilitating the scale up.[165] Different variants of CVD have been used for TiO_2 growth, such as aerosol-assisted CVD or metal-organic CVD (MOCVD). For instance, Gardecka *et al.* successfully synthesized nanostructured and dendritic TiO_2 photoanodes using MOCVD and titanium tetraisopropoxide as the precursor.[139] Other morphologies such as cauliflower-like structures, needle-like structures and compact domes with pyramidal features (doped with W) have also been successfully grown by AACVD using titanium isopropoxide and titanium ethoxide as TiO_2 precursors.[140,172,173,178,235]

In this publication, we present the first formation of nanostructured anatase TiO_2 having the appearance of crystals of gypsum, sand and water, typically known as "desert roses", with a high exposure of one of the most photocatalytically-active TiO_2 {0 1 0} facet. A similar

morphology had only been produced before with rutile TiO_2 phase using a hydrothermal method and MoO_3 to stabilize {0 0 1} sufaces,[236] but never with anatase TiO_2 that is the most photocatalytically-active phase. This "desert rose"-like anatase TiO_2 is grown by AACVD on different substrates using a sophisticated but inexpensive precursor - a titanium oxo/alkoxy cluster, also called cage, with formula $Ti_7O_4(OEt)_{20}$. Upon deposition, the films are covered in carbon residue, but posterior calcination in air reveals the TiO_2 {0 1 0} facet is predominant on the surface of the rose petals. When deposited on a conductive transparent support and tested in PEC cells for water oxidation, the resulting desert-rose TiO_2 photoanodes exhibit high photocurrents and stability and 100% incident-to-photon efficiency (IPCE) performance at 350 nm. Therefore, the results herein presented reveal new strategies for the design and fabrication of nanostructured TiO_2 photoanodes using AACVD technology and metal oxo/alkoxy clusters.

Experimental

Materials

Titanium (IV) ethoxide [$Ti(OEt)_4$], anhydrous toluene (≥99.9%) and ethanol (<0.0003% water) were provided by Sigma Aldrich. Aluminoborosilicate glass (ABS) coated with a fluorine-doped tin oxide (FTO) transparent conductive layer ($8\Omega\ sq^{-1}$) was provided by Solaronix SA, Switzerland. These FTO-ABS substrates withstand 800 °C heating in air, with no deterioration of the FTO conductivity.[237] They were cleaned by ultrasonication in a 2% aqueous Hellmanex III solution, deionized water, acetone and isopropyl alcohol (each step for 3 min), followed by rinsing in deionized water and compressed-air drying and an oxygen plasma treatment for 20 min to enhance surface energy. Alumina substrates (100mm x 100mm x 1mm) for high-temperature studies were provided by Almath and quartz substrates (25mm x12mm) for time-resolved microwave conductivity measurements were provided by H. Baumbach & Co Ltd.

Synthesis of $Ti_7O_4(OEt)_{20}$

$Ti_7O_4(OEt)_{20}$ titanium oxo/ethoxy cluster was synthesized by a controlled hydrolysis in toluene as Eslava et al. previously described.[149] Briefly, 0.34 mL of deionized water and 5.0 mL of anhydrous ethanol were added dropwise to a solution containing 7.0 mL of $Ti(OEt)_4$ in anhydrous toluene (15 mL) under argon atmosphere. After overnight stirring, evaporation of the solvent resulted in the formation of a white/yellowish crystalline solid precipitate of $Ti_7O_4(OEt)_{20}$.

Preparation of TiO_2-Rose and TiO_2 photoanodes

Photoanodes were prepared using AACVD. The aerosol droplets were generated using a TSI Model 3076 Constant Output Atomiser, a 0.05 M solution of $Ti_7O_4(OEt)_{20}$ in toluene, and nitrogen as a carrier gas at a constant flowrate of 1.5 L min^{-1} (Fig. 5-1). Depositions were carried out onto FTO-ABS, quartz or alumina substrates placed horizontally inside a tube furnace. Deposition times of 0.5, 1, 1.5 and 2 h at 500 °C and deposition temperatures of 400, 500, 600 and 700 °C for 1 h were performed to assess the growth mechanism and optimization. The optimal deposition conditions for PEC performance were found to be 500 °C and 1 h. At the end of the deposition, the substrate was left to cool down under nitrogen flow. The obtained films were further annealed in air at a heating rate of 10 °C min^{-1} up to 800 °C, kept at this temperature for 2 h, and then left to cool down in air. The obtained photoanodes at 500 °C with 1 h deposition conditions were denoted as TiO_2-Rose-AD (as-deposited) and TiO_2-Rose-800 (annealed). For comparison, TiO_2 photoanodes were prepared following the same methodology but using 0.05 M $Ti(OEt)_4$ (same precursor molar concentration) and 0.35 M $Ti(OEt)_4$ (same Ti molar concentration) toluene solutions instead. The resultant photoanodes were accordingly denoted as TiO_2-0.05M-AD, TiO_2-0.35M-AD, TiO_2-0.05M-800 and TiO_2-0.35M-800.

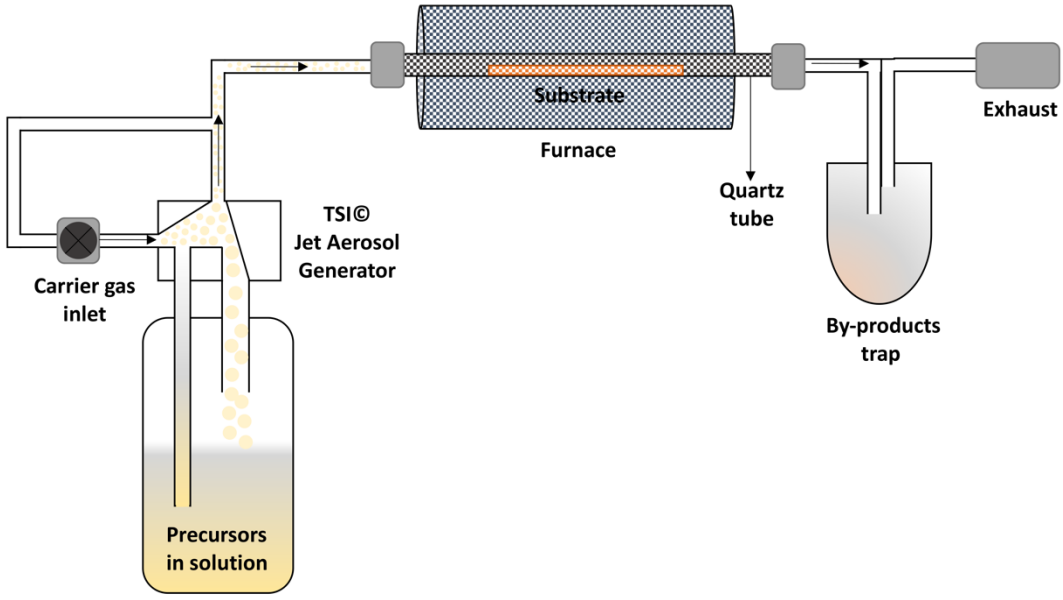

Fig. 5-1 Schematic of the AACVD setup used in the deposition. The aerosol is generated with an aerosol Jet atomizer.

Characterization

Unit cell calculations were performed at 150 K in a RIGAKU SuperNova manufactured by Agilent Technologies. Field-emission scanning electron microscopy micrographs (FE-SEM) were acquired using a JEOL FESEM6301F instrument. X-ray photoelectron spectroscopy

(XPS) was performed using a Thermo Fisher Scientific K-alpha$^+$ spectrometer using a micro-focused monochromatic Al x-ray source (72 W). C 1s peak was used for internal charge correction. X-ray diffraction (XRD) patterns were collected from 10 to 80° (2θ) Bragg-Brentano with a Bruker AXS D8 Advance using Cu Kα (0.154 nm) radiation, 0.023° (2θ) steps and a total integration time of 960 s. The rutile TiO_2 fraction in the films was calculated using the following equation:[238]

$$X_{rutile} = \left(1 + \frac{I_{anatase}}{1.26\, I_{rutile}}\right)^{-1} \qquad 5\text{-}1$$

where $I_{anatase}$ is the measured intensity of the anatase (1 0 1) diffraction plane and I_{rutile} is the measured intensity of the rutile (1 1 0) diffraction plane. The amount of anatase in the film was the remaining fraction ($X_{anatase}$=1-X_{rutile}), since no other phases were observed. The coherent diffraction domain size was calculated using the Scherrer equation at the (1 0 1) anatase TiO_2 diffraction.[239] Preferred crystal orientation in the film was evaluated by calculating texture coefficients ($TC_{(h\ k\ l)}$) using the Harris method and a powder diffraction standard for anatase (ICDD-JCPDS 75-1537).[240] Raman spectroscopy was carried out on a Renishaw inVia system using a 532 nm diode-pumped solid-state laser (DPSS) manufactured by Cobolt. The laser beam was focused onto the sample using a 50x long distance objective. Thermogravimetric analysis (TGA) was performed using a Setaram Setsys Evolution 16 TGA-DTA-DSC equipment for TiO_2 powders (a few mg of TiO_2 was scratched from the FTO). TGA of $Ti_7O_4(OEt)_{20}$ and $Ti(OEt)_4$ precursors were performed in a glove box under argon atmosphere using a PerkinElmer TGA 4000 apparatus. High-resolution transmission electron microscopy (HRTEM) micrographs of films were obtained using a JEOL JEM-2100Plus microscope. For the sample preparation, a few milligrams of film was scratched and dispersed in ethanol followed by TEM grid loading. Time-resolved microwave conductivity measurements (TRMC) were carried out using a set up and procedure previously described in literature.[241–243] During measurements, a change in the microwave power reflected by the cavity upon excitation with a 3 ns pulse laser was monitored. For these experiments, measurements were performed using a wavelength tunable optical parametric oscillator (OPO) coupled to a diode-pumped Q-switched Nd:YAG 3-ns pulse laser at wavelengths of 350, 650 and 1200 nm. A dielectric constant of 41 was used for the calculation of the TRMC signal.[244] Ultraviolet-visible (UV-Vis) absorption spectra were collected in an Agilent Cary 100 diffuse reflectance UV-Vis spectrophotometer. UV-Vis transflectance measurements were collected in a Lambda 950 spectrometer (Perkin Elmer) with an integrating sphere (150 mm InGaAs) and mounting the sample in the center.

PEC measurements

PEC performance of photoanodes was evaluated using a CompactStat. potentiostat (Ivium Technologies). Photocurrents were measured under simulated sunlight (AM 1.5G, 100 $mWcm^{-2}$) from a filtered 300 W xenon lamp source (Lot Quantum Design) or under UV illumination (365 nm, 3.6 $mWcm^{-2}$) from a ModuLight IM3412 LED light (Ivium Technologies). PEC cells were prepared with a three-electrode configuration with Pt as the counter electrode, a silver chloride (Ag/AgCl/3.5M KCl) reference electrode and as-prepared photoanodes as the working electrode. 1 M aqueous KOH (pH=13.7) was used as the electrolyte solution. Illumination was directed towards the back of the FTO-ABS working electrode and a mask was placed on top of the photoelectrode to define the illuminated area. Photocurrent-time curves were measured at an applied bias of 1.23 V *vs* the reversible hydrogen electrode (V_{RHE}). Photocurrent-potential curves were recorded at a scan rate of 20 mV s^{-1}. The measured Ag/AgCl potentials ($E_{Ag/AgCl}$) were converted to RHE potentials ($E°_{RHE}$) and vice versa using the Nernst equation.

PEC impedance spectroscopy (PEIS) was carried out under simulated sunlight (AM 1.5G, 100 mW cm^{-2}) at the light open circuit potential (OCP) of the cell at a frequency range of 10^5–0.1 Hz with an amplitude of 10 mV. EIS measurements at different potentials were also performed under dark conditions to obtain Mott-Schottky plots. These measurements were carried out at a fixed frequency of 500 and 1000 Hz, based on the following equation:[138]

$$\frac{1}{C^2} = \frac{2}{N_d e \varepsilon_0 \varepsilon}\left[(U_s - U_{Fb}) - \frac{K_B T}{e}\right] \qquad 5\text{-}2$$

where C is the semiconductor depletion layer capacitance, N_d the electron carrier density, e the elemental charge value, ε_0 the permittivity of the vacuum, ε the relative permittivity of the semiconductor, U_s the applied potential, U_{Fb} the flat band potential, and $[K_BT/e]$ a temperature-dependent correction term. The electron carrier density (N_D) was obtained from Mott-Schottky plots using the following equation:

$$N_D = \left(\frac{2}{e\varepsilon\varepsilon_0}\right)\left(\frac{d\left(1/C^2\right)}{d(U_s)}\right)^{-1} \qquad 5\text{-}3$$

where ε=41 for anatase TiO_2 and $[d(1/C^2)/d(Us)]^{-1}$ is the inverse of the slope obtained from Mott-Schottky plot.

Incident photon-to-current efficiency (IPCE) measurements were calculated using the same Xe light source and a triple grating Czerny-Turner monochromator.[32] The intensity of monochromatic light was measured at the working electrode position with a SEL033/U

photodetector (International Light Technologies). Oxygen (O_2) measurements were conducted using a Pyroscience FireStingO2 fibre-optic oxygen meter combined with a TROXROB10 oxygen probe, together with a TDIP temperature sensor to give automatic compensation for minor fluctuation in the PEC cell temperature. The probe was fitted into the headspace of the airtight PEC cell, initially purged with a N_2 flow to ensure air O_2 removal before the irradiation started. The O_2 measurements were carried out at 1.23 V_{RHE} bias under simulated sunlight (AM 1.5G, 100 mW cm^{-2}) irradiated for 180 min. O_2 in the electrolyte solution was estimated using Henry's law and added to the measured values in the headspace.[245,246] The Faradaic efficiency was calculated by dividing the calculated amount of evolved O_2 at the end of the experiment (after values stabilized) by the theoretical amount of expected O_2 for measured photocurrents (assuming 100% Faradaic efficiency and O_2 formation by four electrons).

Results and Discussion

Structural characterization

Titanium oxo/ethoxy cluster $Ti_7O_4(OEt)_{20}$ (Fig. 5-2) was firstly reported in 1967 by K. Watenpaugh and C. N. Caughlan as one of the first hydrolysis products of $Ti(OEt)_4$ in dry ethanol bubbled with partially-dried air.[247]

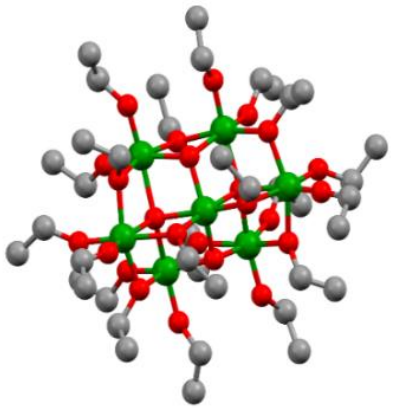

Fig. 5-2 Ball and stick model of $Ti_7O_4(OEt)_{20}$ represented from CDCC 169789.[248] Ti: Green, O: Red and C: Grey. Hydrogen atoms are omitted for clarity.

In this work, we successfully prepared it in gram scale following a controlled hydrolysis of $Ti(OEt)_4$ with distilled water in anhydrous toluene. Unit cell calculations confirmed the successful synthesis of $Ti_7O_4(OEt)_{20}$ with the unit cell parameters [*a* 13.806(8), *b* 20.223(12) and *c* 12.155(5) Å] matching the ones firstly reported by R. Schmid *et al*. (CDCC 169789).[248] Its deposition by AACVD on FTO-ABS substrates resulted in black films due to carbon residues from the ethoxide groups and toluene solvent employed during the deposition (TiO_2-Rose-AD, Fig. 5-3a inset). Annealing in air at 800 °C removed this carbon and films turned white (TiO_2-Rose-800, Fig. 5-3d inset).

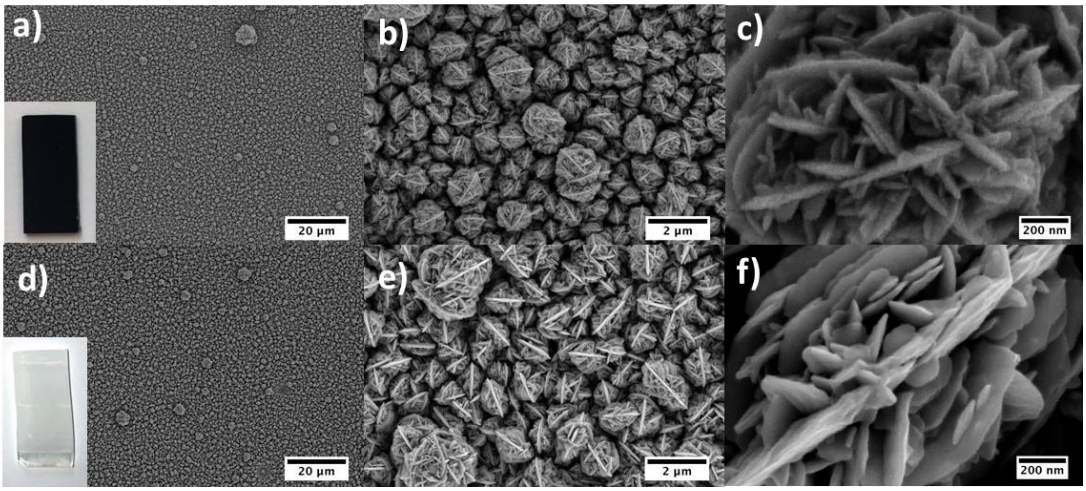

Fig. 5-3 SEM micrographs of TiO_2 photoanodes grown by AACVD. (a-c) TiO_2-Rose-AD and (d-f) TiO_2-Rose-800. Insets in (a) and (d) show photographs of TiO_2-Rose-AD and TiO_2-Rose-800 photoanodes, respectively.

Fig. 5-3 (a-f) shows SEM micrographs of TiO_2-Rose-AD and TiO_2-Rose-800. Both exhibit almost the same morphology, with a structure resembling the crystals of gypsum, sand and water, typically known as "desert roses". Such roses have a size of 1-1.5 µm and consist of many plate-like sheets resembling rose petals. They offer a good and homogeneous coverage of the FTO support. There are no significant structural changes between TiO_2-Rose-AD (Fig. 5-3a-c) and TiO_2-Rose-800 (Fig. 5-3d-f) at low magnifications. However, at highest magnification, TiO_2-Rose-AD shows some surface roughness on the petals assigned to the carbon residues.

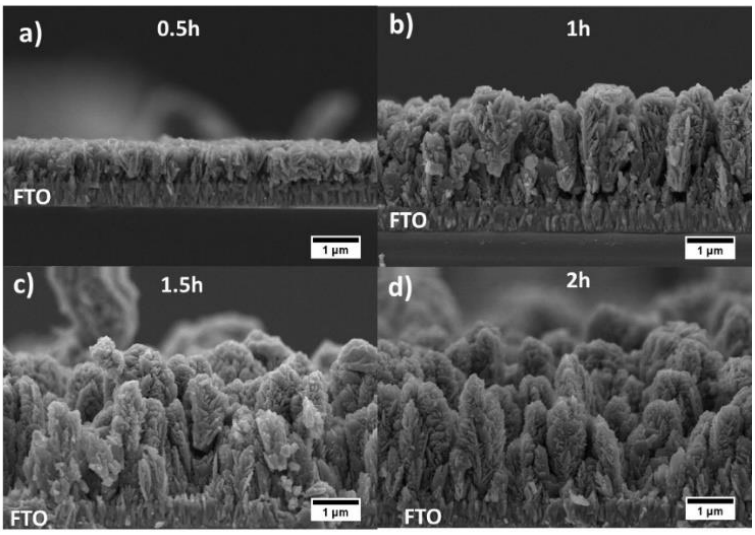

Fig. 5-4 SEM cross-sectional micrographs of TiO_2-Rose-800 photoanodes deposited for (a) 0.5 (b) 1 (c) 1.5 and (d) 2 h.

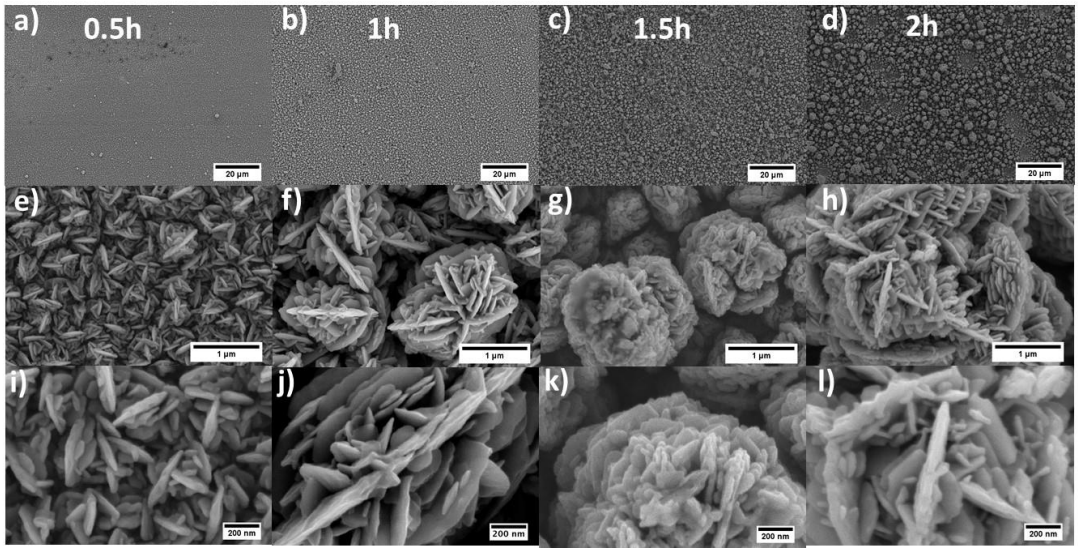

Fig. 5-5 SEM micrographs at different magnifications of TiO_2-Rose-800 photoanodes deposited at different times (a, e, i) 0.5, (b, f, j) 1, (c, g, k) 1.5 and (d, h, l) 2 h on top of FTO-substrates.

The deposition time during AACVD process was studied. Fig. 5-4 shows SEM cross-sectional micrographs of desert rose TiO_2 photoanodes obtained at four different deposition times and all annealed at 800 °C. The thickness of the films increased from 0.77 (σ=0.05) μm for 0.5 h to 2.6 (σ=0.20), 2.8 (σ=0.07), and 2.5 (σ=0.26) μm for 1, 1.5 and 2 h, respectively (σ stands for std deviation). Desert-rose flowers grow perpendicular to the FTO substrate with plate-like petals emerging from the stem of the flower and achieving a good coverage of the support. Interestingly, after 1 h of deposition, the thickness of the films remains practically constant between 2.6 and 2.8 μm, although some random flowers grow as a second layer (see some roses in the background of the micrographs in Fig. 5-4 c-d). This growth is confirmed by top-view SEM micrographs of the same photoanodes (Fig. 5-5). A homogeneous first layer of similar-size roses is achieved at 0.5 and 1 h deposition time, but excessive time leads to some secondary larger flowers above the first layer. A deposition of 1 h was found to be optimal for PEC performance. The deposition temperature was also studied at 400, 600 and 700 °C for 1h. Films did not grow at 400 °C but the higher deposition temperatures were successful (Fig. 5-6 SEM micrographs). Finer nanostructures were observed at higher temperatures, which are typical when precursor decomposition and/or chemical reactions mostly occur in the vapor phase, followed by surface adsorption and heterogeneous reactions.[166] No plate-like "petal" morphologies were obtained at different temperatures, so 500 °C was confirmed to be optimal for nanostructured growth, together with 1 h deposition time. Following work was carried out using films deposited at these conditions. This optimization based on morphology was further confirmed by PEC measurements (results not shown).

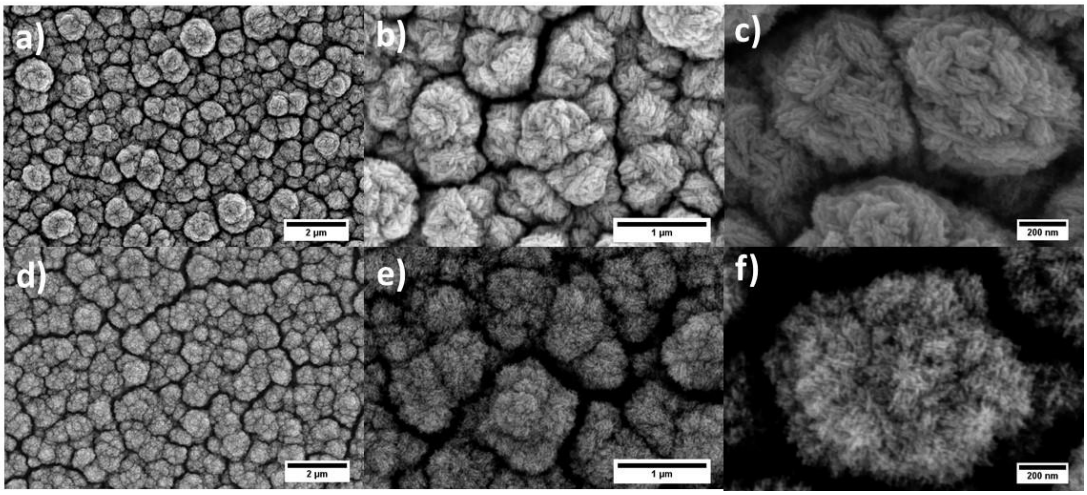

Fig. 5-6 SEM micrographs at different magnifications of (a-c) TiO_2 deposited at 600 °C and (d-f) 700 °C for 1h on top of FTO-substrates.

HR-TEM micrographs of both TiO_2-Rose-AD and TiO_2-Rose-800 film fragments are shown in Fig. 5-7. First, it is noteworthy to highlight the presence of a thin amorphous carbon layer at the crystallite interface of TiO_2 particles for TiO_2-Rose-AD (Fig. 5-7a-c).

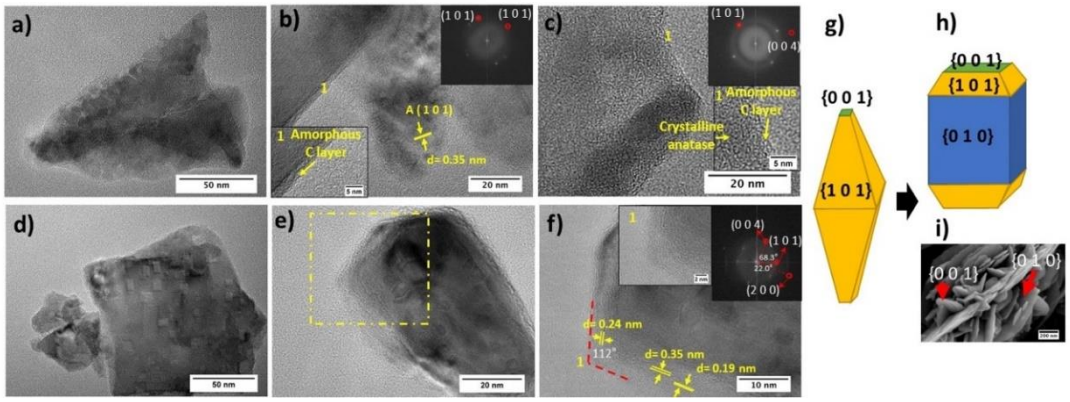

Fig. 5-7 TEM and HRTEM micrographs of (a-c) TiO_2-Rose-AD and (d-f) TiO_2-Rose-800. Fast Fourier transformation (FFT) patterns and inverse FFT image are shown in the inset of (b-c) and (f). (f) Region highlighted in (e). (g) Wulff construction of anatase crystals and (h) evolved shape with high exposure of {0 1 0} facets. (i) SEM micrograph highlighting the facets.

After annealing in air, TiO_2-Rose-800 shows no distinguished amorphous carbon layer (Fig. 5-7d-f). TiO_2-Rose-800 consists of well-defined faceted morphologies (Fig. 5-7d and Fig. 5-7e). Indexing of diffraction spots (Fig. 5-7f) from fast Fourier Transformed (FFT) diffraction patterns correspond to (1 0 1), (0 0 4), and (2 0 0) (see insets in Fig. 5-7f) of anatase TiO_2, suggesting exposure of {1 0 1}, {0 0 1} and {1 0 0}/{0 1 0} facets. The angles of 68.3, 22 and 90° highlighted in the Fig. 5-7f inset are consistent with the theoretical angles between {1 0 1} and {0 0 1}, {2 0 0} and {1 0 1}, and {1 0 0} and {0 0 1} of the anatase crystal, respectively. An equilibrium shape of anatase crystals according to the Wulff construction and the evolved shape with high exposure of {0 1 0} are shown in Fig. 5-7g-h, respectively.[249,250] Fig. 5-7f also shows a 112° angle assigned to the angle between {1 0 1} and {0 0 1} facets,

revealing that the edges of the crystals consist of {0 0 1} and {1 0 1} facets, whereas their central part consist of {0 1 0} facets. Generally, anatase particles preferentially expose {1 0 1} facets as in Fig. 5-7g but TiO_2-Rose films bear a preferential exposure of TiO_2 {0 1 0} facets (Fig. 5-7h). This assignment of facets is shown on a SEM micrograph in Fig. 5-7i.

The composition and chemical state of film surfaces were evaluated using XPS analysis (Table 5-1).

Table 5-1 Atomic percentage (at%) composition of Ti, O and C of TiO_2 photoanodes.

Sample	Ti (at%)	O (at%)	C (at%)
TiO_2-Rose-800	21.9	59.9	18.2
TiO_2-Rose-AD	12.4	31.2	55.7

TiO_2-Rose-AD possess a large amount of carbon on the surface, 55.7 at%, that agrees well with the black color appearance, HR-TEM micrographs and attributed deposited carbon. Conversely, TiO_2-Rose-800 just shows 18.1 at% C, assigned to volatile organic compounds deposited during storage of samples. TGA in air on TiO_2-Rose-AD sample (Fig. 5-8) showed one single predominant step at ~400 °C, indicating the temperature at which carbon deposits burn off in air.

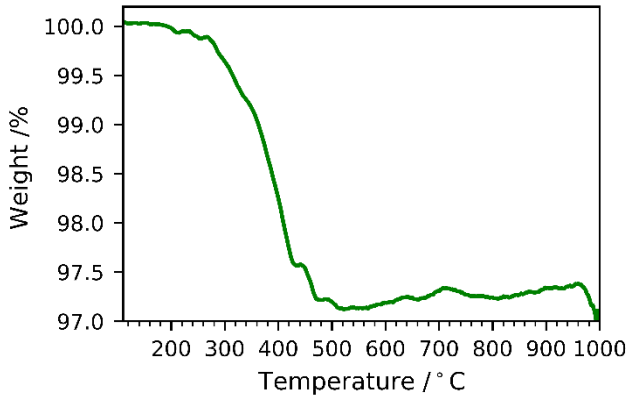

Fig. 5-8 Thermogravimetric analysis (TGA) in air of TiO_2-Rose-AD on FTO-ABS substrate.

Ti 2p high resolution XPS spectra are shown in Fig. 5-9a and corresponding binding energies listed in Table 5-2. In both TiO_2-Rose-AD and TiO_2-Rose-800, the two characteristic peaks of Ti^{4+} in anatase TiO_2 attributed to Ti $2p_{1/2}$ and Ti $2p_{3/2}$ are observed.[251] Interestingly, a shift towards higher binding energies is observed for TiO_2-Rose-AD, indicating the possibility of Ti-O-C bonds in the film.[252] O 1s high resolution XPS spectra are shown in Fig. 5-9b and corresponding binding energies listed in Table 5-2. Three peaks at different binding energies are observed. The main peak at lower binding energies corresponds to crystal lattice O-Ti^{4+} in the TiO_2 lattice structure, whereas the smaller peaks at slightly higher energies are attributed

to hydroxyl groups or adsorbed water on the surface.[199] As observed for Ti 2p, a shift towards higher binding energies is observed for TiO_2- Rose-AD, suggesting that crystal lattice oxygen is also attached to a non-anatase element, supporting the hypothesis of Ti-O-C bonds in the as-deposited samples.[252] Finally, C 1s XPS spectra are shown in Fig. 5-9c. The main peak at 284.8 eV corresponds to C-C bonds whereas the smaller peaks at higher binding energies are assigned to different carbon environments, such as C-OH and C-O-C.[253,254] Interestingly, no additional peaks at ~281.5 eV corresponding to Ti-C are observed for TiO_2-Rose-AD. Therefore, only C-O-Ti bonds are confirmed on TiO_2-Rose-AD films. [252,255] The smaller peaks at ~293 and ~295 eV mainly observed in TiO_2-Rose-800 correspond to K $2p_{3/2}$ and K $2p_{1/2}$, respectively, impurities from the KOH electrolyte used during PEC measurements.[256]

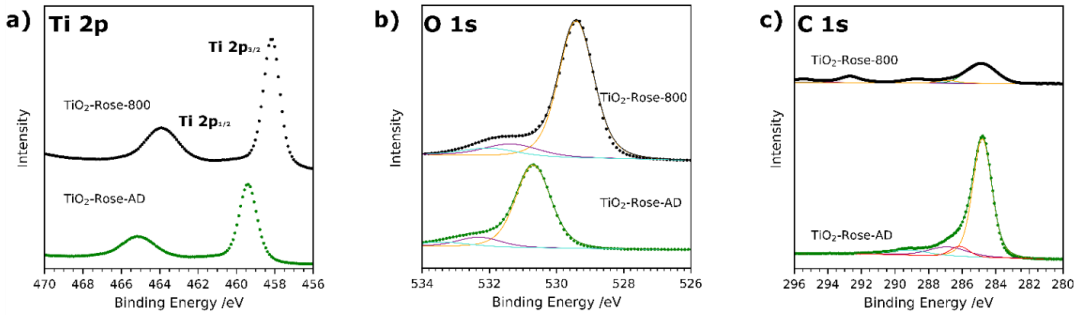

Fig. 5-9 XPS spectra of (a) Ti 2p, (b) O 1s and (c) C 1s of TiO_2-Rose-800 and TiO_2-Rose-AD. Scattered points correspond to raw data acquired in the measurements and solid lines to the fitted values.

Table 5-2 Ti 2p and O 1s of the crystal lattice O-Ti^{4+} binding energies.

Sample	**Ti *2p*$_{1/2}$ /eV**	**Ti *2p*$_{3/2}$ /eV**	**O^{2-} *1s* /eV**
TiO_2-Rose-800	463.9	458.2	529.4
TiO_2-Rose-AD	465.2	459.4	530.7

Fig. 5-10a shows the XRD patterns of both TiO_2-Rose-800 and TiO_2-Rose-AD films on FTO-ABS substrates. All XRD patterns only show the characteristic peaks of tetragonal anatase TiO_2 phase. In particular, the diffraction peaks at 25.2, 48.0, 55.1, 62.8, 75.0 and 76.0 ° (2θ) correspond to (1 0 1), (2 0 0), (2 1 1), (2 0 4), (2 1 5) and (3 0 1) diffraction planes (ICDD-JCPDS 75-1537). These diffraction planes agree with the ones observed in HRTEM micrographs. TC of (1 0 1) and (2 0 0) of TiO_2-Rose samples are listed in Table 5-3.

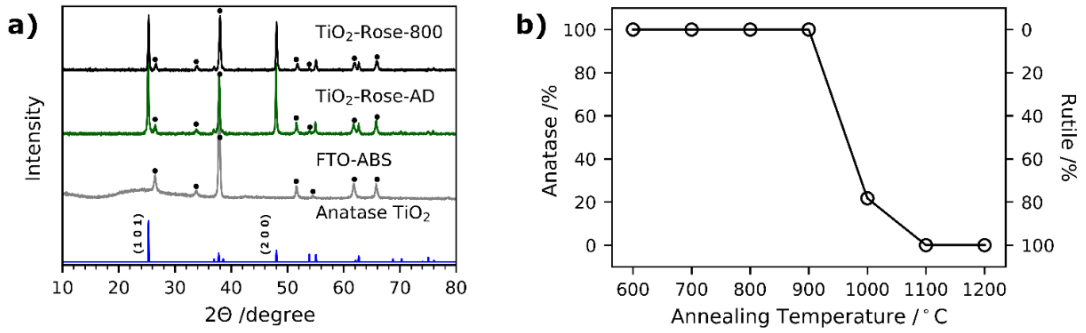

Fig. 5-10 XRD patterns of TiO_2-Rose-800 and TiO_2-Rose-AD photoanodes prepared using $Ti_7O_4(OEt)_{20}$. Standard powder pattern of anatase TiO_2 is shown as well as XRD pattern of FTO-ABS. Dot: FTO-ABS diffraction peak. (b) Percentage of anatase TiO_2 as a function of annealing temperature for TiO_2-Rose photoanodes.

Table 5-3 Texture coefficients for TiO_2-Rose films.

Sample	TC_{101}	TC_{200}
TiO_2-Rose-800	0.51	1.49
TiO_2-Rose-AD	0.61	1.39

The TC_{101} is ~0.55 whereas TC_{200} is ~1.45 for both TiO_2-Rose samples which indicates preferential growth orientation along (2 0 0) diffraction plane. This suggests dominant crystal growth along [0 1 0] direction and exposure of {0 1 0} facets.[229,257,258] The crystal structure of anatase TiO_2 highlighting the crystal planes is shown in Fig. 5-11.

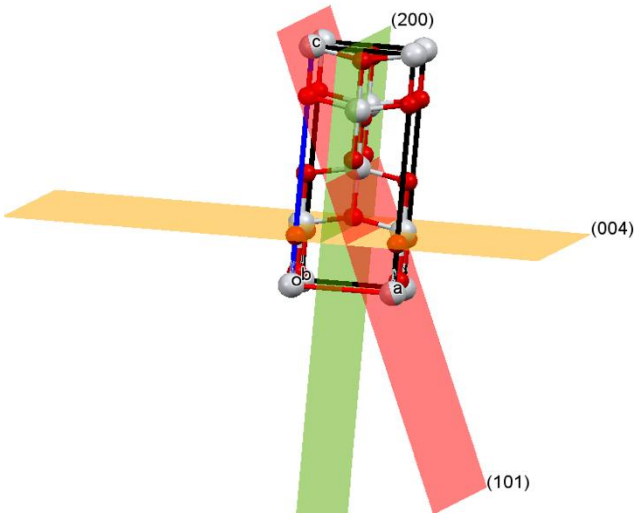

Fig. 5-11 Anatase TiO_2 crystal structure showing different crystal planes: (0 0 4) in orange, (1 0 1) in red and (2 0 0) in green.

The preferred orientation of TiO_2-Rose agrees well with SEM (Fig. 5-3) and HRTEM (Fig. 5-7) micrographs where plate-like sheets and rectangular shape particles are observed, respectively. The diffraction planes together with the morphological analysis carried out in HRTEM micrographs confirm that the TiO_2-Rose films are mainly exposed of {0 1 0} anatase TiO_2 facets with some regions of {1 0 1} and {0 0 1} facets.[229,249,259,260]

None of the diffraction planes shown in Fig. 5-10a are indexed to rutile TiO_2 phase despite annealing at 800 °C, above the typical anatase-to-rutile phase-transformation temperature which is 600 °C for powders and expected to be slightly higher for substrate-constrained films (*ca.* 750 °C).[196,261] To further investigate the maximum temperature until which the metastable but more photocatalytically active anatase phase is preserved, $Ti_7O_4(OEt)_{20}$ precursor was deposited by AACVD on top of alumina substrate at 500 °C and further annealed in air for 2 h at 900-1200 °C. The use of a different support did not affect the final morphology of TiO_2 (Fig. 5-12). The XRD patterns are shown in Fig. 5-13 and the percentage of each phase *vs.* temperature in Fig. 5-10b.

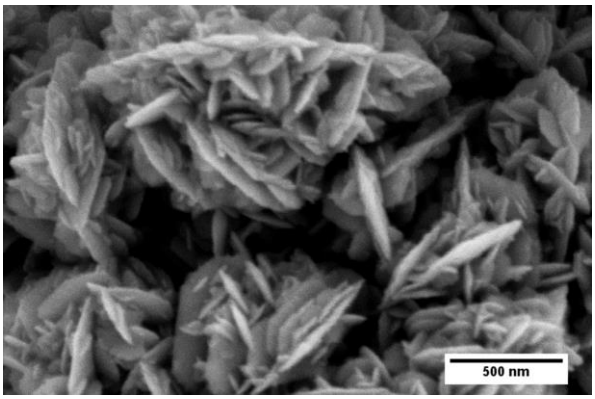

Fig. 5-12 SEM micrograph of TiO_2-Rose deposited on top of alumina at 500 °C.

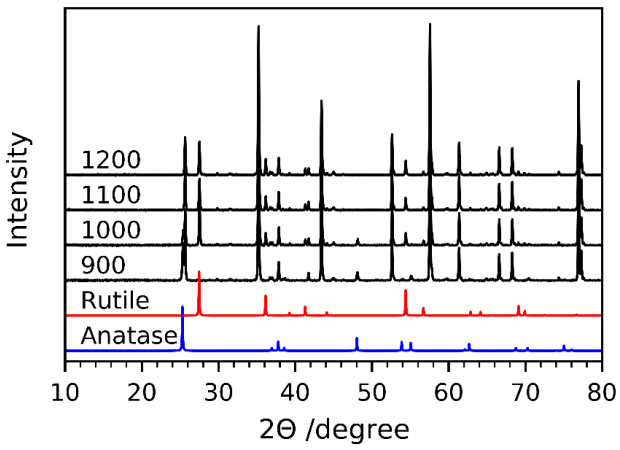

Fig. 5-13 XRD patterns of TiO_2-Rose on alumina substrates. Standard powder patterns of anatase (blue) and rutile (red) TiO_2 are shown for comparison.

TiO_2-Rose shows presence of pure anatase TiO_2 up to 900 °C and a gradual transformation to rutile phase for temperatures of 1000 °C and above (Fig. 5-10b). A high anatase percentage (22 %) is obtained in the film at 1000 °C air annealing. These results reveal that these films achieved using AACVD would offer advantages when used as functional coatings on smart tiles with antibacterial and self-cleaning properties. The ceramics of tiles require temperatures above 900 °C for their preparation, which limits their coating to rutile phase which is less photocatalytically active than anatase.[225]

High-temperature-stable anatase TiO_2 is typically achieved by doping TiO_2 with metal and non-metal ions co-doping (combining both metal and non-metal ions) and by enriching with oxygen, which strengthens Ti-O-Ti bonds and thus delays the transformation to rutile phase.[225] Recently, high-temperature anatase TiO_2 photoanodes have also been synthesized by anodization of titanium foils followed by a solvothermal treatment, keeping stable anatase phase up to 900 °C.[262] The authors attributed the anatase high temperature stability to a phonon confinement effect, typically observed in anatase TiO_2 with small crystallite sizes (~ 30 nm).[263,264] Since neither doping treatment nor oxygen enrichment modifications were undertaken to our TiO_2 samples, coherent crystal domain size calculations and Raman analysis were carried out to further investigate the possibility of this phonon confinement effect on our films. [262,264]

Table 5-4 shows the calculated anatase coherent crystal domain size of TiO_2-Rose photoanodes annealed in air at different temperatures (patterns in Fig. 5-14). The largest domain size is found in the as-deposited sample, 46.6 nm, most likely due to the presence of interstitial carbon in the anatase TiO_2 lattice structure. Substitutional doping of C^{4+} with Ti^{4+} can be discarded owing to the large difference between their ionic radius, being 16 and 61 pm for C^{4+} and Ti^{4+}, respectively.[265] At annealing temperatures ranging from 600 to 800 °C, the domain size is significantly smaller, from 28 to 36 nm, and in the range where phonon confinement can occur.[263,264]

Table 5-4 Anatase coherent crystal domain size of TiO_2-Rose after annealing in air at different temperatures.

Annealing T (°C) [a]	**Size (nm)**
AD	46.6
600	27.6
700	34.3
800	35.9
900	44.6
1000	47.4

1100[b]	62.3
1200[b]	61.1

[a] XRD performed on FTO substrates for all samples except 1000 °C, that was performed on alumina substrates.

[b] It corresponds to the rutile coherent crystal domain size calculated at (110) diffraction plane. Anatase TiO_2 is not present at these temperatures.

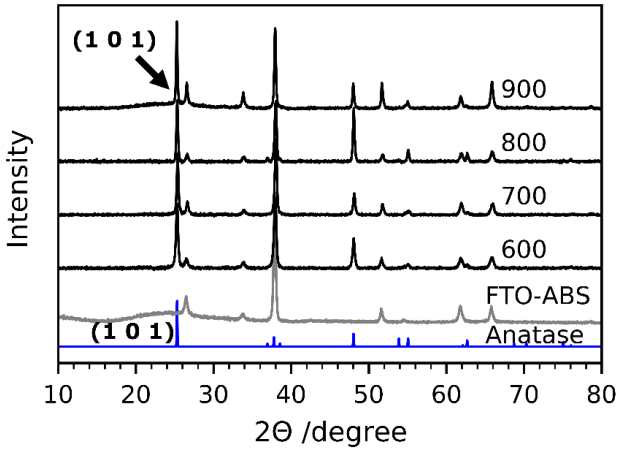

Fig. 5-14 XRD patterns of TiO_2-Rose films prepared using $Ti_7O_4(OEt)_{20}$ and deposited on FTO-ABS substrate. Standard powder pattern of anatase (blue) TiO_2 and FTO-ABS is also shown.

We attribute this reduction in size to the removal of interstitial carbon present in as-deposited samples. Moreover, the presence of amorphous carbon in the anatase TiO_2 grain boundaries must also have limited the TiO_2 domain sizes.[265,266] Amorphous carbon in the interface of TiO_2 crystals was confirmed in HRTEM micrographs of TiO_2-Rose-AD (inset of Fig. 5-7(e-f)) and by XPS analysis, where Ti-O-C bonds were observed. Above 900 °C, grain boundary restrictions disappear and anatase TiO_2 domain sizes grow up to ~50 nm owing to sintering of cyrstals.[210,211] This crystal domain growth is accompanied by a transformation from anatase to rutile (Fig. 5-10b).

Raman spectroscopy was carried out to further confirm the possibility of phonon confinement. As previously reported in literature a shift of the E_g Raman mode at 144 cm^{-1} of anatase TiO_2 towards lower wavenumber supports the phonon confinement model of high-temperature anatase TiO_2.[262,264] Fig. 5-15 shows the Raman spectra of TiO_2-Rose annealed at different temperatures (600 to 900 °C) confirming the shift towards lower wavenumber values when annealing temperature is increased. This Raman shift along with the calculated anatase coherent crystal domain size around 30 nm supports that high-temperature anatase TiO_2 may be achieved through phonon confinement effects, in addition to substrate constraint effects.

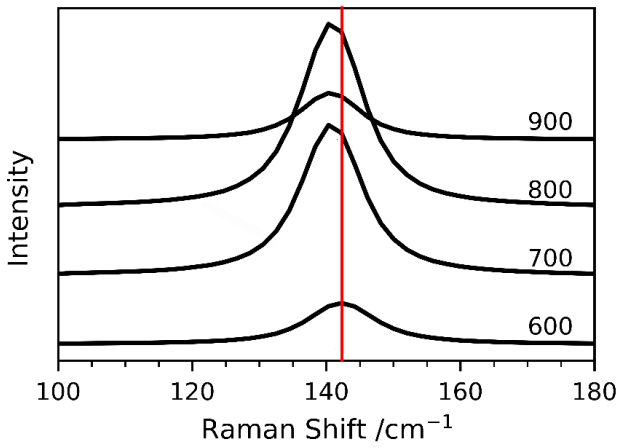

Fig. 5-15 Raman spectra of E_g Raman mode of anatase TiO_2 (144 cm^{-1}) for TiO_2-Rose prepared using $Ti_7O_4(OEt)_{20}$ precursor and annealed at 600, 700 800 and 900 °C for 2 h in air.

Fig. 5-16 shows the Raman spectra of TiO_2-Rose films. In all cases, only Raman bands ascribed to tetragonal anatase TiO_2 are observed, in agreement with XRD patterns. Particularly, the sharp bands at *ca.* 144, 198, 400, 520 and 640 cm^{-1} correspond to E_g, E_g, B_{1g}, B_{1g} and E_g Raman vibration modes of anatase TiO_2, respectively.[267] Two additional bands at *ca.* 1340 and 1590 cm^{-1} appear for TiO_2-Rose-AD only, assigned to D and G bands of graphitic carbon structures (Fig. 5-16b).[268] These results agree well with XPS and HRTEM, where Ti-O-C bonds and amorphous carbon layers were observed for TiO_2-Rose-AD.

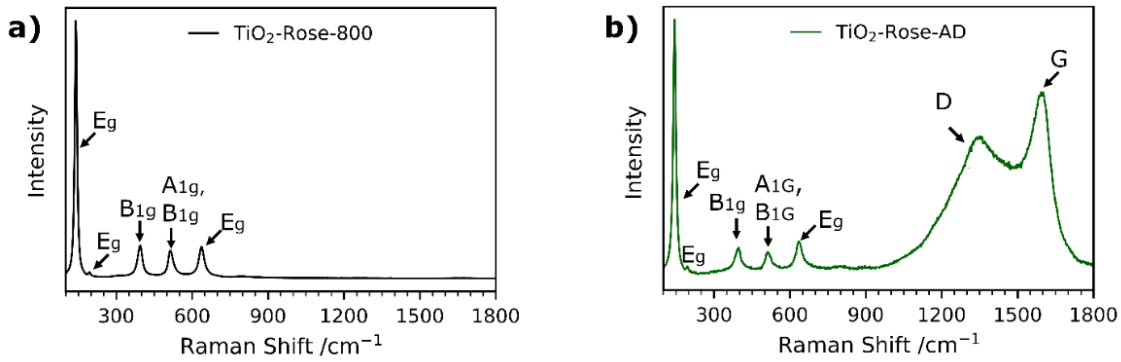

Fig. 5-16 Raman spectra of (a) TiO_2-Rose-800 and (b) TiO_2-Rose-AD photoanodes.

UV- Vis spectroscopy measurements for TiO_2-Rose-800 and TiO_2-Rose-AD are shown in Fig. 5-17. As expected, a clear absorption edge at ~400 nm is observed for TiO_2-Rose-800, whereas lower transflectance values at higher wavelengths with no clear absorption edge is observed for TiO_2-Rose-AD owing to carbon coverage.

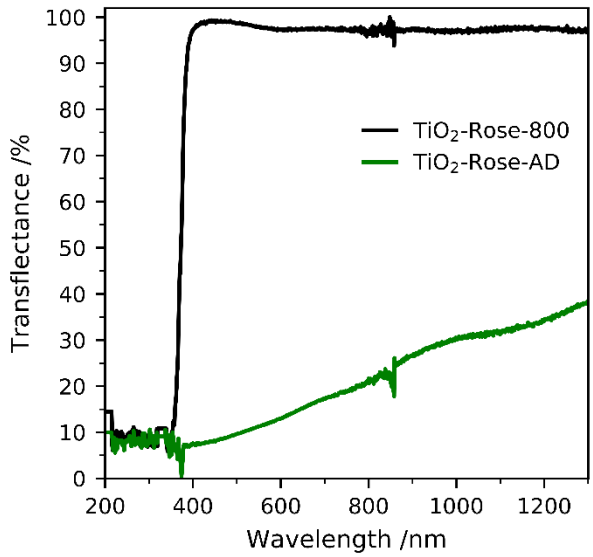

Fig. 5-17 UV-Vis spectra of TiO_2-Rose-800 and TiO_2-Rose-AD on quartz substrates.

Photoelectrochemical characterization

PEC performance of TiO_2-Rose films on FTO-ABS substrates was evaluated. No PEC activity was observed for TiO_2-Rose-AD when irradiated (Fig. 5-18), which we ascribe to the carbon residues coverage and consequent light shielding.

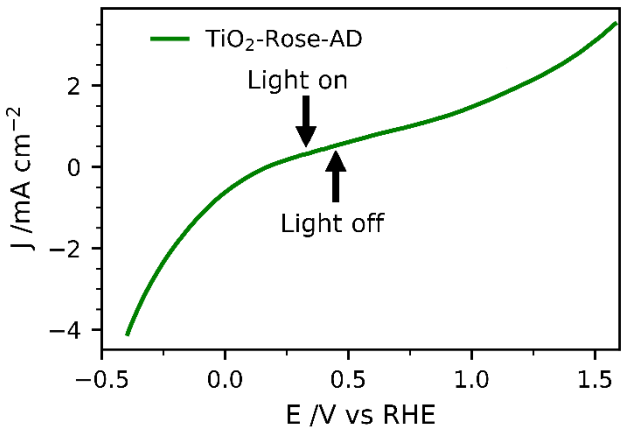

Fig. 5-18 Photocurrent potential curves of TiO_2-Rose-AD and TiO_2-AD under 1 sun chopped illumination (AM 1.5G, 100 mW cm^{-2}) in 1M KOH (pH=13.7) solution.

However, TiO_2-Rose-800 shows high PEC response −a photocurrent plateau of ~ 0.67 mA cm^{-2} with simulated sunlight (Fig. 5-19a) and 3.0 mA cm^{-2} with UV light (365 nm, 3.6 mW cm^{-2}, Fig. 5-19b). Photostability measurements for 2 days including some recovery periods in the dark are shown in Fig. 5-19c. After 24 h of continuous light irradiation, 70 % of the total photocurrent is still maintained and a 6 h period in the dark recovers 15 % of original photocurrent. The photocurrent decrease is assigned to photocorrosion with photogenerated electrons and holes trapped in the structure.[269] Actually, during the irradiation time the TiO_2

changed color from white to brownish, attributed to the reduction of Ti^{4+} to Ti^{3+} by trapped photogenerated electrons (Fig. 5-19c inset).[269] During the recovery period in the dark, the TiO_2 becomes white again, due to the back oxidation to Ti^{4+} with atmospheric oxygen, recovering some PEC activity.

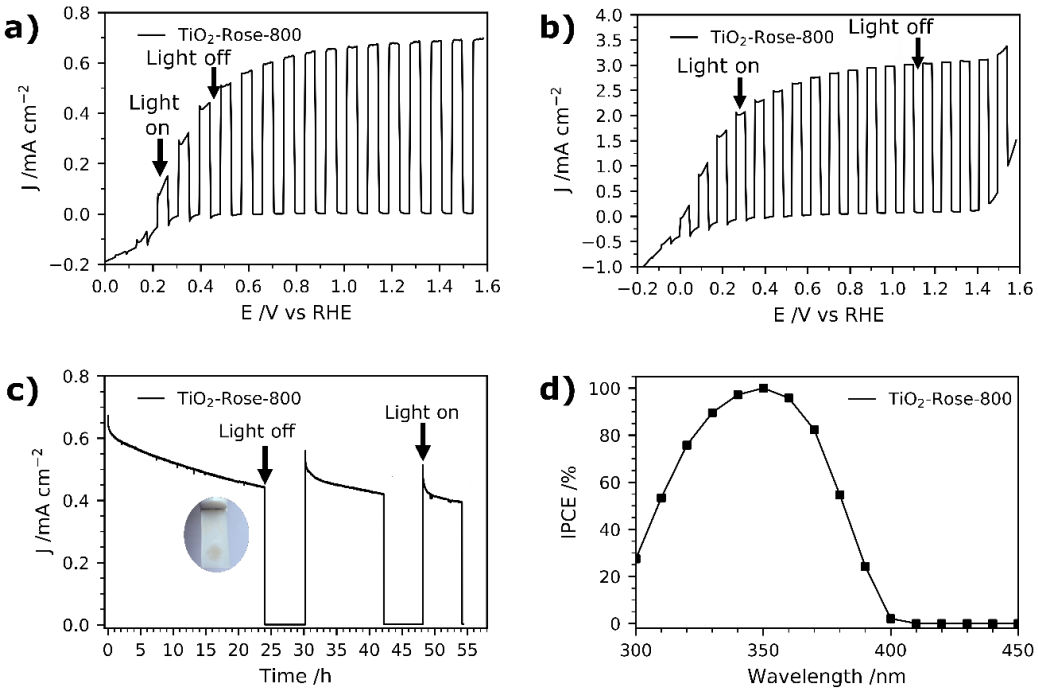

Fig. 5-19 (a) Photocurrent potential curves of TiO_2-Rose-800 under 1 sun chopped illumination (AM 1.5G, 100 mW cm^{-2}). (b) Photocurrent potential curves of TiO_2-Rose-800 under UV chopped illumination (365nm, 3.6 mW cm^{-2}). (c) Photocurrent-times curves of TiO_2-Rose-800 at an applied bias of 1.23 V_{RHE} under 1 sun illumination (AM 1.5G, 100 mW cm^{-2}). Inset shows a photograph of the photonanode with a darkened circular area due to 24 h irradiation. (d) IPCE spectra at 1.23 V_{RHE} of TiO_2-Rose-800. All measurements were performed at 1 M KOH (pH=13.7) from back-side illumination.

IPCE values for TiO_2-Rose-800 start to increase from 400 nm and reach a remarkable 100 % at 350 nm (Fig. 5-19d). Below 350 nm wavelengths IPCE values decrease due to FTO-ABS substrate light absorption, as confirmed by transmittance measurements on FTO-ABS substrates (Fig. 5-20a). The use of front-illumination avoids such decrease at wavelengths below 350 nm, but maximum IPCE values are then 67 % due to a longer electron path where more electron-hole recombination can occur (Fig. 5-20b).[270,271]

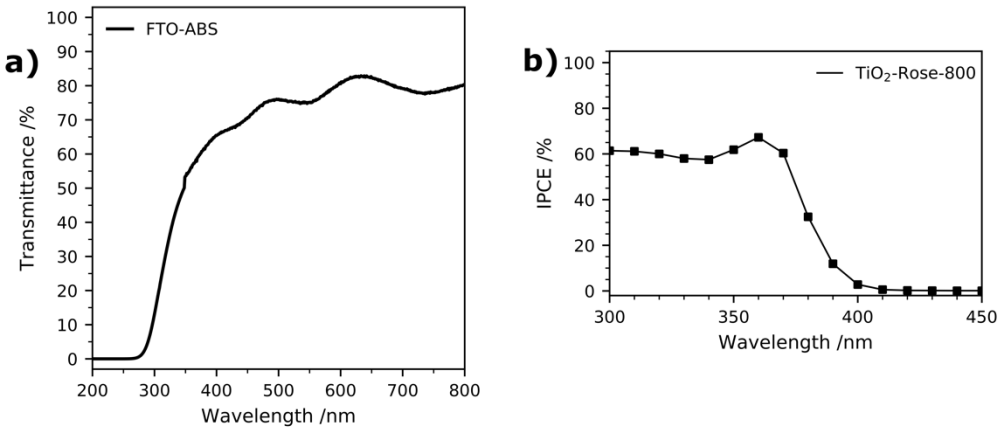

Fig. 5-20 (a) UV- Vis spectrum of FTO-ABS substrate. (b) Front-side IPCE spectra at 1.23 V_{RHE} of TiO_2-Rose-800 in 1M KOH (pH=13.7).

Integrating the product of the IPCE curve (Fig. 5-19d) and the photon intensity in the AM 1.5 G solar spectrum results in a photocurrent density value of 0.9 mA cm^{-2} at 1.23 V_{RHE}, which is slightly higher than the 0.67 mA cm^{-2} obtained in J-V and J-time curves at 1.23 V_{RHE} (Fig. 5-19a and Fig. 5-19d). This variation is attributed to a spectral mismatch between the simulated sunlight (filtered Xe source) used in the J-V and J-time measurements and the real AM 1.5 G solar spectrum used in the IPCE integration.[224] These high IPCE and integrated photocurrent values further confirm the excellent performance of these rose-like shaped photoanodes prepared using $Ti_7O_4(OEt)_{20}$ oxo clusters.

To further understand why the as-deposited dark TiO_2 samples (TiO_2-Rose-AD) show no PEC activity, as compared to those post annealed at 800 ˚C in air (TiO_2-Rose-800), we investigated the charge carrier dynamics (i.e., mobility and lifetime) of these samples deposited onto quartz substrates, by TRMC. This technique probes the generation and decay of mobile charges upon pulsed irradiation at various wavelengths (350, 650 and 1200 nm).

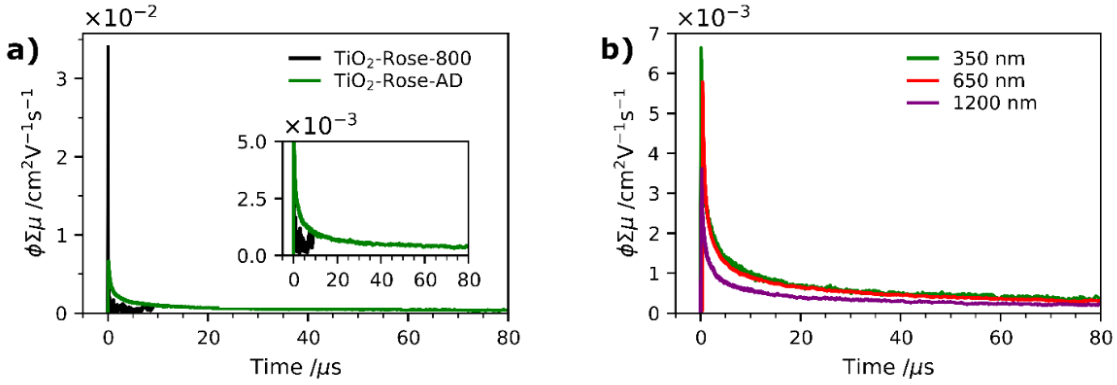

Fig. 5-21 Time resolved microwave conductance signals for TiO_2-Rose-800 and TiO_2-Rose-AD films using a 350 nm laser pulse with a photon flux of 3.97 x 10^{13} photons $cm^{-2}pulse^{-1}$. (b) Time resolved microwave conductance signals for TiO_2-Rose-AD recorded using 350, 650 and 1200 nm laser pulses with a photon flux of 3.97 x 10^{13}, 2.01 x 10^{14} and 1.22 x 10^{14} photons cm^{-2} $pulse^{-1}$, respectively.

Fig. 5-21a shows the microwave conductance transients of TiO_2-Rose-800 and TiO_2-Rose-AD after a 3 ns laser pulse of 350 nm with a photon flux of 3.97 x 10^{13} photons $pulse^{-1}$ cm^{-2}, in which we are probing the charge dynamics for excitation energies above the band gap of anatase TiO_2 (3.2 eV). It has been previously reported that the TRMC signal from TiO_2 is predominately a measure of electron mobility and lifetime, since holes are rapidly trapped.[241,272] A strong initial TRMC signal ($\varphi\Sigma\mu$) for TiO_2-Rose-800 (3.40 x 10^{-2} cm^2 V^{-1} s^{-1}) indicates higher electron mobilities compared to the moderate signal of TiO_2-Rose-AD (6.64 x 10^{-3} cm^2 V^{-1} s^{-1}) at equivalent photon flux. Interestingly, the TRMC signal decays for the two samples are different. As shown in Fig. 5-22a, the TRMC signal for the TiO_2-Rose-800 sample can be fitted with a combination of an exponential decay (< 100 ns) with a time constant τ of 13 ns and a power law decay (> 100 ns) with a decay exponent of ~0.5. The exponential decay is assigned to band-to-band recombination pathway, while the power law decay can be attributed to trap-limited bimolecular recombination mechanism.[273–276] In contrast, the TRMC signal for the TiO_2-Rose-AD sample can be fitted with only a power law decay with a decay exponent of ~0.5 (Fig. 5-22b); only trap-limited bimolecular recombination occurs in this sample. This behavior is consistent with the relatively constant mobility and similar decay kinetics at various light intensities (Fig. 5-23).

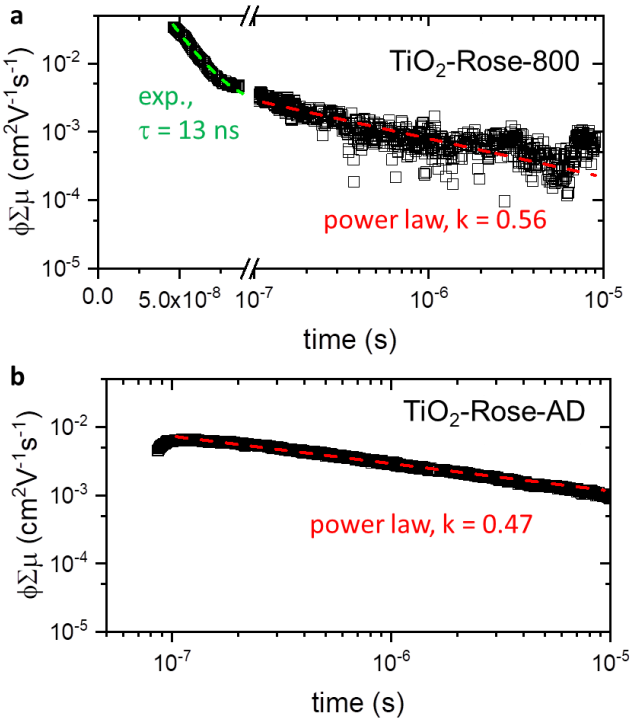

Fig. 5-22 Fitted curves of time resolved microwave conductance signals for (a) TiO_2-Rose-800 and (b) TiO_2-Rose-AD using a 350 nm laser pulse with a photon flux of 3.97 x 10^{13} photons cm^{-2} $pulse^{-1}$.

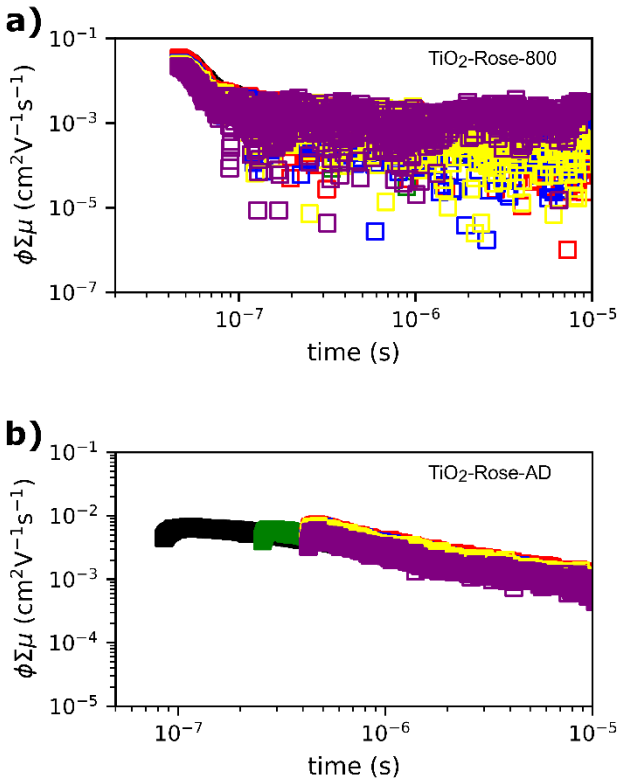

Fig. 5-23 Time-resolved microwave conductance signals for (a) TiO_2-Rose-800 and (b) TiO_2-Rose-AD using a 350 nm laser pulse with various photon flux intensities: 3.97 x 10^{13} (black), 3.11 x 10^{13} (green), 2.0 x 10^{13} (red), 1.80 x 10^{13}(blue), 1.36 x 10^{13}(yellow) and 1.15 x 10^{13} (purple) photons cm^{-2} $pulse^{-1}$.

TRMC measurements were also performed at longer wavelengths of 650 and 1250 nm. Since these wavelength energies are lower than the band gap of TiO_2, these measurements effectively probe the photogenerated charges that can reside within the band gap. Expectedly, no TRMC signal for TiO_2-Rose-800 sample was observed for these excitation wavelengths. However, a clear TRMC transient signal for TiO_2-Rose-AD (Fig. 5-21b) was observed for both 650 and 1200 nm excitation wavelengths. The mobility slightly decreases with increasing wavelength (5.78 x 10^{-3} and 3.61 x 10^{-3} cm^2 V^{-1} s^{-1} for the 650 and 1200 nm excitation, respectively), but the decay still follow the same power law mechanism (see Fig. 5-24). We attribute this to the carbon impurities embedded in the un-annealed samples that introduce localized electron trapping states, delaying the electron and hole recombination, but also minimalizing charge mobility.[277] These localized states sit at energetic positions deep within the band gap of anatase TiO_2. Therefore, photogenerated charge carriers in the carbon doped TiO_xC_y (TiO_2-Rose-AD) samples will not sit below the water oxidation potential, nor have a high enough photovoltage to achieve photoactivity for water splitting. This explains the absence of photocurrent from this sample (Fig. 5-18).

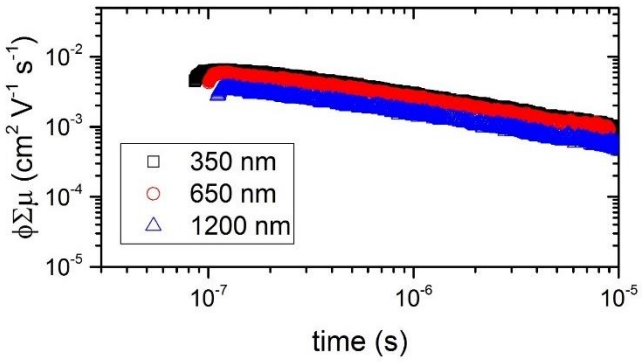

Fig. 5-24 Time resolved microwave conductance signals for TiO_2-Rose-AD using a 350, 650 and 1200 nm laser pulse with a photon flux of 3.97 x 10^{13}, 2.01 x 10^{14} and 1.22 x 10^{14} photons cm^{-2} pulse^{-1}, respectively.

Fig. 5-25 shows a schematic representation of the processes occurring in the two different samples. The main difference between the two is in the absence of band-to-band recombination for the TiO_2-Rose-AD sample. This suggests that carriers, even after excitation beyond the band gap, rapidly decay into the trap states, which later do not contribute to any photocurrent. Our observations are in agreement with surface photovoltage (SPV) measurements of carbon-doped titania which elucidated deep-isolated and catalytically-poor trap states.[278,279]

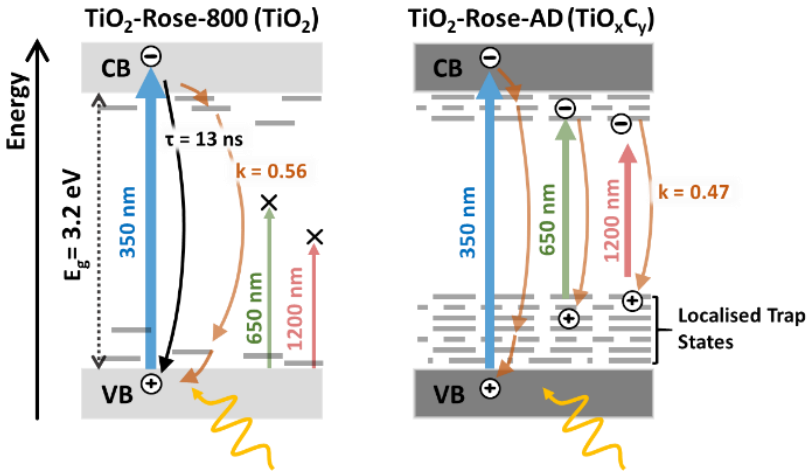

Fig. 5-25 Schematic diagram representing the difference in the photo-generated charge carrier dynamics for TiO_2-Rose-800 and TiO_2-Rose-AD when excited with 350, 650 or 1200 nm laser pulses with a photon flux of 3.97 x 10^{13}, 2.01 x 10^{14} and 1.22 x 10^{14} photons cm^{-2} pulse^{-1}, respectively.

EIS measurements under simulated sunlight were carried out to understand charge transfer processes in the photoanodes. Fig. 5-26a shows Nyquist plots along with the equivalent circuit used, which include a R_1/CPE_1 pair which describes the semiconductor resistance and capacitance at the depletion layer and a second R_2/CPE_2 pair for the resistance and capacitance of the semiconductor at the interface between the electrolyte and photoanode (Helmholtz layer).[280] Based on the obtained fitted results, TiO_2-Rose-800 photoanode has resistance values of 35.6 Ω for R_1 and 821 Ω for R_2. The small resistance values suggest a better

separation efficiency and faster transfer rate for photogenerated electrons and holes at the electrode/electrolyte interface.[280,281] This good charge-transfer properties agree well with *J-V* curves, where high photocurrent performances are obtained for TiO_2-Rose-800.

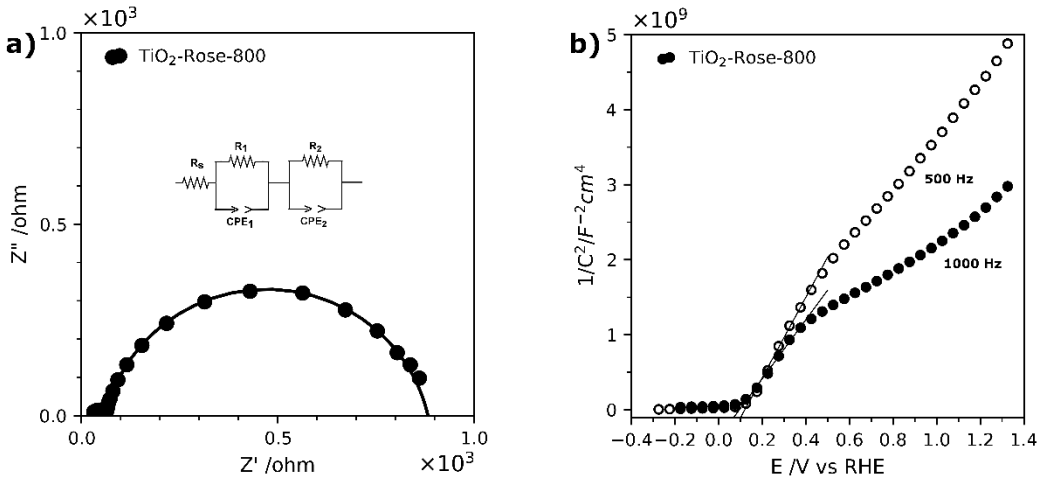

Fig. 5-26 (a) Nyquist plots of TiO_2-Rose-800 at the open circuit potential (OCP) of the cell under 1 sun illumination (AM 1.5G, 100 mW cm^{-2}). (b) Mott-Schottky plots at a fixed frequency of 500 Hz and 1000Hz of TiO_2-Rose-800 in 1M KOH (pH=13.6).

EIS measurements in the dark were carried out to characterize the intrinsic properties of the photoanodes, such as carrier densities (N_D) and flat-band potentials. The EIS data were acquired in the form of Mott-Schottky plots at 500 and 1000 Hz, as shown in Fig. 5-26b. Plots indicate that the sample possess a positive slope, typical of n-type semiconductors.[138] The flat-band potentials, obtained from the X-axis intercept of the Mott-Schottky plots, shows a very small variation of $0.02\ V$ between the two frequencies, which indicates a very low frequency dispersion and true measured value for the flat-band potential.[282] A flat-band potential of 0.12 V_{RHE} and an electron carrier density of 6.43 x 10^{18} cm^{-3} were calculated at 500 Hz. Similar flat-band potential values have been previously reported in literature for nanostructured TiO_2 photoanodes.[138]

O_2 evolution measurements at 1.23 V_{RHE} were carried out for TiO_2-Rose-800 and results are shown in Fig. 5-27. Fig. 5-28 shows the Intensity-time curve obtained during the measurements. The amount of O_2 gas evolved was accumulated inside the cell, and thus O_2 content increased over time. The calculated Faradaic efficiency for TiO_2-Rose-800 photoanodes is ~90 % at the end of the oxygen measurement, providing further evidence that these photoanodes have high activity for oxygen evolution.

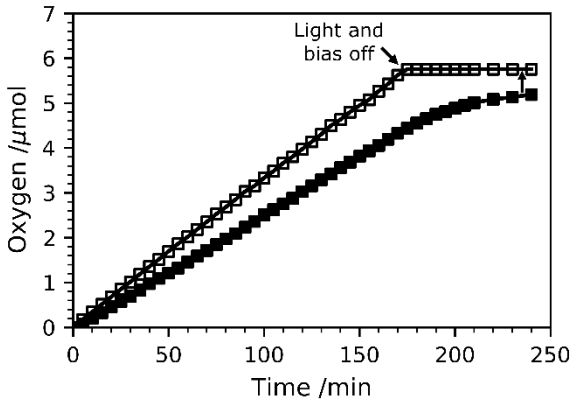

Fig. 5-27 Amount of O_2 gas evolved at 1.23 V_{RHE} under simulated sunlight (AM 1.5G, 100 mW cm^{-2}). The amount of O_2 quantified with a fluorescence probe is represented by solid markers, whereas the theoretical amount of O_2 calculated assuming a 100 % Faradaic efficiency is shown with empty markers.

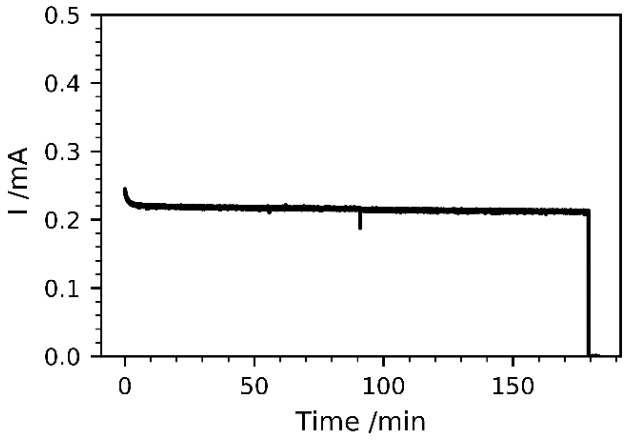

Fig. 5-28 Photocurrent-time curve of TiO_2-Rose-800 obtained during the O_2 measurement experiment at 1.23 V_{RHE}. Simulated sunlight is switched off after 180 min.

Precursor dependence

TiO_2 photoanodes using $Ti(OEt)_4$ as a starting precursor at two different concentrations have also been prepared for comparison. Fig. 5-29 shows SEM micrographs of both TiO_2 photoanodes. Randomly distributed particles of irregular shape are observed for the 0.35 M deposition (TiO_2-0.35M-800) while plate-like particles are observed for the 0.05 M deposition (TiO_2-0.05M-800). As expected, thicker films were obtained when using a 0.35 M solution of $Ti(OEt)_4$. Importantly, the desert-rose morphology is not achieved in any, which indicates that the desert rose morphology is unique to the use of $Ti_7O_4(OEt)_{20}$ precursor.

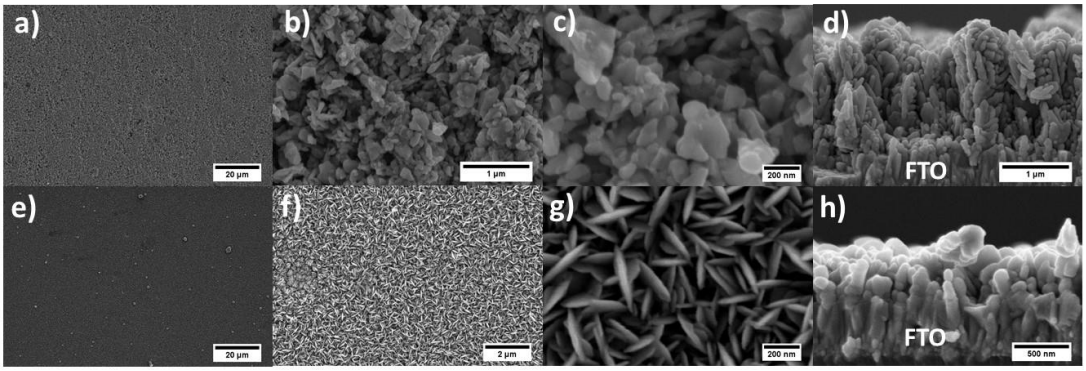

Fig. 5-29 SEM micrographs at different magnifications of (a-d) TiO_2-0.35M-800 photoanodes and (e-h) TiO_2-0.05M-800 photoanodes on top of FTO-substrates.

Their optical properties were compared. Fig. 5-30 shows the Kubelka-Munk function *F(R)* of diffuse reflectance UV-Vis spectra, related to the absorption coefficient (α).[32] TiO_2-Rose-800 shows the highest absorption coefficient at 350 nm, followed by TiO_2-0.35M-800 and TiO_2-0.05M-800. Therefore, the spectra indicate that the desert rose like films absorb the most light, ascribed to their higher film density and thickness.

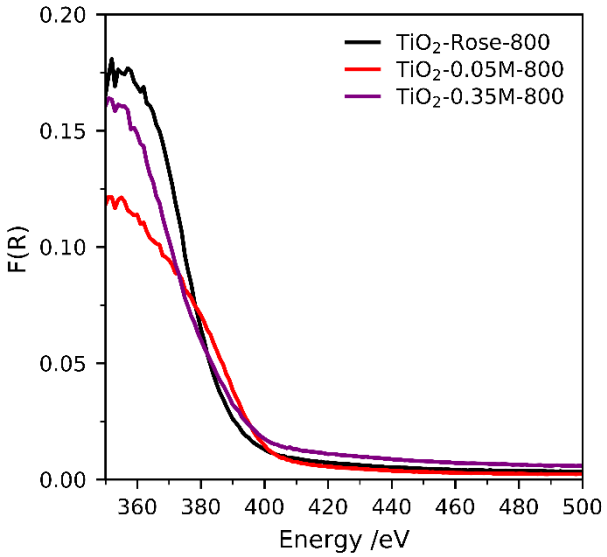

Fig. 5-30 Diffuse reflectance UV-Vis spectra of TiO_2-Rose-800, TiO_2-0.05M-800 and TiO_2-0.35M-800.

Their XRD patterns are shown in Fig. 5-31 showing anatase phase in all the cases. Importantly, the preferred orientation observed for TiO_2-Rose-800 towards the (2 0 0) diffraction plane is no longer observed for TiO_2-0.05M-800 and TiO_2-0.35M-800 films, indicating again that the desert rose morphology with {0 1 0} facets exposed parallel to the FTO-ABS substrate is unique to the use of $Ti_7O_4(OEt)_{20}$ clusters.

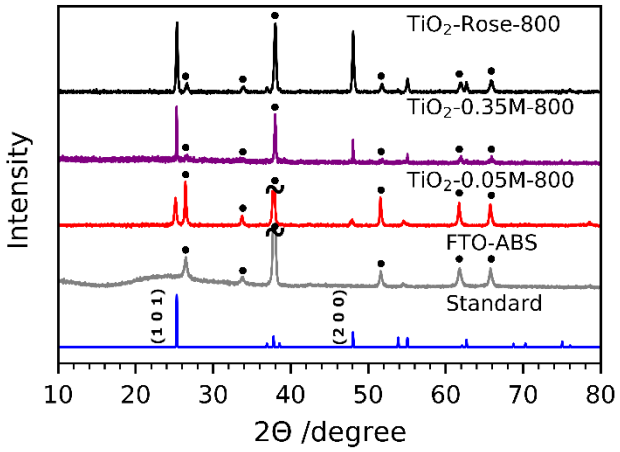

Fig. 5-31 XRD patterns of TiO_2-Rose-800, TiO_2-0.05M-800 and TiO_2-0.35M-800 films on FTO-ABS substrate. Standard powder patterns of anatase TiO_2 (blue) and FTO-ABS (grey) are also shown for comparison.

Finally, PEC and IPCE performances are shown in Fig. 5-32 and Fig. 5-33. TiO_2-Rose-800 exhibits the highest PEC performance at all applied voltages, but specially at low voltages, indicating a better potential onset which we assign to its unique morphology. Furthermore, TiO_2-Rose-800 also has the highest IPCE performance at 1.23 V_{RHE} (Fig. 5-32b).

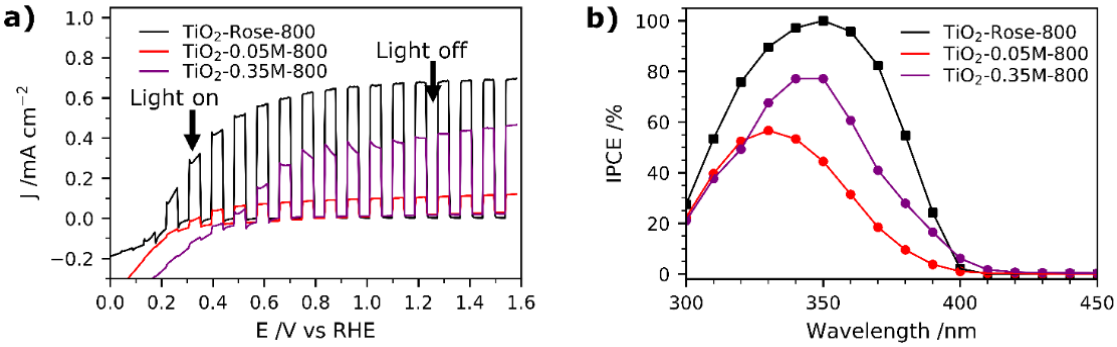

Fig. 5-32 (a) Photocurrent potential curves of TiO_2-Rose-800, TiO_2-0.05M-800 and TiO_2-0.35M-800 under 1 sun chopped illumination (AM 1.5G, 100 mW cm^{-2}). (b) IPCE spectra at 1.23 V_{RHE} of TiO_2-Rose-800, TiO_2-0.05M-800 and TiO_2-0.35M-800. All measurements were performed in 1M KOH (pH=13.7).

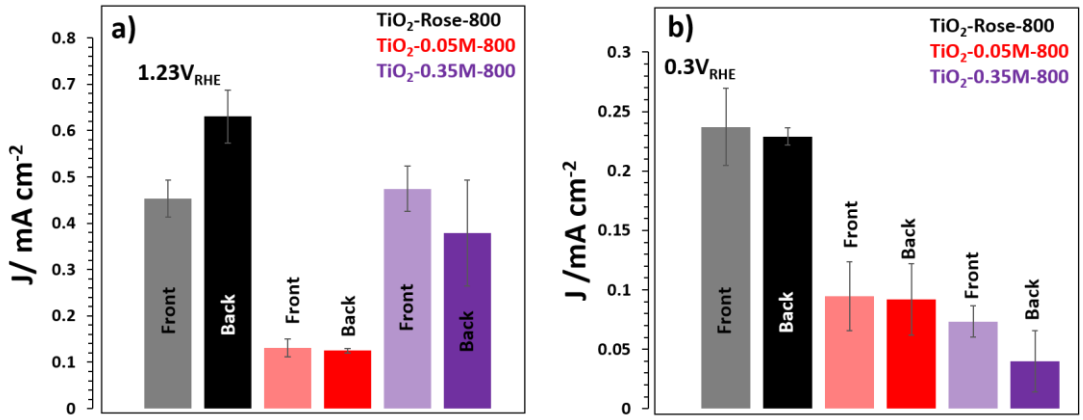

Fig. 5-33 Photocurrent obtained using front and backside illumination for TiO_2-Rose-800, TiO_2-0.05M-800 and TiO_2-0.35M-800 at (a) 1.23 V_{RHE} and (b) 0.3 V_{RHE}.

The significant PEC performance of TiO_2-Rose-800, which reaches 100% IPCE, is mainly attributed to the desert-rose morphology and exposure of {0 1 0} facets at multiple layers. Comparison to TiO_2-0.05M-800 and TiO_2-0.35M-800, which lacks {0 1 0} exposure supports this assignment as well as related literature on the activity of different TiO_2 facets.[132] As revealed by Pan *et al.*, anatase crystals with larger exposure of {0 1 0} facets possess the highest photocatalytic activity owing to the combination of 100% coordinated Ti_{5c} atoms on the surface and a more favorable CB position.[132] The combination of these two factors allows all photogenerated electrons be efficiently transferred via surface Ti_{5c} atoms, reducing the probability of electron-hole recombination and thus improving the PEC performance.[132] Moreover, as revealed in the cross-sectional SEM micrographs of TiO_2-Rose-800, each rose grows perpendicularly to the FTO-ABS substrate, leaving a small gap between each flower for the electrolyte to permeate while exposing multiple layers of TiO_2 {0 1 0} facets per substrate area. This desert-rose characteristic morphology, with multiple plate-like sheets growing from the stem of the flower, also contribute to a superior light scattering and absorption in comparison to more irregular morphologies such as the ones found for TiO_2-0.05M-800 and TiO_2-0.35M-800 samples.[226]

It is believed that the formation of this specific desert-rose morphology arises from the different chemical structure of $Ti_7O_4(OEt)_{20}$ in comparison to $Ti(OEt)_4$ when used as AACVD precursor. For instance, $Ti_7O_4(OEt)_{20}$ precursor has a condensation degree of 0.57 (O/Ti=4/7) unlike 0 (nul) in $Ti(OEt)_4$. It consists of seven TiO_6 octahedra units that form a titanium oxo core which is surrounded by a large number of ethoxide groups, whereas the $Ti(OEt)_4$ lacks such titanium oxo core.[248] Such a different chemical structure might result in a completely different decomposition path during the AACVD deposition. To confirm the different decomposition, we carried out TGA analysis of $Ti_7O_4(OEt)_{20}$. Fig. 5-34a shows that the thermal decomposition of $Ti_7O_4(OEt)_{20}$ occurs in three main steps at 224, 277 and 331 °C giving rise to a mass of 27.4% for the decomposition residue (TiO_2). The biggest weight loss

(51.1%) from *ca.* 100 to 225 °C corresponds mainly to decomposition of alkoxy ligands and formation of fragments containing titanium oxide species.[283] In contrast, the TGA pattern of $Ti(OEt)_4$ shows that decomposition occurs in one single step at ~160 °C (Fig. 5-34b).

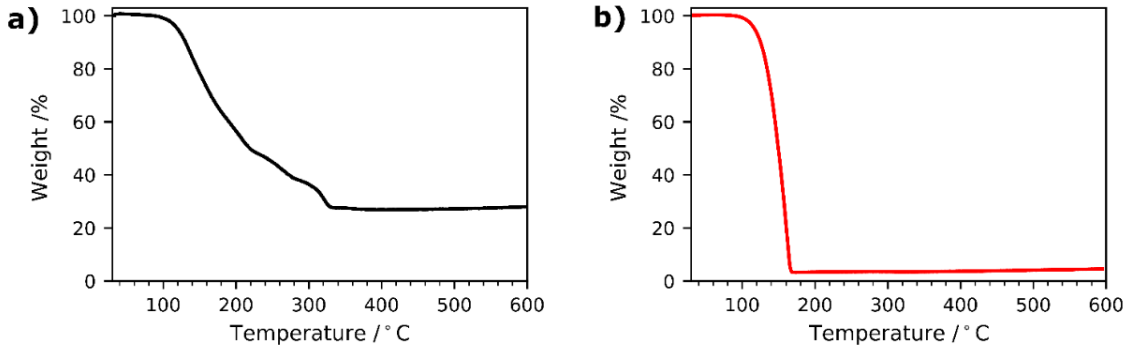

Fig. 5-34 Thermogravimetric analysis (TGA) in Ar of (a) $Ti_7O_4(OEt)_{20}$ and (b) $Ti(OEt)_4$.

Conclusions

We have demonstrated the growth of nanostructured TiO_2 films having a morphology like the crystals of gypsum, sand and water found in nature, known as desert roses. This morphology was successfully grown by AACVD of $Ti_7O_4(OEt)_{20}$ with N_2 as a carrier. The desert-rose TiO_2 consists of plate-like particles with preferential exposure of {0 1 0} anatase TiO_2 facets, further confirmed by analyzing lattice fringes on the surface. Roses grow perpendicular to substrates such as FTO or alumina, offering an excellent substrate coverage with multiple layers of plate-like TiO_2 per substrate area. In addition, desert-rose TiO_2 show a high preservation of the metastable anatase phase despite annealing in air at very high temperatures, even 1000 °C. Rutile phase only appears above 900 °C, unlike typical 600 °C threshold. Such feature could be exploited in smart tiles with antibacterial and self-cleaning properties, whose ceramics require high temperature preparation. When desert-rose TiO_2 films are deposited on FTO-ABS substrates and annealed in air, they offer excellent photoelectrochemical performance as photoanodes for oxygen evolution in aqueous electrolytes. Photocurrent plateaus of ~0.67 mA cm^{-2} under simulated sunlight (100 mW cm^{-2}) or 3.0 mA cm^{-2} under 365 nm UV light (3.6 mW cm^{-2}) are achieved as well as an IPCE of ~100% at 350 nm. Such remarkable performance is attributed to an excellent morphology, preferential exposure of {0 1 0} TiO_2 facets and, upon calcination, the minimization of surface states that would otherwise trap photoinduced charge carriers. On balance, we have extended the use of metal oxo/alkoxy clusters to AACVD for functional coatings, discovering a novel and simple strategy to obtain a faceted semiconductor without the use of dopants. These results will trigger research in using

metal oxo clusters in the preparation of efficient, nanostructured and stable photoelectrodes, as well as, other possible components of energy devices.

Conflicts of interest

There are no conflicts to declare.

Acknowledgements

The authors would like to acknowledge both EPSRC for funding the Centre for Doctoral Training in Sustainable Chemical Technologies at the University of Bath (EP/L016354/1) and the Material and Chemical Characterisation facility (MC^2) at the University of Bath. SE would like to acknowledge the financial support from EPSRC (EP/P008097/1).

All data created during this research are openly available from the University of Bath data archive at https://doi.org/10.15125/BATH-00644

5.1.5 Commentary

5.1.5.1 Influence of post-annealing and deposition temperature on the PEC performance

The PEC performance of photoanodes was also evaluated as a function of annealing temperature. As previously discussed in Section 5.1.4, the optimal annealing temperature in terms of photocurrent density for TiO_2-Rose photoanodes deposited at 500 °C for 1 h in toluene was found to be 800 °C for 2 h. Fig. 5-35 shows additional photocurrent density values obtained using front and backside illumination at 1.23 V_{RHE} of TiO_2-Rose photoanodes annealed at different temperatures (500 to 800 °C) for 2 h in air.

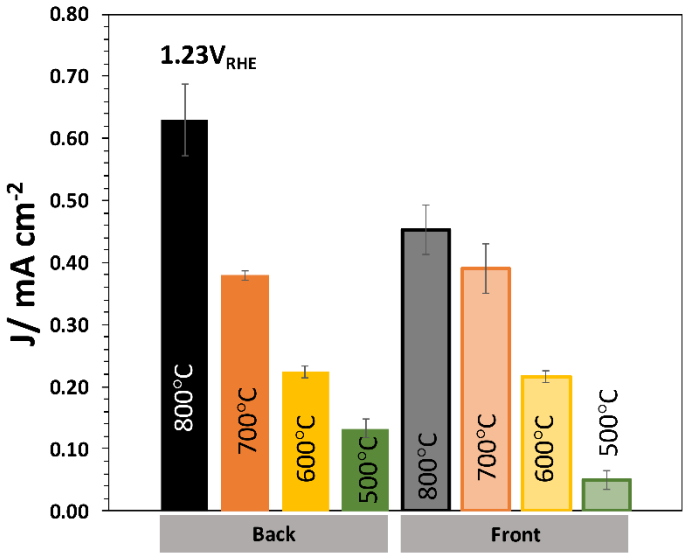

Fig. 5-35 Photocurrent density values obtained from front and back-side illumination for TiO_2-Rose at 1.23 V_{RHE} after annealing in air for 2 h (500 to 800 °C). Measurements were performed in 1M KOH (pH=13.6) under 1 sun illumination (AM 1.5G, 100 mW cm^{-2})

It can be observed how photocurrent densities are mostly higher when illumination is directed from the back of the photoanode (ABS-FTO-TiO_2) suggesting slower electron carrier transport in the film.[14] In addition, the overall increase in photocurrent density values as annealing temperature increases is most likely attributed to the removal of localized trapping states caused by embedded carbon impurities in the film as demonstrated earlier in TRMC measurements for the TiO_2-Rose-AD. Fig. 5-36 shows SEM micrographs of TiO_2-Rose photoanodes post-annealed at 500, 600, 700 and 800 °C. As discussed earlier, there are no significant structural changes between the as-deposited sample (Fig. 5-36a) and the post-annealed in air at temperatures ranging from 500 to 800 °C (Fig. 5-36b-e). Nevertheless, a slightly change in color – from black to brownish to white – is observed as annealing temperature increases (see inset of Fig. 5-36). This change in color is attributed to the presence of amorphous carbon on the surface of the sample, forming trapping states and resulting in poor PEC performances, as shown earlier (Fig. 5-35).

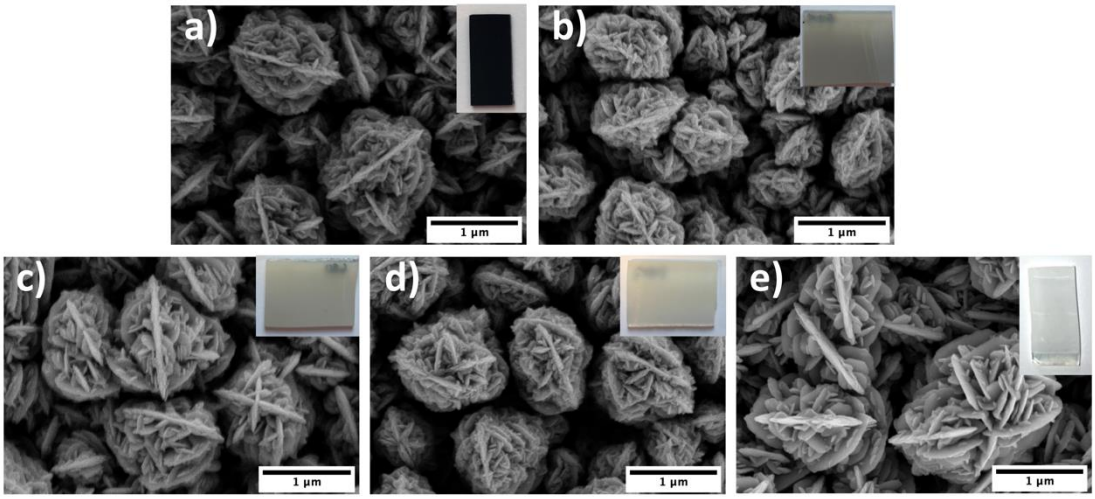

Fig. 5-36 SEM micrographs of TiO_2-Rose photoanodes grown by AA-CVD at 500 °C for 1h and annealed in air for 2 h at (a) as-deposited (no-annealing), (b) 500 (c) 600 (d) 700 and (e) 800 °C. Insets in (a-e) show photographs of TiO_2-Rose annealed at the corresponding temperature.

The presence of carbon on the surface of these samples was further confirmed by Raman spectroscopy. Fig. 5-37 shows Raman spectra of the carbon region (from 800 to 1800 cm^{-2}) of as-deposited and post-annealed samples. As-deposited and TiO_2-Rose-500 samples show strong Raman bands at *ca.* 1340 and 1600 cm^{-1} corresponding to D and G bands of graphitic carbon structures, respectively.[268] As annealing temperature increases, these D and G bands become weaker until 800 °C where these bands disappear, indicating that most of the carbon is removed from the surface. This agrees well with the white color appearance and the high PEC performance obtained for TiO_2-Rose-800.

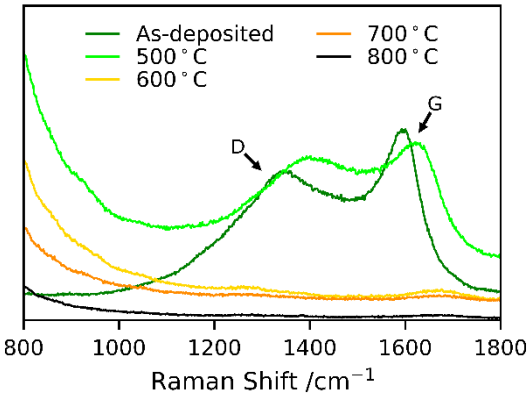

Fig. 5-37 Raman spectra of TiO_2-Rose photoanodes grown by AA-CVD at 500 °C for 1h and annealed at 500, 600, 700 and 800 for 2 h in air.

The deposition temperature of the $Ti_7O_4(OEt)_{20}$ precursor was also studied at 400, 600 and 700 °C for 1 h. As mentioned earlier, no films were obtained at 400 °C but films with finer structures were formed at 600 and 700 °C (Fig. 5-6). As deposited samples were also black in

color due to carbon residues and after post-annealing in air at different temperatures films became white.

Raman spectra and XRD patterns indicate that in spite of the deposition temperature employed only tetragonal anatase TiO_2 is observed (Fig. 5-38 and Fig. 5-39). For instance Raman spectra of as-deposited samples show characteristic Raman bands at *ca.* 144, 198, 400, 520 and 640 cm^{-1} corresponding to E_g, E_g, B_{1g}, B_{1g} and E_g Raman vibration modes of anatase TiO_2, respectively and bands at 1340 and 1590 cm^{-1} corresponding to D and G bands, respectively of graphitic carbon structures are observed.[267,268]

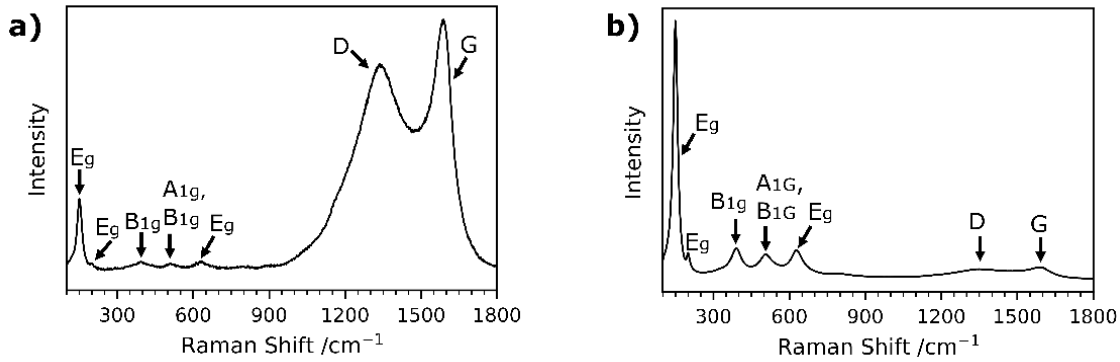

Fig. 5-38 Raman spectra of as-deposited TiO_2 photoanodes grown at (a) 600 °C and (b) 700 °C for 1 h.

Fig. 5-39 shows XRD patterns of TiO_2 films grown at 600 and 700 °C for 1 h and post-annealed for 2 h in air at different temperatures (500-800 °C). As in the films deposited at 500 °C for 1 h, only diffraction peaks corresponding to tetragonal anatase TiO_2 are observed, even after post-annealing at 800°C in air for 2 h. In particular, the diffraction peaks at 25.2, 48.0, 55.1 and 62.8° (2θ) correspond to (1 0 1), (2 0 0), (2 1 1) and (2 0 4) diffraction planes, respectively (ICDD-JCPDS 75-1537).

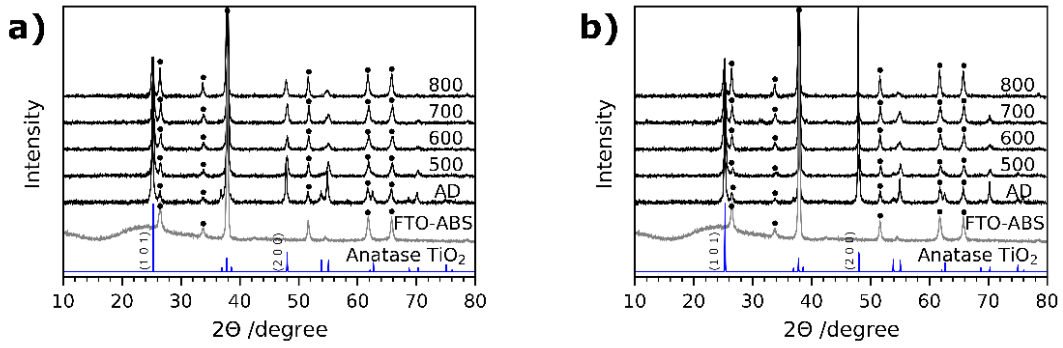

Fig. 5-39 XRD patterns of TiO_2 films grown at (a) 600 and (b) 700 °C for 1h and annealed at different temperatures (600-800 °C). Standard powder pattern of anatase TiO_2 is shown as well as XRD pattern of FTO-ABS. Dot: FTO-ABS diffraction peak. AD: As-deposited film.

Table 5-5 Anatase coherent crystal domain size of TiO_2 films grown at 600 and 700 °C for 1 h and annealed in air for 2 h at different temperatures.

	Deposited at 600 °C	**Deposited at 700 °C**
Annealing T (°C)	**Size (nm)**	**Size (nm)**
AD	54.0	52.8
500	34.0	28.6
600	21.9	22.4
700	26.6	24.8
800	23.3	23.6

Table 5-5 shows the coherent crystal domain size of TiO_2 films prepared at 600 and 700 °C. As in the case of TiO_2 films grown at 500 °C, the largest domain size is found for the as-deposited sample. We attribute this to the presence of interstitial carbon in the anatase TiO_2 lattice structure. As annealing temperature increases, crystal domain sizes are in the range of 20-27 nm, where phonon-confinement can occur. Therefore, we also attribute the high-temperature anatase TiO_2 to a combination of phonon confinement and substrate constrained effects. Interestingly, when comparing crystal domain sizes of samples deposited at 500 with the ones at 600 and 700 °C, samples grown at 500 °C possess slightly larger crystal domain sizes (28-36 nm), being consistent with the finer nanostructures observed for samples deposited at 600 and 700°C.

The PEC performance of these photoanodes post-annealed at 800 °C for 2 h was also evaluated (Fig. 5-40). TiO_2 films deposited at 600 and 700 °C exhibited similar performances of *ca.* 0.1 mA cm^{-1} at 1.23 V_{RHE}, being significantly lower than TiO_2 films deposited at 500 °C for 1 h. The low performance of these samples is most likely due to the finer nanostructures obtained after deposition, as previously shown in Fig. 5-6.

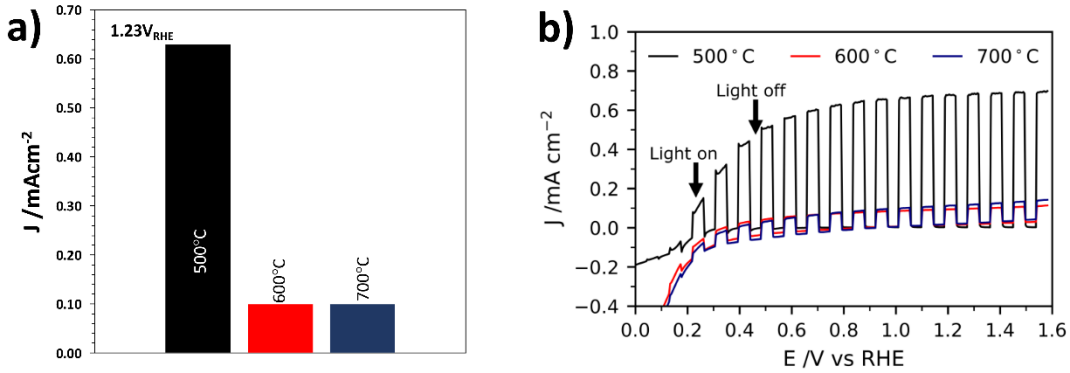

Fig. 5-40 (a) Photocurrent density values obtained from back-side illumination at 1.23 V_{RHE} for TiO_2-Rose photoanodes grown at deposition temperatures of 500, 600 and 700°C and post-annealed in air at 800 °C for 2 h. (b) Representative photocurrent potential curves of TiO_2 grown at deposition temperatures of 500, 600 and 700 °C and post-annealed in air at 800 °C for 2 h. All measurements were performed in 1M KOH (pH=13.6) under 1 sun illumination (AM 1.5G, 100 mW cm^{-2}).

In summary, from these temperature optimization studies it was concluded that optimal post-annealing temperature is 800 °C for 2 h and 500°C for deposition temperature. At these conditions, desert-rose TiO_2 photoanodes with no amorphous carbon were obtained, achieving maximum photocurrent densities of *ca.* 0.65 mA cm^{-2} at 1.23 V_{RHE}.

5.1.5.2 Influence of solvent used on morphology and PEC performance

The effect of two different solvents, tetrahydrofuran (THF) and toluene, towards the final morphology and PEC performance of the photoanodes was also investigated. These solvents were chosen due to the good stability and solubility of the $Ti_7O_4(OEt)_{20}$ precursor under these conditions. Fig. 5-41 shows SEM micrographs of TiO_2-Rose-800 performed in toluene (a-c) and THF (d-f). Interestingly, the desert-rose morphology with plate-like sheets was still obtained when THF was used, although the roses were slightly smaller and composed of a larger number of sheets of smaller size, in comparison to TiO_2-Rose-800 prepared when toluene was used. It must be noted that both samples were prepared under the same experimental conditions (1 h of deposition at 500 °C using N_2 as a carrier gas at a constant flow rate of 1.5 L min^{-1}), but the precursor usage rate was of *ca.* 0.3 and *ca.* 0.7 mL min^{-1} for toluene and THF, respectively. This large difference in precursor usage is mainly attributed to the difference in viscosity between the solvents, being of 0.59 and 0.55 mPa s for toluene and THF, respectively.[284] The aerosol can be easily generated from solutions with lower viscosities so larger amounts of precursor solution are usually used.[179]

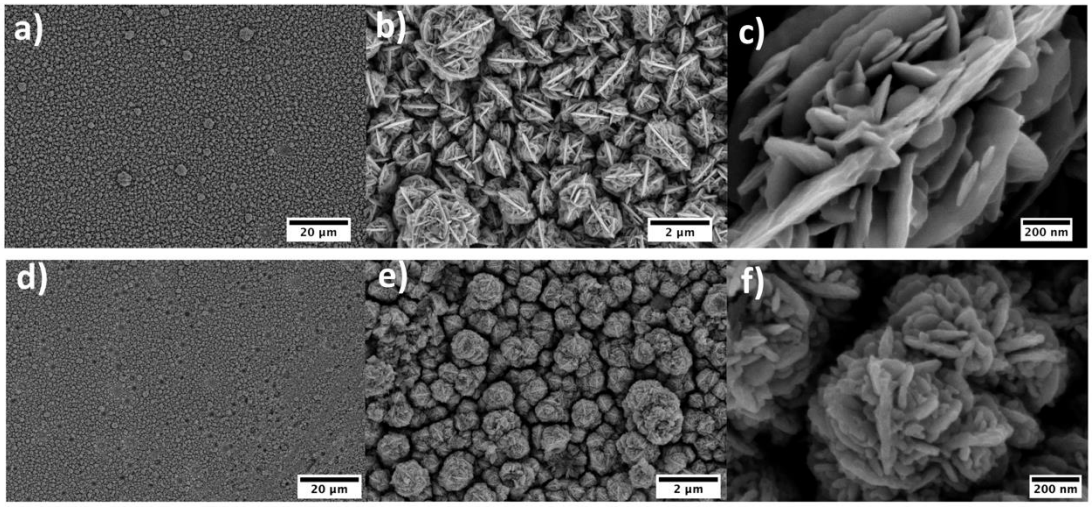

Fig. 5-41 SEM micrographs of TiO_2 photoanodes grown by AA-CVD and annealed at 800 °C for 2 h. Deposition performed in (a-c) toluene and (d-f) THF.

It has been previously reported in literature that in aerosol deposition methods the solvents can play a key role in determining the TiO_2 crystalline phase (anatase or rutile) since each precursor can react differently with the solvent leading to the formation of different intermediates resulting in different TiO_2 crystalline phases deposited, as discussed in detail in

Chapter 3. Fig. 5-42 shows the XRD patterns of TiO_2-Rose prepared in THF and annealed at 600, 700, 800 and 900 °C. All XRD patterns only show the characteristic peaks of tetragonal anatase TiO_2 phase, as when toluene was used as a carrier solvent. In particular, the diffraction peaks at 25.2, 48.0, 55.1, 62.8, 75.0 and 76.0 ° (2θ) correspond to (1 0 1), (2 0 0), (2 1 1), (2 0 4), (2 1 5) and (3 0 1) diffraction planes (ICDD-JCPDS 75-1537). TC_{101} and TC_{200} calculated from XRD patterns (Fig. 5-42) at different annealing temperatures are listed in Table 5-6. TC_{101} fall in the range of 0.6-0.7, whereas TC_{200} are of 1.3-1.4. As in the case of TiO_2-Rose photoanodes prepared using toluene, when THF is employed preferential growth orientation along the (2 0 0) diffraction plane is also observed. This agrees well with SEM micrographs, where plate-like sheets typical of a preferential orientation growth were also observed. This indicates that in this particular case, similar reaction intermediates must be formed when using either toluene or THF, giving rise to tetragonal anatase TiO_2 phase after deposition with a similar desert-rose morphology.

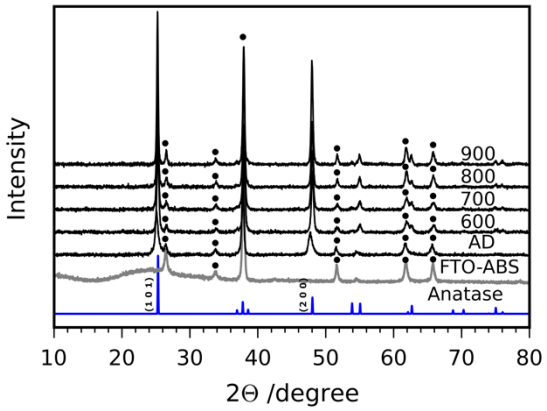

Fig. 5-42 XRD patterns of TiO_2-Rose films prepared using $Ti_7O_4(OEt)_{20}$ and THF annealed at different temperatures (600-800 °C). Standard powder pattern of anatase TiO_2 is shown as well as XRD pattern of FTO-ABS. Dot: FTO-ABS diffraction peak. AD: As-deposited film.

Table 5-6. Anatase coherent crystal domain size and texture coefficients of TiO_2-Rose prepared using THF after annealing in air at different temperatures.

Annealing T (°C)	TC_{101}	TC_{200}	Size (nm)
AD	0.73	1.27	18.6
600	0.62	1.38	26.6
700	0.68	1.32	26.6
800	0.71	1.29	31.2
900	0.60	1.40	39.4

It is to be noted that as in the case of TiO_2-Rose photoanodes prepared using toluene as carrier solvent, none of the XRD diffraction peaks is indexed to rutile TiO_2 phase, even when high annealing temperatures are employed (*i.e.* 900 °C). As before, we attribute this phenomenon

to a combination of phonon confinement and substrate constrained effects. Table 5-6 shows the calculated anatase coherent crystal domain sizes of TiO_2-Rose photoanodes prepared using THF as carrier solvent and annealed in air at different temperatures. Unlike in the case of TiO_2-Rose photoanodes prepared using toluene, the smallest domain size is found in the as-deposited sample. This might indicate that during AACVD deposition, carbon structures are mainly on the surface of the film or in the TiO_2 grain boundaries, instead of being occupying interstitial positions in the anatase TiO_2 structure. As annealing temperature increases, from 600 to 900 °C, crystal domain sizes slightly increase from *ca.* 26 to 39, being still in the range where phonon confinement can occur. [263,264] As before, the presence of carbon in the TiO_2 grain boundaries must have limited the growth of TiO_2 domain sizes. Fig. 5-43 shows the Raman spectra of E_g Raman mode of TiO_2-Rose photoanodes prepared in THF. As in the case of TiO_2-Rose photoanodes prepared in toluene, a slightly shift towards lower wavenumber values is also observed as annealing temperature increases, further supporting the phonon confinement model for high-temperature anatase TiO_2.[262,264]

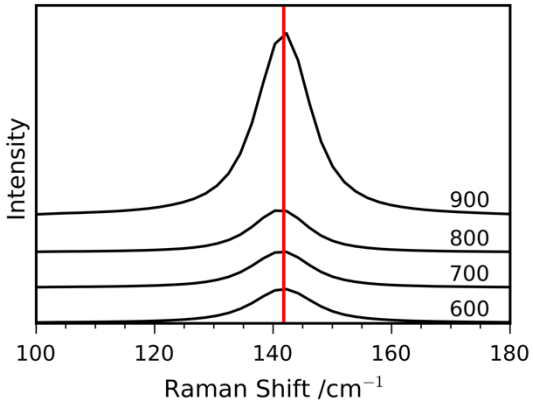

Fig. 5-43 Raman spectra of Eg Raman mode of anatase TiO_2 (144 cm^{-1}) for TiO_2-Rose prepared using THF and annealed at 600, 700, 800 and 900 °C for 2 h in air.

Coherent crystal domain sizes of TiO_2-Roses prepared in THF fall in the range of *ca.* 26 to 39 nm at an annealing temperature range of 600 to 900 °C, whereas when samples are prepared in toluene, crystal domain sizes are slightly larger (*ca.* 28 to 45 nm) at the same annealing temperatures (Table 5-4). This can be explained by the different volatility values of toluene and THF, being of 29 and 200 hPa (20 °C), respectively.[285] When THF is used as carrier solvent, due to being more volatile than toluene, solvent evaporation/decomposition starts earlier and proceeds quicker along the reactor chamber resulting in the formation of multiple small particulates that nucleate forming smaller crystallites. On the other hand, when toluene is used, solvent evaporation/decomposition takes place at a slower rate forming less nucleation sites and allowing larger crystals to be formed.[180] This is also in agreement with SEM

micrographs, where smaller plate-like sheets are observed for TiO_2-Rose samples prepared using THF (Fig. 5-41).

Fig. 5-44 shows the Raman spectra of TiO_2-Rose-800 and TiO_2-Rose-AD prepared in THF and toluene, for comparison. Sharp Raman bands corresponding only to tetragonal anatase TiO_2 are observed in TiO_2-Rose-800 (THF) (Fig. 5-44a). In particular, the bands at *ca.* 144, 198, 400, 520 and 640 cm^{-1} correspond to E_g, E_g, B_{1g}, A_{1g} -B_{1g} and E_g Raman vibration modes of anatase TiO_2, respectively, agreeing well with XRD patterns (Fig. 5-42).[267]

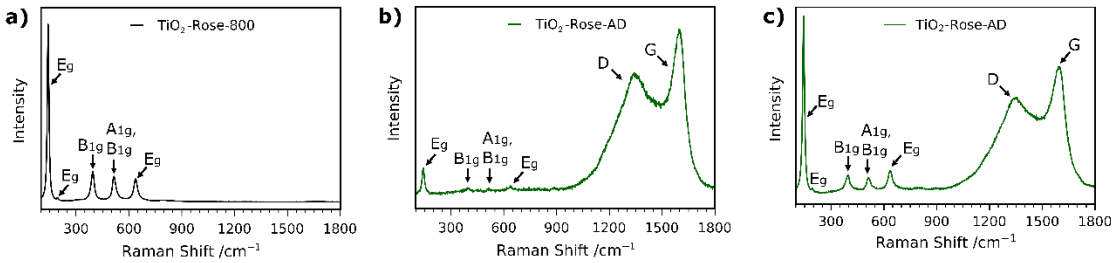

Fig. 5-44 Raman spectra of (a) TiO_2-Rose-800 , (b) TiO_2-Rose-AD prepared using THF and (c) TiO_2-Rose-AD using toluene.

Raman spectrum of TiO_2-Rose-AD (THF) shows two additional intense bands at *ca.* 1340 and 1590 cm^{-1}, corresponding to D and G bands of graphitic carbon structures (Fig. 5-44b).[268] Very weak Raman bands corresponding to tetragonal anatase TiO_2 are observed. When comparing the TiO_2-Rose-AD Raman spectrum of the samples prepared using toluene (Fig. 5-44c) and THF (Fig. 5-44b), it is observed how sharper and more intense Raman bands corresponding to tetragonal anatase TiO_2 are observed when toluene is used (Fig. 5-44c), whereas very weak Raman bands are observed in the case of THF (Fig. 5-44b). This indicates that larger amounts of carbon residues are deposited on the surface of TiO_2-Rose-AD when THF is used. In fact, this is in agreement with the higher precursor usage rate of THF in comparison to toluene.

PEC performances of TiO_2-Rose photoanodes prepared in toluene and THF were evaluated and results are shown in Fig. 5-45. Fig. 5-45a shows a comparison of the photocurrent density values obtained from back-side illumination at 1.23 V_{RHE} at different annealing temperatures in air when either toluene or THF was used as a carrier solvent. Interestingly, photocurrent density values are higher when toluene is used, being 800 °C the optimal post-annealing temperature. The higher PEC performance of TiO_2-Rose photoanodes prepared in toluene is most likely due to the slightly different composition of the desert-rose morphology. As stated earlier, the plate-like sheets forming the roses of the TiO_2-Rose photoanodes prepared in toluene are slightly larger, which might result in more exposed {0 1 0} facets, resulting in an improvement of the PEC performance.

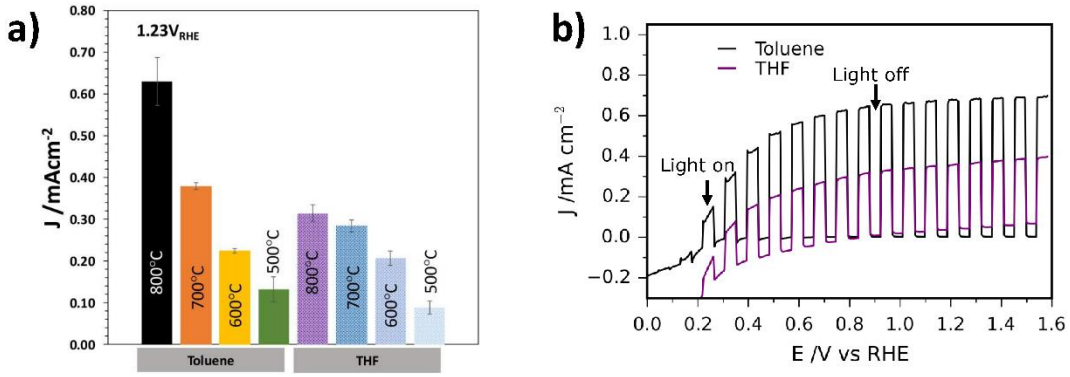

Fig. 5-45 (a) Photocurrent density values obtained from back-side illumination for TiO_2-Rose prepared using toluene and THF and annealed at different temperatures (500 to 800 °C) at 1.23 V_{RHE}. (b) Representative photocurrent potential curves of TiO_2-Rose-800 prepared in toluene and THF from back-side illumination. All measurements were performed in 1M KOH (pH=13.6) under 1 sun illumination (AM 1.5G, 100 mW cm^{-2}).

5.1.5.3 Influence of substrate used on morphology and crystalline phase

A solution of 0.05M of $Ti_7O_4(OEt)_{20}$ in toluene was deposited on top of different substrates including FTO-ABS, alumina, glass and silicon at 500 °C for 1 h using N_2 as a carrier gas in order to study the influence of substrate used in the morphology and crystalline phase (anatase or rutile) of TiO_2 films. Previous reports have shown a substrate-selective deposition, both in terms of morphology and crystalline phase, when using titanium isopropoxide as TiO_2 precursor on either titanium metal, steel or glass substrates, as discussed in Chapter 3.[173] Fig. 5-46 shows SEM micrographs of TiO_2 films prepared by depositing $Ti_7O_4(OEt)_{20}$ precursor on FTO-ABS, alumina, glass and silicon. Two different distinct morphologies are observed when using different substrates. For instance, similar morphologies having the appearance of desert roses are observed when $Ti_7O_4(OEt)_{20}$ is deposited on top of FTO-ABS (Fig. 5-46a) and alumina (Fig. 5-46b), whereas smaller and finer nanostructured roses are formed when using either glass (Fig. 5-46c) or silicon (Fig. 5-46d) as deposition substrate. The fact that two different morphologies are observed when different substrates are used suggest that chemical reaction/precursor decomposition mainly takes place at the surface and not in the vapor phase.[173] Interestingly, both FTO-ABS and alumina substrates have a rough surface, whereas glass and silicon are known to possess very smooth surfaces. This indicates that 'desert rose' morphologies are most likely formed in rough surfaces, whereas finer and smaller roses are formed when flat surfaces, such as glass or silicon are used.

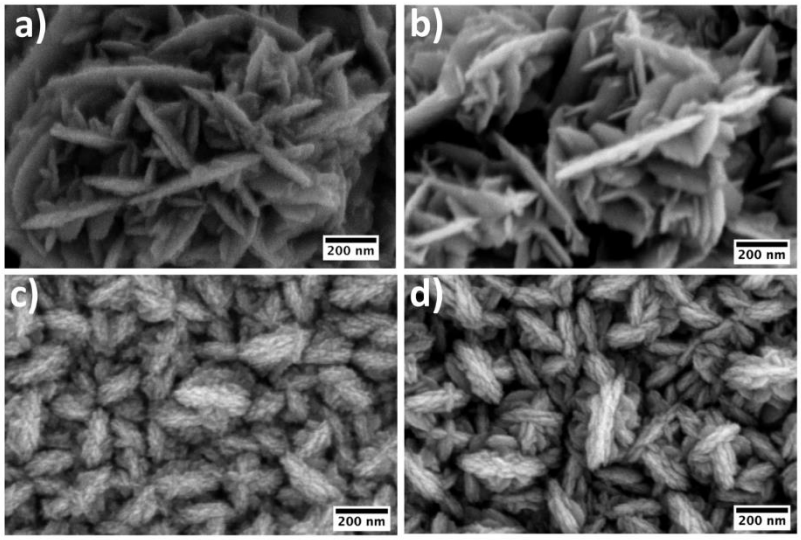

Fig. 5-46 SEM micrograph of TiO_2-Rose deposited at 500 °C for 1 h on top of (a) FTO-ABS, (b) alumina (c) glass and (d) silicon.

XRD patterns of all as-deposited TiO_2 samples are shown in Fig. 5-47. Despite the type of substrate used all samples only exhibit the characteristic peaks of tetragonal anatase TiO_2 phase. None of the diffraction peaks is indexed to rutile TiO_2. TC_{101} and TC_{200} calculated from XRD patterns (Fig. 5-47) are shown in Table 5-7. Interestingly, preferential growth orientation along (2 0 0) is observed when FTO-ABS, glass, alumina and silicon are used, whereas slightly preferred orientation towards (1 0 1) diffraction plane is observed when alumina is used as a substrate.

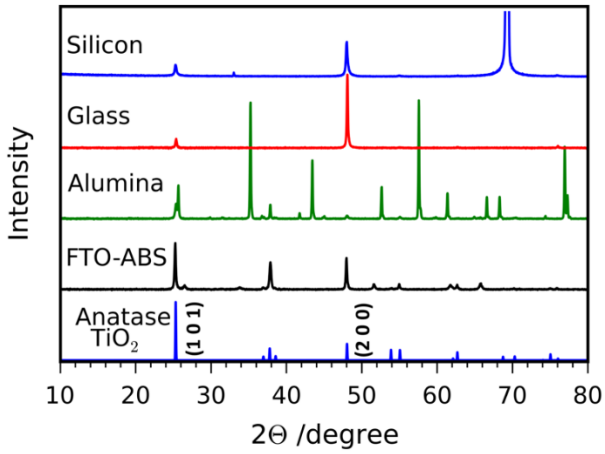

Fig. 5-47 XRD patterns of TiO_2-Rose on FTO-ABS, alumina, glass and silicon. Standard powder pattern of anatase is TiO_2 is also shown.

Table 5-7 Texture coefficients of TiO_2 films deposited on different substrates.

Annealing T (°C)	TC_{101}	TC_{200}
FTO-ABS	0.61	1.39
Alumina	1.21	0.79
Glass	0.14	1.86
Silicon	0.18	1.82

5.1.5.4 Influence of using H_2O_2 and methanol as a hole scavenger and Co-Pi as a co-catalyst on the PEC performance

Hole scavengers, such as H_2O_2 and methanol are commonly used for understanding the charge transport efficiencies of the photoanodes.[286] When a hole scavenger is added in the electrolyte, it is assumed that surface electron and hole recombination is suppressed, due to the fast reaction of photogenerated holes with the scavenger. Therefore, under these conditions, photocurrent onset potentials are expected to shift cathodically and photocurrent density values plateau at lower bias.[286] Fig. 5-48 shows PEC performance of TiO_2-Rose-800 photoanodes with and without hole scavenger (H_2O_2).

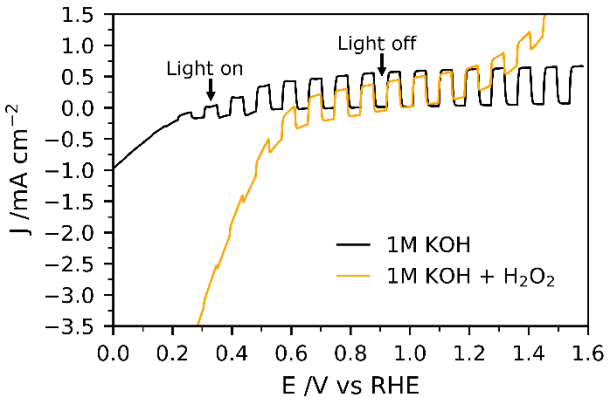

Fig. 5-48 Photocurrent potential curves of TiO_2-Rose-800 measured in 1M KOH (pH=13.6) and 1M KOH + 0.1M H_2O_2 (pH=13.3) from back-side illumination. All measurements were performed under 1 sun illumination (AM 1.5G, 100 mW cm^{-2}).

In the absence of a hole scavenger, the onset potential is of *ca.* 0.2 V_{RHE} and photocurrent density values start to plateau at applied bias above 0.4 V_{RHE}. On the other hand, when H_2O_2 is added the onset potential is slightly shifted towards higher voltages, significantly higher dark currents are observed and photocurrent density values decrease. As reported by H. Zhu *et al.* this infrequent phenomenon indicates that when H_2O_2 is added, a reduction side reaction of H_2O_2 owing to photogenerated trapped electrons takes place, leading to a decrease in saturated photocurrent densities and a positive shift of the onset potential.[287] These results agree well with TRMC measurements discussed in Section 5.1.4, where trap limited recombination exists. Upon light irradiation, electrons can get trapped in these states reducing

the H_2O_2, specially in alkaline conditions, where owing to the fast kinetics of the H_2O_2 reduction reaction, photogenerated electrons tend to reduce H_2O_2 rather than being injected in the conduction band of the semiconductor. In order to assess the maximum performance of these TiO_2-Rose-800 photoanodes, PEC measurements in the presence of a less reactive hole scavenger (methanol) were performed. Fig. 5-49 shows J-V curves of TiO_2-Rose-800 photoanodes in 1M KOH and in 1M KOH with methanol. At these conditions, the onset potential is shifted cathodically (*ca.*-0.1 V_{RHE}) and photocurrent plateaus at lower voltages, since the injection barrier for minority carriers is removed. Overall, photocurrent density values are higher at low bias in the presence of methanol but at higher applied bias (above 0.5 V_{RHE}), where photocurrent plateaus, photocurrent performances are very similar. This indicates that at a high applied bias, electron and hole recombination is minimal even without hole scavenger and all photogenerated holes participate in the water oxidation reaction.

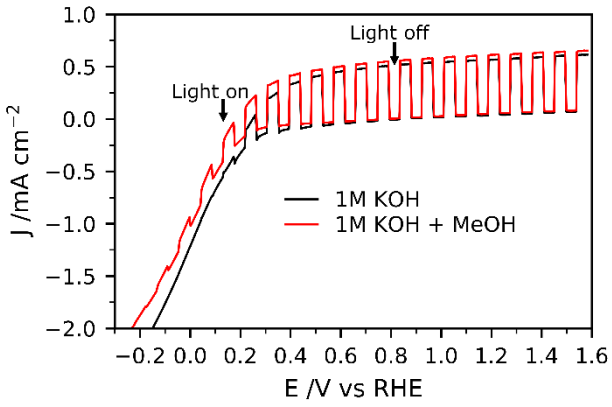

Fig. 5-49 Photocurrent potential curves of TiO_2-Rose-800 measured in 1M KOH (pH=13.6) and 1M KOH + 4 % methanol (pH=13.6) . All measurements were performed under 1 sun illumination (AM 1.5G, 100 mW cm^{-2}).

The effect of co-catalyst towards the PEC performance of TiO_2-Rose-800 photoanodes was also evaluated. It is known that addition of co-catalysts on the surface of photoanodes can contribute in a reduction of the onset potential and enhancement of photocurrent densities due to improved charge transfer.[288] A co-catalyst that has recently attracted great interest within the scientific community is cobalt phosphate (Co-Pi) due to its numerous advantages such as high abundance on earth, functionality under benign conditions and self-healing properties (catalyst corrosion can be reversed upon application of a potential).[289] In line with this, cobalt phosphate (Co-Pi) was photodeposited on the surface of TiO_2-Rose-800 photoanodes following an experimental method previously described in literature.[186,187] Fig. 5-50 shows J-V curves of pristine TiO_2-Rose-800 and TiO_2-Rose-800 photoanodes with different amounts of Co-Pi. The amount of Co-Pi was controlled by the deposition time (20 to 300 s). After addition of Co-Pi the sample changed color, from white to brownish.

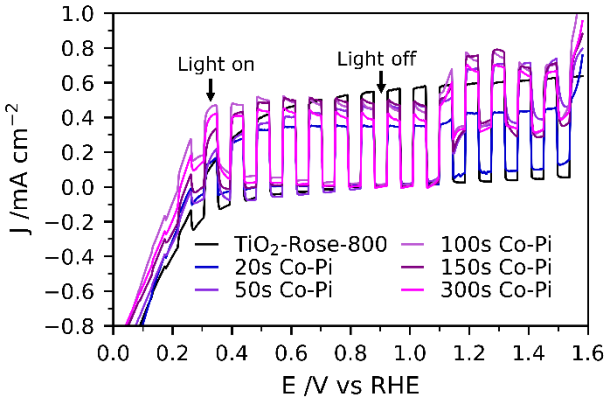

Fig. 5-50 Photocurrent potential curves of TiO_2-Rose-800, TiO_2-Rose-800 with different loadings of Co-Pi. The amount of Co-Pi was controlled by the deposition time. All measurements were performed in 1M KOH (pH=13.6) under 1 sun illumination (AM 1.5G, 100 mW cm^{-2}) from back-side illumination.

Addition of Co-Pi did not result in an improvement neither of the PEC performance nor of the onset potential.[186] At low loading of Co-Pi (20 s of deposition), the onset potential and photocurrent density values at low bias (0.2-0.3 V_{RHE}) are very similar, whereas at higher applied bias photocurrent values are the lowest of all Co-Pi samples studied. When larger amounts of Co-Pi are deposited (50 to 300 s of deposition), slightly higher photocurrents than 20s-Co-Pi samples are observed but still lower than pristine TiO_2. In addition, these samples also exhibit high dark currents above 1.1 V_{RHE} and anodic transients. Similar dark currents were reported in literature when large amounts of co-catalyst were added.[218] The decrease in photocurrent performances at low bias is often related to the thickness of the Co-Pi layer. When the Co-Pi layer is thin enough, only one layer of $Co^{2+/3+}$ is attached to the TiO_2 surface via phosphate groups and photogenerated holes can be easily captured to produce the active species (Co^{4+}) for the photocatalytic reaction and thus an enhancement in photocurrent is observed, especially at low bias. Nevertheless, when this layer is too thick, photogenerated holes are transferred to the Co-Pi/electrolyte interface via multiple Co-Pi molecules resulting in a decrease in photocurrent and an increase in electron and hole recombination.[186] Another reason for the decrease in photocurrent could be light absorption by Co-Pi catalyst. To avoid this, measurements were performed from backside illumination.

The decrease in photocurrent performances for TiO_2-Rose-800 with high loadings of Co-Pi (50 to 300 s) is most likely due to the Co-Pi layer being too thick as demonstrated with the large dark currents observed at high applied bias and the presence of anodic transients. Nevertheless, the decrease in photocurrent when Co-Pi is deposited for 20 s might also arise from other factors. Pristine TiO_2-Rose-800 sample show low onset potential (*ca.* 0.15 V_{RHE}) and high photocurrent values even at low bias, indicating minimal electron and hole recombination, suggesting that even when small amounts of Co-Pi are added, the driving force

for electron-hole separation at small applied bias is larger than the co-catalyst itself, and the co-catalyst might act as a recombination center minimizing the photocurrent performance.

5.1.5.5 Transient absorption and photocurrent spectroscopy measurements

Transient absorption and photocurrent spectroscopy measurements were performed in TiO_2-Rose-800 samples to determine charge carrier dynamics during the water oxidation reaction, using a set-up and procedure previously described in literature.[290,291] The photogenerated charge carrier features were identified after a pulse band gap excitation from which the change in the intensity of a transmitted monochromatic probe light as a function of time was monitored. These measurements were performed in a three-electrode PEC cell configuration with Pt as the counter electrode, a Ag/AgCl reference electrode and the TiO_2-Rose-800 photoanode as working electrode in 1M NaOH (pH=13.6). Measurements were performed from front-side illumination.

Use of hole scavengers to identify photogenerated electron and hole spectra

Transient absorption spectra (TAS) measured at two different potentials, 0.2 V_{RHE} (close to the flat band potential) and 1.23 V_{RHE} and at two different time delays (10 μs and 10 ms) are shown in Fig. 5-51. As previously reported, these spectra are commonly used to identify the regions where photogenerated electrons and holes can be detected.[292] A similar trend is observed at the two potentials studied: at a wavelength range of 650-800 nm absorbance values are relatively constant but rapidly increase at wavelengths below 600 nm. When comparing absorption values below 600 nm for both potentials studied, it is depicted higher absorption values at 1.23 V_{RHE} than at 0.2 V_{RHE}. At higher applied bias (1.23 V_{RHE}) photocarrier recombination diminishes, increasing the lifetime of photocarriers and giving rise to higher absorption values. This is a first indication that this region most likely corresponds to photogenerated holes, since photoelectrons are usually recorded at much higher wavelengths.[292]

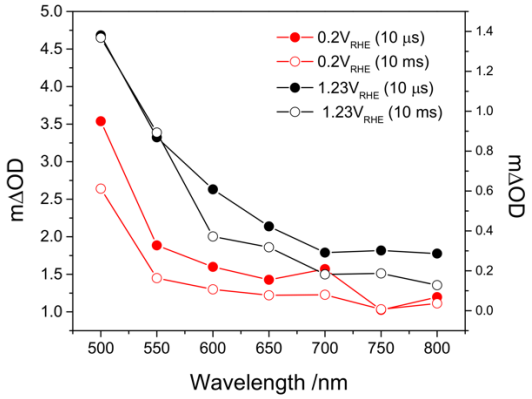

Fig. 5-51 Transient absorption spectra measured at 0.2 V_{RHE} and 1.23 V_{RHE}. Signals were recorded at 10 µs and 10 ms after a 355 nm laser excitation and measured in 1 M NaOH.

TAS spectra were measured in the presence of a hole scavenger to further confirm the nature of this absorption increase. Fig. 5-52a shows TAS spectra measured at 0.2 V_{RHE} with and without the presence of hole scavenger at two different time delays (10 µs and 10 ms). In the presence of a hole scavenger TAS spectra flattens below 600 nm, when compared to a spectrum without hole scavenger, indicating that photoholes are quenched in a premicrosecond time scale. This confirms that photohole fingerprint falls in the range of 500-600 nm, as suggested earlier. The higher increase in absorption values towards the IR region in the presence of methanol might also indicate that some photogenerated electrons are detected at those wavelengths due to longer electron lifetimes in the presence of a hole scavenger. [292,293] Similarly, TAS spectra at potentials above the flat-band potential of TiO_2-Rose are shown in Fig. 5-52b. As expected, in the presence of hole scavenger, photoholes are rapidly quenched below 600 nm, which also confirms the photohole fingerprint region at low wavelengths.

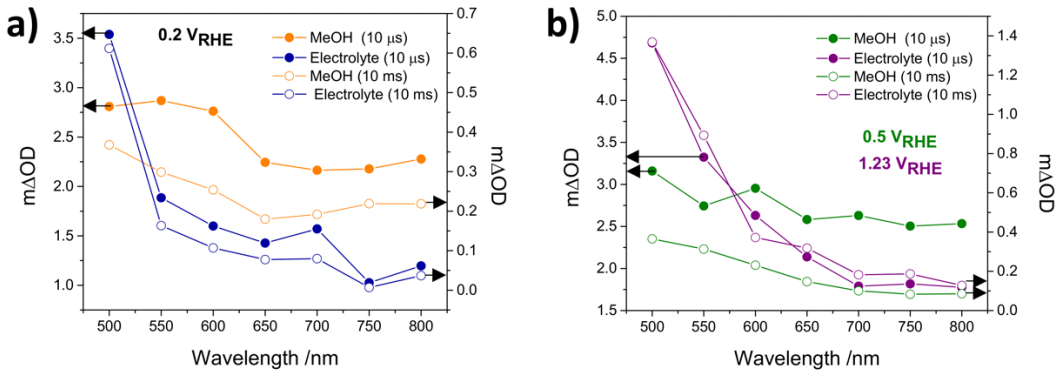

Fig. 5-52 (a) Transient absorption spectra measured at 0.2 V_{RHE}. (b) Transient absorption spectra measured at 1.23 V_{RHE} (NaOH) and 0.5 V_{RHE} (MeOH). Signals were recorded at 10 µs and 10 ms after a 355 nm laser excitation and measured in either 1M NaOH or 1M NaOH + 4 % MeOH.

Transient absorption decays

The dynamics of photogenerated holes and electrons was evaluated by means of transient absorption decays probed at 500 and 800 nm, respectively, with the addition of a hole scavenger (methanol) at 0.2 V_{RHE} (Fig. 5-53). The addition of methanol did not show any significant difference in TAS decays probed at 500 nm (Fig. 5-53a, photoholes region). This might suggest that close to the U_{FB} the scavenging effect is minimal and that holes reach the TiO_2 surface to react with water at similar rates of those when the methanol is present.

Conversely, TAS decays probed at 800 nm (Fig. 5-53b, photoelectron region) show slightly longer decay times in the presence of methanol, suggesting some carriers recombination in absence of methanol. When methanol is added, electron-hole recombination diminishes and electron lifetime increases. This agrees well with front-side J-V curves shown in Fig. 5-54 where some carrier recombination was observed at 0.2 V_{RHE} when comparing measurements with and without hole scavenger. These observed features are related to the characteristic desert-rose morphology of these TiO_2 photoanodes, consisting of multiple plate-like sheets. Upon light irradiation, photogenerated holes are generated close to the semiconductor-electrolyte interface and can easily react with water for the water oxidation reaction, while photogenerated electrons migrate to the back contact. The slightly higher recombination observed in photogenerated electrons in the absence of hole scavenger is due to the larger carrier pathway that electrons have to travel to reach the back contact, which increases their likelihood of recombination (front-side illumination measurements performed).

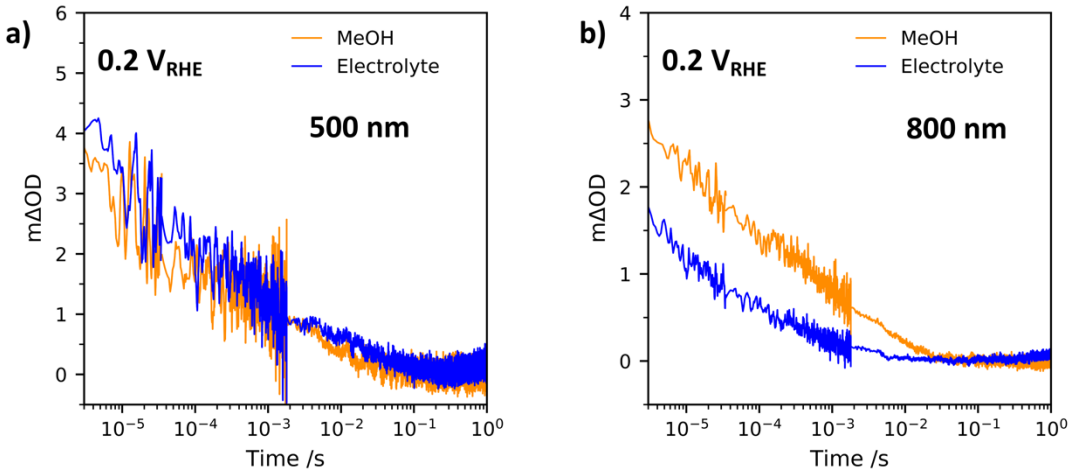

Fig. 5-53 Dynamics of (a) photogenerated holes (probed at 500 nm) and (b) photogenerated electrons (probed at 800 nm). Measurements were performed at 0.2 V_{RHE} in a three-electrode PEC system in 1M NaOH (pH=13.6) with and without hole scavenger (4 % methanol).

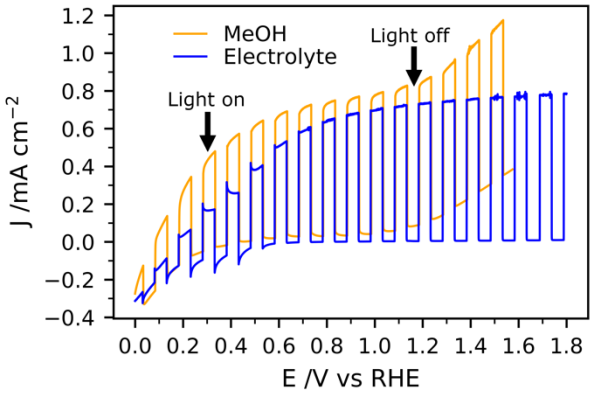

Fig. 5-54 Photocurrent potential curves of TiO_2-Rose 800 measured using a continuous wave 365 nm LED light source in 1 M NaOH (pH=13.6) with and without hole scavenger (4% methanol). Measurements were performed from front-side illumination using the same set-up as in TAS measurements.

To further understand the dynamics of photogenerated holes in the water splitting reaction TAS decays at different applied bias were measured and results are shown in Fig. 5-55.

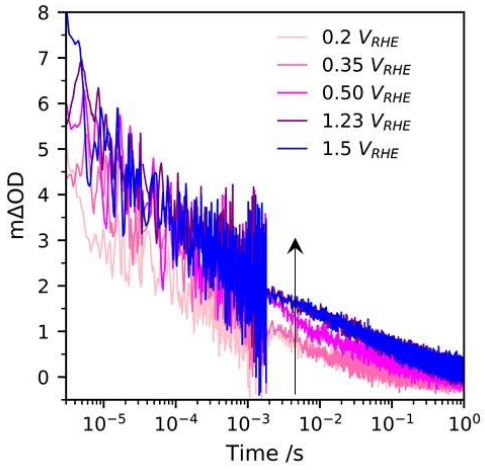

Fig. 5-55 Dynamics of photogenerated holes (probed at 500 nm) as a function of applied bias. Measurements were performed in a three-electrode PEC system in 1M NaOH (pH=13.6).

TAS decays reveal a slightly increase in yield and photogenerated holes lifetime as applied potential increases specially from 0.2 to 1.23 V_{RHE}. In fact, hole signals beyond 10 ms are observed in all applied voltages, even at 0.2 V_{RHE}. This is attributed to a diminishment in electron-hole recombination due to an increase in band-bending and stronger electric field in the space-charge region.[291] At applied bias of 1.5 V_{RHE}, the TAS decay curve is very similar to the one measured at 1.23 V_{RHE}, suggesting that at these potentials electron-hole recombination is minimal and all photogenerated holes participate in the water oxidation reaction.[64,290] This agrees well with measured J-V curves, where photocurrent plateaus at these voltages (Fig. 5-54).

When comparing our TAS decays at different applied voltages with previously reported values for dense and flat anatase TiO_2 films significant differences can be observed.[291] For instance, for flat and dense anatase TiO_2 films (Fig. 5-56), as applied potential increases the photogenerated hole lifetime increase significantly (TAS signals differ significantly), even at 1.5 V_{RHE} whereas in our nanostructured TiO_2 films above and applied bias of 0.5 V_{RHE} TAS decays differences are smaller. Bi-molecular recombination seems to occur on the pre-ms timescale, being consistent with front-side IPCE measurements, where at those conditions IPCE of 100 % was not achieved (Fig. 5-20). Such small variations in photogenerated hole decays are most likely related to the highly nanostructured anatase TiO_2 in the TiO_2-Rose-800 film. With these nanostructures, the relative volume of the space-charge layer with respect to the bulk increases, reducing the electron and hole recombination and increasing the plateau current.[291] This agrees well with J-V curves, where photocurrent values plateau at *ca.* 0.6 V_{RHE} in nanostructured TiO_2 films (Fig. 5-54) and around 1.0 V_{RHE} in flat TiO_2 films.[291]

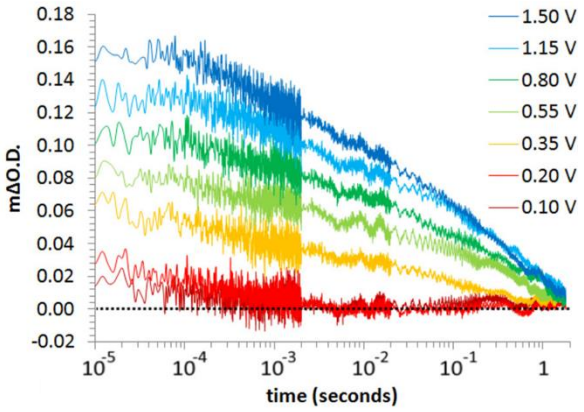

Fig. 5-56 Decay kinetics of holes measured at a probe wavelength of 500 nm for dense and flat anatase TiO_2 photoanodes measured in 1M NaOH (pH=13.6) at various applied potentials (V_{RHE}). Reprinted with permission from ref.[291] Copyright (2017) American Chemical Society.

Light-Induced Spectroelectrochemistry (LI-SEC)

Light-induced spectroelectrochemistry (LI-SEC) was used to determine the kinetics of the water oxidation reaction on TiO_2-Rose photoanodes. For such measurements, the optical absorption was monitored using continuous wave illumination to mimic the behavior of photogenerated charges in a lab-scale PEC setup where continuous simulated sunlight is normally used, as previously described in literature.[294] Photocurrent densities were also measured simultaneously, so that direct correlations with photocurrent transients and

photogenerated holes could be performed. The light-induced absorption recorded at 550 nm and the photocurrent densities measured at 1.23 V_{RHE} are shown in Fig. 5-57.

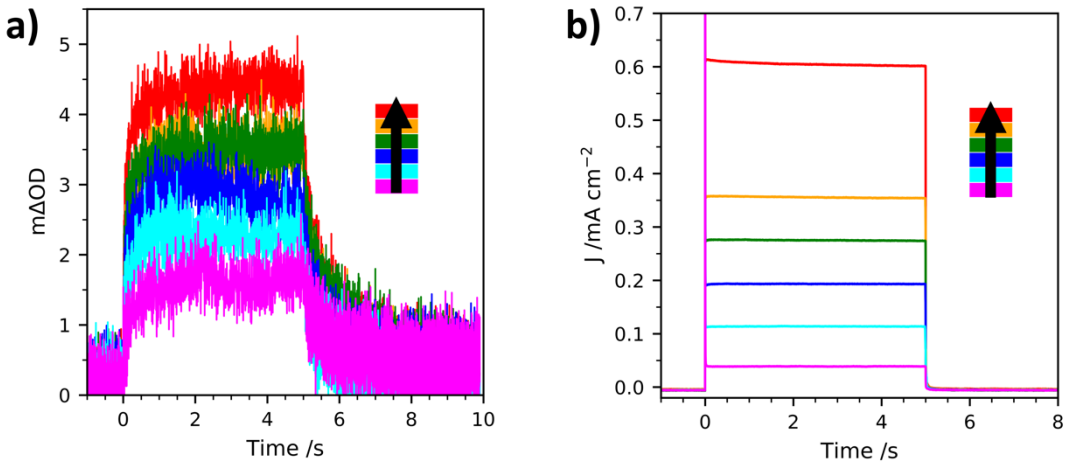

Fig. 5-57 (a) Light-induced absorption of holes at 550 nm measured in 1M NaOH (pH=13.6) at 1.23 V_{RHE}. LI-SEC signals were collected at different light intensities using an excitation wavelength of 365 nm. (b) Transient photocurrent measurements were measured simultaneously.

When the light is turned on (0 s) the LI-SEC absorption signal increases until reaching plateau (*ca.* 1 to 5 s) and slowly decreases when the light is turned off due to slow reaction with water (*ca.* 5.5 to 10 s) (Fig. 5-57a). As previously observed in other metal oxides and anatase TiO_2, the rise and decay processes when the light is turned on and off are faster when light intensity increases.[291,294] When the light is turned off the slow decay in TAS signal is most likely attributed to multiple holes that accumulate at the surface for the water splitting reaction.[291] Unlike LI-SEC signals, significantly faster changes in photocurrent were observed when the light was turned on and off (Fig. 5-57b). For instance, photocurrent values plateau almost at the same time that the light was turned on, and quickly decreased to zero values when the light was turned off after 5 s of continuous light illumination.

Fig. 5-58 shows the relationship that exists between LI-SEC signals and photocurrent densities as a function of light intensity.

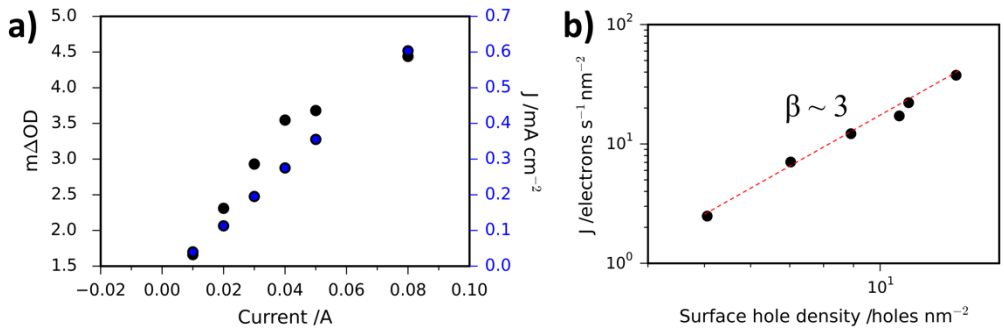

Fig. 5-58 (a) Steady state light-induced signal and photocurrent density *vs.* current used to monitor light intensities. (b) log-log plot of the rate of reaction *vs.* surface hole density.

Photocurrent density values follow a linear relationship with light intensity, whereas a non-linear relationship is observed for light induced signals (Fig. 5-58a). To further analyze these differences a kinetic model described in previous publications has been applied.[294] Briefly, this model is described in equation 5-4:

$$\frac{dp_s}{dt} = J_{holes} - k_{WO}.p_s^{\beta} \qquad 5\text{-}4$$

where the variation of surface holes (p_s) is equal to the incoming hole flux (J_{holes}) minus the holes transferred to the electrolyte for the water oxidation reaction. p_s values can be calculated from light induced signals and assuming a hole extinction coefficient of TiO_2 of 1980 M^{-1} cm^{-1}. In this model the hole consumption from back electron recombination is neglected, since at high applied bias it is assumed that this recombination is minimal. This model also assumes a Faradaic efficiency of 1. Assuming steady state conditions (such as the ones employed for LI-SEC measurements) this model can be further simplified to:[294]

$$\frac{dp_s}{dt} = 0;\ J_{holes} = k_{WO}.p_s^{\beta} \qquad 5\text{-}5$$

in which a log-log plot of equation 5-5 results in a linear relationship where β (order of reaction) and k_{wo} (rate of reaction) can be easily extracted from the gradient and the intercept of the log-log plot, respectively (Fig. 5-58b). From the fitting, a third-order reaction is obtained ($\beta = 2.67 \pm 0.12$) with a rate water oxidation constant of ($k_{wo} = 1.46 \pm 0.12\ holes^{-2}\ s^{-1}\ nm^4$). These results agree well with previous publications with anatase TiO_2, where β~3 was also found under the same experimental conditions employed (1M NaOH, pH=13.6). [291]

Chapter 6. Fe_2TiO_5 based photoanodes grown by aerosol-assisted chemical vapor deposition

6.1 Publication: Zn doped Fe_2TiO_5 photoanodes grown by aerosol-assisted chemical vapor deposition

6.1.1 Preface

Fe_2TiO_5, a hybrid of Fe_2O_3 and TiO_2, has recently awakened great interest within the scientific community. Being a combination of two of the most studied metal oxides in the field of water splitting, this material can overcome some of the main limitations encountered in the corresponding metal oxides. For instance, Fe_2TiO_5 has a band gap of 1.9-2.1 eV, which corresponds to the visible region of the solar spectrum and it shows better charge separation efficiencies than Fe_2O_3 and TiO_2, as briefly discussed in Chapter 2.

Although many publications have emerged based on Fe_2TiO_5 in the last five years, most of them have shown that PEC efficiencies are mainly improved when a thin layer of Fe_2TiO_5 is deposited on top of either TiO_2 or Fe_2O_3 photoanodes to form heterojunctioned systems.[65] In fact, PEC systems consisting only of Fe_2TiO_5 have sometimes shown onset potentials of 1.0 V_{RHE} and maximum photocurrent performances of 0.2 mA cm^{-2} at 1.23 V_{RHE}, being worse that what could be achieved in pristine TiO_2 and Fe_2O_3.[66] Therefore, a feasible approach for improving the performance of Fe_2TiO_5 photoanodes could be doping, since it could allow a modification of the electronic structure of the material resulting in improved PEC performances.

In this work, we demonstrate for the first time Zn-doped Fe_2TiO_5 based photoanodes grown by AACVD. After long annealing temperatures, Fe_2TiO_5 based photoanodes were formed, resulting in an improvement of the PEC performance after incorporation of Zn^{2+} ions into the system. Through the use of extensive characterization techniques such as XPS, UPS, and EIS methods it is demonstrated how addition of Zn^{2+} promotes an upward shift of the energy Fermi level (E_F) and an increase in charge carrier concentration, which overall results in an enhanced PEC performance from *ca.* 0.2 to 0.6 mA cm^{-2} at 1.23 V_{RHE}, for pristine and Zn-doped Fe_2TiO_5 photoanodes, respectively.

In summary, this work highlights the benefits that doping Fe_2TiO_5 with transition metals such as Zn^{2+} has towards its electronic properties and PEC performance and opens up a new path for exploiting doped Fe_2TiO_5 systems.

6.1.2 Declaration of authorship

This declaration concerns the article entitled:				
Zn doped Fe_2TiO_5 photoanodes grown by aerosol-assisted chemical vapor deposition				
Publication status (tick one)				
Draft manuscript X	**Submitted**	**In review**	**Accepted**	**Published**
Publication details (reference)	M. Regue, I. Y. Ahmet, P. S. Bassi, A. L. Johnson, S. Eslava and F.F. Abdi, *draft manuscript*.			
Copyright status (tick the appropriate statement)				
I hold the copyright for this material ☐	Copyright is retained by the publisher, but I have been given permission to replicate the material here ☐			
Candidate's contribution to the paper (provide details, and also indicate as a percentage)	• Formulation of ideas: 45% The candidate, I.Y.A and P. S. B contributed to the formulation of the ideas. • Design of methodology: 40% The candidate, I.Y.A and P. S. B were responsible for designing the methodology of this work. • Experimental work: 80% The candidate performed most of the laboratory work, including material synthesis, deposition and characterization. The candidate participated in acquisition of SEM images and XPS – UPS data. 80% of the experimental work was performed in Helmholtz Zentrum Berlin and 20% at the University of Bath. • Presentation of data in journal format: 90% The candidate collected the data and drafted all the manuscript. The manuscript was then revised and edited by S. Eslava and approved by co-authors.			

Statement from Candidate	This paper reports on original research I conducted during the period of my Higher Degree by Research candidature.		
Signed		**Date**	23/09/2019

6.1.3 Article

Zn doped Fe_2TiO_5 photoanodes grown by aerosol-assisted chemical vapor deposition

Miriam Regue,[a,b] Ibbi Y. Ahmet,[c*] Prince Saurabh Bassi,[c*] Andrew L. Johnson,[d] Salvador Eslava[a,b*] and Fatwa F. Abdi[c*]

[a]*Centre for Sustainable Chemical Technologies, University of Bath, Claverton Down, Bath, BA2 7AY, UK*

[b]*Department of Chemical Engineering, University of Bath, Claverton Down, Bath, BA2 7AY, UK. E-mail: s.eslava@bath.ac.uk*

[c]*Helmholtz-Zentrum Berlin für Materialien und Energie Gmbh, Institute for Solar Fuels, Hahn-Meitner-Platz 1, Berlin 14109, Germany*

[d]*Department of Chemistry, University of Bath, Claverton Down, Bath, BA2 7AY, UK*

Abstract

Photoelectrochemical water splitting is an environmentally-friendly and promising technology for the production of solar fuels. TiO_2 and α-Fe_2O_3 are two of the most studied semiconductors in the field, but they possess several disadvantages that limits their practical application. When combining these two materials, Fe_2TiO_5 can be formed, which possesses more favorable features for the water splitting reaction. Herein, we present the formation of Fe_2TiO_5 photoanodes prepared using aerosol-assisted chemical vapor deposition. When doped with Zn^{2+}, their photoelectrochemical performance increases significantly, from *ca.* 0.2 to 0.6 mA cm^{-2} at 1.23 V_{RHE} outperforming pristine Fe_2TiO_5 photoanodes. Characterization techniques such as XPS, UPS and Mott-Schottky plots reveal that Zn^{2+} plays a role in modifying the electronic properties of Fe_2TiO_5 photoanodes increasing the carrier concentration and leading to an upward shift of the energy Fermi level. In addition, charge transfer efficiency calculations and PEIS measurements reveal improved charge transfer properties for Zn-doped-Fe_2TiO_5, overall demonstrating a promising approach for the design of better-performing Fe_2TiO_5 based photoanodes.

Introduction

Recent reports on climate change, such as the one released by the international panel on climate change (IPCC), have highlighted the urgent need for changing our current energy portfolio highly based on fossil fuels to a more sustainable one where solar energy plays a key role.[4] Solar energy is abundant, reaching the Earth's surface approximately 3.4 10^{24} J in one

year, but we need to develop technologies such as photoelectrochemical (PEC) water splitting to store the solar energy in the chemical bonds of solar fuels.[295] Among the different light harvesting materials used in PEC devices, α-Fe_2O_3 (hematite) and TiO_2 are frequently studied as photoanode absorbers. α-Fe_2O_3 has a band gap of 2.0-2.2 eV, so it can harvest the visible region of the solar spectrum and has the potential to achieve solar-to-fuel conversion efficiencies in the range of 12.7-16.8 %.[56,296] In addition, it is abundant on the Earth's crust and non-toxic. TiO_2, with large minority carrier diffusion length, is also abundant and shows chemical and thermal stability, low cost, good electronic properties and long durability.[88,183] Nevertheless, both materials still possess several challenges for their practical application in PEC devices. For instance, α-Fe_2O_3 suffers from a relatively low absorption coefficient, large overpotential for water oxidation, poor majority carriers conductivity and short diffusion lengths of minority carriers.[56] On the other hand, TiO_2 has a relatively large band gap (3.0-3.2 eV) that only absorbs the UV region of the solar spectrum (~ 4%) and suffers from a fast electron and hole recombination.[129]

Several approaches have been attempted to tackle the drawbacks of α-Fe_2O_3 and TiO_2. For instance, α-Fe_2O_3 has been improved by loading of co-catalysts such as Co-Pi, $CoFeO_x$ or IrO_2, by nanostructuring (as nanowires, nanorods…), through nanoheterostructures or by elemental doping.[56,218,297–299] Along the same lines, TiO_2 has been improved by doping with transition metals (Ta, Fe, and Mo among others), designing nanoheterostructures and nanostructuring.[107,108,139,300,301] Despite the progress, there is still plenty of room for improving these materials to reach enough solar-to-hydrogen conversion efficiencies that would facilitate commercialization. Currently, the highest solar-to-hydrogen efficiency achieved in PEC systems is of 10 % for more than 40 h.[302]

The preparation of Fe_2TiO_5, iron titanate pseudobrookite, a hybrid of α-Fe_2O_3 and TiO_2 with Fe-O-Ti bonds, offers an *n-type* semiconductor with synergistic properties such as a smaller band gap of 1.9-2.1 eV and better separation of photocarriers, together with stability in aqueous media.[66,67] Several synthetic methods have been employed to prepare thin films of Fe_2TiO_5 for PEC applications. In 2014, E. Courtin *et al.* reported for the first time the Fe_2TiO_5 phase in thin films, prepared by sol-gel synthesis along with a dip coating process.[303] Depending on the Fe:Ti ratio used in the precursors, up to three different phases were observed in final films: TiO_2 anatase, α-Fe_2O_3 hematite and Fe_2TiO_5 pseudobrookite. Achieving only pseudobrookite with traces of hematite required the highest $Fe_{0.3}$:$Ti_{0.7}$ molar precursor ratio. Alternatively, P. S. Bassi *et al.* synthesized a pure phase of Fe_2TiO_5 using a solvothermal method and concluded that Fe_2TiO_5 has better band level positions than α-Fe_2O_3 for water splitting applications.[66] The deposition of Fe_2TiO_5 on top of α-Fe_2O_3 has also been attempted. In 2014 Q. Liu *et al.* reported the synthesis of Fe_2TiO_5 on top of aligned TiO_2 nanotubes grown

by electrochemical deposition.[68] The authors showed a significant improvement in the PEC performance of TiO_2 by the addition of a thin layer of Fe_2TiO_5 and CoO_x catalyst. This increased the incident photon to current efficiency (IPCE) at 400 nm and 1.23 V_{RHE} from 5 to 40 %, which was mainly attributed to anisotropic charge carrier transport and reduced charge carrier transfer resistance.[68] Similarly, J. Deng *et al.* demonstrated that a thin layer of Fe_2TiO_5 on α-Fe_2O_3 photoanodes enhanced IPCE from 8 to 19 % at 400 nm and 1.23 V_{RHE} owing to a reduced accumulation of photogenerated holes commonly observed in α-Fe_2O_3 photoanodes.[69] C. Li *et al.* also added 4 nm of Fe_2TiO_5 by atomic layer deposition on α-Fe_2O_3 increasing IPCE at 400 nm and 1.23 V_{RHE} from 5 to 16 %.[304] P. S. Bassi *et al.* demonstrated crystalline heterojunction of Fe_2TiO_5 and α-Fe_2O_3 deposited by solvothermal technique. This type II band alignment between the two oxides resulted in an enhancement of IPCE at 400 nm and 1.23 V_{RHE} from 3 to 17.5 %.[70] Surface state passivation by Al^{3+} along with incorporation of FeOOH as a cocatalyst also resulted successful for improving PEC performance of Fe_2TiO_5 photoanodes, reaching photocurrent density values of 0.52 mA cm^{-2} at 1.23 V_{RHE}.[305]

Doping metal oxide semiconductors with foreign elements is an effective approach to tune their properties. For example, the band gap of TiO_2 has been decreased with Mo, N, C, and others.[128,300,306] Zn^{2+} doping has been explored in both α-Fe_2O_3 and TiO_2, resulting in a cathodic shift of the onset potential of α-Fe_2O_3 or an upwards shift of the Fermi level of TiO_2 providing more electrons to the conduction band.[307–311] To the best of our knowledge the effect of doping Fe_2TiO_5 has rarely been studied, especially for PEC applications. In 2017, O. Linnik *et al.* reported the synthesis of Fe_2TiO_5 thin films doped with N for photocatalytic degradation of pollutants, showing an enhancement of the photocatalytic activity in comparison to non-doped Fe_2TiO_5.[312] Further experiments and characterization of these N-doped Fe_2TiO_5 films also found that N helps stabilize the Fe_2TiO_5 phase at higher annealing temperatures, avoiding segregation of the corresponding single metal oxides.[313]

In this publication, we report the synthesis of Zn-doped Fe_2TiO_5 thin films grown by aerosol-assisted chemical vapor deposition (AACVD). Photoelectrochemical measurements reveal that Zn-doped Fe_2TiO_5 films outperform significantly the pristine Fe_2TiO_5, Fe_2O_3 and Zn-doped Fe_2O_3 films. Characterization techniques such as X-ray photoelectron spectroscopy, (photoelectrochemical) impedance spectroscopy and ultraviolet photoelectron spectroscopy reveal that addition Zn^{2+} modifies significantly the electronic properties of Fe_2TiO_5 contributing in an overall improvement of the charge transfer processes giving rise to better photoelectrochemical performances.

Experimental

Materials

Titanium (IV) isopropoxide, iron (III) acetylacetonate, zinc acetate dihydrate, ethyl acetate and methanol were provided by Sigma Aldrich. Fluorine doped tin oxide (FTO) coated glass substrates (TEC 7) were provided by Pilkington. These substrates were cleaned ultrasonically with a soap solution followed by ethanol and deionized water and finally dried with compressed air.

Preparation of Fe_2TiO_5, Zn-doped Fe_2TiO_5, Fe_2O_3 and Zn-doped Fe_2O_3

All photoanodes were prepared using AACVD. The aerosol droplets were generated using a TSI Model 3076 Constant Output atomizer using argon as a carrier gas. Pristine Fe_2TiO_5 and Zn-doped Fe_2TiO_5 were prepared following a modification of a procedure previously described.[314] Typically, titanium (IV) isopropoxide (1.478 mL, 5.0 mmol) was dissolved in 10 mL of methanol and mixed together with a solution of iron (III) acetylacetonate (3.531 g, 10 mmol) in 100 mL of ethyl acetate. Zn-doped Fe_2TiO_5 photoanodes were prepared by adding zinc acetate dihydrate (0.0549 g, 0.25 mmol) to the previous iron and titanium solution. For comparison, Fe_2O_3 and Zn-doped Fe_2O_3 photoanodes were also prepared removing the titanium precursor from the solution. Therefore, for Fe_2O_3 samples a solution of iron (III) acetylacetonate (3.531 g, 10 mmol) in 100 mL of ethyl acetate and 10 mL of methanol was used and for Zn-doped Fe_2O_3 photoanodes the same solution with additional zinc acetate dihydrate (0.0549 g, 0.25 mmol). All samples were deposited for 1 h at 450 °C. The obtained films were annealed in air at 500°C for 12 h and 650 °C for 2 h using a heating rate of 10 °C min^{-1}. The resultant photoanodes were denoted as Fe_2TiO_5 and Fe_2O_3 for the pristine samples and Fe_2TiO_5-Zn and Fe_2O_3-Zn for the Zn^{2+}-doped samples.

Characterization

X-ray diffraction (XRD) patterns were collected from 10 to 60° (2θ) using a Bruker D8 diffractometer with Cu Kα (0.154 nm) radiation. Measurements were carried out in a grazing incidence geometry. The coherent diffraction domain size was calculated using the Scherrer equation at the (2 0 0) and (1 0 1) for Fe_2TiO_5 and Fe_2O_3 samples, respectively. Raman spectroscopy was performed on a Renishaw inVia system using a 532 nm diode-pumped solid-state laser (DPSS) manufactured by Cobolt. A 50x long distance objective was used to focus the laser beam onto the sample. UV-Vis measurements were carried out in a Lambda 950 spectrometer (Perkin Elmer) with an integrating sphere (150 mm InGaAS). The samples were mounted in the center. Diffuse-reflectance UV-Vis measurements were performed in an Agilent Cary 100 spectrophotometer. Field-emission scanning electron microscopy

micrographs (FE-SEM) were acquired using a JEOL FESEM6301F instrument. X-ray photoelectron spectroscopy (XPS) was performed with a monochromatic Al Kα X-ray-source (1486.74 eV, Specs Focus 500 monochromator). C 1s was used for internal charge correction. Ultraviolet photoelectron spectroscopy (UPS) was carried out with a He I source (E = 21.218 eV) in the same chamber. A hemispherical analyzer (Specs Phoibos 100) was used for both XPS and UPS measurements. The base pressure of the system was ∼10−9 mbar.

PEC measurements

Photoelectrochemical (PEC) performance of photoanodes was measured under simulated solar light using a WACOM Super Solar Simulator (Model WXS-505-5H, AM 1.5, Class AAA) and an EG&G Princeton Applied Research Potentiostat/Galvanostat (Model 273A). PEC cells were prepared using a three- electrode configuration with Pt as the counter electrode, a silver chloride reference electrode (Ag/AgCl-reference electrode, XR300, Radiometer Analytical, $E_{Ag/AgCl}$=0.197 V_{RHE}) and the as-prepared photoanodes as the working electrode. Illumination was directed towards the back of the photoanode (Glass-FTO-sample). 1 M NaOH (pH=13.6) was used as electrolyte. All the measured potentials ($E_{Ag/AgCl}$) were converted to RHE potentials (E_{RHE}) using the Nernst equation. J-V curves for charge injection and charge separation efficiencies were recorded using the above-mentioned configuration but adding 10%(v/v) of H_2O_2 in the 1M NaOH electrolyte. Charge injection efficiencies were calculated using the following equation:

$$\eta_{inj} = \frac{J_{photo\ (NaOH)}}{J_{photo\ (NaOH+H2O2)}} \qquad 6\text{-}1$$

and charge separation efficiencies were calculated using equation 6-2:

$$\eta_{sep} = \frac{J_{photo\ (NaOH)}}{J_{max}} \qquad 6\text{-}2$$

where $J_{photo(NaOH)}$ and $J_{photo(NaOH+H2O2)}$ are the measured photocurrent density values in 1M NaOH and 1M NaOH plus H_2O_2, respectively. J_{max} is the theoretical maximum photocurrent density obtained when all the absorbed photons are converted into current density and it is calculated by integrating the absorbance spectra with standard AM 1.5G spectrum.[70,286]

Incident photon-to-current efficiency (IPCE) measurements were performed using an Xe lamp (LOT, LSH302), an Acton Research monochromator (Spectra Pro 2155) and an electronic shutter (Uniblitz LS6). The intensity of the monochromated light was measured by a calibrated photodiode (PD300R-UV, Ophir) just after a clean FTO-glass substrate placed at the working

electrode position, in the absence of PEC cell quartz window or PEC cell electrolyte. The IPCE was calculated using the equation below:

$$IPCE\ (\lambda) = \frac{|j\ (mA\ cm^{-2})|\ \times 1239.8\ (V\ nm)}{P_{mono}\ (mW\ cm^{-2}) \times\ \lambda\ (nm)} \qquad 6\text{-}3$$

where j is the photocurrent density measured under single wavelength (λ) light illumination and P_{mono} is the incident irradiation power.

Absorbed photon-to-current efficiency (APCE) was calculated according to:

$$APCE\ (\lambda) = \frac{IPCE(\lambda)}{1 - 10^{-\mathrm{A}(\lambda)}} \qquad 6\text{-}4$$

Where A is the absorbance measured at a wavelength λ .

PEC impedance spectroscopy (PEIS) was carried out under simulated sunlight (AM 1.5G, 100 mW cm^{-2}) using a CompactStat. Potentiostat (Ivium technologies). Measurements were performed in a frequency range from 10^5 to 0.1 Hz, with an AC voltage amplitude of 10 mV at a potential range of 0.6 to 1.2 V_{RHE} with 0.05V steps, in 1M NaOH. EIS measurements in the dark were also measured to obtain Mott-Schottky plots. These measurements were performed at a fixed frequency of 100 and 1000 Hz based on the following equation:

$$\frac{1}{C^2} = \frac{2}{N_d e \varepsilon_0 \varepsilon}\left[(U_s - U_{Fb}) - \frac{K_B T}{e}\right] \qquad 6\text{-}5$$

where C is the semiconductor depletion layer capacitance, N_d the electron carrier density, e the elemental charge value, ε_0 the permittivity of the vacuum, ε the relative permittivity of the semiconductor, U_s the applied potential, U_{Fb} the flat band potential, and $[K_BT/e]$ a temperature-dependent correction term. The electron carrier density (N_D) was obtained from Mott-Schottky plots using the following equation:

$$N_D = \left(\frac{2}{e\varepsilon\varepsilon_0}\right)\left(\frac{d\left(1/C^2\right)}{d(U_s)}\right)^{-1} \qquad 6\text{-}6$$

where ε=100 and 80 for Fe_2TiO_5 and Fe_2O_3, respectively, and $[d(1/C^2)/d(Us)]^{-1}$ is the inverse of the slope obtained from Mott-Schottky plot.

Results and discussion

Fig. 6-1 shows the XRD patterns of Fe_2TiO_5, Fe_2TiO_5-Zn, Fe_2O_3 and Fe_2O_3-Zn photoanodes prepared on FTO. Fe_2TiO_5 and Fe_2TiO_5-Zn show the characteristic diffraction peaks of Fe_2TiO_5 pseudobrookite (JCPDS 009-0182) along with some traces of α-Fe_2O_3 (JCPDS 006-

0502) and TiO_2 rutile (diffraction peak at 27.6°, JCPDS 88- 1173). No diffraction peaks corresponding to ZnO or $ZnFe_2O_4$ are observed for Fe_2TiO_5-Zn and Fe_2O_3-Zn, suggesting that Zn^{2+} is homogeneously dissolved in the solid or accumulated in amorphous regions. A broad peak at *ca.* 56° corresponding to $Fe_{1.7}Ti_{0.23}O_3$ is observed in Fe_2TiO_5.[315] Incorporation of Zn^{2+} enhances the crystallinity of Fe_2TiO_5 leading to sharper and narrower diffraction peaks for Fe_2TiO_5 phase. The coherent crystal domain sizes calculated from the full width at half maximum at (2 0 0) diffraction peak for Fe_2TiO_5 and Fe_2TiO_5-Zn are of *ca.* 21 nm. Similarly, crystal domain sizes of Fe_2O_3 and Fe_2O_3-Zn calculated at (1 1 0) diffraction plane are of *ca.* 32 nm. Interestingly, the incorporation of Zn^{2+} did not modify the crystal domain sizes of both doped and undoped Fe_2TiO_5 and Fe_2O_3.

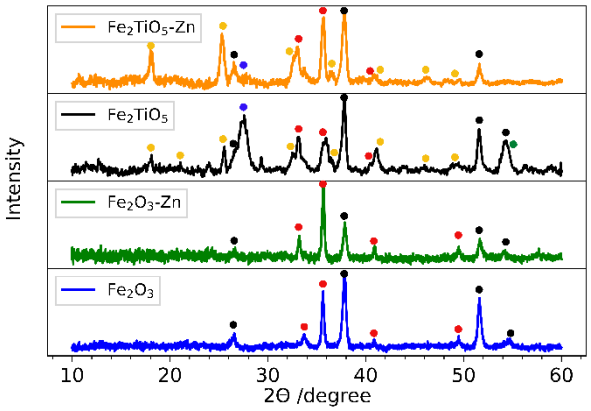

Fig. 6-1 XRD patterns of Fe_2TiO_5-Zn, Fe_2TiO_5, Fe_2O_3 and Fe_2O_3-Zn. Yellow dot: Fe_2TiO_5, red dot: Fe_2O_3, blue dot: TiO_2 rutile, green dot: $Fe_{1.7}Ti_{0.23}O_3$ and black dot: FTO.

The calculated lattice parameters obtained from the XRD patterns are shown in Table 6-1. Small variations are observed in lattice parameters. For instance, for Fe_2TiO_5 samples (orthorhombic system), small differences are observed mainly in *b* and *c* parameters. Similarly, for Fe_2O_3 samples (hexagonal system) small differences are observed in *c*.

Table 6-1 Calculated lattice parameters.

Sample	*a* (Å)	*b* (Å)	*c* (Å)
[a]Fe_2O_3	5.058	n/a	13.455
[a]Fe_2O_3-Zn	5.032	n/a	13.731
[b]Fe_2TiO_5	9.801	9.946	3.729
[b]Fe_2TiO_5-Zn	9.824	9.884	3.763

[a] Lattice parameters calculated considering a hexagonal crystal structure.
[b] Lattice parameters calculated considering an orthorhombic crystal structure.

Raman spectra of Fe_2TiO_5, Fe_2TiO_5-Zn, Fe_2O_3 and Fe_2O_3-Zn are shown in Fig. 6-2. Only Raman bands ascribed to α-Fe_2O_3 are observed for both Fe_2O_3 and Fe_2O_3-Zn, in agreement with XRD patterns. Particularly, sharp bands at 223.7 and 494.4 cm^{-1} corresponding to A_{1g}

vibration modes and 243, 290.8, 408.3 and 607.1 cm^{-1} belonging to E_g vibration modes are observed. [316,317] Additional bands at 204, 342, 410 and 800 corresponding to vibrational modes of Fe_2TiO_5 are observed for Fe_2TiO_5 and Fe_2TiO_5-Zn agreeing well with XRD results.[68,318–320]

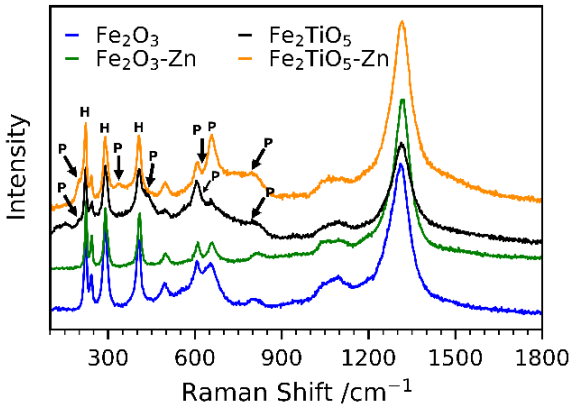

Fig. 6-2 Raman spectra of Fe_2TiO_5-Zn, Fe_2TiO_5, Fe_2O_3 and Fe_2O_3-Zn. P: Fe_2TiO_5 (pseudobrookite) and H: Fe_2O_3 (hematite).

UV-Vis spectra of the as-prepared photoanodes are shown in Fig. 6-3. Both undoped samples, Fe_2TiO_5 and Fe_2O_3, exhibit similar absorption edges at ~ 580 nm, whereas Zn doped samples, Fe_2TiO_5-Zn and Fe_2O_3-Zn, exhibit a red shift of the absorption edge to ~ 590 nm. Higher absorption values are observed for the Zn-doped samples, in agreement with the slightly darker color observed in photographs of the photoanodes (see inset of Fig. 6-3a). Accordingly, Tauc plot analysis shown in Fig. 6-3b reveal smaller band gap values for Zn^{2+} doped samples, being of 2.09 and 2.10 eV for Fe_2O_3-Zn and Fe_2TiO_5-Zn, respectively, in comparison with 2.13 eV for both Fe_2O_3 and Fe_2TiO_5 undoped samples. We attribute the slight decrease in the band gap to the formation of new molecular orbitals below the CB with the addition of Zn.[321] Band-gap values around 2.1 eV are consistent with previously reported band-gap calculations of Fe_2TiO_5 and Fe_2O_3.[59,66,322]

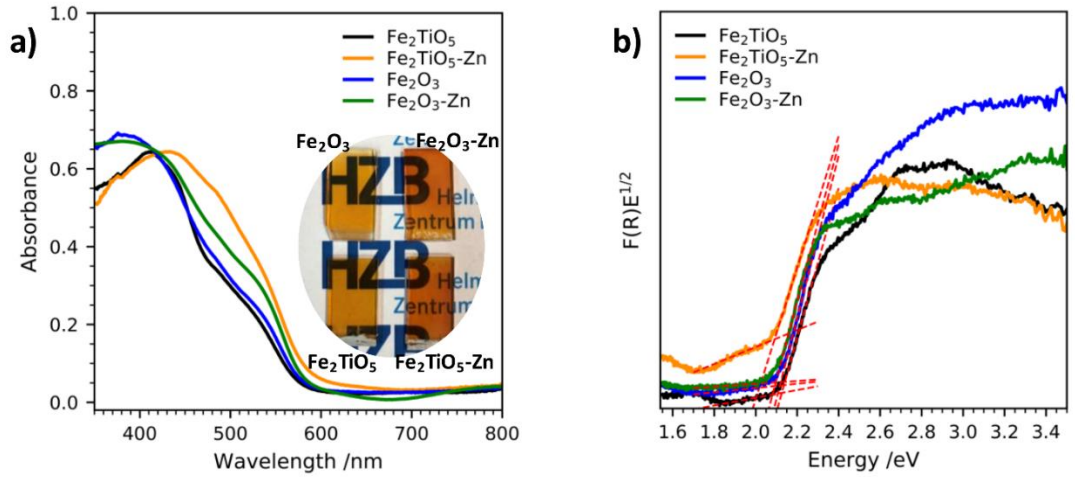

Fig. 6-3 UV- Vis absorbance spectra and (b) Tauc plots measured *via* diffuse reflectance UV-Vis spectroscopy of Fe_2TiO_5-Zn, Fe_2TiO_5, Fe_2O_3 and Fe_2O_3-Zn. Insets in (a) show photographs of all photoanodes prepared.

Fig. 6-4 shows SEM micrographs of Fe_2TiO_5, Fe_2TiO_5-Zn, Fe_2O_3 and Fe_2O_3-Zn. Two different morphologies are observed for Fe_2O_3 and Fe_2TiO_5 based photoanodes: Fe_2TiO_5 and Fe_2TiO_5-Zn (Fig. 6-4 a,b) show a very fine structure consisting of small particles whereas larger particles with a 'worm'-like morphology are depicted for both Fe_2O_3 and Fe_2O_3-Zn samples (Fig. 6-4 c,d). Importantly, the addition of Zn^{2+} did not modify significantly the final morphology of the films. Cross-sectional SEM micrographs (Fig. 6-5) indicate that films' thickness is of 420-560 nm for Fe_2TiO_5 based photoanodes whereas slightly thinner 190 nm films are obtained for Fe_2O_3 based films. Incorporation of Zn^{2+} also results in the formation of more compact films, when compared to pristine Fe_2O_3 and Fe_2TiO_5.

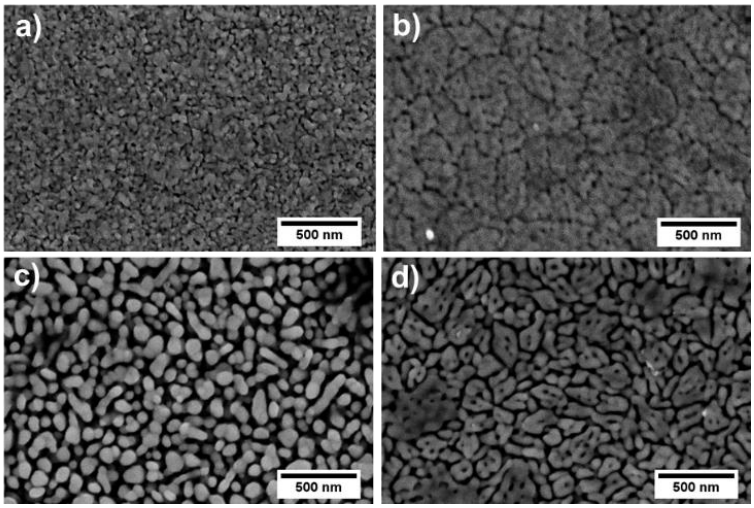

Fig. 6-4 SEM micrographs of (a) Fe_2TiO_5, (b) Fe_2TiO_5-Zn, (c) Fe_2O_3 and (d) Fe_2O_3-Zn.

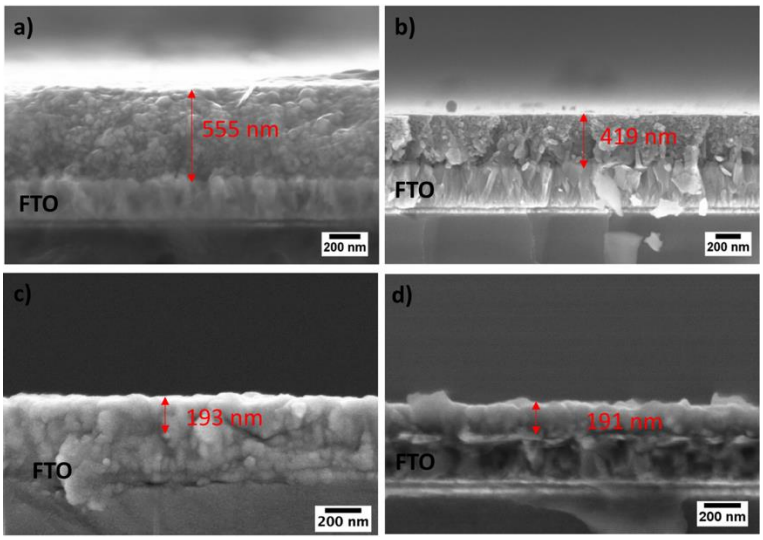

Fig. 6-5 SEM cross-sectional micrographs of (a) Fe_2TiO_5, (b) Fe_2TiO_5-Zn, (c) Fe_2O_3 and (d) Fe_2O_3-Zn.

The composition and chemical state of the surface of the films were evaluated using XPS analysis. Zn $2p_{3/2}$ high-resolution XPS spectra of Fe_2TiO_5-Zn and Fe_2O_3-Zn are shown in Fig. 6-6a. Both samples show the characteristic peak of Zn^{2+} at *ca.* 1020 eV. The signal for Fe_2TiO_5-Zn is significantly lower than Fe_2O_3-Zn. Survey XPS spectra indicate that Fe_2TiO_5-Zn and Fe_2O_3-Zn contains *ca.* 0.11 and 0.60 at% of Zn^{2+} on the surface, respectively. The presence of Zn^{2+} in Fe_2TiO_5-Zn was further confirmed using SEM-EDX (Fig. 6-7).

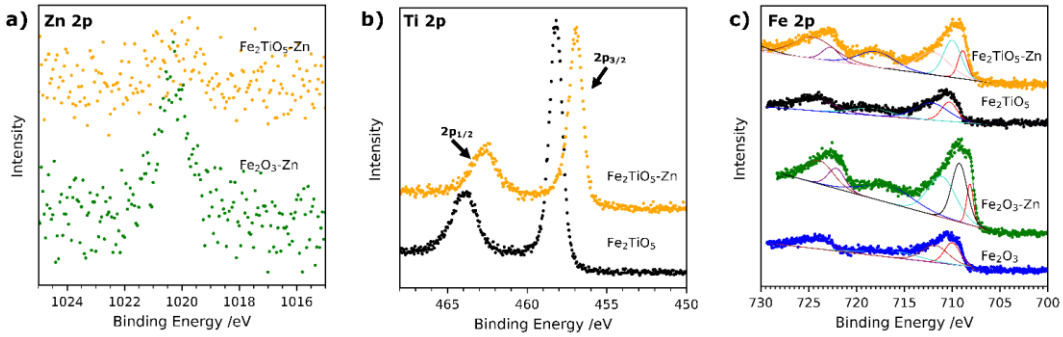

Fig. 6-6 XPS spectra of (a) Zn 2p, (b) Ti 2p and (c) Fe 2p of Fe_2TiO_5-Zn, Fe_2TiO_5, Fe_2O_3 and Fe_2O_3-Zn. Scattered points correspond to raw data acquired in the measurements and solid lines to the fitted values.

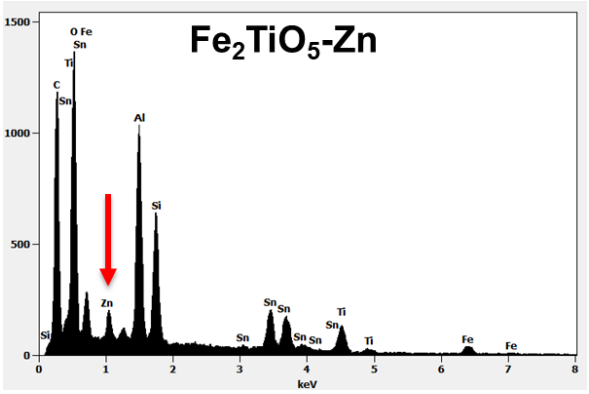

Fig. 6-7 SEM-EDX spectrum of Fe_2TiO_5-Zn.

Ti 2p high resolution XPS spectra of Fe_2TiO_5 and Fe_2TiO_5-Zn are shown in Fig. 6-6b. In both samples, the two characteristic peaks of Ti^{4+} corresponding to Ti $2p_{1/2}$ and Ti $2p_{3/2}$ are observed.[251] Interestingly, a shift towards lower binding energies is observed for Fe_2TiO_5-Zn, suggesting the possibility of oxygen vacancies in the film to compensate charge imbalance introduced into the lattice due to addition of Zn^{2+}.[323,324] Due to the similar difference in ionic radii between Zn^{2+} (0.74 Å) and Ti^{4+} (0.605 Å), Zn^{2+} ions are most likely to be occupying Ti^{4+} positions in the Fe_2TiO_5 lattice structure, without distorting significantly the crystal structure, as demonstrated in calculated lattice parameters (Table 6-1).[321] These results agree well with the absence of changes in crystal domain sizes calculated from XRD patterns with the addition of Zn^{2+} ions. Fig. 6-6c shows Fe 2p high resolution XPS spectra of all photoanodes. All samples show the characteristic peaks of Fe $2p_{1/2}$ and Fe $2p_{3/2}$ at 725 and 711 eV, respectively, along with satellite signals at around 8 eV above the Fe $2p_{3/2}$, corresponding to Fe^{3+}.[325] The characteristic band at 715 eV corresponding to Fe^{2+} was not observed which indicates the unique presence of Fe^{3+} ions on the surface of the samples.[326,327]

The PEC performance of Fe_2TiO_5, Fe_2TiO_5-Zn, Fe_2O_3 and Fe_2O_3-Zn was evaluated under simulated sunlight (Fig. 6-8a). The highest photocurrent density was for Fe_2TiO_5-Zn, where photocurrent densities of *ca.* 0.6 mA cm^{-2} at 1.23 V_{RHE} were achieved. Conversely, significantly lower photocurrent densities values (*ca.* 0.2 mA cm^{-2} at 1.23 V_{RHE}) were observed for Fe_2TiO_5, Fe_2O_3 and Fe_2O_3-Zn. Slightly higher photocurrent density values and better onsets are observed for Fe_2O_3-Zn in comparison to Fe_2O_3 (Fig. 6-8a and Fig. 6-9 c-d). There are high photocurrent spikes, transients, observed for Fe_2O_3 and Fe_2O_3-Zn in comparison with Fe_2TiO_5 and Fe_2TiO_5-Zn (Fig. 6-9). The anodic transients in photoanodes typically indicate the trapping of holes in surface states which initially minimizes electron-hole recombination and allows transfer of electrons to the external circuit.[328] Upon saturation of surface states with holes, electron-hole recombination occurs and photocurrent measured decreases. When light is switched off, surface states are discharged so cathodic transients are observed. Based on this, Fe_2TiO_5 and Fe_2TiO_5-Zn show a lower presence of surface states, since they show smaller photocurrent transients.

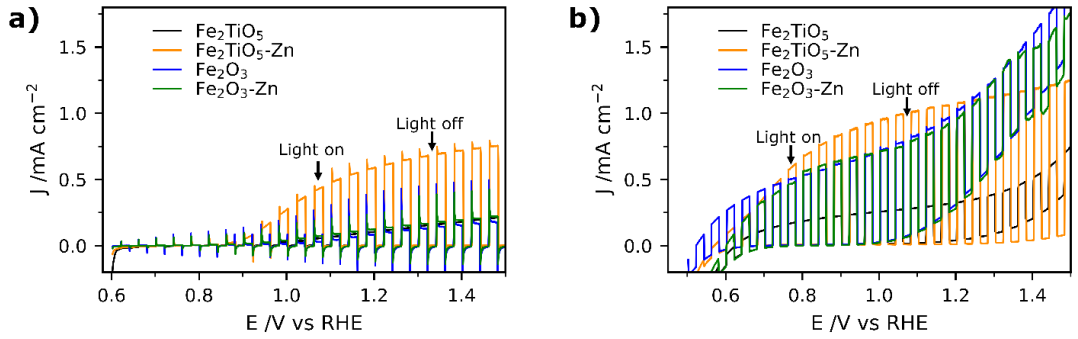

Fig. 6-8 (a) Photocurrent potential curves in 1 M NaOH (pH=13.6) and (b) in 1 M NaOH + 10 % (v/v) H_2O_2 (pH=11.9) of Fe_2TiO_5-Zn, Fe_2TiO_5, Fe_2O_3 and Fe_2O_3-Zn. All measurements were performed under chopped AM 1.5 illumination.

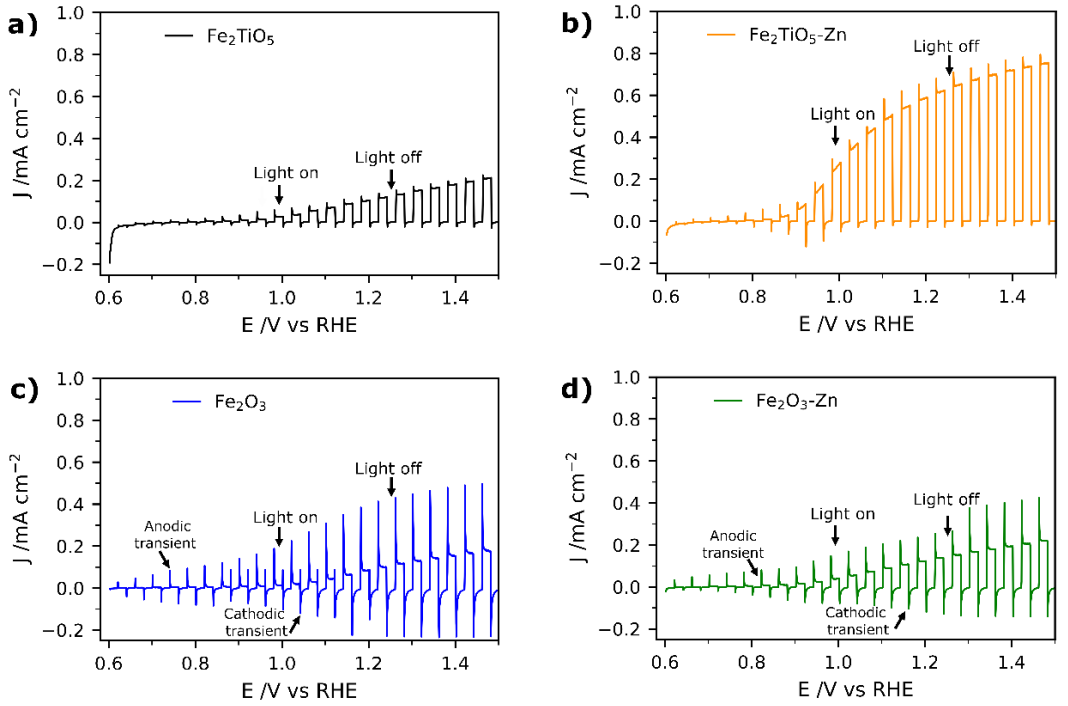

Fig. 6-9 Photocurrent potential curves of (a) Fe_2TiO_5, (b) Fe_2TiO_5-Zn, (c) Fe_2O_3 and (d) Fe_2O_3-Zn highlighting the anodic and cathodic transients. All measurements were performed in 1M NaOH (pH=13.6) under chopped AM 1.5 illumination.

To further investigate charge transport efficiencies, PEC performances were measured in the presence of a hole scavenger (H_2O_2) and results are shown in Fig. 6-8b. Under these conditions, photocurrent transients disappear since all the holes reaching the surface of the sample are transferred to the electrolyte. With the presence of a hole scavenger (H_2O_2), all photocurrent density values are higher, as expected. The highest photocurrent density is observed for Fe_2TiO_5-Zn being of *ca.* 1.1 mA cm^{-2} at 1.23 V_{RHE}. Significantly lower photocurrent density values are obtained for Fe_2O_3, Fe_2O_3-Zn and Fe_2TiO_5, being of *ca.* 0.6 mA cm^{-2} for both Fe_2O_3 and Fe_2O_3-Zn and *ca.* 0.3 mA cm^{-2} for Fe_2TiO_5 at 1.23 V_{RHE}.

Charge separation and charge injection efficiencies have been calculated comparing photocurrents with and without H_2O_2 hole scavenger and results are shown in Fig. 6-10. As firstly reported by H. Dotan *et al.*, charge separation efficiency refers to the fraction of photogenerated holes that do not recombine in the bulk of the photoanode and successfully reach the surface-electrolyte interface, whereas charge injection efficiency refers to the holes that once on the surface-electrolyte interface are injected to the electrolyte for the water oxidation reaction instead of being trapped in surface states.[286] Charge injection efficiencies of all photoanodes show two different trends (Fig. 6-10a). At a first glance, the highest injection efficiencies are observed for Fe_2TiO_5-Zn, where maximum efficiencies of 60 % are achieved. For this sample, injection efficiencies start to increase from *ca.* 8 % at 0.9 V_{RHE} to 60 % at 1.35 V_{RHE} reaching plateau values beyond this voltage. Conversely, a completely different trend is observed for Fe_2TiO_5, Fe_2O_3 and Fe_2O_3-Zn. For these samples, a plateau efficiency is never achieved and injection efficiency gradually increases as a function of applied bias. For Fe_2TiO_5 injection efficiencies increase from 1.6 % at 0.8 V_{RHE} to 90 % at 1.5 V_{RHE}. Similarly, for Fe_2O_3-Zn efficiencies increase from 0.85 % at 0.8 V_{RHE} to 65 % at 1.5 V_{RHE} and finally, for Fe_2O_3 efficiencies increase from 0.8 % at 0.8 V_{RHE} to 45 % at 1.5 V_{RHE}. These two trends indicate that for Fe_2TiO_5-Zn the applied potential is high enough to suppress recombination due to surface states, whereas for Fe_2TiO_5, Fe_2O_3 and Fe_2O_3-Zn samples surface state recombination still takes place even at high applied bias.[329] Overall, the better injection efficiency values for both Fe_2TiO_5-Zn and Fe_2TiO_5 indicate either faster water oxidation kinetics or slower charge recombination at the surface of the photoanodes, whereas the lower efficiency values of Fe_2O_3 and Fe_2O_3-Zn suggest that these two samples possess a larger amount of surface states and defects.[70,329,330]

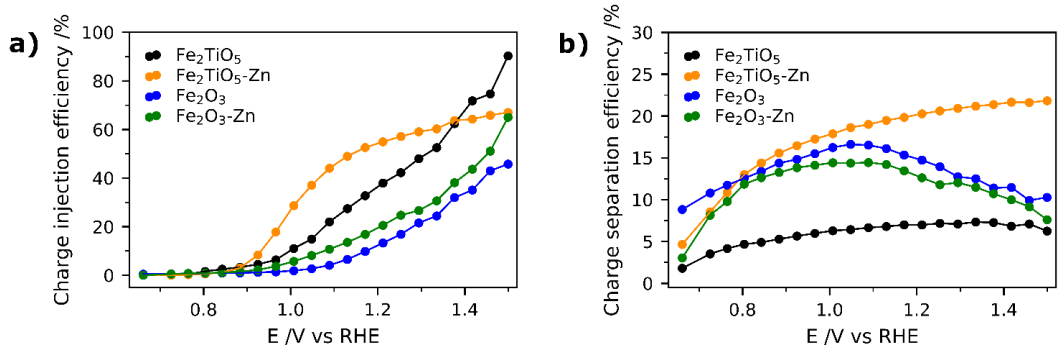

Fig. 6-10 (a) Charge injection and (b) charge separation efficiencies of Fe_2TiO_5-Zn, Fe_2TiO_5, Fe_2O_3 and Fe_2O_3-Zn.

Charge separation efficiencies are shown in Fig. 6-10b. Briefly, this efficiency has been calculated by dividing the J_{photo} in 1M NaOH+H_2O_2 with J_{max} which refers to the maximal theoretical photocurrent density of the films depending on their visible light absorption. This J_{max} value has been obtained by integrating the absorbance spectra with standard AM 1.5G

spectrum.[70,286] The integrated absorbance spectra and the standard AM 1.5G spectrum along with the calculated J_{max} are shown in Fig. 6-11 and Table 6-2.

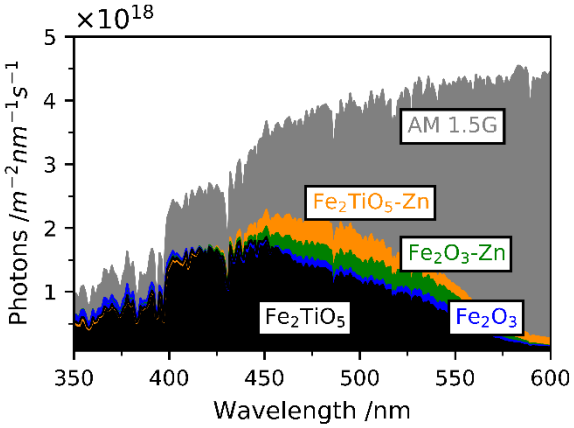

Fig. 6-11 Number of photons absorbed from the solar visible light spectrum (AM 1.5G) for Fe_2TiO_5-Zn Fe_2TiO_5, Fe_2O_3 and Fe_2O_3-Zn.

Table 6-2 Theoretical maximum photocurrent density obtained by integrating the absorbance spectra with AM 1.5G spectrum.

Sample	**J_{max} (mA cm^{-2})**
Fe_2TiO_5	3.94
Fe_2TiO_5-Zn	5.27
Fe_2O_3	4.22
Fe_2O_3-Zn	4.73

Interestingly, at low bias (0.65 V_{RHE}) the highest separation efficiency is observed for Fe_2O_3, being of 8.8 %, followed by Fe_2TiO_5-Zn (4.6 %), Fe_2O_3-Zn (3.0 %) and Fe_2TiO_5 (1.8 %). Nevertheless, from 0.8 to 1.5 V_{RHE} Fe_2TiO_5-Zn has the highest separation efficiency values, whereas Fe_2TiO_5 has the lowest values. This suggests that incorporation of Zn^{2+} in Fe_2TiO_5 lattice structure enhances bulk charge separation. In contrast, charge separation efficiencies of Fe_2O_3-Zn and Fe_2O_3 are very similar and follow the same trend, suggesting that incorporation of Zn^{2+} does not alter the bulk charge separation.

Photostability measurements under simulated sunlight for Fe_2TiO_5-Zn are shown in Fig. 6-12a. As for the J-V curves, an anodic transient is observed when the light is turned on and cathodic transient when the light is turned off, indicating accumulation and dissipation of charges under these conditions.[331] Nevertheless, if discarding the initial anodic transient, after 0.7h of continuous light irradiation 71 % of the initial photocurrent is maintained, indicating a good photostability under simulated sunlight. The observed decrease in photocurrent density over time is most likely due to photocorrosion on the surface of the photoanode by accumulated holes.

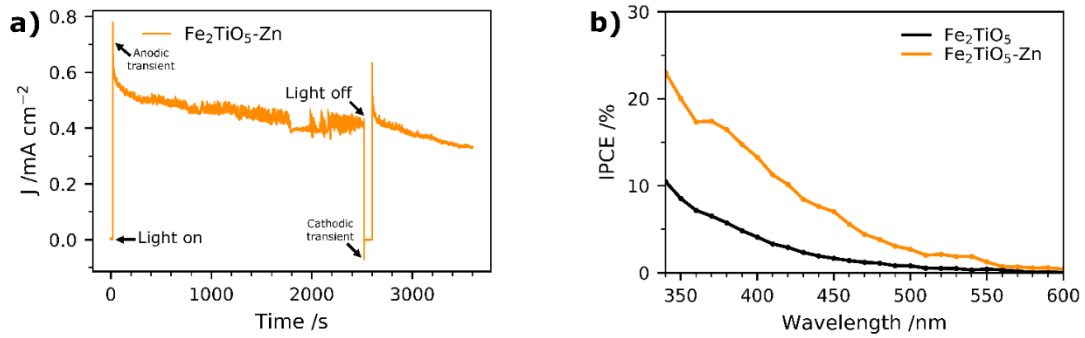

Fig. 6-12 (a) Photocurrent-time curve for 3,600s of Fe_2TiO_5-Zn at an applied bias of 1.23 V_{RHE} under 1 sun solar illumination (AM 1.5). (b) IPCE spectra at 1.23 V_{RHE} of Fe_2TiO_5 and Fe_2TiO_5-Zn. All measurements were performed in 1M NaOH (pH=13.6).

IPCE values of Fe_2TiO_5 and Fe_2TiO_5-Zn are depicted in Fig. 6-12b. The highest IPCE values are obtained for Fe_2TiO_5-Zn. IPCE values of Fe_2TiO_5-Zn gradually start to increase from 0.6 % at 590 nm to 23 % at 340 nm, whereas Fe_2TiO_5 offer lower IPCE values and lower IPCE onset wavelength. Integration of the IPCE curves for Fe_2TiO_5 and Fe_2TiO_5-Zn over AM 1.5G solar spectrum results in a photocurrent density value of 0.19 and 0.62 mA cm^{-2}, respectively, being consistent with the measured photocurrent density values at 1.23 V_{RHE}. Calculated APCE values for Fe_2TiO_5 and Fe_2TiO_5-Zn are shown in Fig. 6-13. The highest values are obtained for Fe_2TiO_5-Zn films, increasing gradually from 4.0 % at 400 nm to 33.9 % at 340 nm. This suggests that after Zn^{2+} incorporation in the Fe_2TiO_5 structure, absorbed photons are utilized more efficiently due to improved charge separation, as previously indicated in calculated charge separation efficiencies.

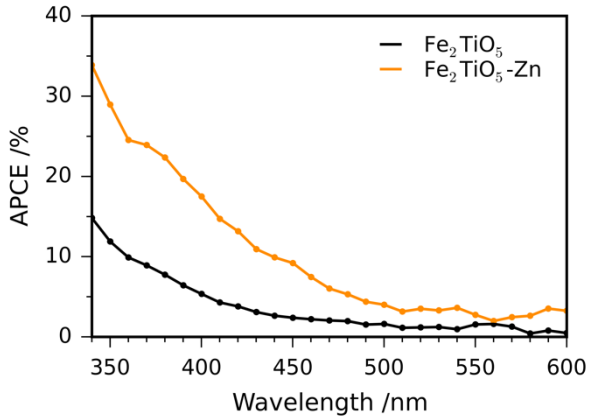

Fig. 6-13 APCE spectra at 1.23 V_{RHE} of Fe_2TiO_5 and Fe_2TiO_5-Zn at 1.23 V_{RHE}.

EIS measurements in the dark were carried out in the form of Mott-Schottky plots to characterize the intrinsic properties of the photoanodes, such as flat band potential (V_{FB}) and carrier concentration (N_D). Mott-Schottky plots of Fe_2TiO_5 and Fe_2TiO_5-Zn recorded at 100 Hz are shown in Fig. 6-14a, whereas Mott-Schottky plots for Fe_2O_3 and Fe_2O_3-Zn recorded at

1000 Hz are shown in Fig. 6-14b. Both plots indicate that the samples possess a positive slope, typical of *n-type* semiconductors.[138] Flat band potentials (V_{FB}) and electron carrier densities (N_D) of all samples are listed in Table 6-3. It was found that incorporation of Zn^{2+} did not modify the V_{FB} of Fe_2TiO_5 and Fe_2O_3 based photoanodes. The highest N_D values are obtained for Fe_2TiO_5-Zn (9.1 x 10^{17} cm^{-3}) whereas significantly lower N_D values are obtained for pristine Fe_2TiO_5 (2.1 x 10^{17} cm^{-3}) indicating better charge transport efficiencies for the Fe_2TiO_5-Zn.[138] These results agree well with charge efficiency calculations (Fig. 6-10) discussed earlier in the text, where higher efficiencies were obtained for Fe_2TiO_5-Zn. Unlike Fe_2TiO_5-Zn and Fe_2TiO_5, N_D values for Fe_2O_3 and Fe_2O_3-Zn are rather similar, 3.4 x 10^{17} and 4.4 x 10^{17} cm^{-3}, respectively. This indicates that Zn^{2+} ions play a role in modifying the electronic properties of Fe_2TiO_5, contributing to an enhancement in the photoelectrochemical performance.

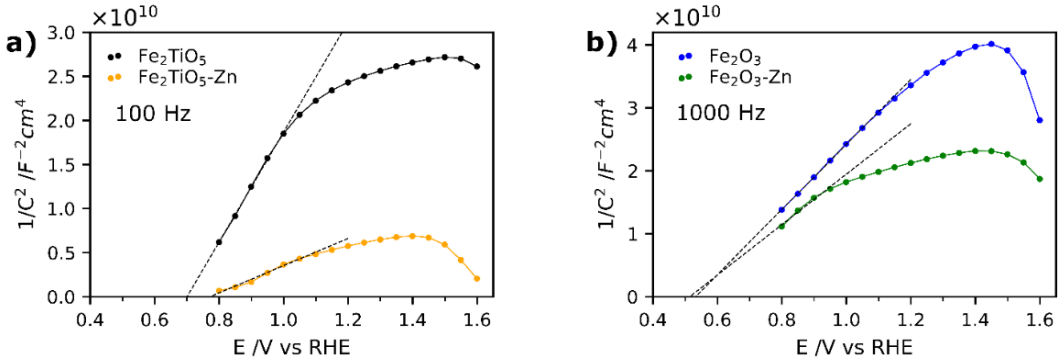

Fig. 6-14 (a) Mott Schottky plots measured at a fixed frequency of 100 Hz of Fe_2TiO_5-Zn and Fe_2TiO_5. (b) Mott Schottky plots measured at a fixed frequency of 1000 Hz of Fe_2O_3 and Fe_2O_3-Zn. All measurements were performed in 1M NaOH (pH=13.6).

Table 6-3 Charge carrier concentration and flat band potential obtained from Mott- Schottky plots.

Sample	**N_D (cm^{-3})**	**V_{FB} (RHE)**
Fe_2TiO_5	2.1 x 10^{17}	0.71
Fe_2TiO_5-Zn	9.1 x 10^{17}	0.76
Fe_2O_3	3.4 x 10^{17}	0.52
Fe_2O_3-Zn	4.4 x 10^{17}	0.55

EIS under simulated solar light at different voltages (0.6 to 1.2 V_{RHE}) was carried out to further understand charge transfer process and determine the role of Zn^{2+} in the photoanodes. EIS data was collected in the form of Nyquist plots and fitted according to the equivalent circuit shown in the inset of Fig. 6-15, consisting of two RC units.[218,332] In this model, R_s refers to the circuit resistance (resistance of electrolyte, FTO and external contact), R_{trap} to the resistance of trapping of holes in the surface states and $R_{ct,ss}$ to the charge transfer resistance of holes from the surface states to the electrolyte. Similarly, the capacitance of the system is accounted with

C_{bulk} which refers to the capacitance of the bulk of the material and C_{ss} which describes the capacitance of the surface states.[218,332]

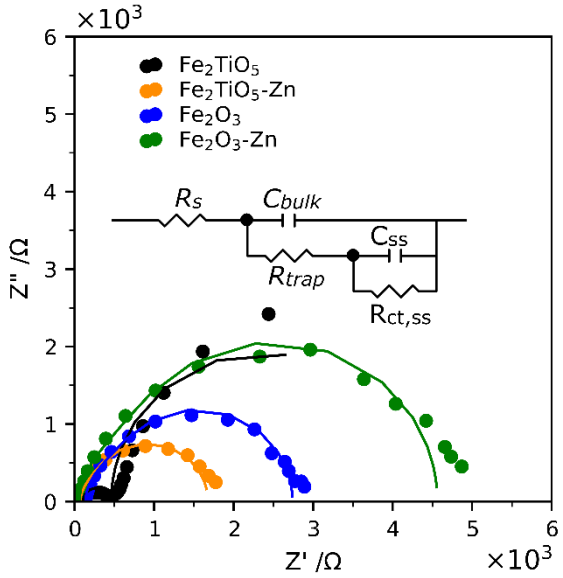

Fig. 6-15 Representative Nyquist plots of Fe_2TiO_5-Zn, Fe_2TiO_5, Fe_2O_3 and Fe_2O_3-Zn measured at 1 V_{RHE} under simulated solar light (AM 1.5). Equivalent circuit used to fit the data is shown in the inset of the plot.

As previously reported in literature, Fe_2O_3 based photoanodes follow predominantly an indirect hole transfer mechanism for the water oxidation reaction, where holes get trapped in surface states before being transferred to the electrolyte.[333,334] Assuming this mechanism for both Fe_2TiO_5 and Fe_2O_3, an increase in C_{ss} values must result in a decrease of $R_{ct,ss}$ values. In line with this, Fig. 6-16a and Fig. 6-16b show the fitted C_{ss} and $R_{ct,ss}$ values *vs.* applied voltage for as-prepared photoanodes. Fe_2O_3 and Fe_2O_3-Zn have the lowest C_{ss} whereas higher values are found for Fe_2TiO_5-Zn and Fe_2TiO_5. As expected, when comparing C_{ss} and R_{ct} values, it can be seen how a deep in the R_{ct} value is consistent with a local maximum in C_{ss} coinciding with an increase in the photocurrent density values. It is to be noted how the local C_{ss} maximum and therefore the local R_{ct} minimum for Fe_2O_3 is slightly shifted towards higher voltages (1.0 V_{RHE}). This can be explained by the large photocurrent transients observed in J-V curves below 1.0 V_{RHE} (Fig. 6-9) and that a steady photocurrent is only observed at voltages above 1.0 V_{RHE}.

Fitted C_{bulk} values are displayed in Fig. 6-16c. The highest C_{bulk} values are observed for Fe_2TiO_5-Zn, followed by Fe_2O_3, Fe_2O_3-Zn and Fe_2TiO_5. C_{bulk} values agree well with Mott-Schottky plots and calculated N_D values in Table 6-3, where Fe_2TiO_5-Zn had the highest N_D value, almost four times higher than Fe_2TiO_5, attributed to Zn doping in the bulk. In addition, Fe_2O_3 and Fe_2O_3-Zn show very similar C_{bulk} values as a function of applied bias, which

suggests that addition of Zn^{2+} did not alter the bulk electronic properties of the material (N_D values are also very similar).

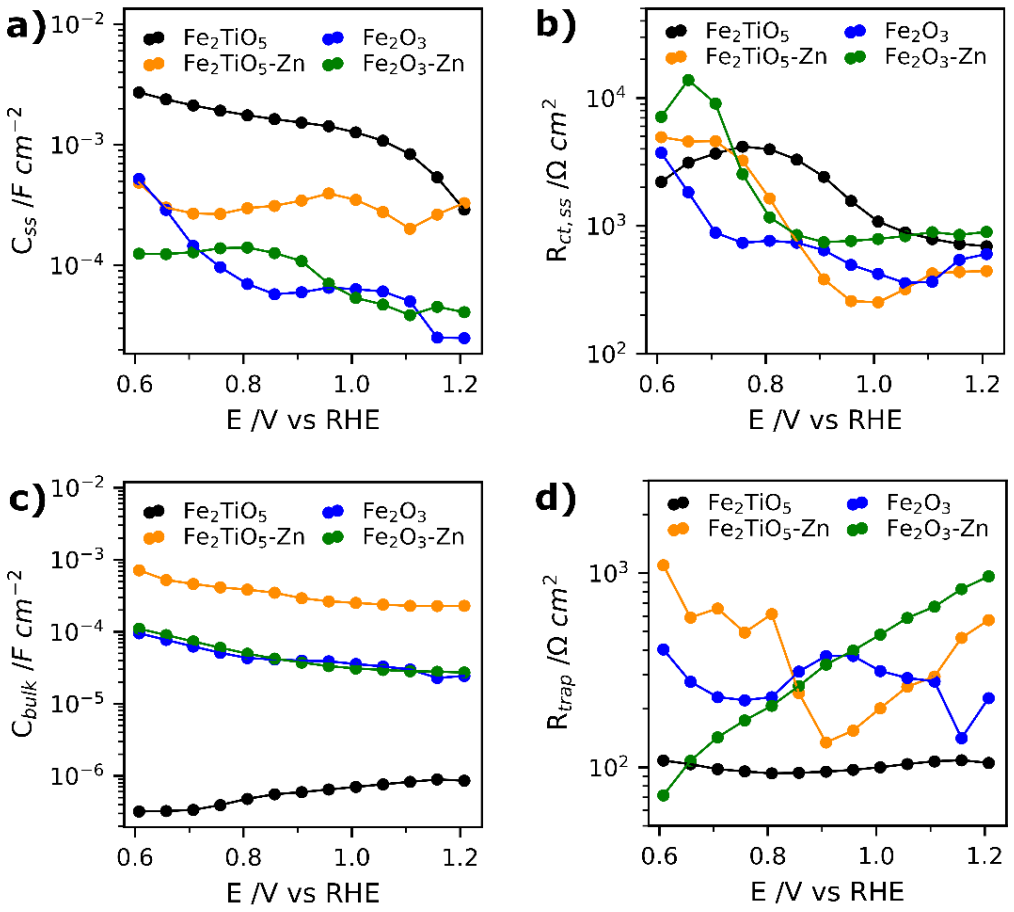

Fig. 6-16 (a) C_{ss}, (b) $R_{ct,ss}$, (c) C_{bulk} and (d) R_{trap} obtained from EIS fitting as a function of applied potential for Fe_2TiO_5-Zn, Fe_2TiO_5, Fe_2O_3 and Fe_2O_3-Zn.

Fitted R_{trap} values are displayed in Fig. 6-16d. The lowest R_{trap} values are found for Fe_2TiO_5-Zn and Fe_2TiO_5 specially at the potential window of 0.85-1.05 $V_{RHE,}$ whereas Fe_2O_3-Zn and Fe_2O_3 exhibit higher resistance. This trend clearly shows that Fe_2TiO_5 based photoanodes show minor hole recombination with surface states in comparison with Fe_2O_3 based photoanodes. Furthermore, a local R_{trap} minimum at 0.9 V_{RHE} is observed for Fe_2TiO_5-Zn, correlating well with its $R_{ct,ss}$ local minimum and C_{ss} maximum profile. All this indicates a more efficient charge transfer kinetics during the water oxidation reaction, which highlights the benefit of incorporating Zn^{2+} in Fe_2TiO_5 materials.[333]

To further understand the effect of incorporating Zn^{2+} in the electronic properties of the material, UPS measurements were undertaken to calculate the position of the Fermi level (E_F), conduction band (CB) and valence band (VB). Fig. 6-17a and Fig. 6-17b show the UPS spectra with bias (U_{bias}= 2 V) and no bias of Fe_2TiO_5, Fe_2TiO_5-Zn, Fe_2O_3 and Fe_2O_3-Zn, respectively,

used to calculate the energy cut-off ($E_{cut\text{-}off}$) region of the secondary electron and the valence band maximum (*VBM*). The work function (ϕ) was calculated using the equation shown in the inset of Fig. 6-17, and results are displayed in Table 6-4.[311,335,336] The calculated values for all samples fall in the range of previously reported values.[66,337]

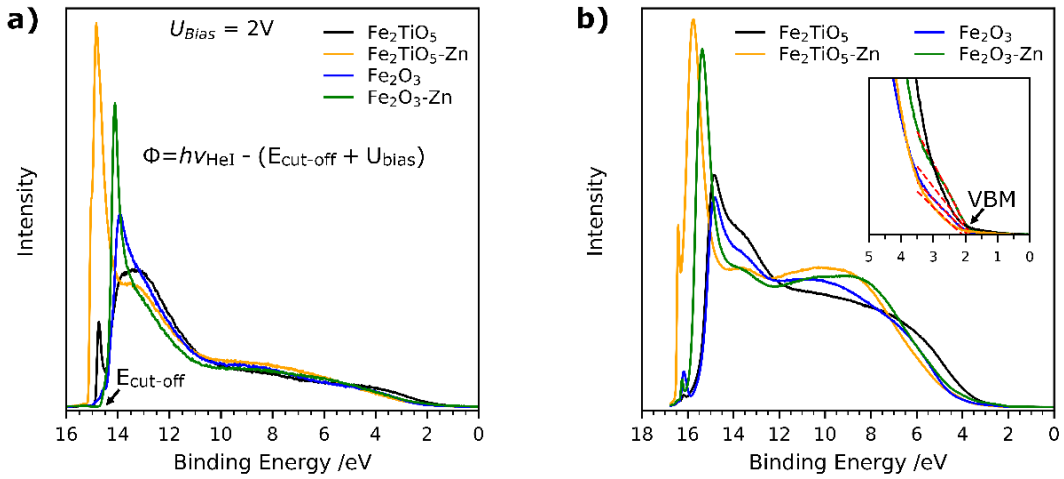

Fig. 6-17 UPS measurements using a He I photon source (E=21.2 eV) with (a) an applied bias of 2 V and (b) without applied bias. From these measurements, $E_{cut\text{-}off}$, work function (ϕ) and valence band maximum (VBM) were determined.

Table 6-4 Work function (ϕ) and valence band maximum (VBM) values obtained from UPS measurements.

Sample	Φ (eV)	VBM (eV)
Fe_2TiO_5	4.36	1.83
Fe_2TiO_5-Zn	4.07	2.10
Fe_2O_3	4.77	1.93
Fe_2O_3-Zn	4.88	1.82

From these values along with the UV-Vis spectra (for determining the CB position), a schematic energy diagram was estimated and represented in Fig. 6-18.

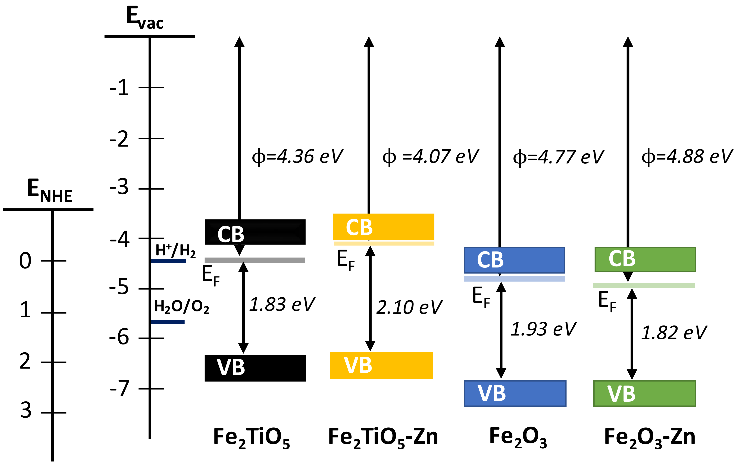

Fig. 6-18 Schematic diagram of band level positions calculated from UPS measurements (Fig. 6-17) for Fe_2TiO_5, Fe_2TiO_5-Zn, Fe_2O_3 and Fe_2O_3-Zn with respect to the vacuum level and the normal hydrogen electrode (NHE) potential.

An upward shift of the E_F towards the CB for Fe_2TiO_5-Zn in comparison with Fe_2TiO_5 is observed, agreeing with Mott-Schottky and N_D calculations, where higher N_D values were found for Fe_2TiO_5-Zn. Higher carrier concentration (N_D) leads to an upward shift of the E_F, facilitating the charge separation at the semiconductor-electrolyte interface.[138,338] Conversely to Fe_2TiO_5 and Fe_2TiO_5-Zn, a minimal variation in the E_F is observed for Fe_2O_3 and Fe_2O_3-Zn, being consistent with calculated N_D values from Mott-Schottky plots, where an insignificant increase in the N_D was observed after incorporation of Zn^{2+}. This band diagram is consistent with previously reported CB and VB positions for Fe_2O_3 and Fe_2TiO_5 based photoanodes.[65] From these differences in the E_F positions it is inferred that incorporation of Zn^{2+} only modifies the electronic properties of Fe_2TiO_5 photoanodes. This may indicate that for the case of Fe_2TiO_5-Zn, Zn^{2+} ions are incorporated into the crystal structure of Fe_2TiO_5, whereas for Fe_2O_3-Zn, Zn^{2+} ions are most likely distributed on the surface of Fe_2O_3, since minimal differences in E_F level are observed. These results are in agreement with charge separation efficiencies and C_{bulk} values obtained from PEIS, where a similar trend was observed for both Fe_2O_3 and Fe_2O_3-Zn, whereas significant differences were found for Fe_2TiO_5 and Fe_2TiO_5-Zn.

Conclusions

In this work we have demonstrated the effect of doping Fe_2TiO_5 photoanodes with Zn^{2+} for photoelectrochemical devices. These photoanodes were grown by aerosol-assisted chemical vapor deposition and relatively dense films with very fine structures were obtained. Photoelectrochemical measurements revealed that optimized Zn-doped Fe_2TiO_5 photoanodes exhibited a 3-fold enhancement in photocurrent density values in comparison with pristine Fe_2TiO_5 at 1.23 V_{RHE}, from *ca.* 0.2 to 0.6 mA cm^{-2}. This enhancement in PEC performance

was attributed to better charge separation and injection efficiencies after incorporation of Zn^{2+} ions. Impedance spectroscopy and Mott-Schottky measurements revealed a significant increase in carrier concentration (N_D) and better charge transfer kinetics for Fe_2TiO_5-Zn samples. Furthermore, ultraviolet photoelectron spectroscopy measurements showed an upward shift of the Fermi level (E_F) after incorporation of Zn^{2+}, agreeing well with the highest N_D values calculated for Fe_2TiO_5-Zn suggesting incorporation of Zn^{2+} in the Fe_2TiO_5 crystal lattice. For comparison, Fe_2O_3 and Fe_2O_3-Zn photoanodes were also prepared under the same conditions. These photoanodes showed significantly lower photoelectrochemical performance and poorer charge transfer efficiencies in comparison to Fe_2TiO_5 based photoanodes. In addition, both Fe_2O_3 and Fe_2O_3-Zn showed very similar photocurrent density values, which was mainly attributed to the most likely distribution of Zn^{2+} ions on the surface of the film features rather than in the bulk. On balance, these results demonstrate, for the first time, a simple methodology for the preparation of Zn-doped Fe_2TiO_5 photoanodes with improved photoelectrochemical performance over pristine Fe_2TiO_5.

Conflicts of interest

There are no conflicts to declare.

Acknowledgements

The authors would like to acknowledge both EPSRC for funding the Centre for Doctoral Training in Sustainable Chemical Technologies at the University of Bath (EP/L016354/1) and the Material and Chemical Characterisation facility (MC2) at the University of Bath. SE would like to acknowledge the financial support from EPSRC (EP/P008097/1).

All data created during this research are openly available from the University of Bath data archive at https://doi.org/10.15125/BATH-00704.

6.1.4 Commentary

6.1.4.1 Optimization of annealing temperature for the formation of Fe_2TiO_5

Formation of Fe_2TiO_5 usually requires long annealing temperatures to allow a successful diffusion of atoms. In the manuscript, we reported that Fe_2TiO_5 based photoanodes were annealed at 500 °C for 12 h followed by 650 °C for 2 h with a ramp rate of 10 °C min^{-1}. This optimized annealing temperature is a result of a temperature optimization study carried out at three different annealing temperatures (500, 600 and 650 °C) at different annealing times. Fig. 6-19 shows a summary of the different crystalline phases (Fe_2O_3, TiO_2 and Fe_2TiO_5) obtained at the studied annealing temperatures and times from XRD patterns. All films were prepared as described in the experimental section of the manuscript (1 h of deposition at 450 °C) and annealed at 500, 600 and 650 °C for different hours. Among the different annealing temperatures studied, annealing at 500 °C for long hours resulted in a majority of the Fe_2TiO_5 phase. At higher annealing temperatures (600 and 650 °C) mainly Fe_2O_3 (hematite) was formed.

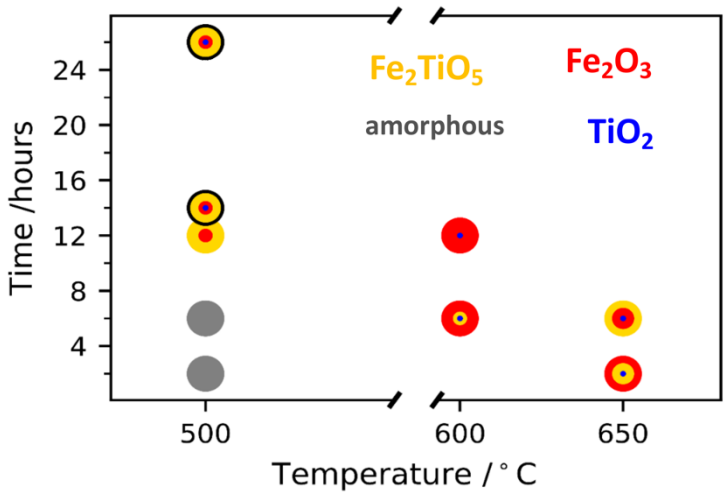

Fig. 6-19 Crystal phases obtained after different annealing temperatures. Circles containing a black outline correspond to samples with an additional post-annealing treatment at 650 °C for 2 h. The larger the color the larger content of the phase. Data obtained qualitatively from different XRD patterns.

Fig. 6-20 shows photocurrent-potential curves of all samples containing the Fe_2TiO_5 phase. The highest photocurrent density values were obtained for the samples annealed at 500 °C for 12 h and 24 h with an additional post-annealing of 650 °C for 2 h, in which photocurrent density values of *ca.* 0.2 mA cm^{-2} at 1.23 V_{RHE} were achieved. The additional annealing at 650 °C for 2 h improved the crystallinity of the Fe_2TiO_5, which resulted in an overall improvement of the PEC performance. In this regard, the optimal annealing temperature of 500 °C for 12 h and 650 °C for 2 h was chosen as the optimal annealing temperature for the formation of Fe_2TiO_5 based photoanodes.

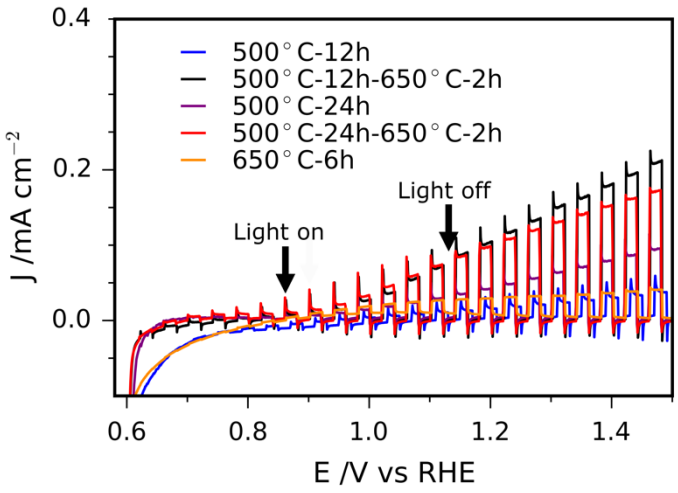

Fig. 6-20 Photocurrent potential curves of samples containing a majority of Fe_2TiO_5 crystal phase. All measurements were performed in 1M NaOH (pH=13.6) under chopped AM 1.5 illumination.

6.1.4.2 Preparation of Zn-doped Fe_2TiO_5 photoanodes with higher loadings of Zn^{2+}

In the manuscript, we have reported the formation of Zn-doped Fe_2TiO_5 (Fe_2TiO_5-Zn) from a solution containing iron (III) acetylacetonate (3.531 g, 10 mmol), titanium (IV) isopropoxide (1.478 mL, 5.0 mmol) and zinc acetate dihydrate (0.0549 g, 0.25 mmol) in ethyl acetate and methanol. Attempts were also performed to study the effect of preparing Fe_2TiO_5-Zn from a solution containing 0.1097 g (0.5 mmol) of zinc acetate dihydrate. Nevertheless, at those Zn^{2+} loadings, the Fe_2TiO_5 could not be achieved and only Fe_2O_3 and TiO_2 phases were formed. Therefore, we believe that addition of high loadings of Zn^{2+} favors phase segregation to Fe_2O_3 and TiO_2.

6.1.4.3 Optimization of film thickness

The preparation of thickest Fe_2TiO_5 films was also attempted by increasing the deposition time of the AACVD process from 1 to 2 h deposition time. This was performed aiming to increase the light absorption of the film and thus improve the PEC performance of the material. Fig. 6-21 shows SEM cross-sectional micrographs of films deposited for 1 h (a) and 2 h (b). After 2 h of deposition, films were ticker (*ca.* 867 nm) and slightly more porous than those films deposited for 1 h.

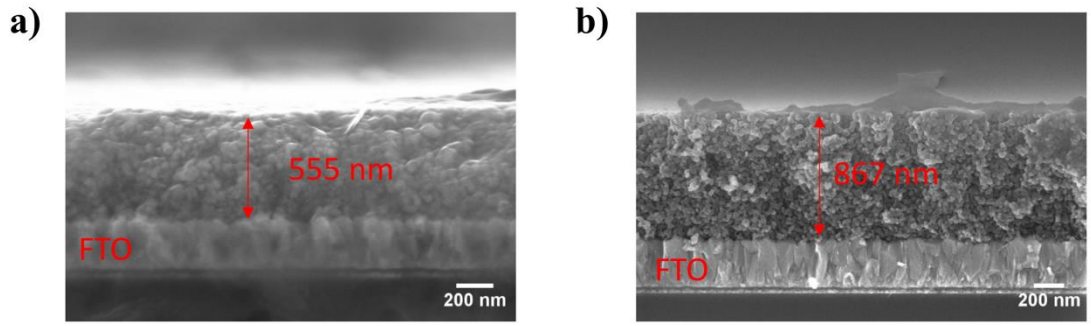

Fig. 6-21 SEM cross-sectional micrographs of films prepared for (a) 1 h and (b) 2 h deposition time. Both films were deposited at 450 °C from a solution containing titanium (IV) isopropoxide (1.478 mL, 5.0 mmol) and iron (III) acetylacetonate (3.531 g, 10 mmol) in ethyl acetate and methanol and annealed at 500 °C for 12 h and 650 °C for 2 h.

XRD patterns (Fig. 6-22) of the films at different annealing temperatures indicated that for those thick films mainly TiO_2 and Fe_2O_3 phases were formed. Such thick films might limit atom diffusion and avoid the formation of Fe_2TiO_5.

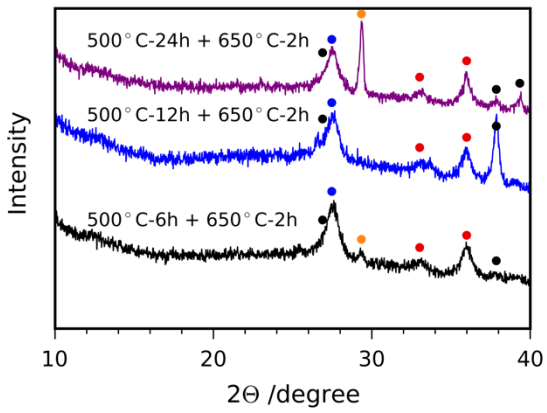

Fig. 6-22 XRD patterns of films deposited for 2 h and annealed at different temperatures. Black dot: FTO substrate, blue dot: TiO_2 (rutile), red dot: Fe_2O_3 and orange dot: Fe_3O_4.

Chapter 7. Conclusions and outlook

This PhD thesis has been primarily focused on the design and fabrication of nanostructured metal oxides, with a special focus on TiO_2 photoanodes for photoelectrochemical (PEC) water splitting applications. It is clear from internationally renowned reports such as the one recently released by the intergovernmental panel on climate change (IPCC), that the need of mitigating the effects of climate change must become a priority for the current society. In this regard, it is essential to establish a synergy between policymakers, scientist and politicians in order to commit towards a more sustainable world, in which, for instance renewable sources of energy become the primary source of energy of the 21st century. As extensively reviewed in this thesis, PEC water splitting could become a feasible alternative technology that could play a key role in this energy transition, primarily because H_2 is considered as the future energy vector. Although a promising technology, it has been shown in Chapter 2 how finding suitable materials that would make this technology both economically and practically feasible still remains a challenge, mainly because materials do not absorb neither the entire spectrum of the solar light, their kinetics for water splitting reaction is slow or carrier lifetimes are short.

This thesis has experimentally demonstrated how the use of polyoxotitanium oxo/alkoxy clusters as metal oxide precursors allows the formation of doped-TiO_2 photoanodes with improved visible-light absorption and highly nanostructured pure-TiO_2 photoanodes with enhanced kinetics and photocurrent performances. In particular, using $[Ti_4Mo_2O_8(OEt)_{10}]_2$ we have shown how optimized Mo-doped TiO_2 photoanodes showed improved PEC performances over a pristine TiO_2 photoanode prepared by a spray pyrolysis method. This work showed the importance of substitutional doping in the TiO_2 lattice structure towards the enhancement of PEC performance and also demonstrated that at high annealing temperatures Mo species evaporated which contributed to the formation of nanostructured and porous photoanodes with improved PEC activity. Secondly, in this thesis we have also shown for the first time the formation of highly nanostructured TiO_2 photoanodes having the morphology of crystals of gypsum, sand and water, also known as ‘desert roses’. These desert-rose TiO_2 photoanodes were grown from the $Ti_7O_4(OEt)_{20}$ titanium oxo/alkoxy cluster using aerosol-assisted chemical vapor deposition (AACVD), a highly versatile deposition method for preparing nanostructured thin films. The resultant photoanodes showed preferential exposure of the {0 1 0} anatase facet, often known to be as one of the most photocatalytic active facets. These desert-rose TiO_2 photoanodes showed high PEC performances, low onset potentials and high preservation of the anatase TiO_2 phase despite annealing at temperatures above 900 °C. Furthermore, the high stability of the metastable anatase TiO_2 allows this material to find applications not only in the PEC field but also in the ceramic industry, for smart tile

applications. Overall, these two studies revealed the so far unexplored advantages of using polyoxotitanium oxo/alkoxy clusters as TiO_2 precursors for PEC water splitting applications.

Finally, in the last experimental work of this thesis, the preparation of Fe_2TiO_5 photoanodes, a hybrid of TiO_2 and Fe_2O_3, has been explored using AACVD. It was found that doping of Fe_2TiO_5 with Zn^{2+} showed a 3-fold enhancement in the PEC performance when compared with pristine Fe_2TiO_5. According to the several characterization methods employed, this enhancement was mainly attributed to better both charge separation and injection efficiencies after addition of Zn^{2+} ions along with higher carrier concentration and better charge transfer kinetics. To the best of our knowledge, this is the first time that Zn-doped Fe_2TiO_5 have been studied as a photoanode. Although some traces of Fe_2O_3 were present in both Fe_2TiO_5-Zn and Fe_2TiO_5 samples, it is clear how Fe_2TiO_5-based photoanodes can play a key role in moving forward in the field of PEC water splitting.

From both the theory and experimental chapters presented in this thesis, it is established that future research in PEC water splitting still needs to be primarily focused on both finding new materials and further understanding the main limitations of existing materials to be able to tackle them. Although throughout the years, the emergence and advancement of new technologies and characterization methods including time-resolved spectroscopies and impedance methods have helped to elucidate the main points to overcome, still PEC water splitting is far away from its practical applications. As mentioned in this thesis, TiO_2 has been extensively studied in the last 40 years and significant progress and improvements have been achieved especially when designing nanostructured TiO_2. However, from the low theoretical solar-to-hydrogen (STH) efficiency values reported for TiO_2 (1.3 and 2.2 %, for anatase and rutile, respectively), being significantly smaller than the current goal of achieving STH > 10 %, it is clear that the future large-scale PEC device will not solely be composed of TiO_2, but of a combination of materials. For instance, Si, III-V and chalcopyrite semiconductors have recently shown high efficiencies for water splitting, but they suffer from photocorrosion when in contact with an electrolyte. To avoid this, TiO_2 is widely used as a protection layer owing to its both high stability over a wide range of pH values and excellent optical transmittance. Therefore, it is obvious to consider that is still essential to develop efficient TiO_2–based photoanodes with improved visible light absorption and understand its photochemical properties in order to advance in the field of PEC water splitting. This PhD thesis has successfully demonstrated several strategies to move one step closer to the milestone of designing a stable visible light photoelectrode with high STH efficiencies: the introduction of dopants, the design of nanostructures and the development of novel materials with improved visible light absorption.

References

1 BP, *BP Statistical Review of World Energy*, 2019.

2 European Commission, *Shedding light on energy in the EU*, 2019.

3 International Energy Agency, *Global Energy and CO2 Status Report*, 2019.

4 Intergovernmental panel on climate change, *Summary for Policymakers of IPCC Special Report on Global Warming of 1.5 °C approved by governments*, 2018.

5 European Commission, *EU climate action*, 2019.

6 Royal Society of Chemistry, *Solar Fuels and Artificial Photosynthesis*, 2012.

7 B. K. Tapan and P. Bénard, in *Hydrogen as an Energy Vector*, Institute of Electrical and Electronics Engineers, 2003, vol. 7, pp. 196–199.

8 Editorial Board, *Nat. Energy*, 2016, **1**, 16127.

9 A. P. Simpson and A. E. Lutz, *Int. J. Hydrogen Energy*, 2007, **32**, 4811–4820.

10 R. J. Detz, J. N. H. Reek and B. C. C. Van Der Zwaan, *Energy Environ. Sci.*, 2018, **11**, 1653–1669.

11 C. L. Muhich, B. D. Ehrhart, I. Al-Shankiti, B. J. Ward, C. B. Musgrave and A. W. Weimer, *Wiley Interdiscip. Rev. Energy Environ.*, 2016, **5**, 261–287.

12 I. Z. Boboescu, V. D. Gherman, G. Lakatos, B. Pap, T. Bíró and G. Maróti, *Bioresour. Technol.*, 2016, **204**, 192–201.

13 B. A. Pinaud, J. D. Benck, L. C. Seitz, A. J. Forman, Z. Chen, T. G. Deutsch, B. D. James, K. N. Baum, G. N. Baum, S. Ardo, H. Wang, E. Miller and T. F. Jaramillo, *Energy Environ. Sci.*, 2013, **6**, 1983–2002.

14 R. Van De Krol and M. Grätzel, *Photoelectrochemical Hydrogen Production*, Springer US, 2012.

15 S. Giménez and J. Bisquert, *Photoelectrochemical Solar Fuel Production: From Basic Principles to Advanced Devices*, Springer International Publishing, 2016.

16 L. M. Peter, in *Photocatalysis*, Royal Society of Chemistry, Cambridge, 2016, pp. 1–28.

17 S. Lany, *J. Phys. Condens. Matter*, 2015, **27**, 283203.

18 L. Liu, Z. Mei, A. Tang, A. Azarov, A. Kuznetsov, Q. K. Xue and X. Du, *Phys. Rev. B*, 2016, **93**, 1–235305.

19 H. Ahmad, S. K. Kamarudin, L. J. Minggu and M. Kassim, *Renew. Sustain. Energy Rev.*, 2015, **43**, 599–610.

20 S. Zhu and D. Wang, *Adv. Energy Mater.*, 2017, **7**, 1700841.

21 U.S. Department of Energy, .

22 R. Sathre, C. D. Scown, W. R. Morrow, J. C. Stevens, I. D. Sharp, J. W. Ager, K. Walczak, F. A. Houle and J. B. Greenblatt, *Energy Environ. Sci.*, 2014, **7**, 3264–3278.

23 K. Maeda and K. Domen, *J. Phys. Chem. C*, 2007, **111**, 7851–7861.

24 D. B. and M. M. Malik Mohibbul Haque, in *Organic Pollutants Ten Years After the Stockholm Convention - Environmental and Analytical Update*, ed. T. Puzyn, InTech, 2012, pp. 293–327.

25 M. Grätzel, *Nature*, 2001, **414**, 338–344.

26 J. Li and N. Wu, *Catal. Sci. Technol.*, 2015, **5**, 1360–1384.

27 K. Maeda, *J. Photochem. Photobiol. C Photochem. Rev.*, 2011, **12**, 237–268.

28 A. Fujishima and K. Honda, *Nature*, 1972, **238**, 37–38.

29 T. Hisatomi, J. Kubota and K. Domen, *Chem. Soc. Rev.*, 2014, **43**, 7520–7535.

30 H.-J. Lewerenz and L. Peter, Eds., *Photoelectrochemical Water Splitting: Materials, Processes and Architectures*, The Royal Society of Chemistry, 2014.

31 S. Kumar, K. Ojha and A. K. Ganguli, *Adv. Mater. Interfaces*, 2017, **4**, 1600981.

32 Z. Chen, H. N. Dinh and E. Miller, *Photoelectrochemical water splitting: standards, experimental methods, and protocols*, Springer, New York, 2013.

33 C. Jiang, S. J. A. Moniz, A. Wang, T. Zhang and J. Tang, *Chem. Soc. Rev.*, 2017, **46**, 4645–4660.

34 S. J. A. Moniz, S. A. Shevlin, D. J. Martin, Z.-X. Guo and J. Tang, *Energy Environ. Sci.*, 2015, **8**, 731–759.

35 J. Turner, G. Sverdrup, M. K. Mann, P.-C. Maness, B. Kroposki, M. Ghirardi, R. J. Evans and D. Blake, *Int. J. Energy Res.*, 2008, **32**, 379–407.

36 S. Chen and L. W. Wang, *Chem. Mater.*, 2012, **24**, 3659–3666.

37 M. Weber and M. Dignam, *Int. J. Hydrogen Energy*, 1986, **11**, 225–232.

38 P. Lianos, *Appl. Catal. B Environ.*, 2017, **210**, 235–254.

39 Q. Huang, Z. Ye and X. Xiao, *J. Mater. Chem. A*, 2015, **3**, 15824–15837.

40 A. Paracchino, V. Laporte, K. Sivula, M. Grätzel and E. Thimsen, *Nat. Mater.*, 2011, **10**, 456–461.

41 S. D. Tilley, M. Schreier, J. Azevedo, M. Stefik and M. Grätzel, *Adv. Funct. Mater.*, 2014, **24**, 303–311.

42 L. Pan, J. H. Kim, M. T. Mayer, M. K. Son, A. Ummadisingu, J. S. Lee, A. Hagfeldt, J. Luo and M. Grätzel, *Nat. Catal.*, 2018, **1**, 412–420.

43 Z. Zhang and P. Wang, *J. Mater. Chem.*, 2012, **22**, 2456–2464.

44 X. Chen, Z. Zhang, L. Chi, A. K. Nair, W. Shangguan and Z. Jiang, *Nano-Micro Lett.*, 2016, **8**, 1–12.

45 R. C. Valderrama, P. J. Sebastián, M. Miranda-Hernandez, J. P. Enriquez and S. A. Gamboa, *J. Photochem. Photobiol. A Chem.*, 2004, **168**, 75–80.

46 R. C. Valderrama, P. J. Sebastian, J. Pantoja Enriquez and S. A. Gamboa, *Sol. Energy Mater. Sol. Cells*, 2005, **88**, 145–155.

47 B. Koo, S. W. Nam, R. Haight, S. Kim, S. Oh, M. Cho, J. Oh, J. Y. Lee, B. T. Ahn and B. Shin, *ACS Appl. Mater. Interfaces*, 2017, **9**, 5279–5287.

48 Y. Chen, X. Feng, M. Liu, J. Su and S. Shen, *Nanophotonics*, 2016, **5**, 468–491.

49 J. Wang, N. Yu, Y. Zhang, Y. Zhu, L. Fu, P. Zhang, L. Gao and Y. Wu, *J. Alloys Compd.*, 2016, **688**, 923–932.

50 R. Liu, Z. Zheng, J. Spurgeon and X. Yang, *Energy Environ. Sci.*, 2014, **7**, 2504–2517.

51 F. E. Osterloh, *Chem. Soc. Rev.*, 2013, **42**, 2294–320.

52 B. Seger, T. Pedersen, A. B. Laursen, P. C. K. Vesborg, O. Hansen and I. Chorkendorff, *J. Am. Chem. Soc.*, 2013, **135**, 1057–1064.

53 P. Dai, J. Xie, M. T. Mayer, X. Yang, J. Zhan and D. Wang, *Angew. Chemie Int. Ed.*, 2013, **52**, 11119–11123.

54 M. J. Choi, J.-Y. Jung, M.-J. Park, J.-W. Song, J.-H. Lee and J. H. Bang, *J. Mater. Chem. A*, 2014, **2**, 2928–2933.

55 M. D. Bhatt and J. S. Lee, *J. Mater. Chem. A*, 2015, **3**, 10632–10659.

56 K. Sivula, F. Le Formal and M. Grätzel, *ChemSusChem*, 2011, **4**, 432–449.

57 Y. Ling and Y. Li, *Part. Part. Syst. Charact.*, 2014, **31**, 1113–1121.

58 J. H. Kennedy, *J. Electrochem. Soc.*, 1981, **128**, 2371–2373.

59 K. Sivula, R. Zboril, F. Le Formal, R. Robert, A. Weidenkaff, J. Tucek, J. Frydrych and M. Grätzel, *J. Am. Chem. Soc.*, 2010, **132**, 7436–7444.

60 A. Kay, I. Cesar and M. Grätzel, *J. Am. Chem. Soc.*, 2006, **128**, 15714–15721.

61 S. C. Warren, K. Voïtchovsky, H. Dotan, C. M. Leroy, M. Cornuz, F. Stellacci, C. Hébert, A. Rothschild and M. Grätzel, *Nat. Mater.*, 2013, **12**, 842–849.

62 Q. Yu, X. Meng, T. Wang, P. Li and J. Ye, *Adv. Funct. Mater.*, 2015, **25**, 2686–2692.

63 D. K. Zhong, J. Sun, H. Inumaru and D. R. Gamelin, *J. Am. Chem. Soc.*, 2009, **131**, 6086–6087.

64 S. D. Tilley, M. Cornuz, K. Sivula and M. Grätzel, *Angew. Chemie Int. Ed.*, 2010, **49**, 6405–6408.

65 S. Kment, F. Riboni, S. Pausova, L. Wang, L. Wang, H. Han, Z. Hubicka, J. Krysa, P. Schmuki and R. Zboril, *Chem. Soc. Rev.*, 2017, **46**, 3716–3769.

66 P. S. Bassi, S. Y. Chiam, J. Barber and L. H. Wong, *ACS Appl. Mater. Interfaces*, 2014, **24**, 2249–22495.

67 Gurudayal, P. S. Bassi, T. Sritharan and L. H. Wong, *J. Phys. D. Appl. Phys.*, 2018, **51**, 473002.

68 Q. Liu, J. He, T. Yao, Z. Sun, W. Cheng, S. He, Y. Xie, Y. Peng, H. Cheng, Y. Sun, Y. Jiang, F. Hu, Z. Xie, W. Yan, Z. Pan, Z. Wu and S. Wei, *Nat. Commun.*, 2014, **5**, 5122.

69 J. Deng, X. Lv, J. Liu, H. Zhang, K. Nie, C. Hong, J. Wang, X. Sun, J. Zhong and S.-T. Lee, *ACS Nano*, 2015, **9**, 5348–5356.

70 P. S. Bassi, R. P. Antony, P. P. Boix, Y. Fang, J. Barber and L. H. Wong, *Nano Energy*, 2016, **22**, 310–318.

71 Z. Li, W. Luo, M. Zhang, J. Feng and Z. Zou, *Energy Environ. Sci.*, 2013, **6**, 347–370.

72 A. Kudo, K. Ueda, H. Kato and I. Mikami, *Catal. Letters*, 1998, **53**, 229–230.

73 F. F. Abdi, L. Han, A. H. M. Smets, M. Zeman, B. Dam and R. van de Krol, *Nat. Commun.*, 2013, **4**, 2195.

74 T. W. Kim and K.-S. Choi, *Science (80-.).*, 2014, **343**, 990–994.

75 J. Su, L. Guo, N. Bao and C. A. Grimes, *Nano Lett.*, 2011, **11**, 1928–1933.

76 P. Chatchai, Y. Murakami, S. -y. Kishioka, A. Y. Nosaka and Y. Nosaka, *Electrochem. Solid-State Lett.*, 2008, **11**, H160–H163.

77 B. J. Trześniewski and W. A. Smith, *J. Mater. Chem. A*, 2016, **4**, 2919–2926.

78 H. S. Han, S. Shin, D. H. Kim, I. J. Park, J. S. Kim, P. S. Huang, J. K. Lee, I. S. Cho and X. Zheng, *Energy Environ. Sci.*, 2018, **11**, 1299–1306.

79 T. Zhu, M. N. Chong and E. S. Chan, *ChemSusChem*, 2014, **7**, 2974–2997.

80 C. Janaky, K. Rajeshwar, N. R. De Tacconi, W. Chanmanee and M. N. Huda, *Catal.*

Today, 2013, **199**, 53–64.

81 C. Chacón, M. Rodríguez-Pérez, G. Oskam and G. Rodríguez-Gattorno, *J. Mater. Sci. Mater. Electron.*, 2015, **26**, 5526–5531.

82 J. Gan, X. Lu and Y. Tong, *Nanoscale*, 2014, **6**, 7142–64.

83 L. E. Fraga and M. V. B. Zanoni, *J. Braz. Chem. Soc.*, 2011, **22**, 718–725.

84 C. W. Lai and S. Sreekantan, *Int. J. Hydrogen Energy*, 2013, **38**, 2156–2166.

85 R. Liu, Y. Lin, L. Y. Chou, S. W. Sheehan, W. He, F. Zhang, H. J. M. Hou and D. Wang, *Angew. Chemie - Int. Ed.*, 2011, **50**, 499–502.

86 J. A. Seabold and K.-S. Choi, *Chem. Mater.*, 2011, **23**, 1105–1112.

87 J. C. Hill and K. S. Choi, *J. Phys. Chem. C*, 2012, **116**, 7612–7620.

88 M. Ni, M. K. H. Leung, D. Y. C. Leung and K. Sumathy, *Renew. Sustain. Energy Rev.*, 2007, **11**, 401–425.

89 X. Chen and S. S. Mao, *Chem. Rev.*, 2007, **107**, 2891–2959.

90 A. Folli, C. Pade, T. B. Hansen, T. De Marco and D. E. Macphee, *Cem. Concr. Res.*, 2012, **42**, 539–548.

91 A. Fujishima and X. Zhang, *Comptes Rendus Chim.*, 2006, **9**, 750–760.

92 M. Pelaez, N. T. Nolan, S. C. Pillai, M. K. Seery, P. Falaras, A. G. Kontos, P. S. M. Dunlop, J. W. J. Hamilton, J. A. Byrne, K. O'Shea, M. H. Entezari and D. D. Dionysiou, *Appl. Catal. B Environ.*, 2012, **125**, 331–349.

93 L. Rozes and C. Sanchez, *Chem. Soc. Rev.*, 2011, **40**, 1006–1030.

94 A. Folli, J. Bloh, M. Strøm, T. Pilegaard Madsen, T. Hensriksen and D. E. Macphee, *J. Phys. Chem. Lett.*, 2014, **5**, 830–832.

95 R. M. Navarro, F. del Valle, J. A. Villoria de la Mano, M. C. Álvarez-Galván and J. L. G. Fierro, in *Advances in Chemical Engineering*, ed. B. S. R. Hugo I. de Lasa, Academic Press, 2009, vol. 36, pp. 111–143.

96 J. H. Park, O. O. Park and S. Kim, *Appl. Phys. Lett.*, 2006, **89**, 1–4.

97 W. Smith, A. Wolcott, R. C. Fitzmorris, J. Z. Zhang and Y. Zhao, *J. Mater. Chem.*, 2011, **21**, 10792–10800.

98 S. Kuang, L. Yang, S. Luo and Q. Cai, *Appl. Surf. Sci.*, 2009, **255**, 7385–7388.

99 Y. Tan, S. Zhang, R. Shi, W. Wang and K. Liang, *Int. J. Hydrogen Energy*, 2016, **41**, 5437–5444.

100 M. Lu, C. Shao, K. Wang, N. Lu, X. Zhang, P. Zhang, M. Zhang, X. Li and Y. Liu, *ACS Appl. Mater. Interfaces*, 2014, **6**, 9004–9012.

101 M. Yang, L. Zhang, B. Jin, L. Huang and Y. Gan, *Appl. Surf. Sci.*, 2016, **364**, 410–415.

102 H. Liu, T. Lv, C. Zhu and Z. Zhu, *Sol. Energy Mater. Sol. Cells*, 2016, **153**, 1–8.

103 J. M. Herrmann, *J. Photochem. Photobiol. A Chem.*, 2010, **216**, 85–93.

104 M. Gao, L. Zhu, C. K. Peh and G. W. Ho, *Energy Environ. Sci.*, 2019, **12**, 841–864.

105 W. Choi, A. Termin and M. R. Hoffmann, *J. Phys. Chem.*, 1994, **98**, 13669–13679.

106 M. Kitano, M. Matsuoka, M. Ueshima and M. Anpo, *Appl. Catal. A Gen.*, 2007, **325**, 1–14.

107 Y. Yan, J. Lee and X. Cui, *Vacuum*, 2017, **138**, 30–38.

108 W. Zhao, Y. Li, M. Zhang, J. Chen, L. Xie, Q. Shi and X. Zhu, *Chem. Eng. J.*, 2016, **283**, 105–113.

109 C. Wang, Z. Chen, H. Jin, C. Cao, J. Li and Z. Mi, *J. Mater. Chem. A*, 2014, **2**, 17820–17827.

110 Q. Liu, D. Ding, C. Ning and X. Wang, *Int. J. Hydrogen Energy*, 2015, **40**, 2107–2114.

111 P. Sudhagar, A. Devadoss, K. Nakata, C. Terashima and A. Fujishima, *J. Electrochem. Soc.*, 2014, **162**, H108–H114.

112 N. M. Mohamed, R. Bashiri, F. K. Chong, S. Sufian and S. Kakooei, *Int. J. Hydrogen Energy*, 2015, **40**, 14031–14038.

113 T. Zhang, B. Yu, D. Wang and F. Zhou, *J. Power Sources*, 2015, **281**, 411–416.

114 S. Wang, L. N. Bai, H. M. Sun, Q. Jiang and J. S. Lian, *Powder Technol.*, 2013, **244**, 9–15.

115 O. Avilés-García, J. Espino-Valencia, R. Romero, J. L. Rico-Cerda, M. Arroyo-Albiter and R. Natividad, *Fuel*, 2017, **198**, 31–41.

116 Y. Yang, X. J. Li, J. T. Chen and L. Y. Wang, *J. Photochem. Photobiol. A Chem.*, 2004, **163**, 517–522.

117 B. Miljević, J. M. van der Bergh, S. Vučetić, D. Lazar and J. Ranogajec, *Ceram. Int.*, 2017, **43**, 8214–8221.

118 V. Štengl and S. Bakardjieva, *J. Phys. Chem. C*, 2010, **114**, 19308–19317.

119 J. Wang, D. N. Tafen, J. P. Lewis, Z. Hong, A. Manivannan, M. Zhi, M. Li and N. Wu, *J. Am. Chem. Soc.*, 2009, **131**, 12290–12297.

120 S. Sato, *Chem. Phys. Lett.*, 1986, **123**, 126–128.

121 R. Asahi, T. Morikawa, T. Ohwaki and Y. Taga, *Science (80-.).*, 2001, **293**, 269–271.

122 Y. Ding and P. Nagpal, *Nanoscale*, 2016, **8**, 17496–17505.

123 S. Hejazi, N. T. Nguyen, A. Mazare and P. Schmuki, *Catal. Today*, 2017, **281**, 189–197.

124 J. Cao, Y. Zhang, H. Tong, P. Li, T. Kako and J. Ye, *Chem. Commun.*, 2012, **48**, 8649–8651.

125 K. Ranganathan, A. Morais, I. Nongwe, C. Longo, A. F. Nogueira and N. J. Coville, *J. Mol. Catal. A Chem.*, 2015, **422**, 165–174.

126 J. H. Park, S. Kim and A. J. Bard, *Nano Lett.*, 2006, **6**, 24–28.

127 M. Mollavali, C. Falamaki and S. Rohani, *Int. J. Hydrogen Energy*, 2015, **40**, 12239–12252.

128 P. Jong Hyeok, K. Sungwook and J. B. Allen, *Nano Lett.*, 2006, **6**, 24–28.

129 J. Tian, Z. Zhao, A. Kumar, I. Boughton and H. Liu, *Chem. Soc. Rev.*, 2014, **43**, 6920–6937.

130 Y. Lin, G. Yuan, R. Liu, S. Zhou, S. W. Sheehan and D. Wang, *Chem. Phys. Lett.*, 2011, **507**, 209–215.

131 G. Liu, H. G. Yang, J. Pan, Y. Q. Yang, G. Q. M. Lu and H. M. Cheng, *Chem. Rev.*, 2014, **114**, 9559–9612.

132 J. Pan, G. Liu, G. Q. Lu and H. M. Cheng, *Angew. Chemie Int. Ed.*, 2011, **50**, 2133–2137.

133 J. Pan, X. Wu, L. Wang, G. Liu, G. Q. Lu and H. M. Cheng, *Chem. Commun.*, 2011,

47, 8361–8363.

134 R. S. Pessoa, M. A. Fraga, L. V. Santos, M. Massi and H. S. Maciel, *Mater. Sci. Semicond. Process.*, 2015, **29**, 56–68.

135 P. Szymanski and M. A. El-Sayed, *Theor. Chem. Acc.*, 2012, **131**, 1–12.

136 M. Liu, N. De Leon Snapp and H. Park, *Chem. Sci.*, 2011, **2**, 80–87.

137 G. Wang, H. Wang, Y. Ling, Y. Tang, X. Yang, R. C. Fitzmorris, C. Wang, J. Z. Zhang and Y. Li, *Nano Lett.*, 2011, **11**, 3026–3033.

138 Z. Zhang and P. Wang, *Energy Environ. Sci.*, 2012, **5**, 6506–6512.

139 A. J. Gardecka, C. Bishop, D. Lee, S. Corby, I. P. Parkin, A. Kafizas and S. Krumdieck, *Appl. Catal. B Environ.*, 2018, **224**, 904–911.

140 A. A. Tahir, T. A. N. Peiris and K. G. U. Wijayantha, *Chem. Vap. Depos.*, 2012, **18**, 107–111.

141 I. S. Cho, Z. Chen, A. J. Forman, D. R. Kim, P. M. Rao, T. F. Jaramillo and X. Zheng, *Nano Lett.*, 2011, **11**, 4978–4984.

142 Z. Zhang, M. F. Hossain and T. Takahashi, *Int. J. Hydrogen Energy*, 2010, **35**, 8528–8535.

143 C. A. Grimes, O. K. Varghese, T. J. Latempa, K. Shankar, M. Paulose and X. Feng, *Nano Lett.*, 2008, **8**, 3781–3786.

144 Y. J. Hwang, C. Hahn, B. Liu and P. Yang, *ACS Nano*, 2012, **6**, 5060–5069.

145 A. Wolcott, W. A. Smith, T. R. Kuykendall, Y. Zhao and J. Z. Zhang, *Small*, 2009, **5**, 104–111.

146 H. Huang, X. Hou, J. Xiao, L. Zhao, Q. Huang, H. Chen and Y. Li, *Catal. Today*, 2019, **330**, 189–194.

147 P. D. Matthews, T. C. King and D. S. Wright, *Chem. Commun.*, 2014, **50**, 12815–12823.

148 P. Coppens, Y. Chen and E. Trzop, *Chem. Rev.*, 2014, **114**, 9645–9661.

149 S. Eslava, B. P. R. Goodwill, M. McPartlin and D. S. Wright, *Inorg. Chem.*, 2011, **50**, 5655–5662.

150 N. Li, P. D. Matthews, H.-K. Luo and D. S. Wright, *Chem. Commun.*, 2016, **52**, 11180–11190.

151 Y. Lv, M. Yao, J. P. Holgado, T. Roth, A. Steiner, L. Gan, R. M. Lambert, D. S. Wright, E. Reisner, X. Liang, R. Li, Z. Xu and Q. Ren, *RSC Adv.*, 2013, **3**, 13659–13662.

152 S. Eslava, A. Reynal, V. G. Rocha, S. Barg and E. Saiz, *J. Mater. Chem. A*, 2016, **4**, 7200–7206.

153 S. L. S. Structures, *J. Clust. Sci.*, 2016, **27**, 635–643.

154 Y.-Y. Wu, P. Wang, Y.-H. Wang, J.-B. Jiang, G.-Q. Bian, Q.-Y. Zhu and J. Dai, *J. Mater. Chem. A*, 2013, **1**, 9862–9868.

155 Y.-H. Lai, C.-Y. Lin, Y. Lv, T. C. King, A. Steiner, N. M. Muresan, L. Gan, D. S. Wright and E. Reisner, *Chem. Commun.*, 2013, **49**, 4331–4333.

156 M. W. Kanan and D. G. Nocera, *Science (80-.).*, 2008, **321**, 1072–1076.

157 Y. Lin, Y. F. Zhu, Z. H. Chen, F. H. Liu, L. Zhao and Z. M. Su, *Inorg. Chem. Commun.*, 2014, **40**, 22–25.

158 W. H. Fang, L. Zhang and J. Zhang, *J. Am. Chem. Soc.*, 2016, **138**, 7480–7483.

159 Y. H. Lai, T. C. King, D. S. Wright and E. Reisner, *Chem. - A Eur. J.*, 2013, **19**, 12943–12947.

160 J.-L. Hou, W. Luo, Y.-Y. Wu, H.-C. Su, G.-L. Zhang, Q.-Y. Zhu and J. Dai, *Dalton Trans.*, 2015, **44**, 19829–19835.

161 A. C. Jones and M. L. Hitchman, *Chemical Vapour Deposition: Precursors, Processes and Applications*, The Royal Society of Chemistry, 2009.

162 P. Marchand, I. A. Hassan, I. P. Parkin and C. J. Carmalt, *Dalt. Trans.*, 2013, **42**, 9406–9422.

163 M. D. Allendorf and A. M. B. van Mol, *Precursor Chem. Adv. Mater.*, 2005, **9**, 1–48.

164 US575002, 1893.

165 K. L. Choy, *Prog. Mater. Sci.*, 2003, **48**, 57–170.

166 X. Hou and K.-L. Choy, *Chem. Vap. Depos.*, 2006, **12**, 583–596.

167 S. N. Ariffin, H. N. Lim, Z. A. Talib, A. Pandikumar and N. M. Huang, *Int. J. Hydrogen Energy*, 2015, **40**, 2115–2131.

168 S. Basharat, C. J. Carmalt, R. Binions, R. Palgrave and I. P. Parkin, *J. Chem. Soc. Dalt. Trans.*, 2008, 591–595.

169 H. Kim, R. O. Bonsu, D. C. Bock, N. C. Ou, R. Y. Korotkov, L. McElwee-White and T. Anderson, *ECS J. Solid State Sci. Technol.*, 2016, **5**, Q3095–Q3105.

170 J. Akhtar, M. A. Malik, P. O'Brien and M. Helliwell, *J. Mater. Chem.*, 2010, **20**, 6116–6124.

171 S. Shakir, H. M. Abd-Ur-Rehman, K. Yunus, M. Iwamoto and V. Periasamy, *J. Alloys Compd.*, 2018, **737**, 740–747.

172 S. Sathasivam, D. S. Bhachu, Y. Lu, N. Chadwick, S. A. Althabaiti, A. O. Alyoubi, S. N. Basahel, C. J. Carmalt and I. P. Parkin, *Sci. Rep.*, 2015, **5**, 10952.

173 C. Edusi, G. Hyett, G. Sankar and I. P. Parkin, *Chem. Vap. Depos.*, 2011, **17**, 30–36.

174 M. A. Ehsan, R. Naeem, A. Rehman, A. S. Hakeem and M. Mazhar, *J. Mater. Sci. Mater. Electron.*, 2018, **29**, 13209–13219.

175 M. A. Mansoor, M. Mazhar, A. Pandikumar, H. Khaledi, H. Nay Ming and Z. Arifin, *Int. J. Hydrogen Energy*, 2016, **41**, 9267–9275.

176 M. Ling and C. Blackman, *Phys. Status Solidi C Curr. Top. Solid State Phys.*, 2015, **12**, 869–877.

177 H. Kim, R. O. Bonsu, C. Odonohue, R. Y. Korotkov, L. McElwee-White and T. J. Anderson, *ACS Appl. Mater. Interfaces*, 2015, **7**, 2660–2667.

178 C. Edusi, G. Sankar and I. P. Parkin, *Chem. Vap. Depos.*, 2012, **18**, 126–132.

179 D. B. Potter, I. P. Parkin and C. J. Carmalt, *RSC Adv.*, 2018, **8**, 33164–33173.

180 N. Noor and I. P. Parkin, *J. Mater. Chem. C*, 2013, **1**, 984–996.

181 A. A. Tahir, H. A. Burch, K. G. U. Wijayantha and B. G. Pollet, *Int. J. Hydrogen Energy*, 2013, **38**, 4315–4323.

182 M. A. Ehsan, H. N. Ming, M. Misran, Z. Arifin, E. R. T. Tiekink, A. P. Safwan, M. Ebadi, W. J. Basirun and M. Mazhar, *Chem. Vap. Depos.*, 2012, **18**, 191–200.

183 K. Nakata and A. Fujishima, *J. Photochem. Photobiol. C Photochem. Rev.*, 2012, **13**, 169–189.

184 C. Sanchez, L. Rozes, F. Ribot, C. Laberty-Robert, D. Grosso, C. Sassoye, C. Boissiere

and L. Nicole, *Comptes Rendus Chim.*, 2010, **13**, 3–39.

185 M. Ibadurrohman and K. Hellgardt, *Int. J. Hydrogen Energy*, 2014, **39**, 18204–18215.

186 G. Ai, R. Mo, H. Li and J. Zhong, *Nanoscale*, 2015, **7**, 6722–6728.

187 D. K. Zhong, M. Cornuz, K. Sivula, M. Grätzel and D. R. Gamelin, *Energy Environ. Sci.*, 2011, **4**, 1759–1764.

188 C. G. Morales-Guio, L. Liardet and X. Hu, *J. Am. Chem. Soc.*, 2016, **138**, 8946–8957.

189 B. K. Kang, G. S. Han, J. H. Baek, D. G. Lee, Y. H. Song, S. Bin Kwon, I. S. Cho, H. S. Jung and D. H. Yoon, *Adv. Mater. Interfaces*, 2017, **4**, 1700323.

190 Y. Duan, S. Zhou, Z. Chen, J. Luo, M. Zhang, F. Wang, T. Xu and C. Wang, *Catal. Sci. Technol.*, 2018, **8**, 1395–1403.

191 X. Jin, W. Sun, C. Chen, T. Wei, Y. Cheng, P. Li and Q. Li, *RSC Adv.*, 2014, **4**, 46008–46015.

192 Y. Li, H. Zhong, R. Li, Y. Zhou, C. Yang and Y. Li, *Adv. Funct. Mater.*, 2006, **16**, 1705–1716.

193 Z. Chen, Q. Li, C. Chen, J. Du, J. Tong, X. Jin, Y. Li, Y. Yuan, Y. Qin, T. Wei and W. Sun, *Phys. Chem. Chem. Phys.*, 2014, **16**, 24499–508.

194 V. V. Pavlishchuk and A. W. Addison, *Inorganica Chim. Acta*, 2000, **298**, 97–102.

195 S. Choopun, P. Mangkorntong, P. Subjareon, N. Mangkorntong, H. Tabata and T. Kawai, *Jpn. J. Appl. Phys.*, 2004, **43**, L91–L93.

196 D. A. H. Hanaor and C. C. Sorrell, *J. Mater. Sci.*, 2011, **46**, 855–874.

197 R. C. Pullar, S. J. Penn, X. Wang, I. M. Reaney and N. Mcn, *J. Eur. Ceram. Soc.*, 2009, **29**, 419–424.

198 W. M. Haynes, D. . Lide and T. . Bruno, *CRC handbook of chemistry and physics: A ready-reference book of chemical and physical data*, CRC Press, Taylor & Francis Group, 97th edn., 2016.

199 J. Yan, G. Wu, N. Guan, L. Li, Z. Li and X. Cao, *Phys. Chem. Chem. Phys.*, 2013, **15**, 10978–10988.

200 M.-C. Wu, P.-H. Lee and D.-L. Lee, *Int. J. Hydrogen Energy*, 2015, **40**, 4558–4566.

201 X. Du, L. Dong, C. Li, Y. Liang and Y. Chen, *Langmuir*, 1999, **15**, 1693–1697.

202 M. Dieterle and G. Mestl, *Phys. Chem. Chem. Phys.*, 2002, **4**, 822–826.

203 N. Illyaskutty, S. Sreedhar, G. Sanal Kumar, H. Kohler, M. Schwotzer, C. Natzeck and V. P. M. Pillai, *Nanoscale*, 2014, **6**, 13882–13894.

204 L. G. Devi and B. N. Murthy, *Catal. Letters*, 2008, **125**, 320–330.

205 R. Sanjinés, H. Tang, H. Berger, F. Gozzo, G. Margaritondo and F. Lévy, *J. Appl. Phys.*, 1994, **75**, 2945–2951.

206 J. G. Choi and L. T. Thompson, *Appl. Surf. Sci.*, 1996, **93**, 143–149.

207 W. Zhou, Z. Yin, Y. Du, X. Huang, Z. Zeng, Z. Fan, H. Liu, J. Wang and H. Zhang, *Small*, 2013, **9**, 140–147.

208 Z. Chen, D. Cummins, B. N. Reinecke, E. Clark, M. K. Sunkara and T. F. Jaramillo, *Nano Lett.*, 2011, **11**, 4168–4175.

209 X. Xiao, T. Ding, L. Yuan, Y. Shen, Q. Zhong, X. Zhang, Y. Cao, B. Hu, T. Zhai, L. Gong, J. Chen, Y. Tong, J. Zhou and Z. L. Wang, *Adv. Energy Mater.*, 2012, **2**, 1328–1332.

210 W. Li, C. Ni, H. Lin, C. P. Huang and S. I. Shah, *J. Appl. Phys.*, 2004, **96**, 6663–6668.

211 Y. F. Chen, C. Y. Lee, M. Y. Yeng and H. T. Chiu, *J. Cryst. Growth*, 2003, **247**, 363–370.

212 Y. Gai, J. Li, S. S. Li, J. B. Xia and S. H. Wei, *Phys. Rev. Lett.*, 2009, **102**, 23–26.

213 B. Choudhury and A. Choudhury, *Phys. E Low-Dimensional Syst. Nanostructures*, 2014, **56**, 364–371.

214 K. Mahesh, S. Karpagam and F. Goubard, *Express Polym. Lett.*, 2018, **12**, 238–255.

215 Z. He, Q. Cai, H. Fang, G. Situ, J. Qiu, S. Song and J. Chen, *J. Environ. Sci.*, 2013, **25**, 2460–2468.

216 Z. Rui, S. Wu, C. Peng and H. Ji, *Chem. Eng. J.*, 2014, **243**, 254–264.

217 Y. Gao, H. Wang, J. Wu, R. Zhao, Y. Lu and B. Xin, *Appl. Surf. Sci.*, 2014, **294**, 36–41.

218 J. Zhang, R. García-Rodríguez, P. Cameron and S. Eslava, *Energy Environ. Sci.*, 2018, **11**, 2972–2984.

219 T. Luttrell, S. Halpegamage, J. Tao, A. Kramer, E. Sutter and M. Batzill, *Sci. Rep.*, 2014, **4**, 4043.

220 R. R. Devarapalli, J. Debgupta, V. K. Pillai and M. V. Shelke, *Sci. Rep.*, 2014, **4**, 1–8.

221 D. C. Cronzmeyer, *Phys. Rev.*, 1959, **113**, 1222–1226.

222 B. D. Cullity, *Elements of X-Ray Diffraction*, Addison-Wesley Publishing Company Inc., London, 2nd edn., 1978.

223 B. Yarmand and S. K. Sadrnezhaad, *J. Optoelectron. Adv. Mater.*, 2010, **12**, 1490–1497.

224 Y. Li, N. Guijarro, X. Zhang, M. S. Prévot, X. A. Jeanbourquin, K. Sivula, H. Chen and Y. Li, *ACS Appl. Mater. Interfaces*, 2015, **7**, 16999–17007.

225 P. Periyat, B. Naufal and S. G. Ullattil, *Mater. Sci. Forum*, 2016, **855**, 78–93.

226 M. Ge, C. Cao, J. Huang, S. Li, Z. Chen, K.-Q. Zhang, S. S. Al-Deyab and Y. Lai, *J. Mater. Chem. A*, 2016, **4**, 6772–6801.

227 L. Liu, Y. Du, X. Niu, W. Li, J. Li, X. Yang and Q. Feng, *ChemistrySelect*, 2018, **3**, 9953–9959.

228 P. Wen, H. Itoh, W. Tang and Q. Feng, *Langmuir*, 2007, **23**, 11782–11790.

229 C. Chen, L. Xu, G. A. Sewvandi, T. Kusunose, Y. Tanaka, S. Nakanishi and Q. Feng, *Cryst. Growth Des.*, 2014, **14**, 5801–5811.

230 D. V Bavykin, V. N. Parmon, A. Lapkin and F. C. Walsh, *J. Mater. Chem.*, 2004, **14**, 3370–3377.

231 Q. Liu, H. Lu, Z. Shi, F. Wu, J. Guo, K. Deng and L. Li, *ACS Appl. Mater. Interfaces*, 2014, **6**, 17200–17207.

232 M. Xu, P. Da, H. Wu, D. Zhao and G. Zheng, *Nano Lett.*, 2012, **12**, 1503–1508.

233 H. Li, Y. Wang, G. Chen, Y. Sang, H. Jiang, J. He, X. Li and H. Liu, *Nanoscale*, 2016, **8**, 6101–6109.

234 G. Wu, J. Wang, D. F. Thomas and A. Chen, *Langmuir*, 2008, **24**, 3503–3509.

235 V. Diesen, C. W. Dunnill, J. C. Bear, S. Firth, M. Jonsson and I. P. Parkin, *Chem. Vap. Depos.*, 2014, **20**, 91–97.

236 J. S. Chen and X. W. (David) Lou, *Chem. Sci.*, 2011, **2**, 2219–2223.

237 M. S. Park, D. Walsh, J. Zhang, J. H. Kim and S. Eslava, *J. Power Sources*, 2018, **404**, 149–158.

238 Y. Hu, C. Li, F. Gu and Y. Zhao, *J. Alloys Compd.*, 2007, **432**, 5–9.

239 J. S. J. Hargreaves, *Catal. Struct. React.*, 2016, **2**, 33–37.

240 G. B. Harris, *London, Edinburgh, Dublin Philos. Mag. J. Sci.*, 1952, **43**, 113–123.

241 J. E. Kroeze, T. J. Savenije and J. M. Warman, *J. Am. Chem. Soc.*, 2004, **126**, 7608–7618.

242 J. T. Carneiro, T. J. Savenije and G. Mul, *Phys. Chem. Chem. Phys.*, 2009, **11**, 2708–2714.

243 F. F. Abdi, T. J. Savenije, M. M. May, B. Dam and R. van de Krol, *J. Phys. Chem. Lett.*, 2013, **4**, 2752–2757.

244 I. Oja, A. Mere, M. Krunks, R. Nisumaa, C. H. Solterbeck and M. Es-Souni, *Thin Solid Films*, 2006, **515**, 674–677.

245 C. R. Lhermitte, J. Garret Verwer and B. M. Bartlett, *J. Mater. Chem. A*, 2016, **4**, 2960–2968.

246 H. Jia, J. Stark, L. Q. Zhou, C. Ling, T. Sekito and Z. Markin, *RSC Adv.*, 2012, **2**, 10874–10881.

247 K. Watenpaugh and C. N. Caughlan, *Chem. Commun.*, 1967, 76–77.

248 R. Schmid, A. Mosset and J. Galy, *J. Chem. Soc., Dalt. Trans.*, 1991, **8**, 1999–2005.

249 Z. Liu, Y. Zheng, T. Gao, J. Zhang, X. Sun and G. Zhou, *Int. J. Hydrogen Energy*, 2017, **42**, 21775–21785.

250 L. Wang, L. Zang, J. Zhao and C. Wang, *Chem. Commun.*, 2012, **48**, 11736–11738.

251 M. C. Biesinger, L. W. M. Lau, A. R. Gerson and R. S. C. Smart, *Appl. Surf. Sci.*, 2010, **257**, 887–898.

252 P. Georgios and S. M. Wolfgang, *Solid State Phenom.*, 2010, **162**, 163–177.

253 Q. Zhang, N. Bao, X. Wang, X. Hu, X. Miao, M. Chaker and D. Ma, *Sci. Rep.*, 2016, **6**, 1–15.

254 D. Zhao, X. Yang, C. Chen and X. Wang, *J. Colloid Interface Sci.*, 2013, **398**, 234–239.

255 A. A. Galuska, J. C. Uht and N. Marquez, *J. Vac. Sci. Technol. A*, 1988, **6**, 110–122.

256 H. Kolev, K. L. Kostov, G. Tyuliev and C. Christov, *Nanosci. Nanotechnol.*, 2013, **13**, 29–32.

257 G. A. Battiston, R. Gerbasi, M. Porchia and A. Marigo, *Thin Solid Films*, 1994, **239**, 186–191.

258 L. Ye, J. Liu, L. Tian, T. Peng and L. Zan, *Appl. Catal. B Environ.*, 2013, **134**–**135**, 60–65.

259 L. Pan, J.-J. Zou, S. Wang, X.-Y. Liu, X. Zhang and L. Wang, *ACS Appl. Mater. Interfaces*, 2012, **4**, 1650–1655.

260 C. K. Nguyen, H. G. Cha and Y. S. Kang, *Cryst. Growth Des.*, 2011, **11**, 3947–3953.

261 N. Avci, P. F. Smet, H. Poelman, N. Van De Velde, K. De Buysser, I. Van Driessche and D. Poelman, *J. Sol-Gel Sci. Technol.*, 2009, **52**, 424–431.

262 B. M. Rao and S. C. Roy, *RSC Adv.*, 2014, **4**, 38133–38139.

263 A. L. Castro, M. R. Nunes, A. P. Carvalho, F. M. Costa and M. H. Florêncio, *Solid State Sci.*, 2008, **10**, 602–606.

264 D. Bersani, P. P. Lottici and X.-Z. Ding, *Appl. Phys. Lett.*, 1998, **72**, 73–75.

265 S. Wang, L. Zhao, L. Bai, J. Yan, Q. Jiang and J. Lian, *J. Mater. Chem. A*, 2014, **2**, 7439–7445.

266 N. L. Wu, S. Y. Wang and I. A. Rusakova, *Science (80-.).*, 1999, **285**, 1375–1377.

267 U. Balachandran and N. G. Eror, *J. Solid State Chem.*, 1982, **42**, 276–282.

268 S. A. El-Khodary, G. M. El-Enany, M. El-Okr and M. Ibrahim, *Electrochim. Acta*, 2014, **150**, 269–278.

269 L. Bin Xiong, J. L. Li, B. Yang and Y. Yu, *J. Nanomater.*, 2012, **2012**, 1–13.

270 L. Zhou, Y. Yang, J. Zhang and P. M. Rao, *ACS Appl. Mater. Interfaces*, 2017, **9**, 11356–11362.

271 W. H. Leng, P. R. F. Barnes, M. Juozapavicius, B. C. O'Regan and J. R. Durrant, *J. Phys. Chem. Lett.*, 2010, **1**, 967–972.

272 R. Katoh, A. Furube, K. I. Yamanaka and T. Morikawa, *J. Phys. Chem. Lett.*, 2010, **1**, 3261–3265.

273 J. Ravensbergen, F. F. Abdi, J. H. Van Santen, R. N. Frese, B. Dam, R. Van De Krol and J. T. M. Kennis, *J. Phys. Chem. C*, 2014, **118**, 27793–27800.

274 M. Kuno, D. P. Fromm, H. F. Hamann, A. Gallagher and D. J. Nesbitt, *J. Chem. Phys.*, 2002, **112**, 3117–3120.

275 J. Nelson and R. E. Chandler, *Coord. Chem. Rev.*, 2004, **248**, 1181–1194.

276 P. H. Sher, J. M. Smith, P. A. Dalgarno, R. J. Warburton, X. Chen, P. J. Dobson, S. M. Daniels, N. L. Pickett and P. O'Brien, *Appl. Phys. Lett.*, 2008, **92**, 101111.

277 S. Nakajima and R. Katoh, *J. Mater. Chem. A*, 2015, **3**, 15466–15472.

278 B. Neumann, P. Bogdanoff, H. Tributsch, S. Sakthivel and H. Kisch, *J. Phys. Chem. B*, 2005, **109**, 16579–16586.

279 T. Guminskaya, K. Ellmer, P. Bogdanoff, U. Koslowski, T. Dittrich and H. Tributsch, *J. Vac. Sci. Technol. A*, 2006, **24**, 2199–2205.

280 X. Wang, J. Xie and C. Ming Li, *J. Mater. Chem. A*, 2015, **3**, 1235–1242.

281 L. Sun, J. Cai, Q. Wu, P. Huang, Y. Su and C. Lin, *Electrochim. Acta*, 2013, **108**, 525–531.

282 R. Beranek, *Adv. Phys. Chem.*, 2011, **2011**, 80–83.

283 P. Piszczek, M. Richert and A. Wojtczak, *Polyhedron*, 2008, **27**, 602–608.

284 L. R. Snyder, J. J. Kirkland and J. W. Dolan, in *Introduction to Modern Liquid Chromatography*, John Wiley & Sons, Inc., Third., 2010, pp. 879–886.

285 C. Reichardt, *Solvents and Solvent Effects in Organic Chemistry*, Wiley-VCH Publishers, 3rd edn., 2003.

286 H. Dotan, K. Sivula, M. Grätzel, A. Rothschild and S. C. Warren, *Energy Environ. Sci.*, 2011, **4**, 958–964.

287 H. Zhu, S. Yan, Z. Li and Z. Zou, *ACS Appl. Mater. Interfaces*, 2017, **9**, 33887–33895.

288 C. Ding, J. Shi, Z. Wang and C. Li, *ACS Catal.*, 2017, **7**, 675–688.

289 Y. Surendranath, M. W. Kanan and D. G. Nocera, *J. Am. Chem. Soc.*, 2010, **132**, 16501–16509.

290 A. J. Cowan, J. Tang, W. Leng, J. R. Durrant and D. R. Klug, *J. Phys. Chem. C*, 2010, **114**, 4208–4214.

291 A. Kafizas, Y. Ma, E. Pastor, S. R. Pendlebury, C. Mesa, L. Francàs, F. Le Formal, N. Noor, M. Ling, C. Sotelo-Vazquez, C. J. Carmalt, I. P. Parkin and J. R. Durrant, *ACS Catal.*, 2017, **7**, 4896–4903.

292 J. Tang, J. R. Durrant and D. R. Klug, *J. Am. Chem. Soc.*, 2008, **130**, 13885–13891.

293 X. Wang, A. Kafizas, X. Li, S. J. A. Moniz, P. J. T. Reardon, J. Tang, I. P. Parkin and J. R. Durrant, *J. Phys. Chem. C*, 2015, **119**, 10439–10447.

294 F. Le Formal, E. Pastor, S. D. Tilley, C. A. Mesa, S. R. Pendlebury, M. Grätzel and J. R. Durrant, *J. Am. Chem. Soc.*, 2015, **137**, 6629–6637.

295 World Energy Council, *Solar*, 2013.

296 Y. Lin, G. Yuan, S. Sheehan, S. Zhou and D. Wang, *Energy Environ. Sci.*, 2011, **4**, 4862–4869.

297 P. S. Bassi, Gurudayal, L. H. Wong and J. Barber, *Phys. Chem. Chem. Phys.*, 2014, **16**, 11834–11842.

298 J. Zhang and S. Eslava, *Sustain. Energy Fuels*, 2019, **3**, 1351–1364.

299 O. S. Hammond, S. Eslava, A. J. Smith, J. Zhang and K. J. Edler, *J. Mater. Chem. A*, 2017, **5**, 16189–16199.

300 M. Regue, K. Armstrong, D. Walsh, E. Richards, A. L. Johnson and S. Eslava, *Sustain. Energy Fuels*, 2018, **2**, 2674–2686.

301 M. Regue, S. Sibby, I. Y. Ahmet, D. Friedrich, F. F. Abdi, A. L. Johnson and S. Eslava, *J. Mater. Chem. A*, 2019, **7**, 19161–19172.

302 E. Verlage, S. Hu, R. Liu, R. J. R. Jones, K. Sun, C. Xiang, N. S. Lewis and H. A. Atwater, *Energy Environ. Sci.*, 2015, **8**, 3166–3172.

303 E. Courtin, G. Baldinozzi, M. T. Sougrati, L. Stievano, C. Sanchez and C. Laberty-Robert, *J. Mater. Chem. A*, 2014, **2**, 6567–6577.

304 Z. Luo, T. Wang, S. Liu, J. Gong and C. Li, *Small*, 2016, **12**, 3415–3422.

305 S. Kuang, M. Wang, Z. Geng, X. Wu, Y. Sun, W. Ma, D. Chen, J. Liu, S. Feng and K. Huang, *ACS Sustain. Chem. Eng.*, 2019, **7**, 14347–14352.

306 G. R. Torres, T. Lindgren, J. Lu, C.-G. Granqvist and S.-E. Lindquist, *J. Phys. Chem. B*, 2004, **108**, 5995–6003.

307 V. R. Satsangi, S. Kumari, A. P. Singh, R. Shrivastav and S. Dass, *Int. Work. Hydrog. Energy - Prod. Storage Appl.*, 2006, **33**, 312–318.

308 C. J. Sartoretti, B. D. Alexander, R. Solarska, I. A. Rutkowska, J. Augustynski and R. Cerny, *J. Phys. Chem. B*, 2005, **109**, 13685–13692.

309 W. B. Ingler, J. P. Baltrus and S. U. M. Khan, *J. Am. Chem. Soc.*, 2004, **126**, 10238–10239.

310 X. Qi, G. She, M. Wang, L. Mu and W. Shi, *Chem. Commun.*, 2013, **49**, 5742–5744.

311 C. Y. Su, L. C. Wang, W. S. Liu, C. C. Wang and T. P. Perng, *ACS Appl. Mater. Interfaces*, 2018, **10**, 33287–33295.

312 O. Linnik, N. Chorna and N. Smirnova, *Nanoscale Res. Lett.*, 2017, **12**, 249.

313 N. Chorna, N. Smirnova, V. Vorobets, G. Kolbasov and O. Linnik, *Appl. Surf. Sci.*, 2019, **473**, 343–351.

314 S. Sathasivam, D. S. Bhachu, Y. Lu, S. M. Bawaked, A. Y. Obaid, S. Al-Thabaiti, S. N. Basahel, C. J. Carmalt and I. P. Parkin, *Chem. Vap. Depos.*, 2015, **21**, 21–25.

315 F. J. Berry, C. Greaves, Ö. Helgason, J. McManus, H. M. Palmer and R. T. Williams, *J. Solid State Chem.*, 2000, **151**, 157–162.

316 B. Ahmmad, K. Leonard, M. Shariful Islam, J. Kurawaki, M. Muruganandham, T. Ohkubo and Y. Kuroda, *Adv. Powder Technol.*, 2013, **24**, 160–167.

317 A. Lassoued, B. Dkhil, A. Gadri and S. Ammar, *Results Phys.*, 2017, **7**, 3007–3015.

318 D. Bersani, P. P. Lottici and A. Montenero, *J. Mater. Sci.*, 2000, **35**, 4301–4305.

319 L. Wang, N. T. Nguyen and P. Schmuki, *ChemSusChem*, 2016, **9**, 2048–2053.

320 L. Wang, N. T. Nguyen, X. Huang, P. Schmuki and Y. Bi, *Adv. Funct. Mater.*, 2017, **27**, 1703527.

321 T. T. Loan, V. H. Huong, V. T. Tham and N. N. Long, *Phys. B Condens. Matter*, 2018, **532**, 210–215.

322 D. Walsh, J. Zhang, M. Regue, R. Dassanayake and S. Eslava, *ACS Appl. Energy Mater.*, 2019, **2**, 2043–2052.

323 Y. Zhao, C. Li, X. Liu, F. Gu, H. L. Du and L. Shi, *Appl. Catal. B Environ.*, 2008, **79**, 208–215.

324 N. Khatun, S. Tiwari, C. P. Vinod, C. M. Tseng, S. Wei Liu, S. Biring and S. Sen, *J. Appl. Phys.*, 2018, **123**, 245702.

325 N. S. McIntyre and D. G. Zetaruk, *Anal. Chem.*, 1977, **49**, 1521–1529.

326 N. Mirbagheri, D. Wang, C. Peng, J. Wang, Q. Huang, C. Fan and E. E. Ferapontova, *ACS Catal.*, 2014, **4**, 2006–2015.

327 N. T. Hahn and C. B. Mullins, *Chem. Mater.*, 2010, **22**, 6474–6482.

328 B. Klahr, S. Gimenez, F. Fabregat-Santiago, J. Bisquert and T. W. Hamann, *Energy Environ. Sci.*, 2012, **5**, 7626–7636.

329 L. Liardet, J. E. Katz, J. Luo, M. Grätzel and X. Hu, *J. Mater. Chem. A*, 2019, 6012–6020.

330 Z. Luo, C. Li, S. Liu, T. Wang and J. Gong, *Chem. Sci.*, 2016, **8**, 91–100.

331 F. Le Formal, K. Sivula and M. Grätzel, *J. Phys. Chem. C*, 2012, **116**, 26707–26720.

332 B. Klahr, S. Gimenez, F. Fabregat-Santiago, T. Hamann and J. Bisquert, *J. Am. Chem. Soc.*, 2012, **134**, 4294–4302.

333 P. Tang, H. Xie, C. Ros, L. Han, M. Biset-Peiró, Y. He, W. Kramer, A. P. Rodríguez, E. Saucedo, J. R. Galán-Mascarós, T. Andreu, J. R. Morante and J. Arbiol, *Energy Environ. Sci.*, 2017, **10**, 2124–2136.

334 D. Monllor-Satoca, M. Bärtsch, C. Fàbrega, A. Genç, S. Reinhard, T. Andreu, J. Arbiol, M. Niederberger and J. R. Morante, *Energy Environ. Sci.*, 2015, **8**, 3242–3254.

335 J. Gao, C. L. Perkins, J. M. Luther, M. C. Hanna, H. Y. Chen, O. E. Semonin, A. J. Nozik, R. J. Ellingson and M. C. Beard, *Nano Lett.*, 2011, **11**, 3263–3266.

336 M. Kölbach, I. J. Pereira, K. Harbauer, P. Plate, K. Höflich, S. P. Berglund, D. Friedrich, R. Van De Krol and F. F. Abdi, *Chem. Mater.*, 2018, **30**, 8322–8331.

337 F. Kraushofer, Z. Jakub, M. Bichler, J. Hulva, P. Drmota, M. Weinold, M. Schmid, M.

Setvin, U. Diebold, P. Blaha and G. S. Parkinson, *J. Phys. Chem. C*, 2018, **122**, 1657–1669.

338 F. Zhu, P. Zhang, X. Wu, L. Fu, J. Zhang and D. Xu, *ChemPhysChem*, 2012, **13**, 3731–3737.